Observatório Nacional

TESE DE DOUTORADO

DE ESTRELAS DO CAMPO A AGLOMERADOS ABERTOS: ESTUDOS QUÍMICOS BASEADOS EM ESPECTROS DE ALTA RESOLUÇÃO

JOSÉ NACIZO HOLANDA LUCIANO JUNIOR

RIO DE JANEIRO
2020

Ministério da Ciência, Tecnologia, Inovações e Comunicações
Observatório Nacional
Programa de Pós-Graduação

Tese de Doutorado

DE ESTRELAS DO CAMPO A AGLOMERADOS ABERTOS: ESTUDOS QUÍMICOS BASEADOS EM ESPECTROS DE ALTA RESOLUÇÃO

por

José Nacizo Holanda Luciano Junior

Tese submetida ao Corpo Docente do Programa de Pós-graduação em Astronomia do Observatório Nacional, como parte dos requisitos necessários para a obtenção do Grau de Doutor em Astronomia.

Orientador: Dr. Claudio Bastos Pereira

Rio de Janeiro, RJ – Brasil
Janeiro de 2020

J837 José Nacizo Holanda Luciano Junior,
De estrelas do campo a aglomerados abertos: estudos químicos baseados em espectros de alta resolução [Rio de Janeiro] 2020.
xxvii, 161 p. 29,7 cm: graf. il. tab.

Tese (doutorado) - Observatório Nacional - Rio de Janeiro, 2020.

1. Estrelas. 2. Abundâncias. 3. Aglomerados Abertos. 4. Estrelas Peculiares. I. Observatório Nacional. II. Título.

CDU 000.000.000

"DE ESTRELAS DO CAMPO A AGLOMERADOS ABERTOS: ESTUDOS QUÍMICOS BASEADOS EM ESPECTROS DE ALTA RESOLUÇÃO"

JOSÉ NACIZO HOLANDA LUCIANO JUNIOR

TESE SUBMETIDA AO CORPO DOCENTE DO PROGRAMA DE PÓS-GRADUAÇÃO EM ASTRONOMIA DO OBSERVATÓRIO NACIONAL COMO PARTE DOS REQUISITOS NECESSÁRIOS PARA A OBTENÇÃO DO GRAU DE DOUTOR EM ASTRONOMIA.

Aprovada por:

Dr. Claudio Bastos Pereira – ON
(Orientador)

Dra. Simone Daflon dos Santos – ON

Dra. Carolina Andrea Chavero – Obs. de Córdoba

Dr. Francisco Ferreira de Souza Maia – UFRJ

Dr. Wagner José Corradi Barbosa – LNA

RIO DE JANEIRO, RJ – BRASIL
28 DE JANEIRO DE 2020

⋆

"Twinkle, twinkle, little star,
How I wonder what you are!
Up above the world so high,
Like a diamond in the sky.

⋆

When the blazing sun is gone,
When he nothing shines upon,
Then you show your little light,
Twinkle, twinkle, all the night.

⋆

Then the traveler in the dark
Thanks you for your tiny spark,
How could he see where to go,
If you did not twinkle so?

⋆

In the dark blue sky you keep,
Often through my curtains peep
For you never shut your eye,
Till the sun is in the sky.

⋆

As your bright and tiny spark
Lights the traveler in the dark,
Though I know not what you are,
Twinkle, twinkle, little star."

⋆

By Jane Taylor
"Rhymes for the Nursery" (1806)

⋆

À memória da pequena Olívia.

Agradecimentos

Meu doutorado no Observatório Nacional foi verdadeiramente transformador. Gostaria de expressar meu mais profundo agradecimento àqueles que me ajudaram ao longo dessa caminhada.

Agradeço imensamente ao meu orientador Cláudio Bastos, por ter aceitado esta orientação e por todos os ensinamentos ao longo do curso de doutorado. Seu conhecimento, paciência e bom humor foram fundamentais para o desenvolvimento deste trabalho.

Também, quero agradecer aos bons professores e colegas do Observatório Nacional. Em especial, Vladimir Ortega, Flávio Pereira, Marcelo Borges, Carolina Feliciano e Marçal Evangelista. Todos tiveram uma participação significativa e motivadora.

Agradeço a todos os funcionários do Observatório Nacional: o pessoal da limpeza, os vigias e os secretários. Todos eles contribuem para a construção de um ambiente confortável e propício para a presquisa científica.

Agradeço à Natalia Drake. Suas críticas, ensinamentos e atenção ajudaram no meu processo de amadurecimento. Muito obrigado, Natália!

Meus agradecimentos também aos colegas do projeto Astronomia na Rua, que partilharam comigo o desejo de comunicar e divulgar Astronomia para pessoas menos favorecidas e carentes de atenção. Vocês representam um sentimento de esperança e mudança muito necessário!

Agradeço à Coordenação de Aperfeiçoamento de Pessoal de Nível Superior (CAPES) e Fundação de Amparo à Pesquisa do Estado do Rio de Janeiro (FAPERJ), que fomentaram minha formação e pesquisa desenvolvidas no Instituto.

Por último, agradeço aos meus familiares que, desde o início, confiaram em mim. À minha esposa, Bruna, por todo o apoio incondicional e por aceitar me dividir com a Astronomia.

José Nacizo Holanda Luciano Junior

DE ESTRELAS DO CAMPO A AGLOMERADOS ABERTOS: ESTUDOS QUÍMICOS BASEADOS EM ESPECTROS DE ALTA RESOLUÇÃO

RESUMO

Este trabalho apresenta quatro estudos químicos compreensivos sobre estrelas gigantes vermelhas pertencentes ao campo e a dois aglomerados abertos. Os alvos são as gigantes do campo HD 150382 e TYC 8327-1678-1, que são consideradas ricas em lítio, e as populações de gigantes vermelhas dos aglomerados abertos jovens NGC 2345 e NGC 6124. O método de análise espectroscópica padrão foi adotado e os nossos resultados estão baseados em espectro de alta resolução, $R \approx 48000$. Ao estudar os aglomerados abertos, nós determinamos abundâncias para 20 espécies químicas e encontramos a velocidade rotacional projetada ($v \sin i$), que em alguns casos pode afetar a abundância de alguns elementos traçadores de mistura profunda/extra. Por outro lado, quando estudamos as estrelas gigantes ricas em Li, nós buscamos testar modelos alternativos e fornecermos vinculos observacionais para o aprimoramento desses, visto que o enriquecimento de lítio em gigantes vermelhas segue como um quebra-cabeças ainda sem solução para a astrofísica estelar. Idade, massa, distância, entre outros, são obtidos e uma discussão pontual onde eventuais peculiaridades, químicas ou cinemáticas, é apresentada. Como parte dos resultados, nós não encontramos um mecanísmo ou hipótese única que explicasse o enriquecimento de lítio nos nossos alvos – defendemos as hipóteses de *cool bottom processing* e *merger* entre anã branca de He e uma estrela gigante vermelha. Sobre os aglomerados, verificamos a baixa abundância média de ferro para o NGC 2345, dada sua distância galactocêntrica, e uma incidência pouco comum de rotadores rápidos e anômolos compondo a população de gigantes vermelhas do NGC 6124.

José Nacizo Holanda Luciano Junior

FROM FIELD STARS TO OPEN CLUSTERS: CHEMICAL STUDIES BASED ON HIGH RESOLUTION SPECTRA

ABSTRACT

This work presents four comprehensive chemical studies about red giant stars belonging to the field and two open clusters. The targets are the giants HD 150382 and TYC 8327-1678-1, which are classified as lithium-rich giant stars, and the red giant populations of the young open clusters NGC 2345 and NGC 6124.The standard spectroscopic analysis method was adopted and our results are based on high resolution spectrum, R≈48000. When studying open clusters, we determined abundances for 20 chemical species and found the projected rotational velocity (v sin i), which in some cases can affect the abundance of some deep/extra mixing tracers. On the other hand, when we study the Li-rich giant stars, we seek to test alternative models and provide observational constraints to improve these models, since the enrichment of lithium in red giants continues as a puzzle for stellar astrophysics. Age, mass, distance, among others, are obtained and a punctual discussion where eventual peculiarities, chemical or cinematic, is presented. As part of the results, we did not find a single hypothesis that explained the lithium enrichment in our targets - we defend the hypotheses of cool bottom processing and merger between an He white dwarf and a red giant star. We verified the low average iron abundance for NGC 2345, given its galactocentric distance, and an uncommon incidence of anomalous and rapid rotators composing the population of red giants of NGC 6124.

Lista de Figuras

Lista de Tabelas

Sumário

Capítulo 1

Introdução

Nos aglomerados estelares abertos podemos supor que todas as estrelas são formadas na mesma nuvem molecular, praticamente ao mesmo tempo, à mesma distância e com composição química similar – essas considerações tornam as estrelas de aglomerados abertos excelentes laboratórios para o estudo da evolução estelar e Galáctica sob o ponto de vista químico. Em particular, os aglomerados abertos jovens são excelentes traçadores da estrutura espiral e ferramentas úteis para estudar a formação estelar recente na Via Láctea (LADA & LADA, 2003).

Neste contexto, apresentamos resultados para as abundâncias elementares de estrelas gigantes vermelhas pertencentes aos aglomerados abertos jovens NGC 2345 e NGC 6124. Os parâmetros atmosféricos e abundâncias químicas das estrelas analizadas foram encontrados com base em dados de espectroscopia de alta resolução (R $\approx$ 48.000) na região do óptico. Encontramos a abundância de elementos leves (Li, C, N), razão isótopica do carbono (^{12}C/^{13}C), elementos de Z-ímpar (Na, Al), elementos-α (Mg, Si, Ca, Ti), elementos do pico do Fe (Cr, Fe , Ni) e elementos produzidos no processo de captura de neutrons (Y, Zr, La, Ce, Nd, Sm, Eu) para cada estrela. As abundâncias dos elementos leves, razão isotópica e európio são obtidas usando a técnica de síntese espectral. Além disso, as velocidades de rotação (v sin i) são encontradas realizando a síntese espectral de linhas isoladas de ferro.

No total, foram analisados cinco espectros provenientes de gigantes vermelhas do NGC 2345 e sete espectros provenientes de gigantes vermelhas do NGC 6124. Nesse último, verificamos que quatro estrelas apresentam valores elevados de velocidade rotacional projetada. É bem conhecido na literatura que ao evoluirem para o Ramo das Gigantes Vermelhas, após a fase de anã da sequência principal, ocorre uma grande expansão da envoltória das estrelas, o que impõe velocidades rotacionais superficiais muito baixas. Contudo, existem gigantes do tipo espectral G e K ($\approx$ 2 %) que apresentam valores altos para v sin i (CARLBERG ET AL., 2011; DE MEDEIROS ET AL., 1996). Por isso, uma etapa importante deste projeto consiste na análise química desses objetos peculiares. O perfil das linhas de absorção de estrelas com valores elevados de v sin i dificulta e às vezes

impossibilita o processo de determinação de abundâncias, portanto, apresentamos solução espectroscópica para quatro gigantes: #1, #29, #36 e #233. As gigantes #14, #34, #43, #50 e #60 do aglomerado NGC 2345 não apresentaram dificuldade semelhante.

Entre os elementos leves, o lítio pode ser considerado o indicador mais útil da evolução estelar. Sensível a eventos de mistura, esse elemento é exaurido à temperaturas $\geqslant 2{,}5 \times 10^6$ K através da reação ^{7}Li(p, α)^{4}He. Isso faz do lítio um elemento singular para compreender processos que ocorrem no interior estelar, mistura-extra e eventuais mecanismos externos de enriquecimento. Normalmente, a depleção do Li remanescente da fase de Sequência Principal ocorre na ascensão para o Ramo das Gigantes Vermelhas, onde a estrela experimenta o primeiro evento de dragagem que leva o material da superfície para as camadas mais internas que estão sob temperaturas mais altas. Não obstante, DRAKE ET AL. (2002) verificou uma possível correlação entre gigantes ricas em lítio e alta velocidade de rotação projetada.

Nesta discussão, inserimos os objetos do campo HD 150382 e TYC 8327-1678-1, que são ricos em lítio. A metologia para o levantamento de informações físicas e químicas foi a mesma adotada no estudo das estrelas dos aglomerados abertos anteriormente citados, exceto no que se refere à síntese de lítio. Neste caso, nós usamos as regiões próximas as linhas 6104 Å e 6708 Å, devido a intensidade das linhas. Além disso, determinamos o estágio evolutivo das duas gigantes do campo para uma posterior discussão acerca dos cenários mais plausíveis que podem explicar o enriquecimento ou a manutenção do Li nesses objetos – por exemplo, acreção planetária, *Cool Bottom Processing*, *merge* entre gigante vermelha e anã-branca de hélio.

Podemos destacar a importância destas pesquisas por se tratarem de investigações acerca não somente de dois aglomerados de estrelas atípicos, mas também de estrelas isoladas que apresentam peculiaridades químicas e físicas inerentes a 1%-2% das estrelas no mesmo estágio evolutivo (BROWN ET AL., 1989; BHARAT KUMAR ET AL., 2011; SMILJANIC ET AL., 2018). O teste de modelos canônicos e não-canônicos de mistura química é de importância ímpar para seu estabelecimento e também na conexão de teorias que possam contemplar e explicar a natureza peculiar de estrelas que são verdadeiros quebra-cabeças para a astrofísica.

Nos Capítulos 2 e 3 nós apresentamos algumas ideias gerais sobre evolução estelar, nucleossíntese e aglomerados abertos. Em seguida, no Capítulo 4, apresentamos a metodologia utilizada no nosso conjunto de trabalhos. Nos Capítulos 5 e 6 nós discorremos sobre os resultados obtidos para as estrelas do campo HD 150382 e TYC 8327-1678-1, onde o texto é baseado nas publicações HOLANDA ET AL. (2020a) e HOLANDA ET AL. (2020b), respectivamente. Nos Capítulos 7 e 8 são expostos os resultados sobre os estudos dos aglomerados abertos NGC 2345 e NGC 6124, que têm o texto fundamentado nos trabalhos HOLANDA ET AL. (2019) e HOLANDA ET AL. (2021; em preparação). Por fim, apresentaremos as conclusões gerais e perspectivas no Capítulo 9.

Capítulo 2

Ideias gerais de Evolução e Nucleossíntese Estelar

Logo após o *Big Bang* o Universo alcançou condições para a formação das partículas fundamentais e núcleos atômicos mais leves à medida que se expandia e esfriava. Nessa nucleossíntese primordial prótons e nêutrons deram origem à espécies como ^{2}H, ^{3}He, ^{4}He e ^{7}Li.

É possível que alguns elementos leves sejam produzidos por reações de espalação – esse processo ocorre no meio interestelar, dando origem principalmente a elementos como ^{6,7}Li, ^{9}Be e ^{10,11}B, como produto das colisões de raios cósmicos com núcleos do meio interestelar (PAGEL, 2009). Além disso, reações que ocorrem no interior estelar podem contribuir como outra fonte e/ou criar espécies químicas mais pesadas. Processos "explosivos" como Novas, Supernovas e *mergers* entre objetos compactos, também são fontes que criam nucleos leves e pesados.

A seguir apresentaremos um breve resumo que aborda a evolução de estrelas de baixa massa e massa intemeriária até a fase de AGB (*Assymptotic Giant Branch*). Iremos considerar a evolução de uma estrela isolada, mas destacamos que sistemas binários estelares são importantes pois representam uma quantidade significativa dos sistemas estelares da Via Láctea. A presença de uma (sub)companheira binária pode complicar significativamente a evolução se os objetos constituirem um sistema próximo – isto é, estrelas separadas por apenas algumas dezenas de unidades astronômicas. A interação por maré entre as estrelas e a formação de um "envelope comum" podem mudar o destino previsto pela teoria de evolução para uma única estrela (IVANOVA ET AL., 2013; VERAS, 2016; ZHANG ET AL., 2020).

2.1 Estrelas de Baixa Massa e Massa Intermediária

Durante sua "vida", uma estrela experimenta variações de luminosidade, massa, raio e consequentemente temperatura efetiva. Basicamente, a massa e a composição química inicial são os parâmetros mais importantes na trajetória evolutiva das estrelas isoladas. Segundo KARAKAS & LATTANZIO (2014), estrelas de baixa massa apresentam massa de 0,5 até 2,0–2,2 $M_{\odot}$. Enquanto estrelas de massa intermediária apresentam limite inferior em 2,0–2,2 e limite superior em 10,0 $M_{\odot}$. Ademais, dentro desse universo de estrelas de massa intermediária, elas podem ser classificadas como intermediária baixa (2,0–7,0 $M_{\odot}$), intermediária média (7,0–9,5 $M_{\odot}$) e intermediária massiva (9,5–10,0 $M_{\odot}$). As principais diferenças na evolução dessas estrelas de massa intermediária está nos estágios finais, mas uma discussão detalhada desses estágios foge do escopo desta revisão.

Sequência Principal

As estrelas se formam a partir de nuvens frias formadas de gás e poeira, também conhecidas como nuvens moleculares. Algumas regiões no interior dessas nuvens alcançam densidade suficiente para desencadear o colapso e a fragmentação da nuvem. A despeito da evolução Pré-sequência Principal, o ingresso na fase de Sequência Principal (*Main Sequence* – MS) é caracterizado pela queima estável de hidrogênio no núcleo estelar. Portanto, a estrela queima quiescentemente hidrogênio no seu núcleo e sua posição muda pouco com o tempo no diagrama de *Hertzsprung–Russel* (H–R). Nessa fase, o tempo necessário para consumir hidrogênio do nucleo através das reações nucleares equivale ao tempo de permanência na MS. De outra forma, seja t_{MS} a escala de tempo de permanência na MS, L a luminosidade e M a massa da estrela, temos que

$$t_{MS} \propto \frac{M}{L}. \tag{2.1}$$

E usando a relação massa-luminosidade, $L \propto M^n$, para $n \sim 3$ (com n variando com a fase evolutiva e massa da estrela), encontramos outra importante relação:

$$t_{MS} \propto M^{-2}, \tag{2.2}$$

de onde podemos concluir que estrelas de menor massa permanecem mais tempo na fase de MS, logo, queimam seu "combustível" sob uma taxa menor. Em geral, essa escala de tempo é muito longa se comparada às etapas posteriores da evolução estelar (MACIEL, 1999).

A Tabela 2.1 apresenta as reações envolvidas na cadeia próton-próton (PP), que é a principal cadeia de reações responsável pela produção de energia em estrelas de baixa massa que estão na MS. Alternativa à PP I, a cadeia PP II ocorre quando ^{3}He é capturado por ^{4}He, preferencialmente quando T $> 1{,}4 \times 10^7$ K. A terceira possibilidade (PP III)

Tabela 2.1: As cadeias próton-próton. Adaptado de CLAYTON (1983).

Cadeia	Reações
PP I	$H + H \rightarrow D + e^+ + \overline{\nu}_e$
	$D + H \rightarrow {}^3He + \gamma$
	${}^3He + {}^3He \rightarrow {}^4He + 2\,H$
PP II	${}^3He + {}^4He \rightarrow {}^7Be + \gamma$
	${}^7Be + e^- \rightarrow {}^7Li + \overline{\nu}_e$
	${}^7Li + H \rightarrow {}^4He + {}^4He$
PP III	${}^7Be + H \rightarrow {}^8B + \gamma$
	${}^8B \rightarrow {}^8Be + e^+ + \overline{\nu}_e$
	${}^8Be \rightarrow 2\,{}^4He$

Tabela 2.2: Reações do ciclo CNO. Adaptado de CLAYTON (1983).

Ciclo	Reações
CNO_I	${}^{12}C + H \rightarrow {}^{13}N + \gamma$
	${}^{13}N \rightarrow {}^{13}C + e^+ + \overline{\nu}_e$
	${}^{13}C + H \rightarrow {}^{14}N + \gamma$
	${}^{14}N + H \rightarrow {}^{15}O + \gamma$
	${}^{15}O \rightarrow {}^{15}N + e^+ + \overline{\nu}_e$
	${}^{15}N + H \rightarrow {}^{12}C + {}^4He$
CNO_{II}	${}^{15}N + H \rightarrow {}^{16}O + \gamma$
	${}^{16}O + H \rightarrow {}^{17}F + \gamma$
	${}^{17}F \rightarrow {}^{17}O + e^+ + \overline{\nu}_e$
	${}^{17}O + H \rightarrow {}^{14}N + {}^4He$

ocorre para $T > 2{,}3 \times 10^7$ K, logo após a produção de ^{7}Be. Os símbolos e^+, $\overline{\nu}_e$ e γ referem-se à emissão de pósitron, neutrino do elétron e raio gamma, respectivamente.

Por outro lado, em estrelas de massa intermediária a temperatura do núcleo é suficientemente alta ($> 2 \times 10^7$ K) para que a principal fonte de energia seja o ciclo CNO. Neste caso, ^{12}C entra no conjunto de reações como catalisador do ciclo CNO_I, que tem como produto final o ^{4}He. Já o ciclo CNO_{II}, também chamado de ciclo ON, ocorre em temperaturas maiores que $1,7 \times 10^8$ K (MACIEL, 1999). Todo processo é cíclico e pode começar por qualquer reação listada na Tabela 2.2. A primeira fase, também conhecida por CN, é dominante em ocorrência. O ciclo CNO_{II} corresponde a 0,03 % dos casos.

2.1.1 Ramo das Subgigantes e das Gigantes Vermelhas

Exaurido o hidrogênio no núcleo, a estrela sai da MS e ascende ao Ramo das Subgigantes (*Sub Giant Branch* – SGB). Nessa fase curta, o núcleo de hélio se contrai progressivamente e o hidrogênio passa a queimar em uma camada externa, que envolve o núcleo. A contração e o aumento da temperatura nuclear são acompanhados pelo aumento do raio da estrela e, como consequência, diminuição da temperatura na sua superfície. O resfriamento das camadas externas aumenta a extensão da envoltória convectiva e a estrela

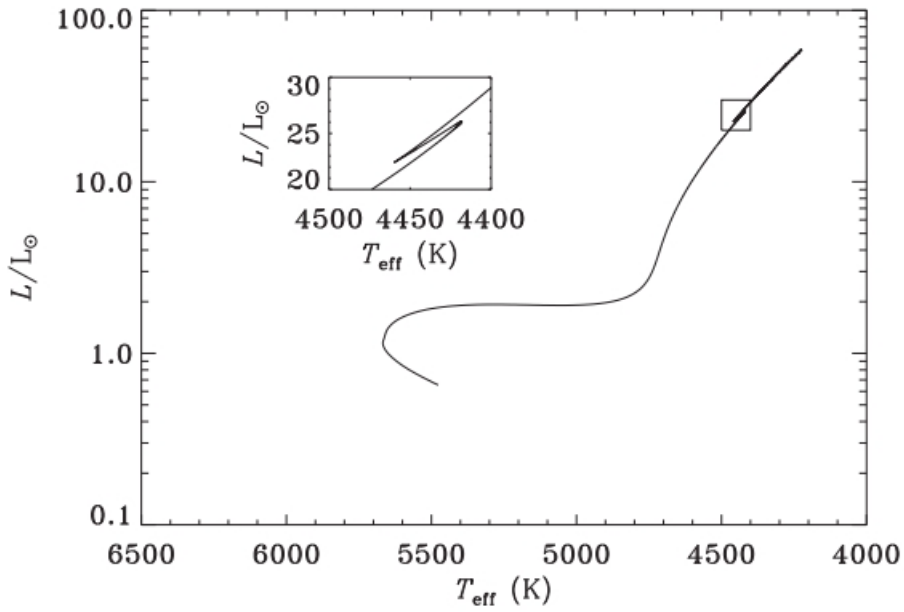

Figura 2.1: Modelo de trajetória evolutiva para estrelas de 1.0 $M_{\odot}$. Destaque para a região conhecida como "bump", que remete à variação na luminosidade. Fonte: CHRISTENSEN-DALSGAARD (2015).

entra no Ramo das Gigantes Vermelhas (*Red Giant Branch* - RGB). Quando a base da envoltória convectiva da estrela alcança regiões mais profundas no interior estelar, elementos como ^{4}He, ^{13}C e ^{14}N são levados até a superfície. Esse evento é conhecido como *primeira dragagem* (IBEN , 1967) e é responsável pela primeira mudança significativa das abundâncias na atmosfera estelar.

Durante a ascenção ao topo do RGB as estrelas experimentam um aumento significativo da luminosidade. Esse aumento é interrompido repentinamente quando a camada de queima de hidrogênio atinge a vizinhança da descontinuidade da composição química deixada para trás pela primeira dragagem. Essa variação não monotônica de luminosidade é conhecida como "*bump*" (CHRISTENSEN-DALSGAARD, 2015; IBEN , 1968). A Figura 2.1 apresenta um modelo de trajetória evolutiva para uma estrela de 1.0 $M_{\odot}$ no diagrama de $T_{\rm eff}$–$L/L_{\odot}$.

Na fase de RGB as estrelas de baixa massa apresentam núcleo com degenerescência de elétrons – o que quer dizer que o núcleo é sustentado contra a gravidade não mais pela pressão térmica, mas sim pela pressão de degenerescência. Portanto, nesta condição, o material que compõe o núcleo não obedece às leis clássicas segundo as quais a pressão de um gás é proporcional à sua temperatura e densidade. No topo do RGB, o núcleo alcança condições para iniciar a queima de hélio, quando ocorre o primeiro *flash de hélio* fora do centro do núcleo. O processo é chamado *flash*, pois, devido à degenerescência, os acréscimos de temperatura causados pelo início da queima de He levam à grande intensificação do processo triplo–α (Equações 2.3–2.6). Após o primeiro *flash*, sucessivos *subflashes*

removem o estado de degenerescência dos elétrons, desde uma região mais externa para outra mais interna do núcleo, ao longo de dois milhões de anos, transformando assim o objeto em uma estrela que queima He no seu núcleo (BILDSTEN ET AL., 2012; MACIEL, 1999). No caso de estrelas de massa intermediária, o núcleo de hélio não alcança o estado de degenerescência dos elétrons, pois atinge a temperatura necessária para a queima de hélio antes que ele esteja suficientemente denso para estar degenerado. Portanto, a fusão do hélio se inicia muito mais "suavemente".

Em linhas gerais, a nucleossíntese durante a queima do He consiste nas reações (CLAYTON, 1983):

$$^4\mathrm{He} + {}^4\mathrm{He} \rightarrow {}^8\mathrm{Be}, \tag{2.3}$$

$$^8\mathrm{Be} + {}^4\mathrm{He} \rightarrow {}^{12}\mathrm{C} + \gamma, \tag{2.4}$$

$$^{12}\mathrm{C} + {}^4\mathrm{He} \rightarrow {}^{16}\mathrm{O} + \gamma \tag{2.5}$$

e às vezes,

$$^{16}\mathrm{O} + {}^4\mathrm{He} \rightarrow {}^{20}\mathrm{Ne} + \gamma. \tag{2.6}$$

Ao passo que o processo triplo–α requer apenas He para suas reações, a disponibilidade de ^{12}C torna possível a produção de outros elementos mais pesados que consomem ^{4}He através do processo α (ou reações α), que produz elementos cujo número de massa é múltiplo inteiro da massa do núcleo de ^{4}He. O *flash* de hélio do núcleo de estrelas de baixa massa pode levar a episódios de mistura, conduzindo à superfície elementos recém sintetizados (He, C e elementos α). Segundo CASSISI ET AL. (2002), a baixa eficiência da camada de queima de hidrogênio permite que a zona convectiva conduzida pelo *flash* de He penetre em camadas ricas em hidrogênio, com subsequente enriquecimento dos produtos de queima na superfície estelar. Também é possível que o *flash de hélio* esteja associado à formação das raras gigantes vermelhas ricas em lítio, que são observadas principalmente na fase posterior ao topo do RGB (BHARAT KUMAR ET AL., 2011).

2.1.2 Ramo Horizontal das Gigantes

A fase seguinte se inicia com a diminuição da luminosidade e do raio estelar, o chamado ramo horizontal (*Horizontal Branch* – HB), onde todas as estrelas queimam He no núcleo e o hidrogênio passa a ser queimado em uma camada externa envolvendo o caroço central. O HB recebe este nome porque em aglomerados globulares as estrelas que estão nesta fase se encontram dispostas ao longo de uma região mais ou menos horizontal, no diagrama H-R. As gigantes *clump*, estrelas pertencentes ao chamado *red clump*, são relativamente mais jovens e mais ricas em metais do que as estrelas do HB. Tanto as estrelas do HB quanto as gigantes *clump* realizam a fusão do hélio em seus núcleos, mas as diferenças na estrutura de suas camadas externas resultam nos diferentes raios, temperaturas efetivas, e cor GIRARDI (2016).

2.1.3 Ramo Assintótico das Gigantes

Exaurido o hélio nuclear, o "caroço" sofre uma nova contração e a estrela passa por novo reajuste em sua estrutura. Tanto estrelas de baixa massa quanto estrelas de massa intermediária, ao alcançarem a fase de AGB, apresentam núcleo composto por carbono e oxigênio (com elétrons em estado degenerado) e queimam hélio e hidrogênio em camadas mais externas sob um regime complexo que proporciona as condições necessárias para a produção de vários elementos químicos, inclusive misturá-los com o material das camadas mais superficiais.

Basicamente, a evolução estelar no AGB conta com duas fases bastante distintas. A fase inicial (Early-AGB), é a etapa evolutiva em que não há ocorrência de pulsos térmicos e a principal fonte de energia da estrela é o processo triplo-α, que ocorre em uma camada externa ao núcleo da estrela. Por outro lado, a fase que apresenta pulsos térmicos é conhecida como *Thermally Pulsing Asymptotic Giant Branch* (TP-AGB). Ao alcançar a fase de AGB, o núcleo de carbono e oxigênio se contrai e libera uma quantidade significativa de energia potencial, somando-se à energia liberada pela fusão na camada de hélio. A consequência disto é a nova expansão da estrela. Neste contexto, estrelas de massa intermediária ($> 4\,M_{\odot}$) apresentam envoltória convectiva que penetra o suficiente para extinguir a camada de queima de hidrogênio, levando elementos recém sintetizados à superfície estelar (IBEN & RENZINI , 1983). Tal episódio recebe o nome de *segunda dragagem* (Figura 2.2).

A envoltória convectiva na primeira dragagem se estende para o interior estelar e incorpora regiões onde ocorreu o processamento parcial de carbono e nitrogênio no passado, durante a fase de MS. Na *segunda dragagem* a região convectiva penetra além da posição da extinta camada de hidrogênio e, portanto, mistura os produtos da queima de H na envoltória.

As estrelas AGBs apresentam uma grande variedade de processos de nucleossíntese, portanto, são de importância ímpar no enriquecimento químico do meio interestelar – são produtoras importantes de poeira, também. Como principais fontes para estes processos, pode-se destacar a instabilidade térmica da camada de hélio, responsável pelos *pulsos térmicos*. Também ocorre a queima no fundo quente da envoltória convectiva (*Hot Bottom Burning*–HBB), para massas maiores que $4,0 - 5,0\,\mathrm{M}_{\odot}$ (dependendo da metalicidade). Na seção seguinte nós discutiremos alguns mecanísmos extras necessários para explicar determinados padrões de abundância que as dragagens convectivas não conseguem resolver sozinhas.

Apesar de permanecer maior parte do tempo inativa na fase TP-AGB, a camada de queima de hélio apresenta periodicamente *flashes* que liberam uma grande quantidade de energia. Essa energia liberada cria a *flash-driven convection zone*, que se estende da camada de queima de hélio até uma região inferior á camada de hidrogênio. Tal região é

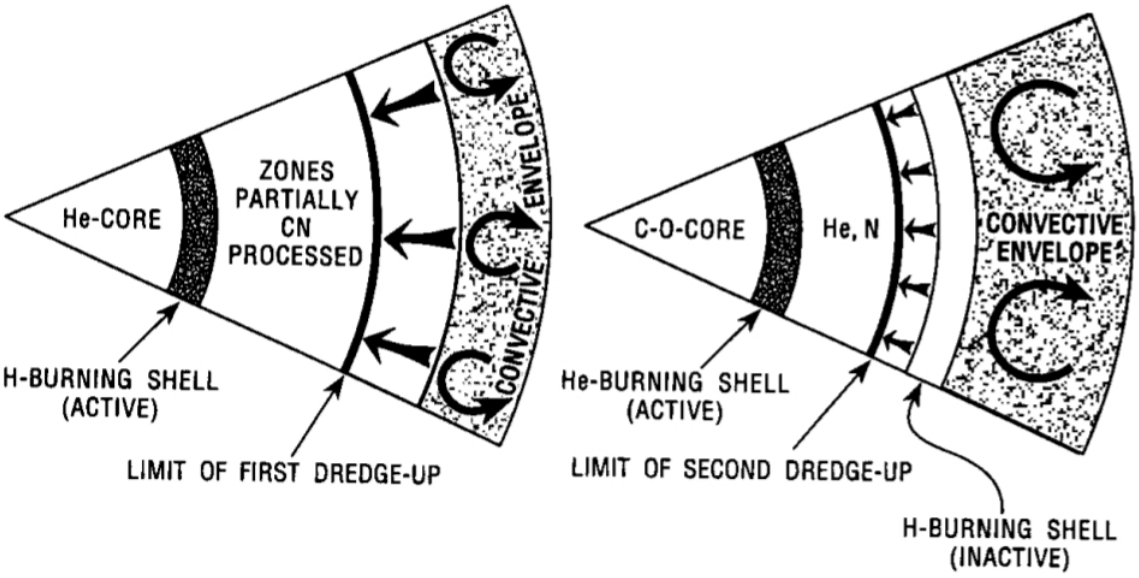

Figura 2.2: Esquema da estrutura interna da estrela durante a primeira dragagem (esquerda) e segunda dragagem (direita). Fonte: BUSSO ET AL. (1999).

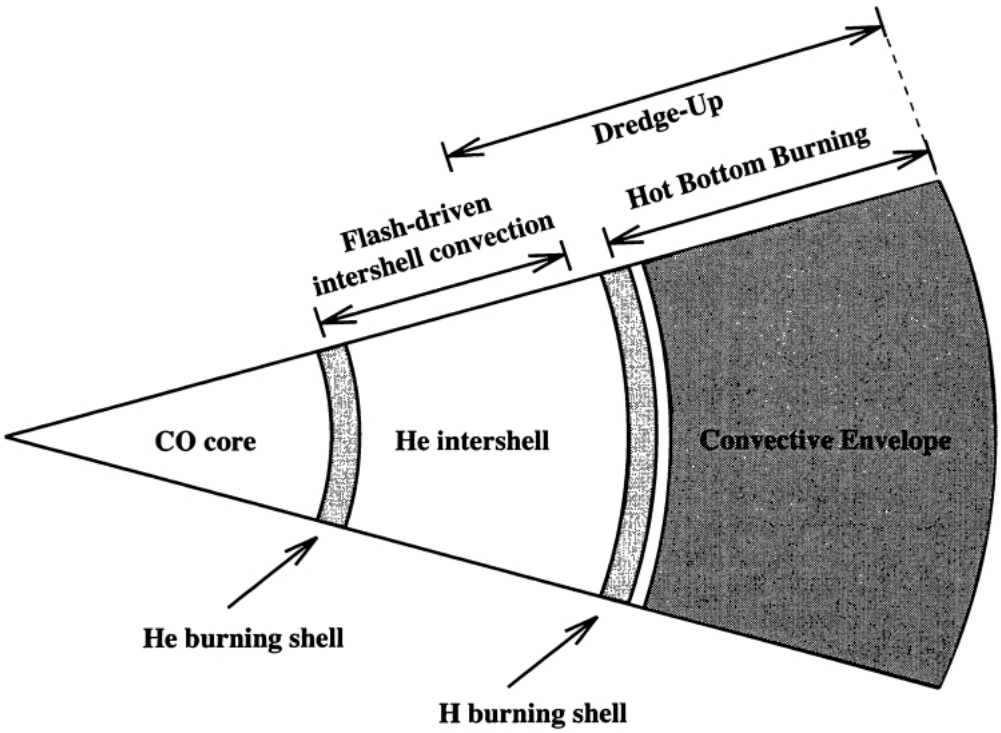

Figura 2.3: Interior de uma estrela AGB. Esquematizados o alcance da terceira dragagem, *hot bottom burning* e *flash-driven intershell convection*. Extraído de LATTANZIO & FORESTINI (1999).

responsável pela mistura de ^{12}C (produzido via triplo-α) na envoltória convectiva, pois, ao cessar o *flash* de He, a energia liberada na envoltória convectiva causa a expansão da estrela. Assim, a camada de queima de hidrogênio desaparece (temporariamente) e a região convectiva alcança regiões ainda mais profundas no interior estelar, realizando o que se conhece como *terceira dragagem* (como ilustrado na Figura 2.3). A etapa seguinte, *fase interpulso*, inicia com contração da estrela e proporciona condições para que a camada de hidrogênio volte a queimar, alimentando a camada de hélio com o seu produto (LATTANZIO & FORESTINI , 1999). A simultânea atuação dos pulsos térmicos e eventos de dragagem eventualmente transforma estrelas oxigenadas em estrelas carbonadas, resultado do aumento significativo de ^{12}C e ^{13}C na atmosfera estelar, segundo a sequência espectral: M $\rightarrow$ MS $\rightarrow$ S $\rightarrow$ SC $\rightarrow$ C (tipo N), onde, em ordem crescente, cada classe espectral apresenta maior valor para a razão C/O (ABIA ET AL., 2003).

Outra consequência importante da terceira dragagem é o enriquecimento de elementos do processo de captura lenta de nêutrons, conhecida como *processo-s* (por exemplo, Zr, Y, Sr, Ba e Tc). De maneira geral, o *processo-s* consiste no aumento da massa atômica através da captura de nêutrons, enquanto o número atômico se mantém constante, mas o núcleo atômico logo se torna instável e sofre um decaimento β^-, ou seja, transforma um nêutron em um próton e emite um elétron e um neutrino. Sucessivos decaimentos podem acontecer até que o núcleo alcance a estabilidade. O ferro atua como núcleo "semente" e, portanto, o processo depende da disponibilidade de nêutrons e da quantidade inicial de ferro. Assim, tal processo desempenha um papel importante na evolução química da Galáxia ao produzir elementos mais pesados que o ferro.

Os nêutrons necessários para o processo-s são liberados especialmente pelas reações abaixo (BUSSO ET AL., 1999):

$$^{13}\mathrm{C} + {}^{4}\mathrm{He} \rightarrow {}^{16}\mathrm{O} + \mathrm{n} \tag{2.7}$$

e

$$^{22}\mathrm{Ne} + {}^{4}\mathrm{He} \rightarrow {}^{25}\mathrm{Mg} + \mathrm{n}. \tag{2.8}$$

Por outro lado, o processo r (ou o processo de captura rápida de nêutrons) é invocado para tentar explicar a produção de núcleos ricos em nêutrons, estáveis ou radioativos de longa duração, que são observados em estrelas de várias massas e metalidades – samário e európio, por exemplo. Os elementos majoritariamente produzidos no processo r, e observados no Sistema Solar, necessitam de uma densidade extrema de neutrons para sua criação e é possível que essa condição seja alcançada em Supernovas do tipo II ou por *merger* de estrelas de nêutrons (THIELEMANN ET AL., 2002, 2017).

2.2 A Necessidade de Outras Misturas

2.2.1 Mistura Termohalina

É importante destacar a possível atuação da mistura termohalina. O seu nome vem da sua ocorrência na água salgada dos oceanos – fenômeno popularmente conhecido devido a formação dos "dedos de sal". Em termos físicos, trata-se de uma instabilidade hidrodinâmica que surge quando um gradiente instável na composição química passa a ser estabilizado por um gradiente na temperatura. Nas estrelas, essa mistura pode acontecer quando existe um gradiente de peso molecular médio inverso em um meio termicamente estável (CANTIELLO & LANGER, 2010).

A mistura termohalina não consegue explicar o enriquecimento de lítio em estágios evolutivos como o RGB, mas mostra-se necessária para conciliar o padrão de abundâncias de estrelas com luminosidades mais altas, visto que existe divergência com as previsões da primeira dragagem (CHARBONNEL & LAGARDE, 2010). Além disso, a mistura termohalina, bem como outras mistura não-tradicionais, podem explicar a quantidade de ^{3}He observada no meio interestelar. As estrelas de baixa massa são produtoras importantes de ^{3}He (cadeia PP, Tabela 2.1), que é ejetado para o meio interestelar através da perda de massa comum das estrelas no RGB. Contudo, a teoria padrão prevê o dobro da quantidade ^{3}He observada no meio interestelar (LAGARDE ET AL., 2012). Nesse sentido, a inversão do peso molecular médio e o "consumo" desse isótopo de hélio estão associados à equação:

$$^{3}\mathrm{He} + {}^{3}\mathrm{He} \rightarrow {}^{4}\mathrm{He} + 2\mathrm{p}. \tag{2.9}$$

No geral, a mistura termohalina é capaz de reproduzir muito bem as abundâncias de C e N e ^{12}C/^{13}C em uma ampla faixa de metalicidades (LAGARDE ET AL., 2019).

2.2.2 Cool Bottom Processing

Outro mecanismo de mistura é o *Cool Bottom Processing* (CBP), que é responsável pela sobre-abundância de lítio e baixas razões de ^{12}C/^{13}C no RGB e AGB, para estrelas de baixa massa. Considerado *ad hoc*, o CBP consiste no trafnsporte de material do fundo frio do envelope convectivo para regiões radiativas mais profundas e quentes, onde ocorre a queima por CNO (BOOTHROYD & SACKMANN, 1999; LAGARDE ET AL., 2019; SACKMANN & BOOTHROYD, 1999) – como apresenta a Figura 2.4. Por fim, o material processado é conduzido até a atmosfera estelar e as mudanças na composição fotosférica da estrela podem ser identificadas através da espectroscopia, conforme a Tabela 2.3. Ainda, é possível associar o gatilho do CBP com o "engolimento" de um planeta ou uma anã marrom (SIESS & LIVIO, 1999a).

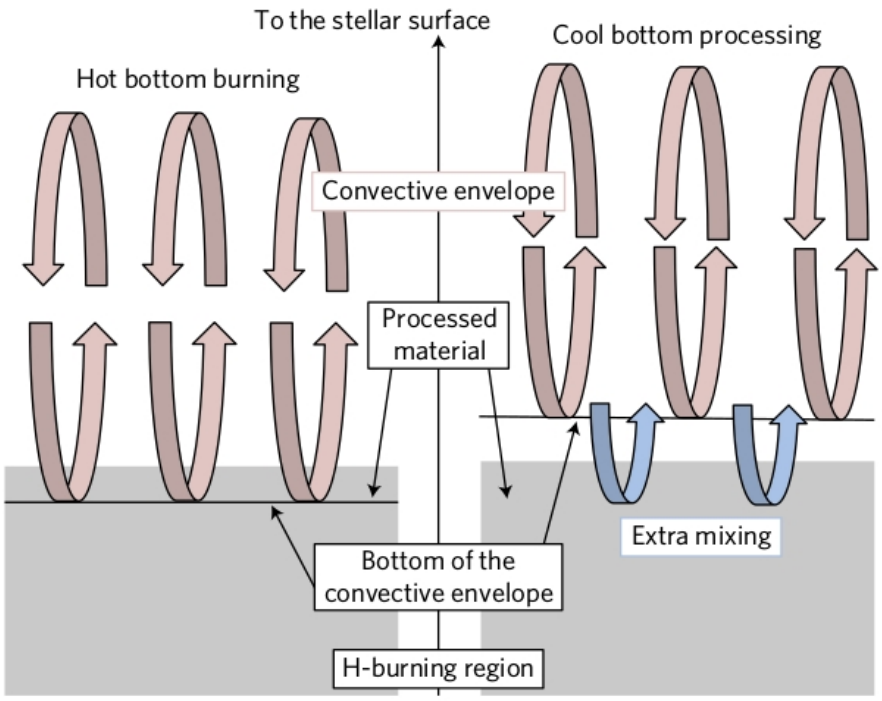

Figura 2.4: Esquema da estrutura interna de uma estrela AGB. O HBB (esquerda) ocorre em massas maiores, e conduz material processado na região de queima de H para a superfície estelar. O CBP (direita) ocorre em estrelas menos massivas. Extraído de LUGARO ET AL. (2017).

2.2.3 Hot Bottom Burning

O HBB, por sua vez, é um processo que desencadeia uma mudança significativa nas abundâncias químicas nas atmosferas de estrelas mais luminosas e massivas do AGB ($> 4,5\,M_{\odot}$), e, basicamente, deriva do aprofundamento da região convectiva que se estende até o topo da camada de H (o fundo quente da envoltória convectiva), durante a fase interpulso (SMITH & LAMBERT, 1989, 1990). Nesse evento, a temperatura na parte inferior da envoltória é da ordem de 10^8 K, e, portanto, não apenas o ciclo CNO, mas também os ciclos Ne-Na e Mg-Al ocorrem – esse último responsável pela substancial produção de ^{26}Al. O HBB leva ao reprocessamento do ^{12}C em ^{13}C e ^{14}N, por captura de prótons.

Outra importante consequência do HBB (e também do *bump*) é a produção de lítio através do mecanismo de CAMERON & FOWLER (1971), descrito pelas reações abaixo:

$$^{3}\mathrm{He} + {}^{4}\mathrm{He} \rightarrow \gamma + {}^{7}\mathrm{Be} \tag{2.10}$$

e

$$^{7}\mathrm{Be} + \mathrm{e}^{-} \rightarrow {}^{7}\mathrm{Li} + \overline{\nu}_{\mathrm{e}}. \tag{2.11}$$

O ^{7}Li é rapidamente destruído pela captura de prótons ao experimentar temperaturas

Tabela 2.3: As principais espécies afetadas pelos eventos de dragagem e HBB ao longo da evolução estelar até a fase de AGB. Adaptado de KARAKAS & LATTANZIO (2014).

Evento	Mudança
Primeira Dragagem	Aumento no ^{4}He, ^{13}C, ^{14}N, ^{17}O e ^{23}Na. Diminuição no ^{12}C, ^{7}Li, ^{16}O e ^{18}O.
Segunda Dragagem	Aumento no ^{4}He, ^{14}N e ^{23}Na. Diminuição no H, ^{12}C, ^{13}C e ^{15}N.
Terceira Dragagem	Aumento no ^{12}C e elementos dos processo-s.
Hot Bottom Burning	Aumento no ^{13}C e ^{14}N. Diminuição no ^{12}C.
Cool Bottom Processing	Aumento no ^{4}He, ^{7}Li, ^{13}C, ^{14}N, ^{17}O e ^{23}Na. Diminuição no ^{12}C, ^{16}O e ^{18}O.

próximas a 2×10^{6} K. Entretanto, episódios de mistura extra podem favorecer a produção de lítio, mostrando que esse elemento sob determinadas condições pode ser também produzido no interior estelar (WALLERSTEIN & KNAPP, 1998; YAN ET AL., 2018).

Capítulo 3

Aglomerados Abertos: Os Laboratórios de Astrofísica

Neste capítulo apresentaremos uma breve revisão dos principais assuntos pertinentes ao estudo dos aglomerados estelares abertos da Via Láctea. Para isso, falaremos um pouco sobre a Via Láctea e a formação e evolução desses conjuntos de estrelas que servem à astrofísica como verdadeiros laboratórios e, portanto, são úteis em diversas áreas de pesquisa.

3.1 A Via Láctea

A Via Láctea é uma galáxia espiral barrada e contém um número de estrelas da ordem de 10^{11}. As principais componentes estruturais da Via Láctea são o bojo central, o disco e o halo, conforme está esquematizado Figura 3.1. O diâmetro do disco é de cerca de 50 kpc, estando ele dividido em disco fino e disco espesso. Ao redor do disco está o halo galáctico, que se estende muito além do disco. O Sol está localizado acerca de 8,0 kpc do centro da Galáxia, no disco.

O disco fino é composto de estrelas jovens (*população* I), poeira e gás – principalmente hidrogênio atômico e molecular –, e desempenha um papel fundamental na química da Galáxia, uma vez que as grandes nuvens moleculares são os locais de formação de estrelas. Uma parte do disco fino, que às vezes é chamada de disco fino jovem, também corresponde ao plano central da distribuição galáctica de poeira e gás; ele tem uma escala de altura estimada entre 35 e 90 pc, onde a escala de altura é a distância na qual a densidade numérica diminui em e^{-1}. O disco espesso, que é composto por uma população mais velha de estrelas, tem uma escala de altura de aproximadamente 1 kpc. O número de estrelas por unidade de volume no disco espesso é da ordem de 8,5% do que se observa no disco fino (BINNEY & TREMAINE, 2011).

Ao longo do disco fino, na direção do centro galáctico, a escala vertical aumenta onde

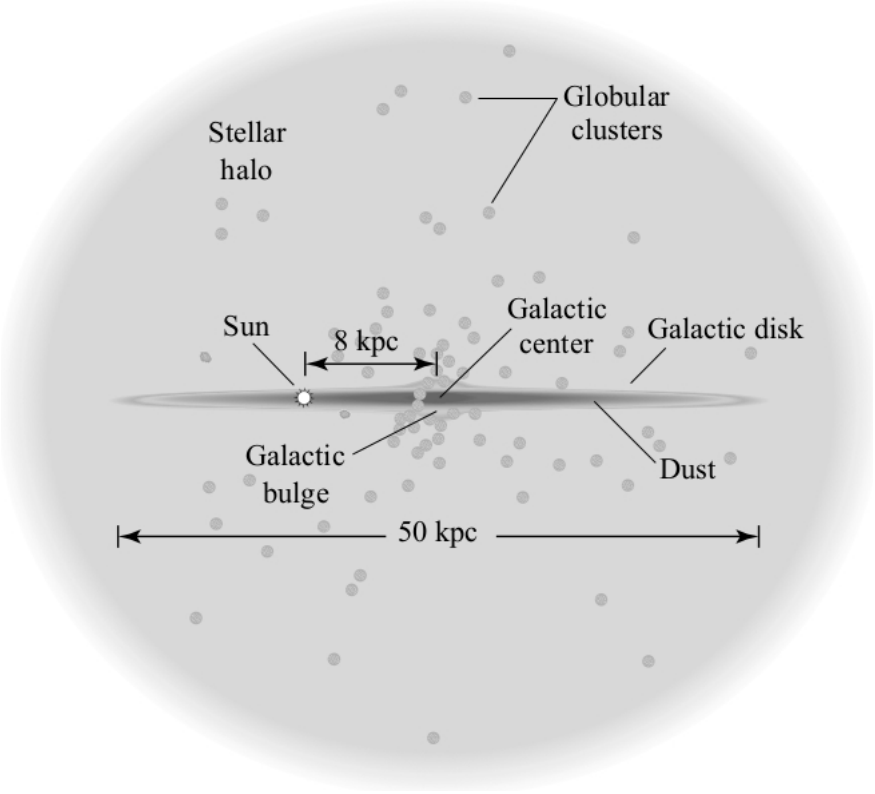

Figura 3.1: Uma ilustração esquemática da Via Láctea (fora de escala). Obtido de CARROLL & OSTLIE (2017).

o disco encontra a protuberância galáctica chamada bojo – esta estrutura não é simplesmente uma extensão do disco. Sua forma é quase quadrada, alongada, e pode ser facilmente identificada em imagens formadas por combinações de bandas no infravermelho. No centro, está um buraco negro de massa estimada de $4 \times 10^6\, M_\odot$ (BINNEY & TREMAINE, 2011). Devido à extinção causada pela grande quantidade de poeira, observar as regiões centrais da Galáxia é uma tarefa seriamente difícil – a janela de Baade, por exemplo, é uma região onde os efeitos são menos graves para a região do espectro ótico.

O halo, que também conhecido como halo estelar, é um componente aparentemente esférico que, basicamente, é populado por estrelas velhas e de baixa metalicidade (*população* II) que estão dispostas no campo ou em aglomerados. Mais externo, existe o halo escuro que se estende por pelo menos 230 kpc. O halo escuro é o maior componente estrutural, mas também o menos conhecido e explica a órbita de estrelas e gás em órbitas mais externas (CARROLL & OSTLIE, 2017). A Tabela 3.1 apresenta algumas estimativas que proporcionam uma visão geral sobre os componentes estruturais da Via Láctea.

3.2 Aglomerados Estelares

O que são aglomerados de estrelas? Como distinguir aglomerados de sistemas múltiplos? Com as respostas para essas perguntas nós podemos introduzir o assunto a ser revisado

Tabela 3.1: Valores aproximados para vários parâmetros associados aos componentes da Via Láctea. Adaptado de CARROLL & OSTLIE (2017).

	Massa ($10^{10}\,M_\odot$)	Raio (kpc)	Escala de Altura (kpc)	Idade (10^9 anos)	[Fe/H] (dex)
Gás Neutro	0.5	25.0	<0.1	⩽10.0	$> +0.1$
Disco Fino	6.0	25.0	0.35	8.0	-0.5 até $+0.3$
Disco Espesso	0.2 até 0.4	25.0	1.0	10.0	-2.2 até -0.5
Bojo	1.0	4.0	0.1 até 0.5	<0.2 até 10.0	-2.0 até 0.5
Halo	0.3	>100	3	11.0 até 13.0	< -5.4 até -0.5
Halo Escuro	190	>230	170	≈13.5	—

nesta seção.

Segundo PORTEGIES ZWART ET AL. (2010), um aglomerado estelar é um conjunto de estrelas que estão gravitacionalmente ligadas entre si (mas muito fracamente ligadas). De outra forma, LADA & LADA (2003) define um aglomerado como um conjunto de estrelas com uma densidade de massa de $1\,M_\odot\,\mathrm{pc}^{-3}$ que resiste à interações de marés com estuturas vizinhas o suficiente para evitar a sua evaporação por 100 Myr. Basicamente, os aglomerados estelares são de dois tipos e eles se diferenciam em vários aspectos, onde os principais são: idade, número de estrelas e sua distribuição espacial, localização, velocidades e composição química.

Os *aglomerados globulares* são mais são ricos, velhos, esféricos e massivos, apresentando tipicamente 10^4–10^6 estrelas. Todos os aglomerados globulares da Via Láctea estão muito distantes do Sol, e apresentam um diâmetro típico da região de alta densidade estelar de dezenas de parsecs – as densidades centrais são da ordem de 10^3 pc^{-3}. Já os *aglomerados abertos* são agrupamentos irregulares de 10^2–10^4 estrelas, geralmente dispostas mais ou menos ao acaso ou não apresentando uma concentração em direção ao centro do aglomerado tão evidente quanto nos aglomerados globulares. Outro tipo de agrupamento de estrelas sÃ£o as associaÃ§Ãµes, *comdestaqueparaasassocia§µesdotipoOBquems£oformadasporestrelasdotipoespec*

3.2.1 Formação e Evolução

Os aglomerados de estrelas são importantes em grande parte da astrofísica moderna: o estudo da função de massa inicial, dinâmica gravitacional, evolução estelar e cosmologia. KRUMHOLZ ET AL. (2019) sugere, através de uma grande revisão de literatura recente, que:

- Os aglomerados se formam em nuvens moleculares gigantes, que essencialmente convertem gás em estrelas sob uma taxa relativamente baixa de tempo dinâmico.
- Nos primeiros ≈ 100 Myr, após a remoção do gás, os aglomerados se dispersam moderadamente rápido através do relaxamento de dois corpos e interações com

nuvens moleculares gigantes. Este processo afeta principalmente os aglomerados de baixa massa.

- Mesmo após a dispersão ou evaporação de suas estrelas, alguns aglomerados permanecem "coerentes" e, portanto, detectáveis sob o ponto de vista químico ou espacial.

3.3 Aglomerados Abertos

Aglomerados Abertos (OCs – acrônimo do inglês *Open Clusters*) são grupos de estrelas que nasceram da mesma nuvem molecular e estão claramente próximas umas das outras. As estrelas de um aglomerado do tipo aberto apresentam uma pequena dispersão de velocidade radial e movimento próprio (SODERBLOM, 2010). Além disso, suas estrelas apresentam uma química relativamente homogênea.

Existe divergência na literatura sobre esses OCs serem formados por estrelas fisicamente "ligadas" ou não, mas o fato é que na maioria dos casos eles formam um conjunto facilmente reconhecido no campo de visada de um observador. Recentemente, com o advento dos dados de astrometria e fotometria da Missão Gaia (GAIA COLLABORATION ET AL., 2018), dezenas de novos aglomerados abertos estão sendo descobertos – grupos de estrelas em regiões densas e/ou obscuras que só são identificados graças a qualidade e quantidade desses dados (por exemplo, FERREIRA ET AL., 2019, 2020).

Aglomerados abertos jovens ($< 1.0\,\mathrm{Gyr}$) são muito úteis para astrofísica estelar e galáctica. Por exemplo, os OCs podem funcionar como traçadores da formação recente de estrelas na estrutura em espiral de discos galácticos, como observamos na Via Láctea (LADA & LADA, 2003). Por outro lado, aglomerados abertos velhos podem prover testes da evolução química do disco Galáctico (FRIEL, 1995) – aglomerados mais antigos são raros, pois a maioria foi dissolvida por "choques" gravitacionais causados pela passagem de nuvens de gás interestelar.

Essas facilidades que os aglomerados abertos proporcionam são possíveis devido às seguintes considerações: (i) as estrelas estão na mesma distância; (ii) as estrelas têm a mesma idade; (iii) as estrelas têm a mesma composição química; e (iv) as estrelas diferem em sua massa. Se o volume do aglomerado é relativamente pequeno (em alguns casos comparável ás incertezas) as estrelas que o formam têm valores de distância iguais ou insignificantemente diferentes. No tocante à idade, um único valor é plenamente confiável para OCs de idade intermediária e velhos, mas é menos confiável para aglomerados extremamente jovens, visto que podemos identificar nesses casos estrelas de maior massa em estágios avançados da evolução estelar e também estrelas de menor massa que ainda podem estar se contraindo – naturalmente, o estudo detalhado dessa classe de aglomerados pode ajudar na compreensão de como as estrelas se formam e evoluem. Estudos químicos baseados em espectroscopia de alta resolução, onde as incertezas são menores,

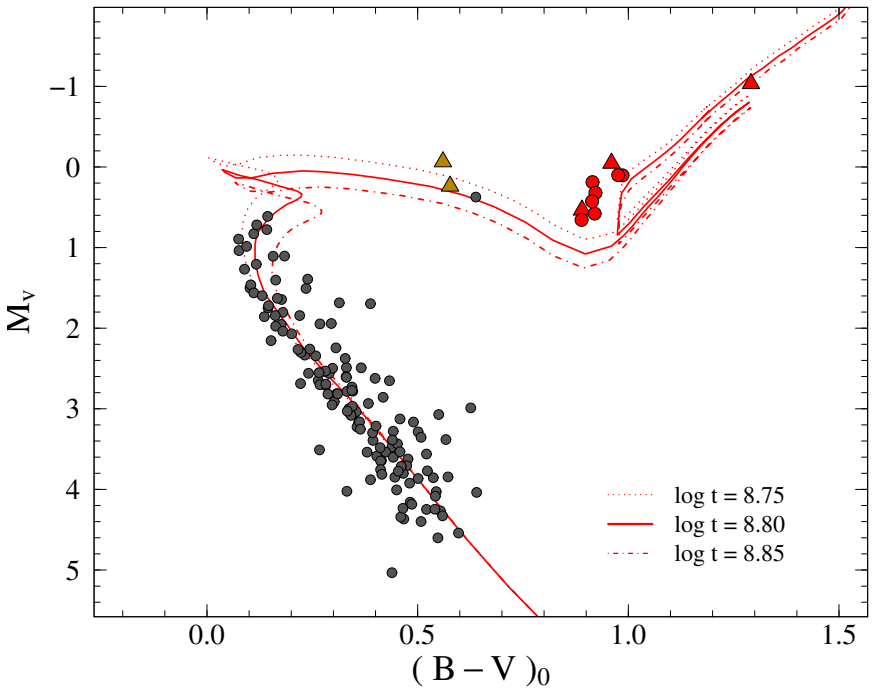

Figura 3.2: Ajuste de isócronas para as estrelas do campo do aglomerado NGC 2539 observadas nas bandas B e V. Os triângulos representam binárias e o circulos representam estrelas *single*. Em destaque, os símbolos nas cores amarelo (*yellow stragglers*) e vermelho, as estrelas estudadas em MARTINEZ ET AL. (2020). Os dados de fotometria foram obtidos de LAPASSET ET AL. (2000) e as isócronas de GIRARDI ET AL. (2000).

dão suporte ao ponto (iii). Diferente do que ocorre em alguns aglomerados globulares, ainda não foi verificada nenhuma evidência da existência de múltiplas gerações em OCs. Por último, as estrelas de diferentes massas evoluem em ritmos diferentes, logo, é possível observar objetos ocupando fases evolutivas diferentes, como pode ser observado no diagrama cor–magnitude apresentado na Figura 3.2.

3.3.1 Estrelas Binárias e *Stragglers*

Sistemas binários e *stragglers* são comuns em aglomerados abertos. FRIEL (1995) levantou em sua revisão que a população de binárias representa de 20 a 50% das estrelas em OCs velhos. Além disso, a incidência de sistemas binários próximos pode estar ligada à formação de estrelas "retardatárias".

Dentro do universo de *stragglers* existem algumas distinções: estrelas *blue stragglers*, que se localizam acima da região de turn-off no diagrama de cor–magnitude do aglomerado; estrelas *yellow stragglers*, que estão acima do ramo das subgigantes, no diagrama cor magnitude; estrelas sub-subgigantes, que são menos brilhantes que as subgigantes e mais vermelhas que as subgigantes comuns; e, por fim, as *red stragglers*, que são objetos mais vermelhos que as gigantes comuns de um aglomerado estelar. É provável que exista uma íntima ligação entre esses objetos. LANDSMAN ET AL. (1997) sugere que as *yellow*

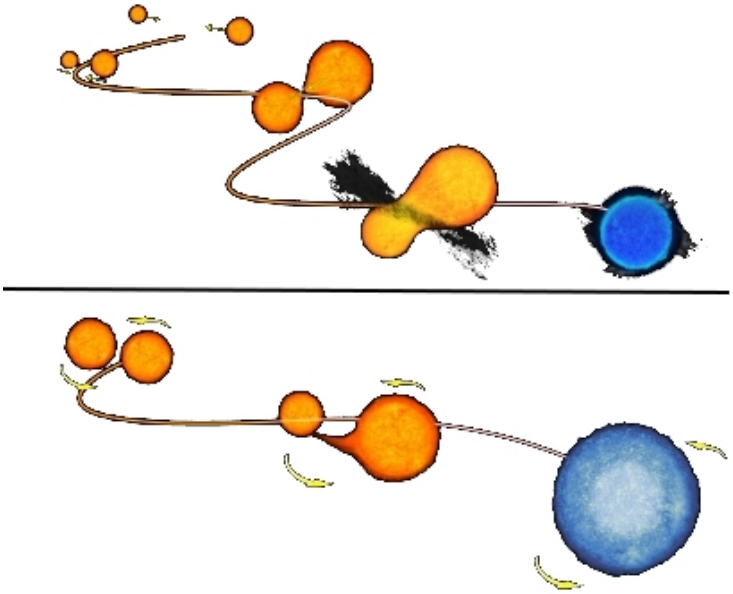

Figura 3.3: Ilustrações que representam a formação de uma estrela *blue straggler* a partir de um *merge* (acima) e a partir da troca de matéria (abaixo) entre duas estrelas. Adaptado de NASA/ESA website.

stragglers são o estágio evolutivo seguinte das *blue stragglers*, enquanto GELLER ET AL. (2017a,b) e LEINER ET AL. (2017) apresentam diferenças entre as *red stragglers* e sub-subgigantes, até então com nomeclatura confusa na literatura, e apontam a possibilidade das duas classes estarem relacionadas e terem mecanismos de formação semelhantes.

Como as estrelas *blue stragglers* são mais massivas e mais brilhantes, estão acima da região de turn-off, é possível que elas devam ter ganhado massa após a sua formação. Existem dois cenários de "rejuvenescimento" conhecidos na literatura que podem criar essas estrelas *blue stragglers*: duas estrelas podem colidir e da fusão delas se formar uma estrela massiva (MCCREA, 1964); e uma estrela pode ganhar massa de uma companheira binária próxima e, portanto, se tornar mais massiva e mais luminosa (HILLS & DAY, 1976). A Figura 3.3 ilustra as duas hipóteses de formação de estrelas blue stragglers. Quanto às sub-subgigantes, LEINER ET AL. (2017) discute três hipóteses de formação: transferência de massa em um sistema binário; remoção do envelope de um subgigante, talvez durante um encontro dinâmico; e luminosidade reduzida devido a campos magnéticos que reduzem a eficiência convectiva e produzem grandes manchas estelares.

Capítulo 4

O Método de Análise Espectroscópica

Neste capítulo será descrito o método de análise espectroscópica que é adotado nos estudos apresentados nos capítulos seguintes. Antes, faremos uma breve revisão conceitual que fundamenta a nossa ferramenta de análise espectroscópica.

4.1 A Atmosfera Estelar

Entente-se por atmosfera estelar a região de transição do interior estelar e o meio interestelar. Estruturalmente, a parte mais interna chama-se subfotosfera, que é seguida da fotosfera, cromosfera e coroa – é na fotosfera que a maior parte do espectro visível se origina, ou seja, é essa região que nos interessa nesta revisão. Uma atmosfera estelar é constituída de átomos isolados, íons e elétrons livres, que compõem um meio de alta temperatura e baixa densidade. Nas atmosferas de estrelas relativamente frias também é possível que moléculas se formem. E, devido às baixas densidades, o gás pode ser descrito como um gás ideal (GRAY ET AL., 2005; MIHALAS, 1978).

Consideramos um gás ideal aquele que é composto por partículas que não interagem entre si – é um critério impossível de ser satisfeito, mas a aproximação é razoável se a energia média de interação entre as partículas for muito menor do que suas energias térmicas.

No ambiente de fotosfera estelar as partículas se deslocam por distâncias relativamente curtas em comparação com a distância que a temperatura muda significativamente, antes de colidirem com outras partículas. As taxas dos processos de colisão atômica são, além disso, muito rápidas em comparação com as taxas de mudança do estado termodinâmico local. Esses fatos nos permitem adotar uma simplificação muito importante na descrição da física das atmosferas estelares: o equilíbrio termodinâmico local, ETL. Nas condições de ETL, todas as propriedades da matéria são calculáveis em termos de composição química, densidade e temperatura (CLAYTON, 1983). Portanto, assumimos que ETL é uma aproximação válida para cada elemento de volume na atmosfera estelar.

Da teoria cinética dos gases, nós podemos descrever a relação entre temperatura local

(T), pressão (P) e o número de partículas por unidade de volume através da lei dos gases ideais. A relação entre essas variáveis pode ser expressa da seguinte forma

$$P \;=\; N\,k\,T, \tag{4.1}$$

onde k é a constante de Boltzmann. Ainda, podemos descrever a distribuição das partículas $\left(\frac{\mathrm{d}N(v)}{N}\right)$, para um intervalo de velocidade v e $v+dv$, através da distribuição de Maxwell-Boltzmann, tal como

$$\frac{\mathrm{d}N(v)}{N} \;=\; \left(\frac{2}{\pi}\right)^{1/2} \left(\frac{m}{k\,T}\right)^{3/2} v^2\,\mathrm{e}^{-mv^2/2kT}\,\mathrm{d}v, \tag{4.2}$$

onde o máximo da distribuição, ou o valor mais provável, ocorre em

$$v_{max} \;=\; \left(\frac{2\,k\,T}{m}\right)^{1/2}. \tag{4.3}$$

Nesse sentido, a fração de átomos excitada ao nível enésimo é proporcional ao peso estatístico g_n e ao chamado fator de Boltzmann, de onde a razão das populações nos dois níveis m e n pode ser expressa por

$$\frac{N_n}{N_m} \;=\; \frac{g_n}{g_m}\mathrm{e}^{-\Delta\chi/kT}, \tag{4.4}$$

onde g_m e g_n são os chamados pesos estaísticos dos estados N_m e N_n, que são relativos a diferença entre os estados de energia que estão acima do estado fundamental ($\Delta\chi = \chi_m - \chi_n$). T, dessa vez, é a temperatura de excitação.

Em 1920 o físico indiano Meghnad Saha utilizou a mecânica estatística para derivar o número de íons por unidade de volume (N_{i+1}) em relação ao número de átomos no estado fundamental por unidade de volume (N_i), para um gás em ETL. A partir dessa condição nós temos

$$\frac{N_{i+1}}{N_i}\,P_e \;=\; \frac{2\,U_{i+1}(T)}{U_i(T)}\,\frac{(2\,\pi\,m_e)^{3/2}\,(k\,T)^{5/2}}{h^3}\,e^{-\frac{E_{i,i+1}}{k\,T}} \tag{4.5}$$

onde $\frac{U_{i+1}}{U_i}$ representa a razão das funções de partição iônica e neutra, P_e a pressão de elétrons, m_e a massa do elétron, h a constante de Plank e $E_{i,i+1}$ a energia de ionização a partir do estado fundamental.

Na prática, nós definimos uma temperatura T local que é usada na descrição da distribuição de velocidades das partículas que compõem a atmosfera estelar – que se expressa por uma distribuição maxwelliana –, para calcular os números de ocupação dos níveis atômicos das diferentes espécies, através da lei de Boltzmann e dos equilíbrios de ionização obtidos pela lei de Saha (BONIFACIO ET AL., 2012). Na próxima seção nós iremos discorrer brevemente sobre as características gerais da grade de modelos de atmosfera adotados nos trabalhos apresentados nesta tese.

4.2 O Modelo de Atmosfera

Nós adotamos o modelo de atmosfera ATLAS9 (KURUCZ, 1993). Esse modelo de atmosfera unidimensional é fundamentado nas condições de equilíbrio termodinâmico local e equilíbrio hidrostático, e pode ser aplicado ao estudo espectroscópico de estrelas dos tipos espectrais F, G e K.

O ATLAS9 modela uma atmosfera estática, ou seja, os parâmetros atmosféricos não variam com o tempo – não é possível modelar pulsações, por exemplo. Além disso, esse modelo de atmosfera é relativamente fino (72 camadas) se comparado ao raio estelar, o que viabiliza a consideração de camadas plano-paralelas e homogêneas. Em outras palavras, os parâmetros mudam somente com a profundidade. E, por fim, as abundâncias químicas são constantes em toda a atmosfera (BONIFACIO ET AL., 2012; NESVACIL ET AL., 2003).

4.3 Linhas Espectrais

As linhas espectrais de emissão e absorção se formam a partir da mudança da quantidade de energia "contida" em um determinado átomo. As linhas de emissão são produzidas quando um átomo passa de um estado excitado para um estado de menor excitação, emitindo um fóton. Já as linhas de absorção se formam em uma situação oposta, ou seja, o elétron absorve um fóton e passa para um nível de energia maior – é neste tipo de linha que focamos a nossa análise.

4.3.1 Larguras Equivalentes

De forma prática, as linhas de absorção surgem quando a radiação atravessa um gás frio, que no nosso caso é a fotosfera estelar. De modo que o fluxo de cada linha, ou a área "faltante", é dado por

$$F_l = \int_{\lambda_1}^{\lambda_2} [F(\lambda) - F_c]\, d\lambda, \tag{4.6}$$

onde λ_1 e λ_2 representam o intervalo de comprimento de onda que contém a linha, enquanto F_c representa o fluxo na região do contínuo na vizinhança da linha.

Já a largura equivalente de uma linha de absorção é definida como a largura de um retângulo que possui uma área igual à linha de absorção – e é proporcional à força da linha (Figura 4.1). Essa quantidade pode ser expressa como

$$EW = \int \frac{F_c - F_\lambda}{F_c}\, d\lambda. \tag{4.7}$$

A largura equivalente depende da temperatura, da pressão de elétrons e de algumas

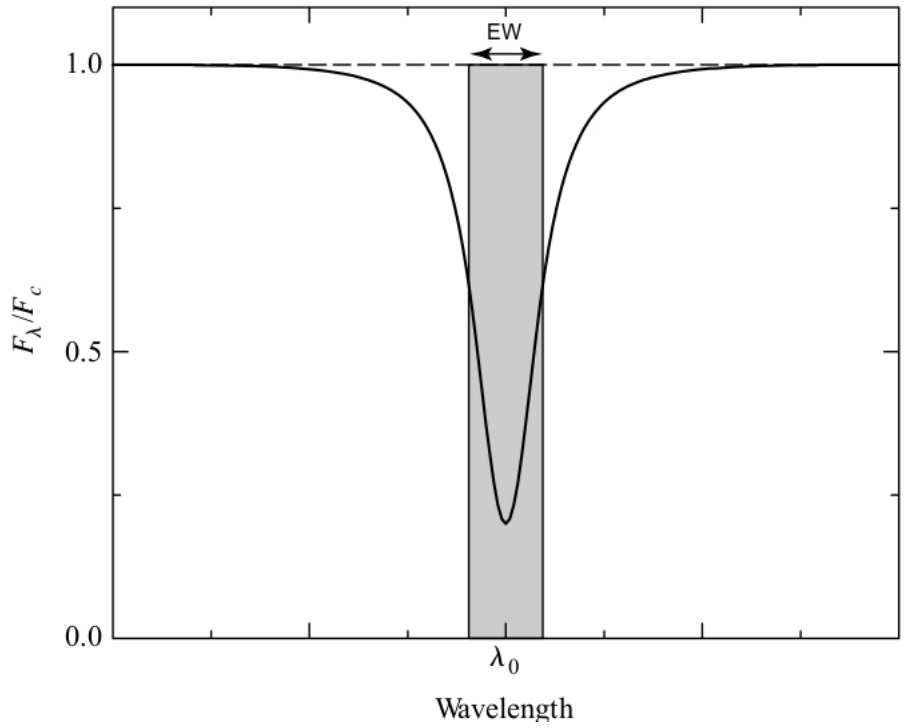

Figura 4.1: O perfil de uma linha de absorção típica. Adaptado de CARROLL & OSTLIE (2017).

constantes atômicas. Outra quantidade útil é a chamada largura à meia altura (FWHM, acrônimo do inglês *full width at half maximum*), que é uma medida do alargamento da linha.

4.3.2 Processos de alargamento das linhas espectrais

A força e a forma das linhas espectrais contém informações preciosas sobre a atmosfera das estrelas. Vários processos físicos contribuem para o coeficiente de absorção responsável pela formação da linha observada. A absorção de energia associada à linha acontece quando um elétron realiza uma transição de um orbital para outro. Cada comprimento de onda é associado à energia do fóton que foi absorvido e a profundidade e a forma da linha estão relacionadas à probabilidade de transição, à população do nível energético inferior e à abundância da espécie química que absorveu o fóton. A seguir, nós vamos abordar brevemente os três processos principais que atuam no alargamento das linhas espectrais.

O *alargamento natural* da linha de absorção está associado ao princípio da incerteza de Heisenberg. Nesse caso, a incerteza na energia do átomo permite que fótons de comprimentos de onda ligeiramente diferentes sejam absorvidos na mesma transição, o que explica o surgimento de uma "janela" de absorção. A incerteza na energia do orbital é aproximadamente

$$\Delta E \approx \frac{\hbar}{\Delta t}, \tag{4.8}$$

onde $\hbar$ é a constante de Planck reduzida ($h/2\pi$). A saber que a energia de um fóton é dada por $E_f = h\,c/\lambda$, podemos expressar a incerteza no comprimento de onda do fóton como

$$\Delta\lambda_N \approx \frac{\lambda^2}{2\,\pi\,c}\left(\frac{1}{\Delta t_i} + \frac{1}{\Delta t_f}\right), \tag{4.9}$$

onde Δt_i e Δt_f representam o tempo de vida do elétron em seu estado inicial e o tempo de vida no estado final, respectivamente.

A contribuição do *alargamento Doppler*, também conhecido como alargamento térmico, está associada ao movimento aleatório dos átomos que compõem a atmosfera de uma estrela – existe uma velocidade relativa ao observador para esses átomos, o que muda as frequências observadas (deslocamento Doppler). E, partindo da ideia de um gás em equilíbrio térmico, cuja função de distribuição de Maxwell-Boltzmann é válida, nós podemos esboçar os comprimentos de onda da radição absorvida em função de T como

$$\Delta\lambda_D \approx \frac{2\,\lambda}{c}\left(\frac{2\,k\,T}{m}\right)^{1/2}. \tag{4.10}$$

Por fim, o *alargamento por pressão e colisional* é causado pelo campo elétrico de um grande número de íons, relativamente próximos, e quando os orbitais de um átomo são perturbados devido à colisão com um átomo. O alargamento da linha espectral devido à pressão é da magnitude de

$$\Delta\lambda_C \approx \frac{\lambda^2}{c}\,\frac{n\,\sigma}{\pi}\sqrt{\frac{2\,k\,T}{m}}, \tag{4.11}$$

onde n e σ são a densidade numérica de átomos e a constante de Stefan-Boltzmann. Nessa expressão, notamos que o alargamento por pressão é proporcional à densidade numérica de átomos e, portanto, torna-se mais pronunciado em atmosferas estelares mais densas como as de estrelas anãs da MS.

A forma como o alargamento por pressão e natural atuam na linha é semelhante, e às vezes eles são chamados de *damping*, ou amortecimento – a forma é característica do espectro de radiação emitida por uma carga elétrica em movimento harmônico amortecido (CARROLL & OSTLIE, 2017). A Figura 4.2 mostra a forma dos alargamentos do tipo *damping* e Doppler, que dominam as "asas" e o centro de uma linha composta, respectivamente. O resultado da combinação desses perfis é chamado de Perfil de Voigt.

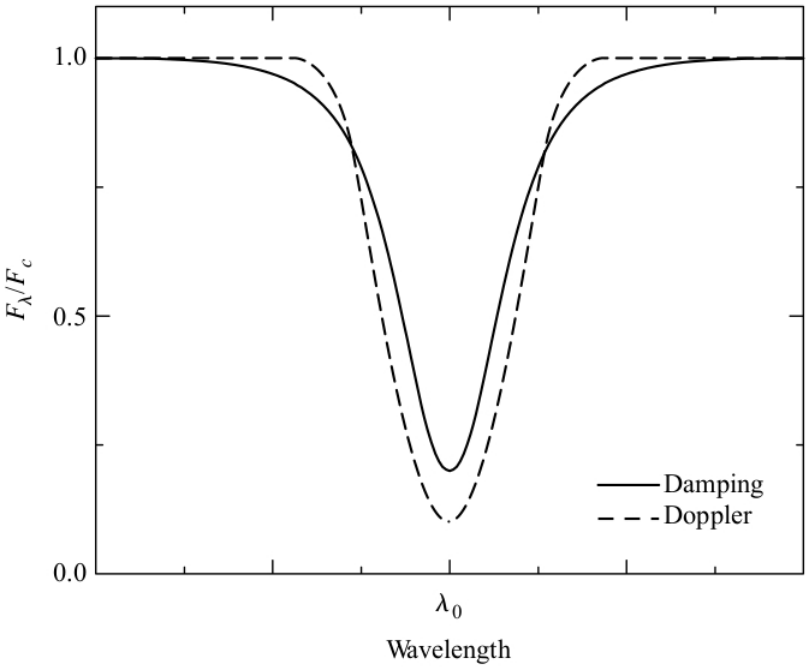

Figura 4.2: Os perfis de linha *damping* e Doppler em escala para a mesma largura equivalente. Obtido de CARROLL & OSTLIE (2017).

4.4 MOOG: o programa de análise espectral

O MOOG é um programa escrito em FORTRAN que proporciona uma análise espectral com uma grande variedade de ferramentas. Sobretudo, a principal aplicação do MOOG é a determinação da composição química de estrelas onde a condição de ETL é considerada razoável (SNEDEN, 1973). O programa apresenta o pacote gráfico SUPERMONGO, que facilita a visualização das saídas no processo iterativo adotado para determinar as abundâncias e os parâmetros atmosféricos (próxima seção).

A tarefa *abfind* é uma opção de execução do MOOG que força/ajusta as abundâncias de espécies química através das medidas de larguras equivalentes. Outra opção de execução, chamada de *synth*, calcula um conjunto de espectros sintéticos de teste e os compara a um espectro observado já normalizado. As abundâncias podem ser estimadas pela inspeção visual do gráfico ou por minimização da diferença dos espectros sintéticos menos o espectro observado. No caso de uma abundância encontrada pelo método de larguras equivalentes, o programa oferece a abundância média como resultado e a incerteza atribuída a ela.

Nós exportamos os resultados obtidos em tabelas, arquivos de texto, para posterior análise e "plotagem" usando a linguagem R, com suporte do RStudio[1]. A linguagem R é voltada à manipulação, análise e visualização de dados, pois oferece muitas facilidades através de pacotes estatísticos e gráficos que tornam o "produto" visualmente mais

[1]Site oficial: http://www.rstudio.com/.

atraente.

4.5 Parâmetros Atmosféricos

4.5.1 Temperatura

A temperatura efetiva ($T_{\rm eff}$) foi determinada através da condição de equilíbrio de excitação. Dito de outra maneira, nós consideramos a independeência entre o potencial de excitação e a abundância de ferro neutro [A(Fe I)]. Essa condição pode ser verificada através do ajuste linear entre as duas quantidades: neste procedimento iterativo, realizado através do programa MOOG, nós consideramos um resultado satisfatório quando o *slope* da reta de ajuste linear se aproxima de zero. Na prática, observamos uma pequena dispersão para as abundâncias de Fe I, o que é normal. Em caso de uma temperatura efetiva incorreta, nós encontraríamos uma dispersão significativamente maior e um maior impacto nas linhas associadas aos potenciais de excitação menores. Nesse sentido, adotamos duas listas de linhas de Fe I com grande diversidade nos valores de potencial de excitação.

Além disso, a temperatura espectroscópica foi comparada com a temperatura fotométrica em todos os trabalhos. Nos artigos que serão apresentados nas próximas seções, nós adotamos os polinômios de ALONSO ET AL. (1999) e GONZÁLEZ HERNÁNDEZ & BONIFACIO (2009) para o índice de cor ($B-V$). Esses polinômios do tipo $\theta_{teff} = P(\text{cor}, [\text{Fe/H}])$ têm base empírica e nos fornecem um diagnóstico da qualidade da temperatura obtida por espectroscopia.

Alternativamente, nós também comparamos o resultado espectroscópico com o resultado obtido através do método *the line-depth ratio* (LDR; BIAZZO ET AL., 2007), que usa a profundidade de linhas de silício, vanádio, escândio, titânio, ferro e níquel para estimar a temperatura efetiva de estrelas de classes de luminosidade entre V e III e temperaturas no intervalo $3800 \leqslant T_{eff} \leqslant 6000$. Esse método também leva em conta o $\log g$ e a velocidade rotacional projetada da estrela.

Eventuais discordâncias entre os resultados obtidos por diferentes métodos foram pontualmente discutidas nos trabalhos.

4.5.2 Velocidade de Microturbulência

A velocidade de microtrubulência atua nas linhas no sentido de alargá-las e sua origem pode estar associada ao movimento de massas em pequena escala, ou pequenas células. Essas micro regiões têm dimensões pequenas se comparadas com a unidade de profundidade ótica. De outra forma, esse parâmetro está vinculado ao alargamento térmico.

Nós determinamos a velocidade de microturbulência através da condição de independendência entre o logarítimo da largura equivalente reduzida ($\log(EW/\lambda)$) e a abundância de ferro neutro. De forma semelhante à temperatura, essa condição pode ser verificada

através do ajuste linear entre as duas quantidade envolvidas, Fe I e $\log(EW/\lambda)$. Para todos os casos, nós consideramos um resultado satisfatório aquele que apresenta um *slope* da reta de ajuste $-0.005 \leqslant \rho \leqslant +0.005$.

4.5.3 Gravidade Superficial

A gravidade superficial foi determinada ao considerarmos o equilíbrio de ionização. Nós podemos verificar essa condição através da relação $\mathrm{A(Fe\,I)} \approx \mathrm{A(Fe\,II)}$, isto é, abundâncias iguais (ou muito próximas) para o ferro neutro e ferro uma vez ionizado – não é raro encontrar na literatura trabalhos que também consideram o equilíbrio de excitação para o elemento titânio. O fato é que, para estrelas do tipo espectral F, G e K, as linhas de ferro neutro e ionizado são numerosas e estão presentes (nítidas ou isoladas) em todo o espectro visível.

Assim como acontece com o parâmetro de temperatura efetiva, também podemos obter a gravidade superficial fotométrica (ou evolutiva) e comparar os dois resultados. Para isso, precisamos conhecer a massa, o módulo de distância, a correção bolométrica e a T_{eff} fotométrica de cada estrela. Fazemos isso usando a relação entre a luminosidade, o raio e a temperatura da estrela, $L = 4\,\pi\,R^2\,\sigma\,T^4$, de onde se pode obter

$$\log g_\star = \log\left(\frac{M}{M_\odot}\right) + 0.4\,(V - A_V + BC_V) + 4\,\log T_{\rm eff}^{(B-V)} - 2\,\log r\,(\mathrm{kpc}) - 16.5, \tag{4.12}$$

onde A_V, BC_V e r representam a extinção interestelar no visível, a correção bolométrica para o visível e a distância. Nós usamos uma expressão analítica obtida por CHEN ET AL. (1999) para encontrar a extinção interestelar em função da longitude galáctica e da distância, enquanto que a correção bolométrica foi encontrada através do polinômio de ALONSO ET AL. (1999). Por fim, nós utilizamos as distâncias individuais de BAILER-JONES ET AL. (2018), que são derivadas a partir das paralaxes obtidas pela Missão Gaia (GAIA COLLABORATION ET AL., 2018).

No geral nós encontramos boa concordância entre as gravidades superficiais espectroscópica e fotométrica. Conforme sinaliza ALLENDE PRIETO ET AL. (1999), o método comparativo é confiável quando lidamos com a análise de estrelas na faixa de metalicidade $-1.0 \leqslant [Fe/H] \leqslant 0.0$.

4.5.4 Metalicidade

A metalicidade é a média da abundância dos metais presentes na atmosfera estelar. Nós consideramos que a abundância do elemento ferro é representativa dessa quantidade, de modo que uma alta abundância de ferro implica em uma pressão eletrônica maior, visto que esse elemento contribui com elétrons "extras".

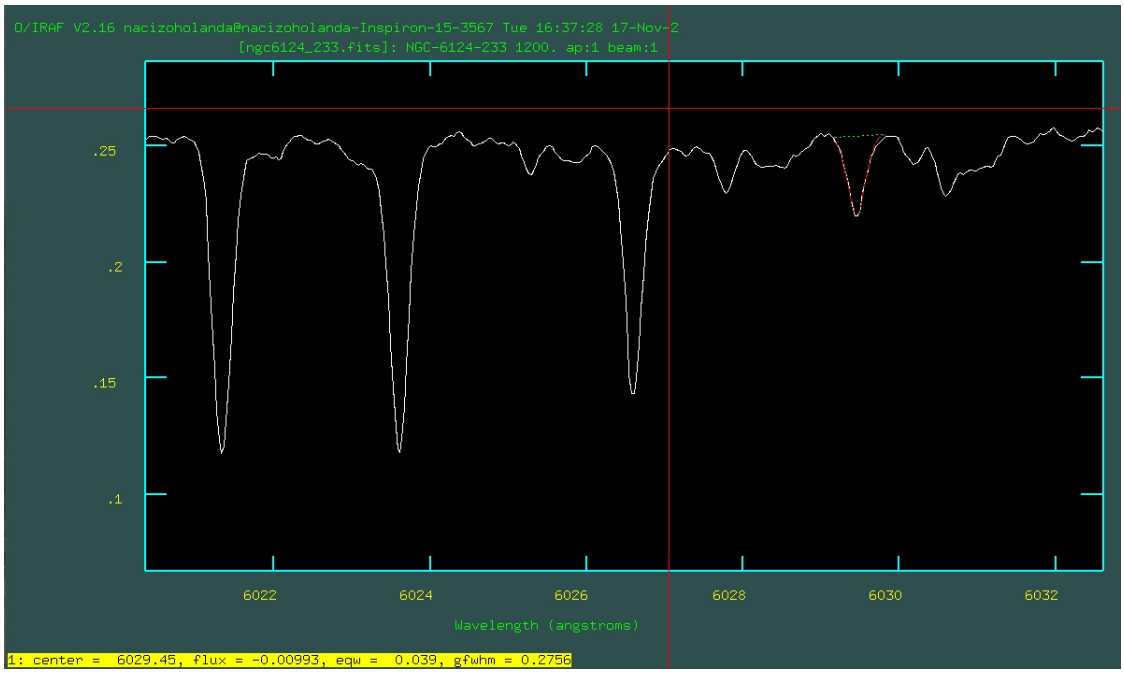

Figura 4.3: Exemplo da utilização da tarefa *splot* em um espectro reduzido.

A abundância de ferro relativa à abundância de hidrogênio pode ser obtida através da seguinte expressão

$$[\mathrm{Fe/H}] = \log_{10}\left(\frac{N_{\mathrm{Fe}}}{N_{\mathrm{H}}}\right)_{\star} - \log_{10}\left(\frac{N_{\mathrm{Fe}}}{N_{\mathrm{H}}}\right)_{\odot}, \tag{4.13}$$

onde N_{Fe} e N_{H} referem-se ao número de átomos de ferro e hidrogênio por unidade de volume, respectivamente. Sabendo que o somatório da fração de massa do hidrogênio (X), hélio (Y) e metais (Z) é igual a um, podemos relacionar a metalicidade de uma estrela com a fração de massa dos metais através da seguinte relação

$$\log_{10}\left(\frac{Z}{Z_{\odot}}\right) \approx [\mathrm{Fe/H}]. \tag{4.14}$$

E quando $Z_{\odot} = 0.02$, temos

$$[\mathrm{Fe/H}] \approx \log Z + 1.699. \tag{4.15}$$

A determinação dos parâmetros atmosféricos teve início com as medidas das larguras equivalentes das linhas de absorção de Fe I e Fe II, onde empregamos o IRAF (*Image Reduction and Analysis Facility*). Eventualmente, linhas contaminadas e com largura equivalente superior à 170 mÅ foram descartadas, de modo que a lista de linhas final muda de estrela para estrela. A lista inicial de linhas compreende as linhas usadas por LAMBERT ET AL. (1996) e HEKKER & MELÉNDEZ (2007). A Figura 4.3 ilustra a utilização da tarefa *splot* na etapa de medição das larguras equivalentes.

4.5.5 As Abundâncias Químicas

Conhecidos os parâmetros atmosféricos, nós podemos determinar a abundância química de espécies diferentes do ferro. A abundância dá força à linha, que por sua vez pode ser quantificada através da largura equivalente.

Podemos relacionar a largura equivalente reduzida com algumas quantidades de interesse, inclusive, com a abundância A para um dado elemento, da seguinte forma:

$$\log\left(\frac{EW}{\lambda}\right) = \log\left(\frac{\pi\, e^2}{m\, c^2}\,\frac{N_i/N}{U_n(T)}\,N_{\rm H}\right) + \log\, A + \log\,(gf\,\lambda) - \left(\frac{5040}{T}\right)\chi - \log\,\kappa_\nu, \quad (4.16)$$

onde N_i/N representa a razão do número de átomos de um elemento de interesse no estado i relativo ao número total de átomos desse mesmo elemento, $A = N/N_{\rm H}$ é a abundância do elemento de interesse em relação ao hidrogênio, e a carga do elétron, κ_ν é o coeficiente de absorção do contínuo e o conjunto gf pode ser interpretado como a probabilidade de transição – g é o peso estatístico e f é a força do oscilador. Olhando para essa expressão, podemos perceber que o primeiro termo da expressão é constante para um íon de interesse, enquanto A varia inversamente com T e diretamente com gf.

Além disso, a Equação 4.16 está intimamente ligada aos parâmetros atmosféricos, direta ou indiretamente. Desse modo, um modelo de atmosfera é necessário para obter a abundância das espécies de interesse – em nossa metodologia, nós adotamos os métodos de largura equivalente e síntese espectral. Utilizamos a técnica de síntese espectral para determinar a abundância de elementos químicos leves (C, N, O, Li) e alguns dos elementos produzidos através da captura de nêutrons, como Eu e La – a abundância de lantânio foi determinada por largura equivalente em alguns casos. As demais espécies químicas (Na, Al, Mg, Si, Ca, Ti, Cr, Ni, Y, Zr, La, Ce, Nd, e Sm) tiveram suas abundâncias determinadas via método de largura equivalente.

O arquivo de linhas usado para o método de larguras equivalentes é constituído pelo comprimento de onda da transição, a identificação da espécie química associada à transição, o gf, o potencial de excitação e a largura equivalente. No caso da síntese espectral, ainda é necessário um espectro normalizado da região de formação da linha ou banda de interesse. A Figura 4.4 ilustra a tela inicial da tarefa *synth* do código MOOG.

4.5.6 Velocidade Radial e Velocidade Rotacional Projetada

A velocidade radial foi estimada a partir do deslocamento Doppler observado nas linhas de absorção com larguras equivalentes medidas. Para isso, nós utilizamos o comprimento de onda de repouso (λ_0) e o comprimento de onda observado (λ), tal como

$$v_R = c\,\frac{\lambda_0 - \lambda}{\lambda_0}. \quad (4.17)$$

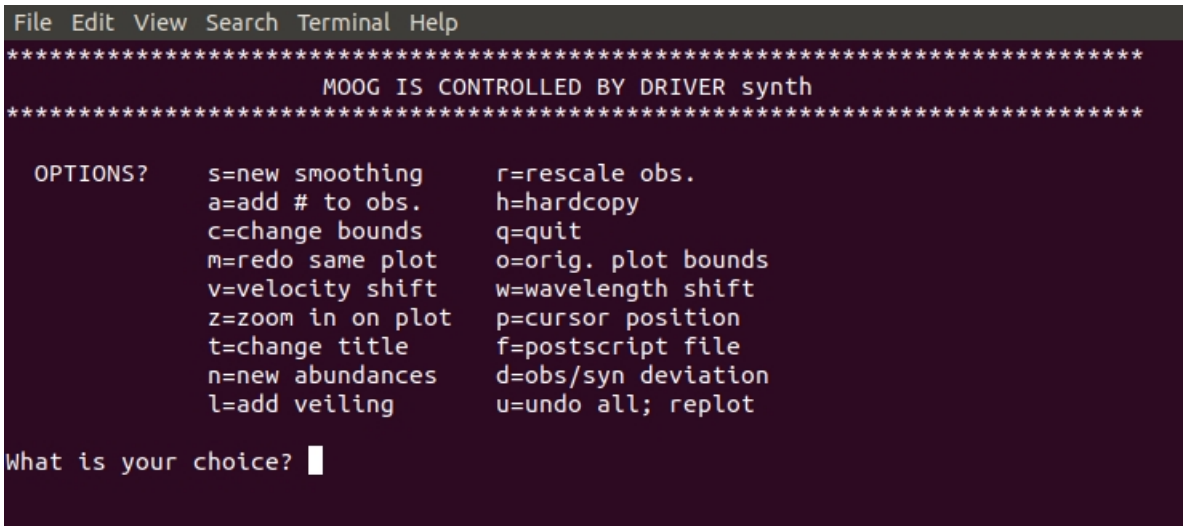

Figura 4.4: Tela inicial de comando da tarefa *synth*, no MOOG.

Na maioria dos casos, nós comparamos o nosso resultado com os resultados divulgados pela Missão Gaia (GAIA COLLABORATION ET AL., 2018). No geral, como produto desse processo, nós obtivemos excelente concordância para as velocidades radiais associadas às estrelas isoladas, não participantes de sistemas binários.

A rotação das estrelas constitui um dado de grande valia. Afinal, a circulação de material na envoltória convectiva, a estrutura interna e atividade magnética podem estar ligadas à rotação. Posto isso, a velocidade rotacional projetada (v sin i) das estrelas das nossas amostras foi determinada através do perfil de linhas isoladas de Fe. No procedimento de síntese espectral, foram adotadas macroturbulência de $3\,\mathrm{km\,s^{-1}}$, típica de gigantes G e K (FEKEL ET AL., 1997), e largura à meia altura de 0.13 Å, típica das linhas de tório-argônio usadas para a calibração do comprimento de onda para o espectrógrafo FEROS.

4.6 Observações

Os espectros analisados ao longo desse projeto foram obtidos através de observações realizadas no Chile através do acordo entre Observatório Nacional e *Max Planck Gesellschaft/European Southern Observatory* (ESO). O equipamento utilizado foi o *Fiberfed Extended Range Optical Spectrograph* (FEROS; KAUFER ET AL., 1999) acoplado ao telescópio de 2.2 metros. O FEROS é um espectrógrafo de alta resolução ($\lambda/\Delta\lambda \approx 48000$) e eficiência ($\approx$ 20%) que oferece uma ampla janela espectral de exposição única (3600 Å até 9200 Å – 39 ordens, 2 fibras). A Figura 4.6 mostra um espectro "cru" obtido com a configuração descrita.

A aquisição de dados se deu da forma tradicional: no começo da noite foram obtidas as imagens de calibração como *bias*, *flat* e a lâmpada de calibração de Th–Ar, para que o

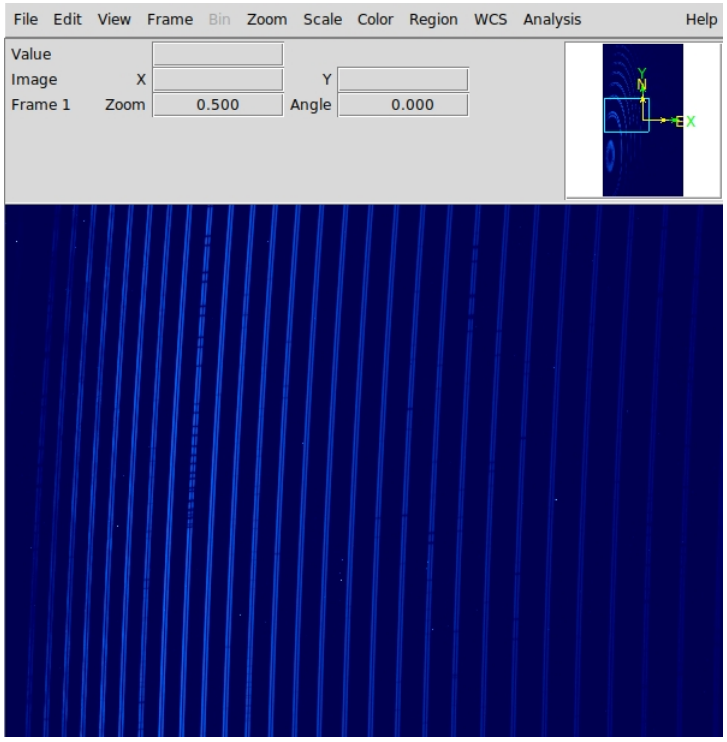

Figura 4.5: Espectro obtido através do espectrógrafo FEROS acoplado ao telescópio de 2.2 m do ESO.

restante da noite fosse dedicado à aquisição das imagens referentes aos alvos da missão. O processo de redução foi realizado através do pacote de redução MIDAS (*The Munich Image Data Analysis System*), que efetuou a subtração, divisão, calibração em comprimentos de onda entre as imagens dos espectros e as imagens de calibração.

Os espectros reduzidos apresentam uma razão sinal-ruído alta, 100–200, o que é suficientemente bom para os estudos químicos que nos propomos a realizar. No total, foram analisados 14 espectros. A Tabela 4.1 apresenta os objetos estudados, magnitudes no visível, tempo de exposição e suas datas de observação. Além disso, os dados de espectroscopia foram complementados por dados de fotometria e astrometria disponíveis na literatura.

Tabela 4.1: Estrelas estudadas nesta tese com suas respectivas magnitudes (V), tempo de exposição e datas de observação.

Objeto	Mag (V)	Exp. (s)	Data
NGC 2345-14	10.730	2400	11/03/2016
NGC 2345-34	9.940	1200	11/03/2016
NGC 2345-43	10.700	2400	11/03/2016
NGC 2345-50	10.400	1500	11/03/2016
NGC 2345-60	10.480	1500	11/03/2016
NGC 6124-1	9.085	1200	18/03/2016
NGC 6124-14	9.155	1200	19/03/2016
NGC 6124-29	9.255	1500	20/03/2016
NGC 6124-33	8.685	1500	20/03/2016
NGC 6124-35	8.995	1500	20/03/2016
NGC 6124-36	9.165	1500	20/03/2016
NGC 6124-233	8.750	1200	20/03/2016
HD 150382	6.830	300	11/04/2016
TYC 8327-1678-1	11.443	2700	20/03/2016

Capítulo 5

HD 150382: uma estrela rica em lítio na fase early-AGB?

Neste capítulo nós reportamos a descoberta de uma nova gigante rica em lítio, HD 150382, uma estrela que se encontra no estágio evolutivo de pós-clump do ramo das gigantes vermelhas. Os parâmetros atmosféricos, as abundâncias para 17 elementos químicos e o valor razão isotópica do carbono, $^{12}C/^{13}C$, foram determinados usando os métodos de largura equivalente e síntese espectral. A abundância de lítio foi obtida via síntese espectral do dupleto de ressonância em λ 6708 e a linha em λ 6104, que revelou $\log \epsilon(\mathrm{Li}) = 2.55$. Além disso,nós usamos modelos de trajetórias evolutivas para determinar a massa e luminosidade da gigante HD 150382, para então comparar com outras gigantes ricas em lítio bem conhecidas na literatura. Os nossos resultados mostram que a estrela HD 150382 é um objeto que está rotando lentamente e tem uma metalicidade próxima à metalicidade solar. Nós também mostramos que essa gigante não está enriquecida em elementos que são produzidos no processo de captura lenta de neutros, o que está de acordo com o seu estágio evolutivo. Finalmente, baseados nos resultados para suas abundâncias, nós estudamos os possíveis cenários de enriquecimento de lítio.

Este capítulo refere-se à publicação: **Holanda, N., Drake, N. A., & Pereira, C. B., 2019, The Astronomical Journal, 159, 9 (Artigo 2)**.

5.1 Introduction

The dilution of main-sequence remaining Li occurs during the first ascent to the red giant branch (RGB), due to the development of an extensive convective envelope. Hence, it is estimated that objects with an exceptional amount of Li in their atmospheres ($\log \epsilon(Li) \geqslant 1.5$), the so-called lithium-rich giants, consist of only $1\% - 2\%$ of the RGB stars (BROWN ET AL., 1989; BHARAT KUMAR ET AL., 2011; SMILJANIC ET AL., 2018; WALLERSTEIN & SNEDEN, 1982).

Lithium atoms can be synthesized via the Cameron-Fowler mechanism (CAMERON & FOWLER, 1971), but this scenario requires physical and chemical conditions for beryllium to be produced and quickly transported to cool regions where lithium could finally be created [^{3}He(α, γ) ^{7}Be(e$^-$, ν)^{7}Li]. This mechanism, also called ^{7}Be-transport, occurs in the bump in the luminosity function for stars on the RGB (CHRISTENSEN-DALSGAARD, 2015; IBEN , 1968) and it is possible that some giants become lithium-rich at the core-He burning phase, since most of these peculiar objects are classified as RGB clump stars (BHARAT KUMAR ET AL., 2011; CASEY ET AL., 2019; DEEPAK & REDDY, 2019).

The cool bottom processing (CBP), as a consequence of a deep extra mixing, is the most likely answer for the material that is subjected to partial nuclear processing in the neighborhood of the outer edge of the H-burning shell and back to the envelope in low-mass stars (BOOTHROYD & SACKMANN, 1999; SACKMANN & BOOTHROYD, 1999). One of the important products of this extra mixing is the destruction of ^{3}He and the creation of ^{7}Be, but its efficiency depends on complex parameters such as mixing speeds, geometry, and episodicity. Additionally, to find a possible solution for the high ^{7}Li abundance in low-mass star atmospheres ($\leqslant 2.5\,M_\odot$), the CBP is (also) commonly invoked to explain the low ^{12}C/^{13}C ratio in red giant stars. Nevertheless, CBP is not related to any physical explanation that supports its predictions in stellar surface abundances. More complete and literature-based processes, such as Thermohaline Mixing, fail to predict the lithium abundances found on the surface of these classes of chemically peculiar giants before the thermally pulsing asymptotic giant branch (TP-AGB; CANTIELLO & LANGER, 2010; CHARBONNEL & LAGARDE, 2010; LAGARDE ET AL., 2019). SMITH & LAMBERT (1989, 1990) showed that the existence of Li-rich stars in the TP-AGB stage also occurs via the Cameron-Fowler mechanism. The lithium content in these luminous stars are in good agreement with the theoretical predictions considering hot bottom burning, which consists in a H-burning shell condition in which the outer part of the shell is included in the envelope convection (HERWIG, 2005; SACKMANN ET AL., 1974; SCALO ET AL., 1975). Therefore, lithium self-enrichment is also possible to occur in luminous stars at the TP-AGB phase of intermediate-mass stars ($\geqslant$4.0-7.0 $M_\odot$).

The discovery of Li-rich stars in the early-AGB phase proves to be a difficult task. GRATTON & D'ANTONA (1989) reported an example of a metal-poor giant ([Fe/H] = -0.5) with strong lithium lines, HD 39853. Today this well-studied giant dissociates from the others Li-rich stars because it is a low-mass star that has low surface gravity and effective temperature (respectively, 1.5 $M_\odot$; 1.16 dex; 3900 K). However, the authors showed that HD 39853 is not as lithium-rich [$\log \epsilon$(Li) = 2.8] compared to some other stars at the RGB clump, such as IRAS 13539-4153 [$\log \epsilon$(Li) = 4.10; REDDY & LAMBERT, 2005]. Another reported Li-rich star at the early-AGB phase was investigated by REDDY & LAMBERT (2005), IRAS 12327-6523, which presents a small lithium enrichment [$\log \epsilon$(Li) = 1.60]. In a more recent discovery, ALCALÁ ET AL. (2011) show

that IRAS 12556-7731 is the first M-type Li-rich star. The metallicity found by them is close to solar ([Fe/H] = -0.05) and the lithium abundance is similar to that of HD 39853 [log ϵ(Li) = 2.4]. Withal, IRAS 12556-7731 is a low-mass star (1.0 $M_{\odot}$; ALCALÁ ET AL., 2011). Therefore, it is possible that the preservation and/or production of lithium occurs after the RGB-bump phase due to the He-core flash or extra-mixing events that could explain the existence of these low-mass objects in more advanced stages of stellar evolution such as early-AGB stars. The fact is that these giants are less enriched, or have not fully depleted the manufactured lithium or received in stages previous to the AGB stage.

In this work, we reported the discovery of a new lithium-rich star, HD 150382, which is probably at the early-AGB phase. HD 150382 was selected for observation after a search in the literature for K-giant stars that have not yet been spectroscopically observed with high resolution with the aim to find some stars with chemical peculiarities, such as those with enrichment of the s-process elements, lithium enrichment, or new weak G-band stars. HD 150382 is a bright star (V = 6.83) classified as K3/4 III (HOUK & SWIFT , 1999) and is located in Ophiuchus, (l, b) = (05°.79, +22°.05), at a distance of 0.320 kpc (GAIA COLLABORATION ET AL., 2018). Here, we present the first chemical analysis of this giant star.

5.2 The Giant HD 150382

5.2.1 Observations

The spectroscopic observation was carried out on 2016 April 11, and was made using the Fiber-fed Extended Range Optical Spectrograph (FEROS; KAUFER ET AL., 1999) at the 2.2 m Max Planck Gesellschaft/European Southern Observatory (ESO) Telescope in La Silla, Chile. The FEROS provides a resolving power of R $\approx$ 48,000 and a full wavelength coverage between 3800-9200 Å. The exposure time for HD 150382 was 300 s to a typical signal-to-noise ratio (S/N) = 100-150. Further, the reduction was performed using the FEROS Data Reduction System pipeline.

5.2.2 Atmospheric Parameters

The atmospheric parameters of HD 150382, namely the effective temperature (T_{eff}), surface gravity (log g), microturbulence (ξ), and metallicity ([Fe/H]) (we use the notation [X/H] = $\log(N_X/N_H)_{\star}$ $\log(N_X/N_H)_{\odot}$), were determined in the same way as in HOLANDA ET AL. (2019) in the study of K-giants of the open cluster NGC 2345. The absorption lines selected for this task were taken from LAMBERT ET AL. (1996). In particular, for the atmospheric analysis we adopted the local thermodynamic equilibrium (LTE), the model atmospheres of KURUCZ (1993), and the spectral analysis code MOOG (2013 version; SNEDEN, 1973) to analyze the absorption spectrum of HD 150382.

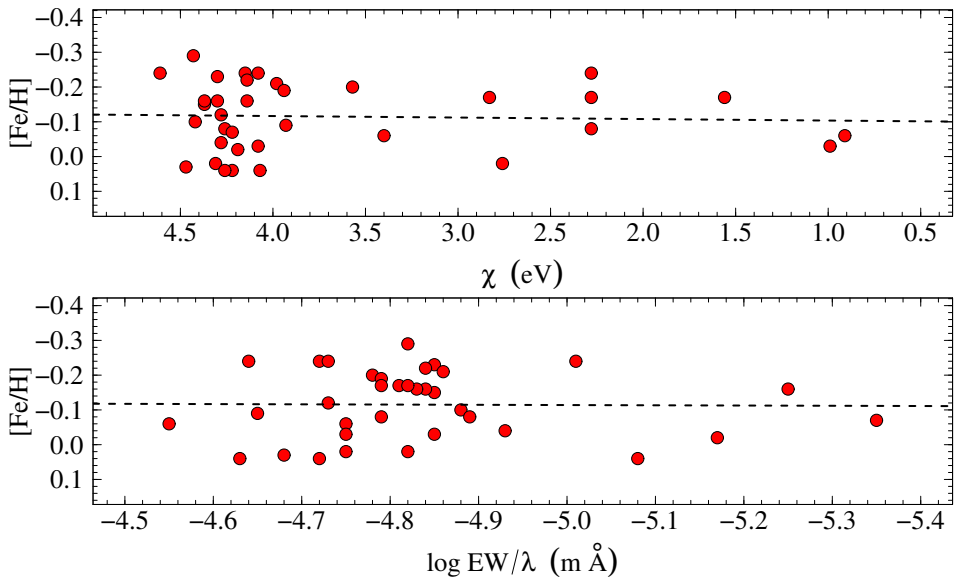

Figura 5.1: Fe I abundances vs. excitation potential (top) and vs. reduced equivalent width $\log \mathrm{EW}/\lambda$ (bottom). Dashed lines represent the linear regression with the angular coefficient close to zero.

The effective temperature ($T_{\rm eff}$) was obtained requiring that the abundance of lines does not depend on the lower-level excitation potential (χ). Furthermore, the microturbulence velocity (ξ) was found requiring that the abundance of Fe I lines does not also depend on the reduced equivalent width (EW/λ). These two conditions are seen in Figure 5.1, where it shows, respectively, the diagrams that correspond to the abundances of individual Fe I lines plotted versus the excitation potential and the reduced line strength for the atmospheric parameters adopted for HD 150382. Also, the surface gravity ($\log g$) was determined based on the ionization equilibrium requiring $[\log \epsilon(\mathrm{Fe\,I}) \approx \log \epsilon(\mathrm{Fe\,II})]$.

The uncertainties in the atmospheric parameters were estimated following the same methodology as HOLANDA ET AL. (2019), i.e., the error in effective temperature was estimated from the uncertainty in the slope of relation [Fe I/H] versus the excitation potential, while the error in the microturbulent velocity was estimated from the uncertainty in the slope of [Fe I/H] versus $\log \mathrm{EW}/\lambda$. For gravity, the error is estimated by changing the $\log g$ value until the difference in the average abundances of Fe I and Fe II equals the standard deviation of the mean [Fe I/H].

In this context, we compare the derived spectroscopic gravity with the evolutionary gravity $\log g_\star$ using the previously determined mass M from the isocrone adjustment using the equation

$$\log g_\star = \log\left(\frac{M}{M_\odot}\right) + 0.4\,(V - A_V + BC_V) + 4\log T_{\rm eff}^{(B-V)} - 2\log r\,(\mathrm{kpc}) - 16.5.$$

In the equation above, V, A_V, BC_V, $T_{\rm eff}$, and r are the visual magnitude, interstel-

Tabela 5.1: Main parameters of HD 150382.

Parameter	Value	Reference
ℓ	$05^{\circ}.79$	—
b	$+22^{\circ}.05$	—
log t (Gyr)	9.00 ± 0.20	This Work
$R_{\rm GC}$ (kpc)	7.65 ± 0.05*	This Work
$T_{\rm eff}$ (K)	$4\,070 \pm 80$	This Work
log g (dex)	1.35 ± 0.08	This Work
$\xi_{\rm t}$ (km s^{-1})	1.64 ± 0.08	This Work
[Fe/H] (dex)	-0.09 ± 0.10	This Work
v sin i (km s^{-1})	3.70 ± 0.80	This Work
$\langle$RV$\rangle$ (km s^{-1})	5.36 ± 0.48	This Work
$\langle$RV$\rangle$ (km s^{-1})	4.44 ± 0.12	GAIA COLLABORATION ET AL. (2018)
d (pc)	320.8 ± 4.1	GAIA COLLABORATION ET AL. (2018)
classification	K3/4 III	HOUK & SWIFT (1999)

*We adopted $R_{\rm GC\odot} = 7.95$ kpc.

lar absorption in the V band (CHEN ET AL., 1999), bolometric correction (ALONSO ET AL., 1999), photometric temperature in the (B - V) color (ALONSO ET AL., 1999), and distance (GAIA COLLABORATION ET AL., 2018), respectively. The solar values used are $M_{\rm bol} = 4.75$, log $g_{\odot} = 4.44$ dex, and $T_{\rm eff\odot} = 5777$ K. The result is $log\, g = 1.37$ dex, which is in good agreement with the spectroscopic result. Based on $(B - V)_0$ we determined a temperature of 3715 K, but this color index is no longer useful for cool giants ($T_{\rm eff} < 4000$ K; ALONSO ET AL., 1999; DA SILVA ET AL., 2006). On other hand, we also derive photometric temperature through $(V - K)_0$ and find a similar value. However, some authors caution that stars with $K < 3.0$ are saturated (HD 150382 has $K = 2.6$), and the error of their colors is huge (CUTRI ET AL., 2003; DA SILVA ET AL., 2006). For these results and limitations, we adopted our spectroscopic temperature.

Additionally we determined the projected rotational velocity (v sin i) and the radial velocity of HD 150382. The projected rotational velocity was obtained based on the spectral synthesis of the Fe I 6151.6 Å line. In this procedure, was adopted the macroturbulent velocity of 3.0 km s^{-1} (FEKEL ET AL., 1997) and FWHM of 13.0 mÅ (corresponding to the FWHM thorium-argon lines used for the wavelength calibration for FEROS). Thus, with the atmospheric parameters previously determined, we find the v sin $i = 3.7 \pm 0.8$ km s^{-1}. The radial velocity was obtained by measuring the Doppler shifts of the Fe I lines used to determine the atmospheric parameters. The final atmospheric parameters and other basic information for HD 150382 are listed in Table 5.1.

5.2.3 Stellar Abundances

The chemical abundances of the elements sodium to nickel (Na, Mg, Al, Ca, Ti, Cr, and Ni), the elements whose solar system abundances have been predominantly synthesized

Tabela 5.2: Chemical abundances of the elements derived for HD 150382. The second column gives the abundance in the notation [X/Fe] with the respective abundance dispersion among the lines of the elements with more than three available lines. The last column refers whether the abundances were derived either using spectrum synthesis technique (syn) or based on the equivalent width measurements. In this latter case we provide the number of lines (n) used for the abundance determination. For lithium and sodium we also provide the NLTE abundances.

Species	Abundances	n
$\log\,\epsilon(\mathrm{Li})_{\lambda\,6104}$	$+2.08$	syn
$\log\,\epsilon(\mathrm{Li})^{\mathrm{NLTE}}_{\lambda\,6104}$	$+2.36$	–
$\log\,\epsilon(\mathrm{Li})_{\lambda\,6708}$	$+2.50$	syn
$\log\,\epsilon(\mathrm{Li})^{\mathrm{NLTE}}_{\lambda\,6708}$	$+2.55$	–
[C I/Fe]	-0.22	syn
[N I/Fe]	$+0.83$	syn
[O I/Fe]	-0.07	syn
$^{12}\mathrm{C}/^{13}\mathrm{C}$	18	syn
[Na I/Fe]	$+0.28$	2
$[\mathrm{Na\,I/Fe}]^{\mathrm{NLTE}}$	$+0.12$	2
[Mg I/Fe]	$+0.18 \pm 0.11$	5
[Al I/Fe]	$+0.15 \pm 0.11$	5
[Ca I/Fe]	$+0.03$	2
[Ti I/Fe]	$+0.08 \pm 0.05$	3
[Cr I/Fe]	$+0.07 \pm 0.09$	10
[Fe I/H]	-0.09 ± 0.10	35
[Fe II/H]	-0.08 ± 0.08	5
[Ni I/Fe]	$+0.00 \pm 0.10$	10
[Y II/Fe]	$+0.04$	2
[Zr I/Fe]	$+0.19 \pm 0.12$	13
[Ce II/Fe]	$+0.19 \pm 0.07$	3
[Nd II/Fe]	$+0.09 \pm 0.13$	5
[Eu II/Fe]	$+0.18$	syn
$[\alpha/\mathrm{Fe}]$	$+0.10 \pm 0.08$	–
[s/Fe]	$+0.13 \pm 0.08$	–

in the s-process (Y, Zr, Ce, and Nd), and an element whose solar system abundance are predominantly attributed to the r-process (Eu) was determined in the same way as in HOLANDA ET AL. (2019) where we also applied the line-synthesis code MOOG. The equivalent widths of the absorption lines are given in Table A.2. In addition, the abundances of lithium, carbon, nitrogen, oxygen, europium, and the isotopic ratio $^{12}\mathrm{C}/^{13}\mathrm{C}$ were determined using the spectral synthesis technique. All abundances determined here were normalized using the solar abundances of ASPLUND ET AL. (2009).

The lithium abundance was determined using the Li I resonance doublet at $\lambda\,6708$ and the excited line at $\lambda\,6104$, which assumes LTE conditions. The wavelengths and oscillator strengths for the individual components for the lithium lines were taken from SMITH ET AL. (1998) and HOBBS ET AL. (1999), and the Vienna Atomic Line Database (VALD;

KUPKA ET AL., 1999) for the λ6104 and λ6708 lines. The resolution of the FEROS spectrum is not sufficient to rule out a contribution from ^{6}Li at λ6708, but we estimated an upper limit of $^6\mathrm{Li}/^7\mathrm{Li} = 0.04$. Later, the correction for non-LTE (NLTE) effects was applied using data from LIND ET AL. (2009). These corrections were based on the model $T_{eff} = 4000$ K, log $g = 1.0$ dex, $\chi = 2.0$ km s^{-1}, and [Fe/H] = 0.0 where positive and particular corrections were found for each absorption line ($\Delta \log \epsilon(\mathrm{Li})_{\lambda 6104} = +0.28$ and $\Delta \log \epsilon(\mathrm{Li})_{\lambda 6708} = +0.05$).

The carbon and nitrogen abundances were obtained through C_2 (λ5635 region) and CN (λ8003 region) using the same line lists as described in HOLANDA ET AL. (2019), as well as to obtain the isotopic ratio $^{12}\mathrm{C}/^{13}\mathrm{C}$. The oxygen abundance was obtained based on the [O I] forbidden line at 6300 Å where we adopted log gf = -9.72 from ALLENDE PRIETO ET AL. (2001). We also take into account the contribution of CN and Ni I (Kupka et al. 1999) in the region of the oxygen absorption line. The europium abundance was based on the absorption lines at 6645 Å (KUPKA ET AL., 1999; MUCCIARELLI ET AL., 2008). Figure 5.2 shows the observed and synthetic spectra around the lithium lines at 6708 and 6104 Å, while Figure 5.3 shows the fit around the oxygen forbidden line, the CN lines between 8002 and 8005 Å, and the europium line at 6645 Å. In all of these cases, the dots represent the normalized observed spectra and the solid lines represent the synthetic spectra. We used atomic data and NLTE corrections given by LIND ET AL. (2011) for two lines used to determine the sodium abundance (λ6154 and λ6161). Therefore, we had a slight decrease in the final sodium abundance for HD 150382 ($\Delta \log \epsilon(\mathrm{Na}) = -0.16$). Table 5.2 provides the results in notation relative to iron, except in the case of lithium ($\log \epsilon(\mathrm{Li}) = \log\ \mathrm{N_{Li}/N_H} + 12.0$).

5.2.4 Abundance Uncertainties

Tables 5.3 and 5.4 show the influence of the uncertainties of the atmospheric parameters over the chemical abundances for HD 150382. In Table 5.3 we also show the abundance variations due to the uncertainty of 3.0 mÅ in the equivalent width of the observed lines for all chemical species (ΔEW), considering the FEROS spectral resolution and the S/N (CAYREL, 1988). Also, the last column in Table 5.3 provides the abundance dispersion between the lines for each element with more than three available lines. The seventh column of Table 5.3 and the last column of Table 5.4 provide the total abundance uncertainty calculated as the root square of the sum of the various sources of uncertainties [$(\Sigma \sigma^2)^{1/2}$].

Table 5.3 reveals that neutral species exhibit higher sensitivity to temperature variation while ionized species exhibit greater differences due to the uncertainties in the surface gravities. The uncertainties in the carbon abundance affect the nitrogen and oxygen abundances and vice versa once we used ^{12}CN and C_2 molecular lines for carbon and

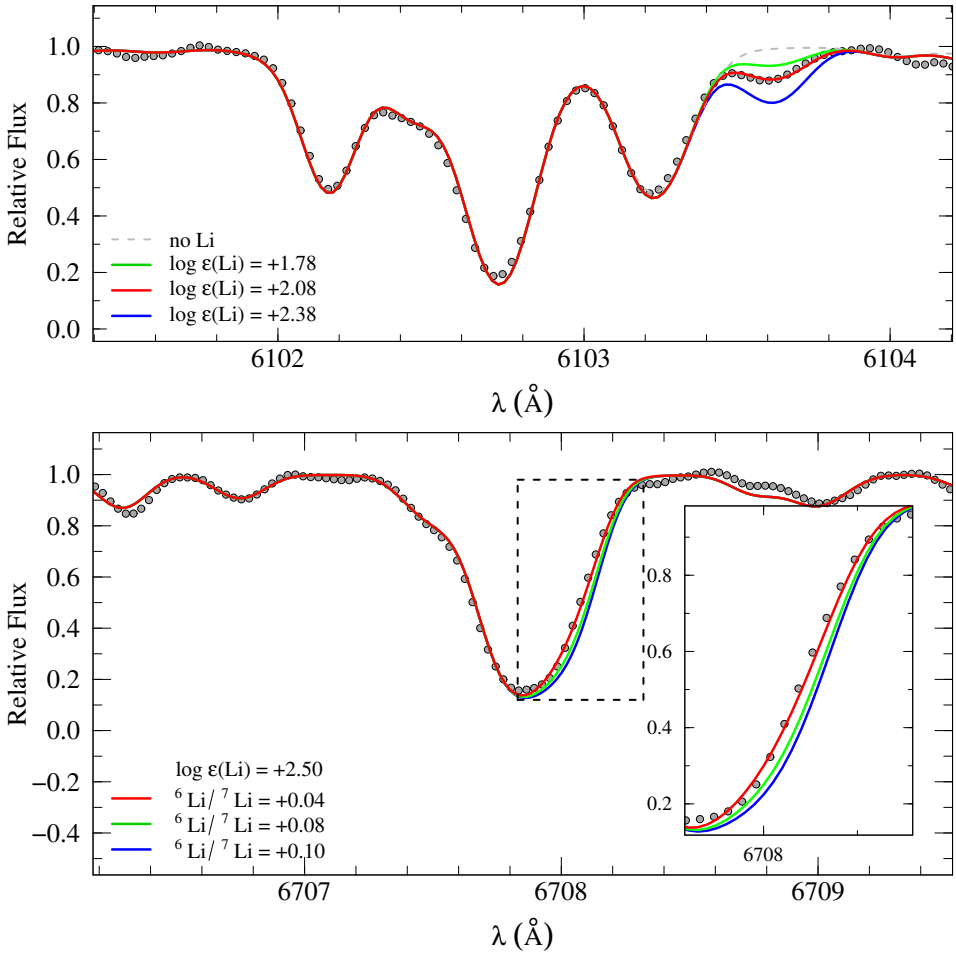

Figura 5.2: Observed (black dots) and synthetic spectra (gray, green, red, and blue solid lines) in the region of the lithium lines at 6103.6 Å (top) and at 6707.8 Å (bottom).

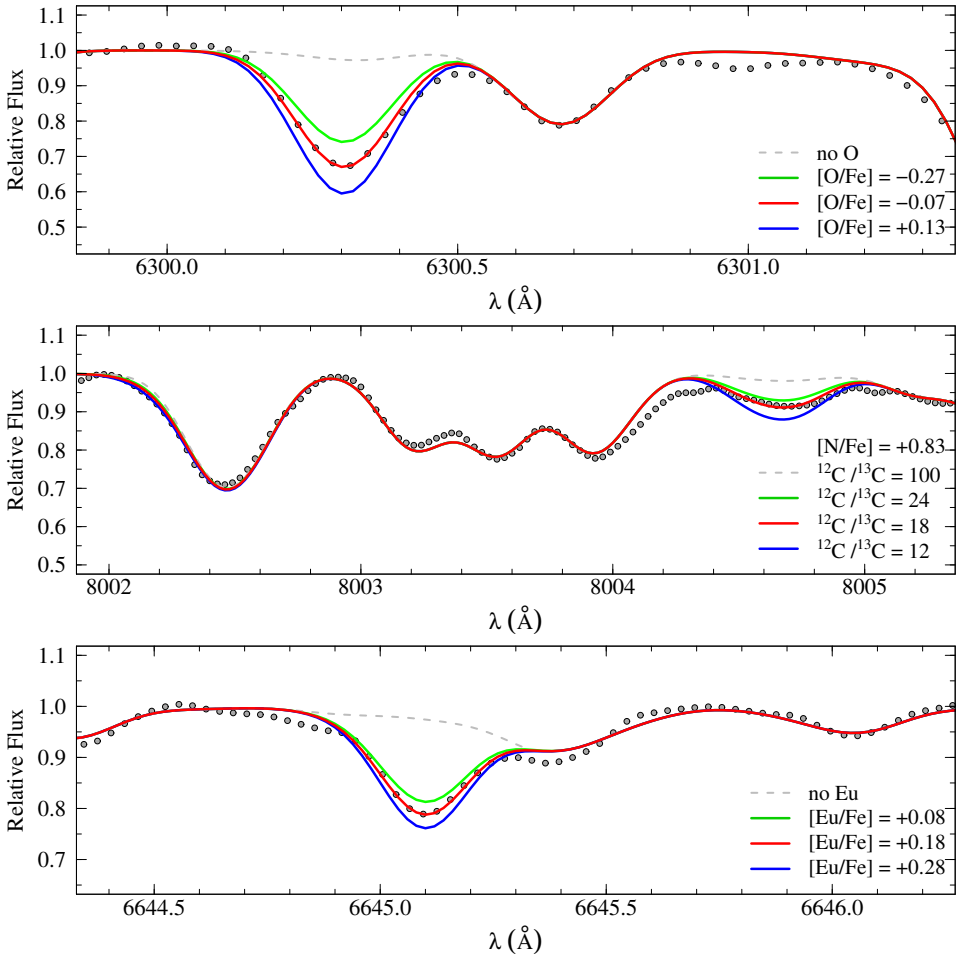

Figura 5.3: Observed (black dots) and synthetic spectra (gray, green, red, and blue solid lines) in the region of the oxygen forbidden line (top), in the region of the CN lines used to determine the nitrogen abundance and the $^{12}C/^{13}C$ ratio (middle), and in the region of the europium line (bottom) of HD 150382.

nitrogen abundance determinations.

5.3 Discussion

5.3.1 The Position of HD 150382 in the log g-T_{eff} Diagram

Figure 5.4 shows the position of HD 150382 and other known Li-rich giants (the main parameters are listed in Table A.1) in the log g - T_{eff} diagram. In this diagram, evolutionary tracks were taken from GIRARDI ET AL. (2000) for a metallicity of $Z = 0.019$ for stars with masses between 1.0 and 4.0 $M_{\odot}$. Based on the position in the diagram we obtained a mass of 2.20 ± 0.30 and hence $\log L/L_{\odot} = 2.86 \pm 0.10$ for our giant. Furthermore, using the theoretical isochrones of GIRARDI ET AL. (2000) for the same metallicity considered, we determined the age of HD 150382 as $\log t = 9.00 \pm 0.20$. An important fact that helps us estimate the evolutionary status of HD 150382 is that for these isoch-

Tabela 5.3: Effects on derived abundances resulting from model changes.

species	$\Delta T_{\rm eff}$ (K) $+80$ K	$\Delta \log g$ $+0.08$	$\Delta \xi$ $+0.08\,{\rm km\,s^{-1}}$	Δ[Fe/H] $+0.10$ dex	ΔEW $+3$ mÅ	$(\Sigma\,\sigma^2)^{1/2}$	σ_{obs}
log ϵ(Li)$_{\lambda\,6104}$	+0.03	+0.02	−0.03	+0.03	—	±0.06	—
log ϵ(Li)$_{\lambda\,6708}$	+0.04	+0.01	−0.04	+0.03	—	±0.06	—
[Na I/Fe]	+0.07	+0.00	−0.04	+0.00	+0.05	±0.09	—
[Mg I/Fe]	−0.03	+0.00	−0.02	+0.00	+0.05	±0.06	±0.11
[Al I/Fe]	+0.04	−0.01	−0.02	−0.01	+0.04	±0.06	±0.11
[Ca I/Fe]	+0.07	−0.01	−0.03	−0.01	+0.04	±0.09	—
[Ti I/Fe]	+0.09	+0.00	−0.08	+0.00	+0.06	±0.13	±0.05
[Cr I/Fe]	+0.07	+0.01	−0.03	+0.01	+0.06	±0.10	±0.09
[Fe I/H]	−0.03	+0.01	−0.05	+0.00	+0.05	±0.08	±0.10
[Fe II/H]	−0.16	+0.03	−0.03	+0.01	+0.07	±0.18	±0.08
[Ni I/Fe]	−0.02	+0.02	−0.04	+0.02	+0.06	±0.08	±0.10
[Y II/Fe]	+0.00	+0.02	−0.05	+0.03	+0.06	±0.09	—
[Zr I/Fe]	+0.13	+0.01	−0.05	+0.01	+0.06	±0.15	±0.12
[Ce II/Fe]	+0.01	+0.03	−0.05	+0.03	+0.07	±0.10	±0.08
[Nd II/Fe]	+0.02	+0.03	−0.02	+0.04	+0.06	±0.08	±0.13
[Eu II/Fe]	+0.00	+0.03	−0.03	+0.02	—	±0.05	—

Tabela 5.4: Influence of the errors in atmospheric parameters over the abundances of CNO elements.

species	$\Delta T_{\rm eff}$ (K) $+80$ K	$\Delta \log g$ $+0.08$ dex	$\Delta \xi$ $+0.08$ km s^{-1}	[Fe/H] $+0.10$ dex	$\Delta \log$(C) $+0.20$ dex	$\Delta \log$(N) $+0.20$ dex	$\Delta \log$(O) $+0.20$ dex	$(\Sigma \sigma^2)^{1/2}$
[C/Fe]	+0.02	+0.06	−0.02	−0.08	—	−0.02	+0.08	±0.13
[N/Fe]	−0.08	+0.03	−0.02	+0.02	−0.43	—	+0.30	±0.53
[O/Fe]	+0.07	+0.02	−0.02	+0.02	−0.02	+0.02	—	±0.08

rones Girardi and colleagues estimate that the end of the core-He burning phase occurs at $\log L/L_{\odot} \approx 2.06$ and the TP-AGB phase begins at $\log L/L_{\odot} \approx 3.40$. Apart from that, we also obtained abundances of elements heavier than iron that are produced through neutron-capture processes, since TP-AGB stars are mainly responsible for the creation of these elements. Figure 5.5 presents the literature determinations for disk red clump giants (MISHENINA ET AL., 2006; open diamonds) and local disk field giants (LUCK & HEITER , 2007; yellow filled triangles) as well as dwarf stars in the solar neighborhood (BATTISTINI & BENSBY, 2016; blue open triangles). HD 150382 is located inside the cloud of objects from the three samples and, therefore, does not present chemical indications of production of the s-process elements. The mean of s-elements over iron is defined as $[s/Fe] = \frac{1}{4}([Y\,II/Fe] + [Zr\,I/Fe] + [Ce\,II/Fe] + [Nd\,II/Fe])$.

There are a few Li-rich stars classified as early-AGB stars or as possible AGB stars with masses $\leqslant 4.0$ $M_{\odot}$ studied in the literature (marked with an asterisk in Table A.1). Among them, also based on Figure 5.4, we included HD 150382. Note that among the 83 lithium-rich giants, there are only seven early-AGB stars. Therefore, the Li-rich giants that are at or near the AGB stage constitute a small and interesting subgroup. But, what do these early-AGB Li-rich stars have in common? And, what is the most likely lithium maintenance or enrichment scenario for these evolved stars?

5.3.2 The Early-AGB Lithium-rich Stars

Based on the abundance pattern for the light elements, HD 150382 presents the abundances of carbon and nitrogen affected (i.e., ^{12}C reduced and ^{14}N increased). Further, the $^{12}C/^{13}C$ isotopic ratio is useful for understanding what is happening in the stellar interior, so we determined a low value of $^{12}C/^{13}C = 18$ for HD 150382. Hereupon, there are few studies in the literature that have determined the $^{12}C/^{13}C$ isotopic ratio for lithium-rich giants and this seems to be a blind spot in the surveys that uncover a large number of stars. Figure 5.6 displays two interesting distributions that can help map a common profile of early-AGB lithium-rich stars – the v sin i as a function of the carbon isotopic ratio (left panel) and v sin i as a function of the lithium abundance (right panel). In these panels, the red dashed line represents the limit v sin i, where rotational velocities higher than $8.0\,km\,s^{-1}$ are considered as fast rotators and otherwise those below are considered as slow rotators – using the definition by DRAKE ET AL. (2002). The red circles (Figure 5.6) represent values for HD 150382, and the gray symbols and the blue circles represent the RGB and early-AGB lithium-rich giants, respectively, with data taken from the literature. It is worth mentioning that there is a lack of $^{12}C/^{13}C$ isotopic ratio determination among fast rotators, which would be a good indication of atypical events in standard evolutionary theory. But, within the particular class of slow rotator Li-rich giants, HD 150382 has typical values of the $^{12}C/^{13}C$ isotopic ratio and $\log \epsilon(Li)$. The high $^{12}C/^{13}C$ isotopic

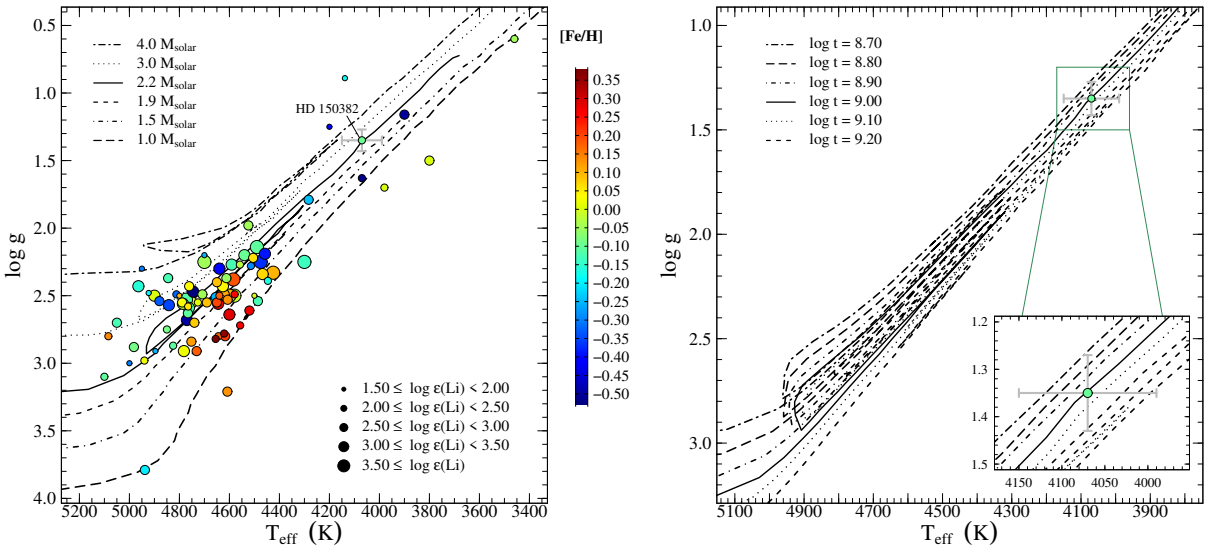

Figura 5.4: Position of HD 150382, other Li-rich stars and evolutionary tracks for a metallicity of Z = 0.019 for masses between 1.0 and 4.0 $M_{\odot}$ in the log g - T_{eff} diagram (left), and the position of HD 150382 with isochrone fits for ages between log $t = 8.7$ and 9.2 in the log g - T_{eff} diagram (right). Evolutionary tracks and isochrones were taken from GIRARDI ET AL. (2000). In the left diagram, the size of the circles indicates the Li abundance of a star as shown in the legend at the bottom. Typical error bars are ± 100 K in T_{eff} and ± 0.10 dex in log g.

ratio (when compared to other early-AGBs) may be due to recent initiation of the early-AGB phase or due to the still incomplete performance of a mechanism responsible for its chemical peculiarities.

As far as sodium is concerned, it can be classified as a tracer of a convective mixing event. We obtained a high [Na/Fe] ratio, +0.28 (Table 5.2), which after correcting for NLTE effects we obtained $+0.12 \pm 0.06$. Furthermore, it is possible that in intermediate-mass giants sodium enrichment occurs when the evolved stars experience a deep mixing and their product is brought to the surface (LAGARDE ET AL., 2012). In this case, it is quite possible that HD 150382 has experienced an extra-mixing episode during the RGB phase which produced sodium, lithium, and ^{13}C, diluting ^{12}C. Another object that may belong to the early-AGB phase is HD 787 ($\log \epsilon(\mathrm{Li}) = 2.20$; DA SILVA ET AL., 1995, which has a significant amount of sodium in its atmosphere ([Na/Fe] = +0.50; TAKEDA & TAJITSU, 2017). The carbon isotopic ratio for HD 150382 is close to the value presented by HD 787, $^{12}C/^{13}C = 15$ DA SILVA ET AL., 1995. Curiously, da Silva and colleagues also found low ^{12}C abundance and moderate ^{14}N enrichment ([C/Fe] = -0.20 and [N/Fe] = +0.10), corroborating in this way with the scenario of extra mixing for low-mass evolved group giants. Another low-mass Li-rich giant that may be in the early-AGB stage has even lower carbon isotope ratios, HD 39853 with $^{12}C/^{13}C = 7.0$ (GRATTON & D'ANTONA, 1989).

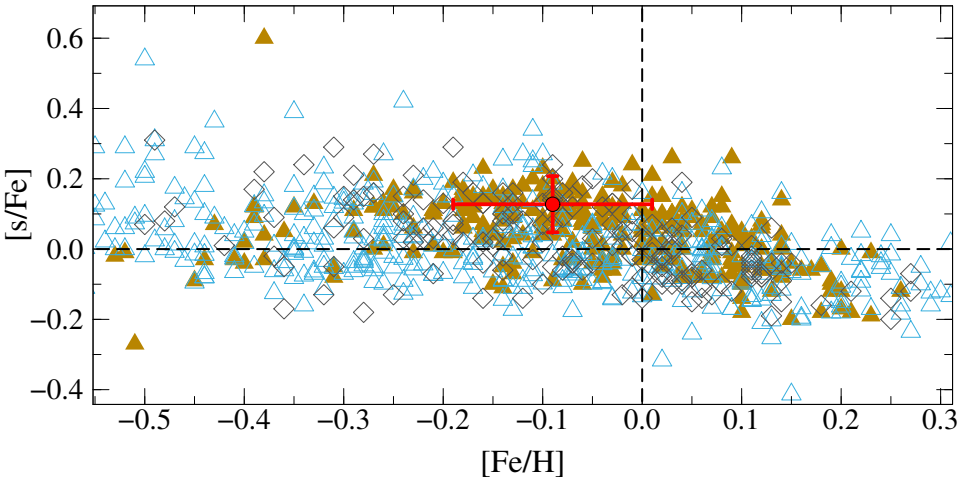

Figura 5.5: Abundance ratio [s/Fe] vs. [Fe/H] for HD 150382 comparative to literature values. The yellow filled triangles and open diamonds represent the giants analyzed by LUCK & HEITER (2007) and MISHENINA ET AL. (2006), respectively, while the blue open triangles represent the dwarfs studied by BATTISTINI & BENSBY (2016). Dashed lines indicate the solar value.

5.3.3 Cool Bottom Processing?

In a scenario where Li enrichment is caused by the accretion of a brown dwarf or planet, according to SIESS & LIVIO (1999a,b), the mass accretion may be traced by a change in the photospheric chemical composition, rotation, X-ray emission, and ejection of a shell. In the first point, the models by Siess and Livio indicate a simultaneous enrichment of $^{6+7}$Li and beryllium and small amounts of boron. Theses signatures depend on parameters such as star mass, accreted mass, planet/brown dwarf composition, mass accretion rate, and evolutive stage of the star. Nevertheless, there is a limitation in these models to endorse enrichment $\log \epsilon(\mathrm{Li}) \leqslant 2.80$ – early-AGB Li-rich stars do not present higher ^{7}Li abundances than this, as seen in Figure 5.6 (right). The beryllium abundance is commonly verified by analyzing the spectral region around 3100 Å but, unfortunately, the FEROS spectrum does not cover this wavelength range. Recently, based on a large number of normal and Li-rich giants of different subgroups, TAKEDA & TAJITSU (2017) did not detect any beryllium enrichment in sample stars they analyzed. Furthermore, DRAKE ET AL. (2017) investigated the presence of boron in atmospheres of four Li-rich giants (including HD 787), and verified that those stars did not present a significant amount of this element.

In some fast rotator stars, they present traces of chromospheric activity and mass loss (DRAKE ET AL., 2002). From this perspective, we examined the profile of the Hα and Na D lines in the spectrum of HD 150382 and did not find any sign that would be indicative of losing mass and chromospheric activity. In addition to what has been said, as can be seen in Figure 5.6, early-AGB stars do not show rotation greater than 8.0 km s^{-1}, but we do not rule out the possibility of high rotation having any influence on Li enrichment at

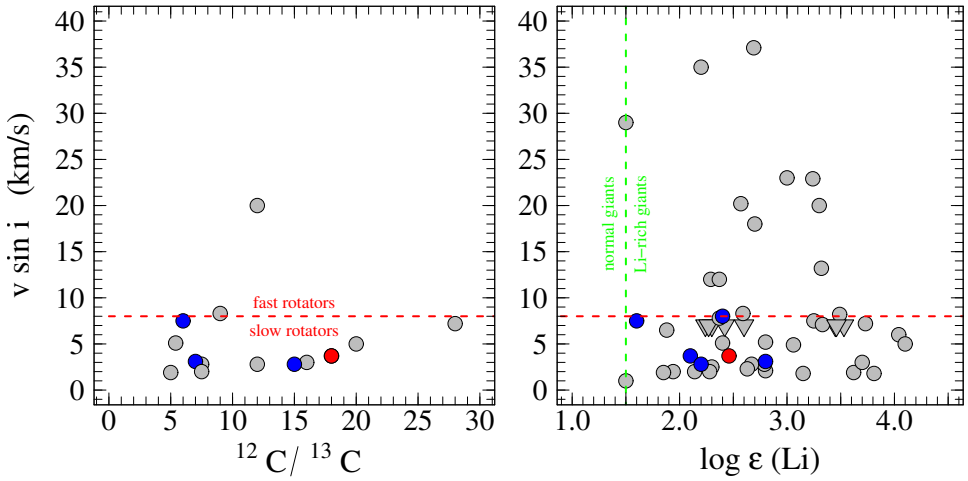

Figura 5.6: v sin i as a function of the isotopic ratio $^{12}C/^{13}C$ (left) and lithium abundance log ϵ(Li) (right) for lithium-rich giants. The horizontal red line is fixed in v sin $i = 8.0\,\mathrm{km\,s^{-1}}$, adopted as the limit for slow ($<8.0\,\mathrm{km\,s^{-1}}$) and fast ($>8.0\,\mathrm{km\,s^{-1}}$) rotators. HD 150382 is represented by red circles (after correction from NLTE effects for lithium). For those objects whose abundances were taken from the literature triangles represent the upper limits.

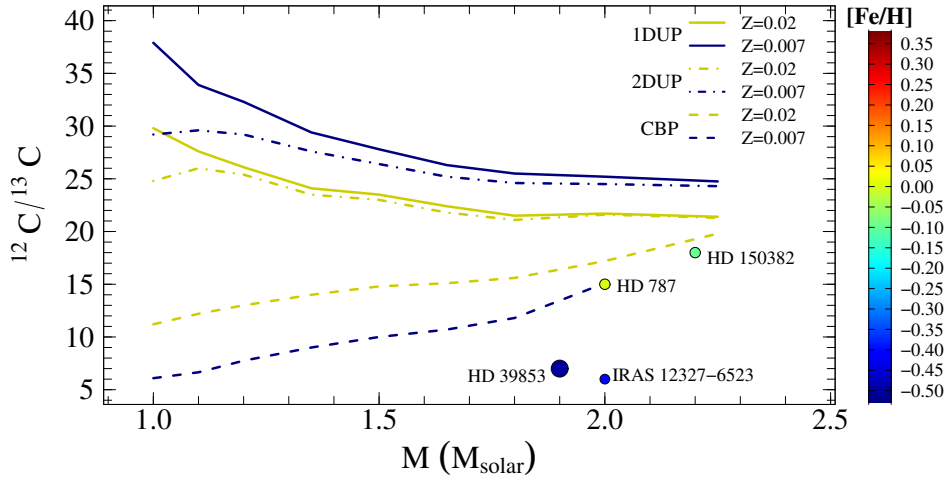

Figura 5.7: $^{12}C/^{13}C$ ratio vs. stellar mass for early-AGB Li-rich stars. The theoretical curves are taken from BOOTHROYD & SACKMANN (1999). Solid lines represent first dredge-up, dottedâdashed lines represent second dredge-up, and long-dashed lines represent cool bottom processing models. Colors refer to metallicities Z = 0.02 (yellow) and Z = 0.007 (dark blue).

some point in the past (not so recent). A planet or a stellar (sub)companion accretion can affect rotation, due to the transfer of angular momentum (CARLBERG ET AL., 2010, 2012), and even trigger other mechanisms that may be associated with Li enrichment.

Observations show that the carbon isotopic ratio continues to decrease after the first dredge-up event for some stars on the RGB stage. This suggests that a deep extra mixing occurs inside these objects and is responsible for very high ^{13}C abundance in their atmospheres. CBP appears to be the source of this extra-mixing mechanism that acts when the H-burnings shell erases the molecular weight discontinuity established by the first dredge-up and is attributed to the destruction of ^{3}He and the creation of ^{7}Li in low-mass RGB stars. The efficiency of this mechanism is governed by parameters such as mixing speed, geometry, and episodicity. The amount of lithium can reach a value of log ϵ(Li) 4.0 in the atmosphere of these RGB stars (regardless of previous lithium history of the giant; SACKMANN & BOOTHROYD (1999) and BOOTHROYD & SACKMANN (1999). Although speculative, it is possible that the substellar companion accretion scenario may trigger instabilities responsible for CBP SIESS & LIVIO (1999b). However, if deep circulation acts for a long time, a continuous process, stars that have enriched themselves through this mechanism can completely destroy beryllium and boron. This can erase the chemical predictions of Siess and Livio.

Since low-mass AGB stars have a similar internal structure to the RGB tip stars, CBP can also occur at the early-AGB phase SACKMANN & BOOTHROYD (1999). As observed in Figure 5.6 (left) Li-rich giants present ^{12}C/^{13}C $\leqslant 20$, i.e., more ^{13}C is expected than in the first and second dredge-up events, but if the Li enrichment occurs by the early-AGB this happens less clearly in relation to the RGB that goes through the same process.

Figure 5.7 displays the ^{12}C/^{13}C isotopic ratio verses stellar mass for a few early-AGB Li-rich stars, including HD 150382. The theoretical curves were taken from BOOTHROYD & SACKMANN (1999) and solid, dotted-dashed, and long-dashed lines represent, respectively, first and second dredge-up and CBP models. Colors refer to different metallicities, Z = 0.02 (yellow) and Z = 0.007 (dark blue). Despite the few data (we found in the literature only four with the ^{12}C/^{13}C isotopic ratio determined), the agreement between abundances of these objects with predictions by CBP is clear. The performance of CBP can be more easily seen in stars of lower mass and low metallicity, also envisaged by BOOTHROYD & SACKMANN (1999). Finally, we emphasize the importance of determining mixer traces for lithium-enriched objects in the early-AGB stage.

5.4 Conclusions

We estimated the age of 1.0×10^{9} yr and a mass of 2.20 $M_{\odot}$ for HD 150382. In addition, this star is a low rotator having a metallicity close to solar, and has a low carbon isotopic

ratio besides a lithium overabundance. Due to its luminosity and chemical composition, this giant is probably an early-AGB giant.

We determined that HD 150382 presents few process-s nuclei at the surface, which is in good concordance with dwarfs and clump RGB giants samples (BATTISTINI & BENSBY, 2016; LUCK & HEITER , 2007; MISHENINA ET AL., 2006). We also found high values for the [N/Fe] and [Na/Fe] ratios, but a low value for the [C/Fe] ratio. This abundance pattern is consistent with that expected for a material that has been subjected to mixing events. The other elements analyzed do not present any abnormality.

The existence of low-mass stars ($<4.0\,M_{\odot}$) at the early-AGB phase requires that an extra-mixing mechanism can simultaneously explain the chemical mixing tracers (e.g., $^{12}C/^{13}C$, C, N, Li, and Na). In this context, we suggest that the CBP is responsible for the peculiar abundance peculiarities observed in HD 150382 and this may be supported by the $^{12}C/^{13}C$ value if compared with the models predicted by BOOTHROYD & SACKMANN (1999).

Capítulo 6

TYC 8327-1678-1: uma nova gigante K super-rica em lítio

Neste capítulo serão apresentados resultados para a gigante vermelha de baixa massa TYC 8327-1678-1, que apresenta super abundância de lítio em sua atmosfera. Para tal, foi usada espectroscopia de alta resolução para determinar os parâmetros atmosféricos, as abundâncias químicas para os elementos leve e razão isotópica para o carbono $^{12}C/^{13}C$ usando técnicas de síntese espectral e medidas de largura equivalente. Também, foram usadas trajetórias evolutivas para levantar a massa e o estágio evolutivo da TYC 8327-1678-1. A abundância de lítio foi determinada usando o dubleto de ressonância Li I em 6708 Å e a linha subordinada em 6104 Å que proporcionaram um valor médio de $log\,\epsilon(\mathrm{Li})_{NLTE} = 3.48$. A velocidade rotacional projetada (v sin i) foi determinada usando a técnica de síntese espectral baseada em linhas de Fe I suficientemente isoladas. Os resultados obtidos para a gigante TYC 8327-1678-1 mostram que ela tem $\mathrm{M} = 1.60 \pm 0.20\,\mathrm{M}_{\odot}$, uma baixa velocidade rotacional projetada (v sin $i = 2.35 \pm 0.24\,\mathrm{km\,s^{-1}}$) e uma metalicidade de $[\mathrm{Fe/H}] = +0.23 \pm 0.09$. Por fim, é realizada uma discussão sobre a possibilidade de TYC 8327-1678-1 ter se tornado rica em lítio após um merge envolvendo uma estrela gigante vermelha e uma anã branca de hélio.

O conteúdo deste capítulo foi retirado da publicação: **Holanda, N., Drake, N. A., & Pereira, C.B., 2020, Monthly Notices of the Royal Society, 498, 77 (Artigo 3)**.

6.1 Introduction

Lithium-rich red giants challenge the stellar astrophysics. These peculiar stars present overabundance of the Li – a sensitive element that should has been diluted during the first ascent of the star to the red-giant-branch (RGB) phase. The convective region deepens at this phase of stellar evolution and brings the material to the star's surface from its

the interior. Despite to the drastical dilution of the Li amount in the first dredge-up process, 1 per cent to 2 per cent of the GK giants present a high Li abundance and yet this is a puzzle for the standard stellar evolution and mixing models (BROWN ET AL., 1989; BHARAT KUMAR ET AL., 2011; GAO ET AL., 2019; SMILJANIC ET AL., 2018). Notwithstanding, the report of "super" lithium-rich giants in the literature (stars with abundance greater than meteoric lithium abundance) is significantly scarce, with a few examples known (e.g. ADAMÓW ET AL., 2015; BHARAT KUMAR ET AL., 2011; DRAKE ET AL., 2002; MONACO ET AL., 2014; STRASSMEIER ET AL., 2015; SINGH ET AL., 2019; ZHOU ET AL., 2018. These rare objects are generally located near the bump in the luminosity function and/or in the clump of RGB on the H-R diagram.

Among the several scenarios proposed in the literature to explain the anomalous high lithium abundance in these cool giants, some deserves to be emphasize: the enrichment by a planet or a sub-companion accretion (ALEXANDER, 1967; AGUILERA-GÓMEZ ET AL., 2016; SIESS & LIVIO, 1999b); merger between a red giant star and a companion helium white dwarf (ZHANG ET AL., 2020); accretion of enriched material ejected by nova-explosions (GRATTON & D'ANTONA, 1989) or from a thermally pulsing AGB (TP-AGB) companion (KIRBY ET AL., 2016) and internal enrichment by fresh lithium through an extra-mixing in low-mass giants (BOOTHROYD ET AL., 1995; FEKEL & BALACHANDRAN, 1993; HOLANDA ET AL., 2020a; SACKMANN & BOOTHROYD, 1999). The stage at which this in situ enrichment happens is still a matter of debate in the literature – BHARAT KUMAR ET AL. (2011) argue that the RGB clump is more populated by Li-rich stars and that this enrichment may be triggered by helium flash at RGB tip. The trigger mechanism responsible for an auto-enrichment has been discussed and eventually is considered to be related with an accretion of planets or brown dwarfs and, more recently, with tidal interactions between binary stars (CASEY ET AL., 2019; SIESS & LIVIO, 1999a). However, JORISSEN ET AL. (2020) reported that the binary frequency among Li-rich K giants is normal when compared to that found in a sample of giants of same spectral type, which seems to refute the hypothesis that all enrichment processes derives from tidal interactions.

Sometime ago, DE LA REZA ET AL. (1996) proposed that K giants undergo a sudden mass-loss process and a lithium enrichment of short duration – a cycle of approximately 10^5 yr. Sometime later, DRAKE ET AL. (2002) considered a possible high incidence of Li enrichment in rapid rotators with a mass-loss and a consequent infrared excess by accretion of some material that would act by increasing the angular momentum of the giant star: these are characteristics that do not confer on all Li-rich giants, but REBULL ET AL. (2015) perceived that among stars with infrared excess it is easier to find Li-rich giants.

Here, we take into account the most plausible hypotheses, olds and recents, in an attempt to elucidate the super lithium abundance found in giant TYC 8327-1678-1. For

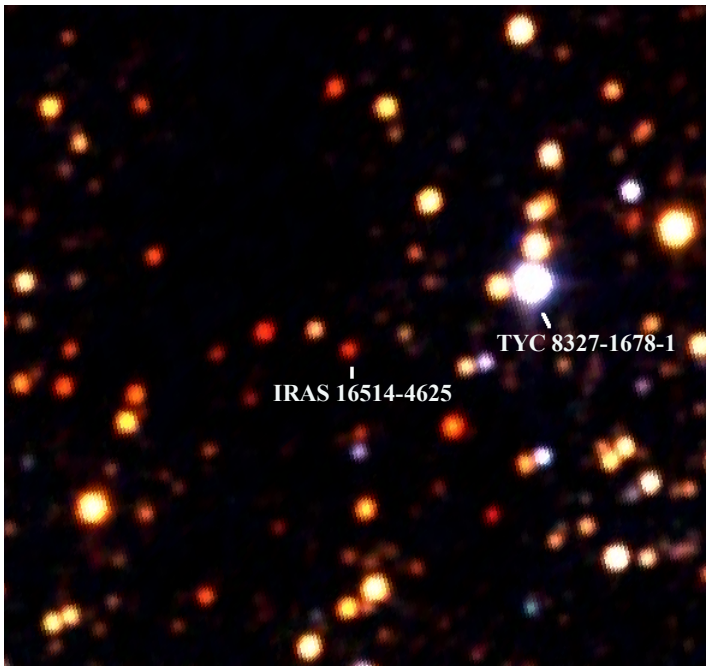

Figura 6.1: 2MASS image from CDS portal for IRAS 16514-4625 and TYC 8327-1678-1 (PDS 432) field. As denoted by REBULL ET AL. (2015), infrared source IRAS 16514-4625 has no optical equivalent.

this purpose, we have organized this article as follows: in Section 6.2, we describe our observation and give details of our analysis applied to the star TYC 8327-1678-1. In Section 6.3, we discuss the properties of this super lithium-rich giant in the context of the existing body of literature. Finally, concluding remarks are provided in Section 6.4.

6.2 The Giant TYC 8327-1678-1

TYC 8327-1678-1 was identified as lithium-rich star by DE LA REZA ET AL. (1997), who also considered this star with a possible infrared excess in the colour-colour diagram based on data from Infrared Astronomy Satellite (IRAS; NEUGEBAUER ET AL., 1984). In a more recent study about the infrared excess associated with Li-rich K giants, REBULL ET AL. (2015) find this confusion in the equatorial coordinates of IRAS 16514-4625 and TYC 8327-1678-1. In other words, TYC 8327-1678-1 is not responsible for the infrared flux detected by IRAS. Fig. 6.1 displays the field around the two objects. TYC 8327-1678-1 is located near the Galactic Plane (l = 339.9, b = -01.9) was previously classified as K3 III (PICKLES & DEPAGNE, 2010), and has an estimated distance in d = 844.406 pc (BAILER-JONES ET AL., 2018). The main parameters estimated obtained by us in this work and those taken from the literature are given in Table 6.1.

Tabela 6.1: Derived Stellar Parameters of TYC 8327 - 1678 - 1.

Parameter	Value	Reference
V	11.443	HENDEN ET AL. (2015)
B−V	1.427	HENDEN ET AL. (2015)
RA (J2000)	16 55 06.193	—
DEC (J2000)	−46 29 55.377	—
Spectral type	K3III	PICKLES & DEPAGNE (2010)
T_{eff} (K)	4460 ± 70	This work
log g (dex)	2.55 ± 0.10	This work
ξ (km s^{-1})	1.69 ± 0.09	This work
[Fe I/H] (dex)	$+0.23 \pm 0.09$	This work
[Fe II/H] (dex)	$+0.23 \pm 0.09$	This work
v sin i (km s^{-1})	2.35 ± 0.24	This work
M ($M_{\odot}$)	1.60 ± 0.20	This work
V_r (km s^{-1})	-0.88 ± 0.45	This work
V_r (km s^{-1})	-0.13 ± 0.31	GAIA COLLABORATION ET AL. (2018)
π (mas)	1.157 ± 0.044	GAIA COLLABORATION ET AL. (2018)

6.2.1 Observations

The high-resolution spectrum of TYC 8327-1678-1 was obtained on 2016 March 23, with the Fiberfed Extended Range Optical Spectrograph (FEROS; KAUFER ET AL., 1999 at the 2.2 m telescope at the European Southern Observatory in La Silla, Chile. Its spectrum covers a wavelength interval between 3800 and 9000 Å and provide a resolution of R ≈ 48000. After a data reduction process, using the FEROS pipeline, we estimated a typical signal-to-noise ratio of our spectrum of S/N ≈ 120-150.

In addition, we used photometric and astrometric information given by HENDEN ET AL. (2015) and GAIA COLLABORATION ET AL. (2018) in order to better constrain the nature of TYC 8327-1678-1.

6.2.2 Atmospheric Parameters

To obtain the model atmosphere for TYC 8327-1678-1 that best represents the physical conditions of its atmosphere, we first measure the equivalent widths of 19 Fe I and 6 Fe II lines using the IRAF and the routine splot. The original list was taken from HEKKER & MELÉNDEZ (2007), with features between 5700 and 7800 Å, and especially appropriate for the analysis of cool giants, avoiding lines blended with the CN lines (Table 6.2). These iron lines were used to constrain the best stellar atmosphere with the help of the code MOOG (2013 version; SNEDEN, 1973) and Kurucz (KURUCZ, 1993) model atmospheres, considering local thermodynamic equilibrium (LTE).

Basically, the method consists as follows: effective temperature was derived by minimizing a slope between the abundance and the lower level excitation potential (χ) of Fe I lines. Simultaneously to that, the microturbulent velocity (ξ) was found by minimizing a

slope between Fe I abundance and reduced equivalent width (EW/λ) values. Finally, the surface gravity was obtained by imposing that the mean Fe I abundance be equal to that of the mean Fe II - ionization equilibrium. This procedure is performed by changing the value of log g until equality is reached.

The uncertainties in the atmospheric parameters were estimated following the same methodology by HOLANDA ET AL. (2019), i.e. the error in effective temperature was estimated from the uncertainty in the slope of relation Fe I versus excitation potential, while the error in the microturbulent velocity was obtained from the uncertainty in the slope of [Fe I/H] versus log EW/λ. For gravity, the error is estimated by changing the log g value until the difference in the average abundances of Fe I and Fe II equals the standard deviation of the mean [Fe I/H].

We better constrained the effective temperature using two other methods: (i) the line-depth ratio (LDR) (BIAZZO ET AL., 2007) and (ii) the photometric calibration (GONZÁLEZ HERNÁNDEZ & BONIFACIO, 2009). In these two cases, we found good agreement, for instance, $T_{\rm eff}$ (LDR) = 4426 K and $T_{\rm eff}^{(}B - V)$ = 4586 K. Previous works such as BAI ET AL. (2019), MCDONALD ET AL. (2017), and AMMONS ET AL. (2006) obtained 4205, 4492, and 4466 K, respectively, that are in good agreement to one find by us based on spectroscopic analysis (also given in Table 6.1). In this context, we also compare the derived spectroscopic gravity with the evolutionary gravity log $g_\star$ that may be determined using the equation

$$\log g_\star = \log\left(\frac{M}{M_\odot}\right) + 0.4\,(V - A_V + BC_V) + 4\log T_{\rm eff}^{(\rm B-V)} - 2\log r\,(\rm kpc) - 16.5.$$

In the equation above, V, A_V, BC_V , T_{eff} , and r are, respectively, the visual magnitude, interstellar absorption in the V band (CHEN ET AL., 1999), the bolometric correction (ALONSO ET AL., 1999), the photometric temperature in (B-V) colour GONZÁLEZ HERNÁNDEZ & BONIFACIO (2009), and the distance (BAILER-JONES ET AL., 2018; GAIA COLLABORATION ET AL., 2018). To obtain the equation above, we adopted solar values for the absolute bolometric magnitude, surface gravity, and effective temperature, respectively, of M_{bol} = 4.75, log g = 4.44 dex, and T_{eff} = 5777 K. Finally, we find a log $g_\star$ = 2.53, which is in good concordance with the value based on the spectroscopic analysis.

Despite the small difference between the values for the surface gravity, MCDONALD ET AL. (2017) found a value that is similar to that of obtained here based on spectroscopic analysis (log g $\approx$ 2.52). Based on log L/$L_\odot$ = 1.72 from GAIA data, our derived effective temperature and the evolutionary tracks by GIRARDI ET AL. (2000), we obtained a mass of 1.60 $M_\odot$ for a metallicity of Z = 0.030 (Table 6.1).

Fig. 6.2 shows the position of TYC 8327-1678-1 in the $T_{\rm eff}$ - log L diagram that will help

Tabela 6.2: Neutral and ionized iron lines.

λ	specie	χ	log gf	EW
5775.08	Fe I	4.22	−1.300	105
5848.13	Fe I	4.61	−0.900	103
5902.47	Fe I	4.59	−1.750	45
5916.25	Fe I	2.45	−2.990	136
6027.05	Fe I	4.08	−1.300	113
6093.64	Fe I	4.61	−1.410	62
6096.66	Fe I	3.98	−1.810	84
6098.24	Fe I	4.56	−1.800	62
6120.25	Fe I	0.92	−5.950	91
6151.62	Fe I	2.18	−3.300	131
6187.99	Fe I	3.94	−1.650	103
6240.65	Fe I	2.22	−3.390	130
6574.23	Fe I	0.99	−5.000	144
6703.57	Fe I	2.76	−3.150	112
6725.36	Fe I	4.10	−2.300	62
6726.67	Fe I	4.61	−1.170	89
7421.56	Fe I	4.64	−1.800	53
7547.90	Fe I	5.10	−1.100	57
7723.21	Fe I	2.28	−3.620	125
5264.81	Fe II	3.23	−3.130	48
5425.26	Fe II	3.20	−3.220	54
6247.56	Fe II	3.89	−2.300	49
6369.46	Fe II	2.89	−4.110	30
6432.68	Fe II	2.89	−3.570	50
6456.38	Fe II	3.90	−2.050	60

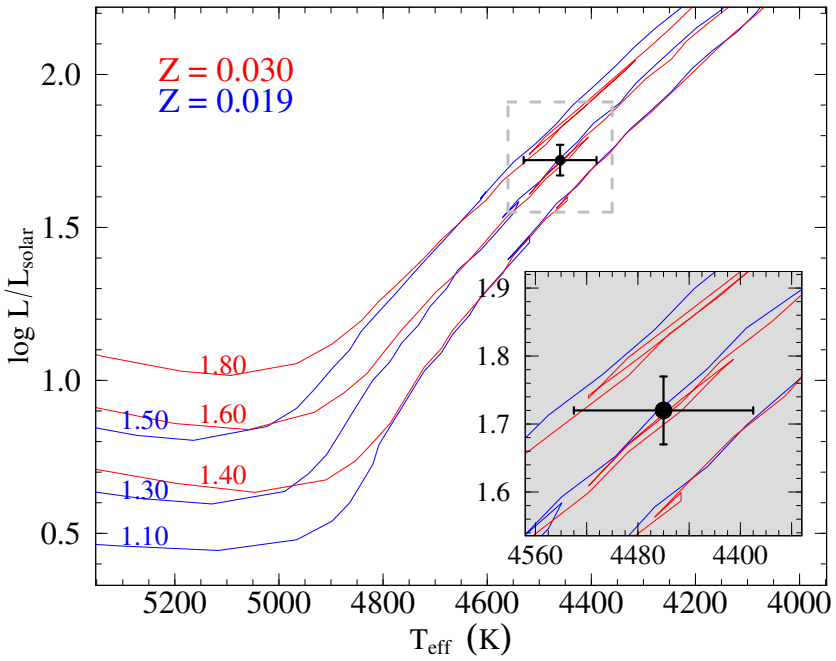

Figura 6.2: The location of TYC 8327-1678-1 in the T_{eff} - log g diagram. The evolutionary tracks for Z = 0.019 (blue), while tracks for 1.8, 1.6, and 1.4 $M_{\odot}$ are displayed for Z = 0.030 (red).

us to discuss the evolutionary status of this lithium-rich star. In this graph were used tracks for Z = 0.019 (solar) and Z = 0.030, that are represented in blue and red colours, respectively.

6.2.3 Stellar Abundances

Based on the atmospheric parameters previously determined, we obtained abundances using spectral synthesis technique for carbon, nitrogen, oxygen and lithium and also the carbon isotopic ratio $^{12}C/^{13}C$, while for sodium we used equivalent width to obtain its abundance.

The lithium abundance was determined using the resonance doublet at λ 6708 and the line at λ 6104, which we assume in both cases under LTE conditions. The wavelengths and oscillator strengths for the individual components for the lithium lines were taken from SMITH ET AL. (1998) and HOBBS ET AL. (1999), and the Vienna Atomic Line Database (VALD; KUPKA ET AL., 1999) for both lines. The resolution of the FEROS spectrum is not sufficient to rule out a contribution from ^{6}Li at λ 6708; therefore, we do not include the isotopic ratio $^{6}Li/^{7}Li$ in the synthesis of this feature. The fits of these two regions is shown in Fig. 6.3, where grey crosses represent the observed spectrum and red solid lines represent the best fit for both cases.

The carbon abundance was obtained using the C_2 (0, 1) band of Swan system $A^3\Pi_g$ – $X^3\Pi_u$ at 5636 Å (KOVŽACS , 1969; LAMBERT, 1978; PHILLIPS & DAVIS, 1968). The

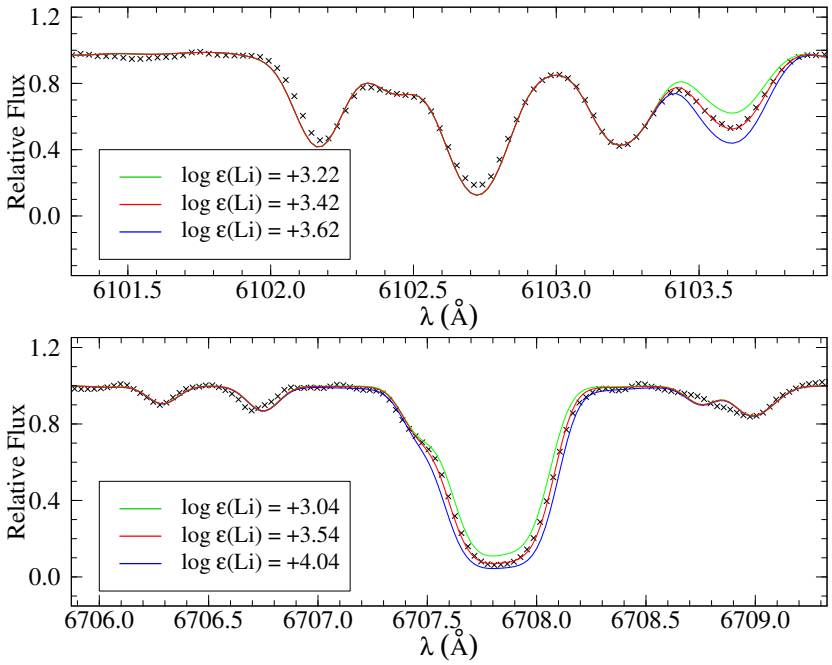

Figura 6.3: Best fits obtained between the synthetic and the observed FEROS spectra of TYC 8327-1678-1 around 6708 Åand 6104 Å lithium lines.

nitrogen abundance and the carbon isotopic ratio $^{12}C/^{13}C$ were obtained by comparing the synthetic profiles of ^{12}CN and ^{13}CN lines of the 2–0 band of the CN red system $A^2\Pi - X^2\Sigma$, that are near to 8004 Å. The ^{13}CN feature is strong when the isotopic ratio $^{12}C/^{13}C$ is low, that is when the star is enriched in ^{13}C. The lines $^{12}C/^{13}C$ lines in the Swan band around 5200 Åwere not used for TYC 8327-1678-1 because of they are weak since most of the carbon in this star is concentrated in form of ^{12}C. In addition, the oxygen abundance was derived from the analysis of the [O I] λ 6300.3 Å line (ALLENDE PRIETO ET AL., 2001). VALD was again useful in building input files for this analysis. Fig. 6.4 shows these three regions and with their best fits obtained using the code MOOG .

As mentioned before, the sodium abundance was obtained by measuring the equivalent widths of the doublet lines at 6154 Å and 6161 Å where log gf were taken from REDDY ET AL. (2003). The abundances obtained by these two lines do not significantly differ from each other ($\log \epsilon(\mathrm{Na})_{\lambda 6154} = 6.52$ and $\log \epsilon(\mathrm{Na})_{\lambda 6161} = 6.50$) and we adopt the average as the final abundance in LTE conditions.

It is well known that lithium and sodium lines in giants suffer significant non-LTE effects. In this sense, we have calculated non-local thermodynamic equilibrium (NLTE) abundances for Li and Na abundances with a grid of corrections taken from LIND ET AL. (2009) and LIND ET AL. (2011), respectively. We find values of $\Delta \mathrm{Li}^{6104}_{\mathrm{NLTE}} = +0.17$ and $\Delta \mathrm{Li}^{6708}_{\mathrm{NLTE}} = -0.17$ with an average value of $\Delta \mathrm{Na}_{\mathrm{NLTE}} = -0.08$. Table 6.3 shows all abundances for LTE and NLTE conditions that have been computed for TYC 8327-1678-1 in this work. The abundances were normalized to solar values given in ASPLUND ET AL. (2009) ($\log \epsilon(\mathrm{X})_{\odot}$).

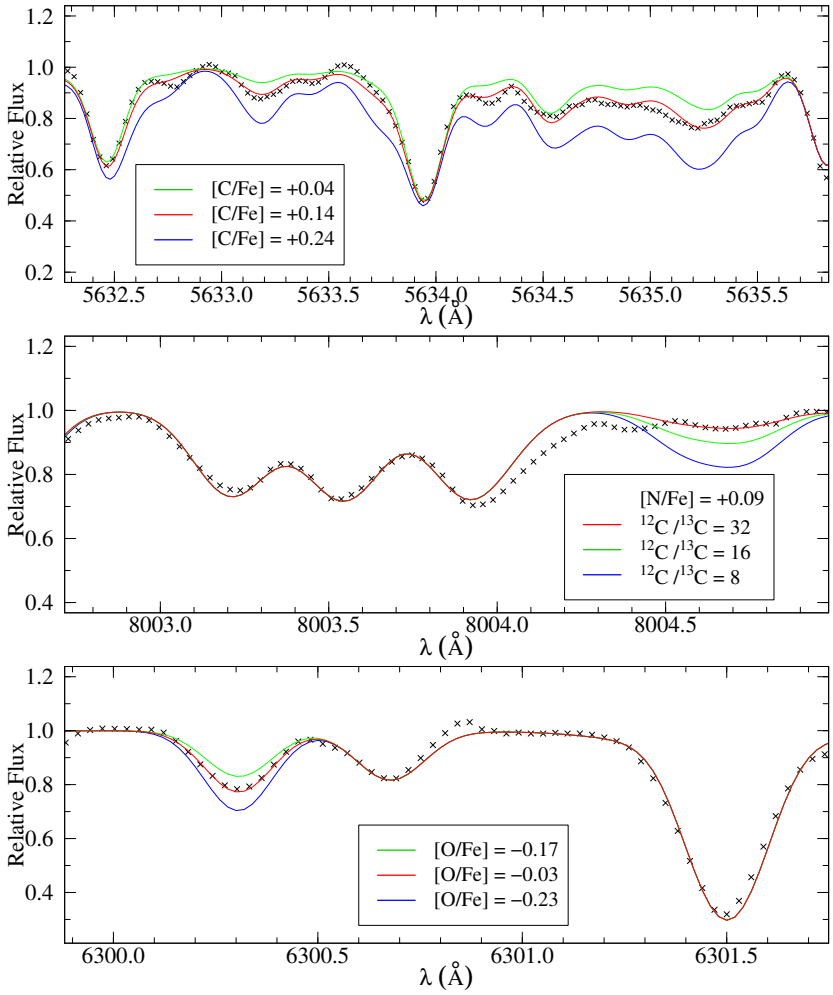

Figura 6.4: Best fits obtained between the synthetic (red solid lines) and the observed FEROS spectra (grey crosses) of TYC 8327-1678-1 around 5635, 8002, and 6300 Å.

Tabela 6.3: Derived chemical abundances of TYC 8327 - 1678 - 1. The third column refers to the number of lines used and the fourth column to solar values adopted by ASPLUND ET AL. (2009).

Specie	log ϵ(X)$_{\rm LTE}$	log ϵ(X)$_{\rm NLTE}$	[X/Fe]	log ϵ(X)$_{\odot}$
Li I $_{\lambda6104}$	3.42	3.59	—	1.05
Li I $_{\lambda6708}$	3.54	3.37	—	—
C (C_2)	8.80	—	+0.14	8.43
N (CN)	8.15	—	+0.09	7.83
O I	8.89	—	−0.03	8.69
$^{12}C/^{13}C$	$\geqslant$32	—	—	—
Na I	6.51	6.43	−0.04	6.24

Tabela 6.4: Influence of the errors in atmospheric parameters over the abundances of elements analysed.

Specie	$\Delta T_{\rm eff}$ (+ 70)	Δ log g (+ 0.10)	ξ (+0.09)	$(\Sigma\,\sigma^2)^{1/2}$
Li I $_{\lambda6104}$	+0.04	+0.01	−0.01	±0.04
Li I $_{\lambda6708}$	+0.02	−0.03	−0.06	±0.07
C (C_2)	+0.01	+0.02	+0.02	±0.03
N (CN)	−0.02	+0.00	−0.03	±0.04
O I	+0.02	+0.05	+0.01	±0.05
Na I	+0.06	+0.00	−0.03	±0.07

Table 6.4 shows the influence of the uncertainties of the atmospheric parameters over the chemical abundances for TYC 8327-1678-1. Also, the last column provide the total abundance uncertainty calculated as the root square of the sum of the various sources of uncertainties [$(\Sigma\,\sigma^2)^{1/2}$].

6.3 Results and Discussion

6.3.1 Abundance Pattern

A large amount of lithium was found in the TYC 8327-1678-1's atmosphere - this quantity exceeds the meteoric abundance for this element (3.26; ASPLUND ET AL., 2009). When trying to understand how this large amount of lithium was produced and/or transferred to our target has been analysed some chemical tracers of stellar evolution and was compared our results with the other star products reported in the literature. To guide a discussion about that, we also search for ordinary low-mass giant stars (lithium-poor) and similar giant stars to our target, i.e. super lithium-rich giants, as display Fig. 6.5 (ADAMÓW ET AL., 2015; BHARAT KUMAR ET AL., 2015, 2018; BROWN ET AL., 1989; BHARAT KUMAR ET AL., 2011; CARLBERG ET AL., 2010; DRAKE ET AL., 2002; MONACO ET AL., 2014; REDDY & LAMBERT, 2005; STRASSMEIER ET AL., 2015; SINGH ET

AL., 2019; ZHOU ET AL., 2018; YAN ET AL., 2018).

Additionally, we compared these peculiar stars with giants classified as RGB stars (with degenerate cores) or red clump stars (RC; burning helium in the core) based on asteroseismology data HAWKINS ET AL. (2016); TING ET AL. (2018). Looking at Fig. 6.5, it appears that the group of giant stars with less lithium in the atmosphere have a larger amplitude in the possible values of $^{12}C/^{13}C$: despite of scarcity of objects with very high lithium, the low carbon isotopic ratio is a common feature. Furthermore, TYC 8327-1678-1 presents the higher carbon-12 abundance among these super Li-rich and Li-poor giant stars.

It is expected that a significant dilution of carbon is observed at the same time with an increase in the amount of nitrogen in the RGB of the star atmosphere. Hereupon, we identified a moderate carbon abundance [$\log \epsilon(C) = 8.80$] and a not so high nitrogen abundance [$\log \epsilon(N) = 8.15$] in TYC 8327-1678-1 atmosphere, which gives an abundance ratio of [C/N] = +0.05. In Fig. 6.5 (bottom), we plotted [C/N] versus [Fe/H] for normal RC (small red circles) and RGB (small black circles) stars and compare with some super Li-rich giants: there is a slight difference between the means (solid lines), but the large spread of RC stars compromises any categorization based on these abundances and it is opportune to emphasize the high [C/N] of TYC 8327-1678-1 to its iron abundance.

Unlike lithium, the sodium abundance seems to agree with standard predictions for low-mass giants; that is, there is no enrichment for this element. The sodium enrichment is expected for intermediate-mass stars ($\geqslant 2.20\,M_\odot$) according to recent mixing models LAGARDE ET AL. (2012).

6.3.2 Rotational Velocity and Infrarred Excess

Rotation is a data in stellar physics that can be a very important tool in the investigation of magnetic activity, circulation of convective material and the internal structure of a giant star, and is helpful in the diagnostic of a interaction with a binary companion (CARLBERG ET AL., 2011). In this sense, the projected rotational velocity ($v \sin i$) of TYC 8327-1678-1 was estimated using the spectral synthesis of unblended Fe I lines – this sample is compose for lines at 5775.1, 6027.1, 6151.6, and 6302.6 Å. In this procedure, it was adopted the macroturbulent velocity that is a typical value for K giants ($3.0\,km\,s^{-1}$; FEKEL ET AL., 1997) and a full width at half-maximum (FWHM) of 0.13 Å that corresponds to the FWHM of thorium-argon lines used for the wavelength calibration for FEROS spectrograph. We found a value of $v \sin i = 2.35\,km\,s^{-1}$, which is low but is expected for low-mass giants due to evolutionary effects, as shown by DE MEDEIROS ET AL. (1996). It is possible that the first dredge-up adds angular momentum in the convective envelope or that accretion of planets or sub-companion affects the convective envelope, but this effect is not seen in TYC 8327-1678-1.

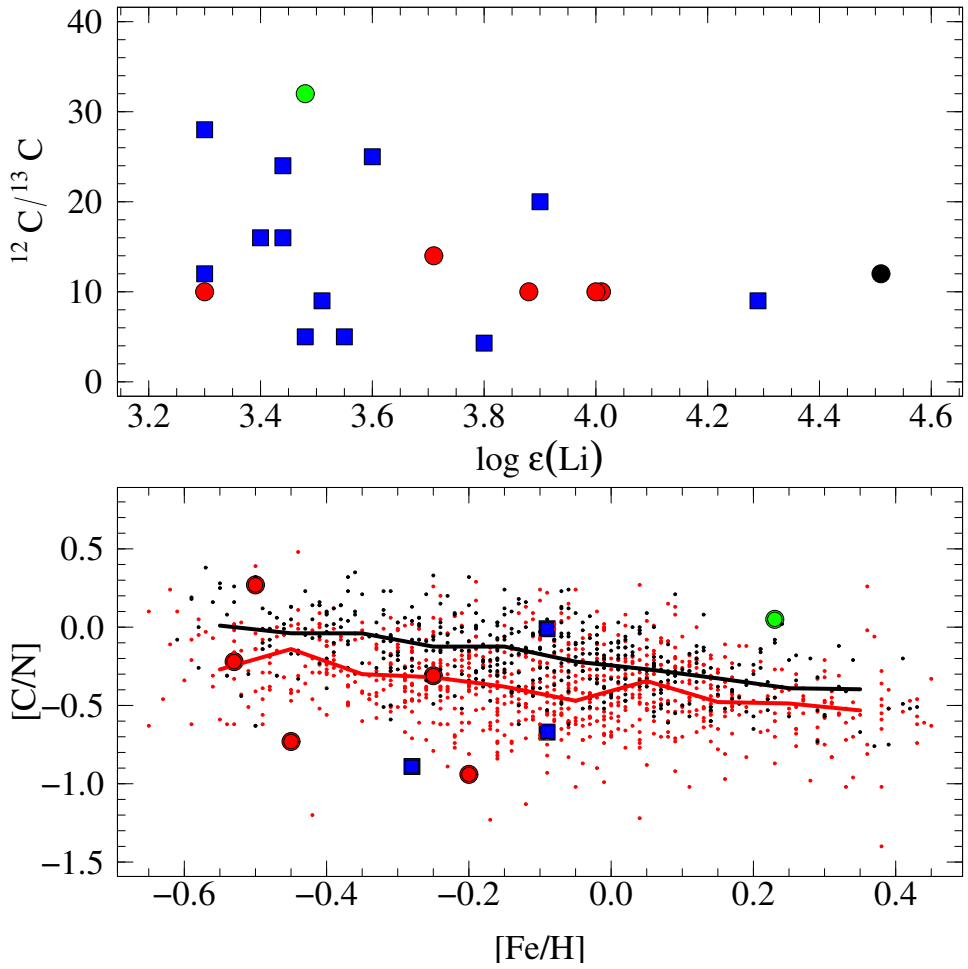

Figura 6.5: Distributions of log ϵ(Li) versus (top) and [C/N] versus [Fe/H] (bottom) for super Li-rich. On plots, we present normal RC (small red circles) and RGB (small black circles) stars, RC (big red circles) and RGB (big black circle) super Li-rich stars, non-classified stars (blue squares), and TYC 8327-1678-1 (green circle). Red and black solid lines constituted of a set of medians of the [C/N] at intervals of 0.10 dex in [Fe/H]. Normal stars has been chemical and asteroseismology data that were taken from HAWKINS ET AL. (2016) and TING ET AL. (2018), respectively. The super Li-rich are following: HD 9746 (Brown et al. 1989); PDS 365 (DRAKE ET AL., 2002); IRAS 13539-4153 and HD 19745 (REDDY & LAMBERT, 2005); G0928+73.2600 (CARLBERG ET AL., 2010); HD 8676, HD 10437, and HD 77361 (BHARAT KUMAR ET AL., 2011); Trumpler 5 - 3416 (MONACO ET AL., 2014); HD 233517 (STRASSMEIER ET AL., 2015); HD 107028 (ADAMÓW ET AL., 2015); HD 19745 (BHARAT KUMAR ET AL., 2015); KIC 12645107 and KIC 2305930 (BHARAT KUMAR ET AL., 2018); TYC 3251-581-1 (ZHOU ET AL., 2018); TYC 429-2097-1 (YAN ET AL., 2018); TYC 1751-1713-1 and HD 24960 (SINGH ET AL., 2019).

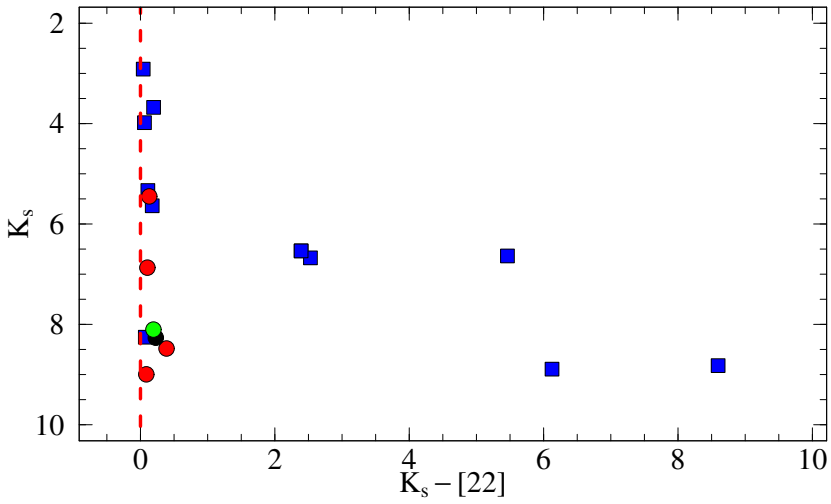

Figura 6.6: K_s versus K_s - [22] for a sample of super lithium-rich giants of literature and TYC 8327-1678-1. The photometric data was obtained from The Two Micron All Sky Survey (2MASS: SKRUTSKIE ET AL., 2006) and Wide-field Infrared Survey Explorer (WISE: WRIGHT ET AL., 2010). Notation is as in Fig. 6.5. The vertical red dashed line at K_s - [22] = 0.0 indicates no infrared excess. Here, we consider giants with infrared excess only objects with significant K_s - [22] > 0.0.

The profile of the Hα line in the spectrum of red giant stars is useful for the diagnosis of mass-loss in red giant since a possible correlation between these episodes and lithium enrichment can be true (DE LA REZA ET AL., 1996, 1997). The Hα line in our giant's spectra is observed in absorption and symmetric, with equivalent width EW $\approx$ 1.03 Åand a line depth of $R_c \approx 0.25$, which are values typical for red giants according to EATON ET AL. (1995). Reinforcing this idea, the Na D lines at λ 5890 do not show any additional minor lines shift in relation to the central lines.

Fig. 6.6 shows a colour-magnitude diagram that is useful to identify giants with some infrared excess. In this plot, we make a point for TYC 8327-1678-1 that do not have a significant infrared excess as was reported to IRAS 16514-4625 by DE LA REZA ET AL. (1997). Furthermore, only five super lithium-rich giants in this sample present larger infrared excesses. Larger infrared excesses are relatively rare in the literature, but according to REBULL ET AL. (2015) are at least twice as common among Li-rich K giants.

6.3.3 Scenarios of Lithium Enrichment

Based on the results presented above in Section 6.3, we attach hypotheses that can elucidate a probable scenario for lithium amount found in the atmosphere of TYC 8327-1678-1. Our atmospheric parameters and luminosity derived from GAIA data showed that TYC 8327-1678-1 lies at an ambiguous region between RGB-bump and red clump, if we consider the uncertainties, as seen in Fig. 6.2. This region is vastly populated by Li-rich giants reported in the literature. Probably, the best answer for this question about its

classifying is in asteroseismology data. However, TYC 8327-1678-1 does not have any data of asteroseismology nature. Knowing this, we resort to chemical signatures: in general RGB stars have higher values of [C/N] when compared to RC stars (HAWKINS ET AL., 2016; SINGH ET AL., 2019; TING ET AL., 2018). Here, we performed a comparison based on asteroseismology data combined with chemical abundance studies (Fig. 6.5) for ordinary giants and a sample of main super Li-rich stars reported in the literature - some these peculiar stars have no estimate of their evolutionary stage. Even with precise measurements of abundances of carbon and nitrogen, TYC 8327-1678-1 is far from have a larger distance relative to the star averages confirmed as RGB and RC by asteroseismology.

The production of ^{7}Li atoms is based on ^{3}He atoms and follows the reaction ^{3}He(α, γ)^{7}Be with the transport of beryllium atoms to cool regions, where conversion to lithium occurs by electron capture, i.e. ^{7}Be($^{-}$e, ν)^{7}Li (CAMERON & FOWLER, 1971). Without the beryllium-transport occurs the destruction of lithium atoms by p-capture, which depends on the mixing efficiency of which lithium may be destroyed before it reaches the surface. Degenerate helium core stars may experience some enrichment in luminosity bump, when the mean molecular weight discontinuity left over by the first dredge-up is erased, so allowing the raise of the extra mixing process. Nevertheless, the value for the isotopic carbon ratio leads us to consider an extra mixture as less probable, since significant amounts of ^{13}C is the best mixing tracer and this is not verified for TYC 8327-1678-1.

Also, we considered as unlikely a lithium enrichment from a planet or brown dwarf, whereas the lithium amount seen in atmosphere of TYC 8327-1678-1 is very high. In the first ascent to RGB, the star expands and its radio significantly increases, which can result in the engulfment of a planet or sub-companion. However, AGUILERA-GÓMEZ ET AL. (2016) argue that in this case the upper limit would be about $\log \epsilon(\mathrm{Li}) \approx 2.2$, which makes this scenario incompatible with the giant analysed here.

Recently, CASEY ET AL. (2019) observed a big number of lithium-rich giants based on LAMOST data (LUO ET AL., 2015; ZHAO ET AL., 2012). According to them, binary systems can drive lithium production in low-mass red giant stars: the companion, secondary star, can provide higher diffusion by tidal effect in the envelope of the primary star, allowing lithium production. However, the radial velocity obtained by analysing the Doppler shifts of the iron lines seems to be in agreement with the value estimated by the GAIA mission: the difference less than $1.0\,\mathrm{km\,s^{-1}}$ lead us to consider that this is a single star (today).

Helium white dwarf-red giant star merger

This year, ZHANG ET AL. (2020) provided results that support the merging event involving a He-white dwarf with a red giant star as a possible origin of (super) Li-rich giants. Essentially, they suggest that the final surface Li abundances depend on the masses of the progenitor helium white dwarfs: $0.35 \leqslant \mathrm{M}_{WD} \leqslant 0.40$ for creating Li-rich giants. In these

models, other masses also can create another class of chemically peculiar stars, such as early-R carbon stars.

For the model by ZHANG ET AL. (2020), the He-white dwarf and the red giant star create a common envelope when they get in contact: the dwarf will merge in the helium core of giant if a spiral occurs before the entire envelope is ejected. As a product, a new object is formed. This new star presents a degenerate nucleus surrounded by a shell rich in hydrogen and will be heated by a series of He-flashes. Finally, the helium core burning is established and this new red clump star can present peculiar chemical abundances in its surface, with dependence on initial conditions of merger. This post-merger model is in good concordance with observations for the most of Li-rich giants with respect to effective temperature, surface gravity, surface luminosity, and surface abundance ($\log \epsilon$(Li) and ^{12}C/^{13}C). As an important limitation, rotation velocities were not included in the this post-merger models. For future works, according to the authors, the models can take into account the transport of angular momentum during the merger.

The results found here for TYC 8327-1678-1 are also in excellent agreement with the predictions for the merge model for a metallicity of Z = 0.030. This is the only model in the literature that can explain simultaneously the amounts of $\log \epsilon$(Li) and ^{12}C/^{13}C as well as our results for surface gravity, effective temperature and luminosity. This giant star appears to have in the same evolutionary status to the sample of 30 well-studied giants compiled by ZHANG ET AL. (2020), although not all are super lithium-rich stars. TYC 8327-1678-1 presents a temperature near to the lowest temperature in Zhang's sample and a high metallicity and atypical carbon-nitrogen ratio. Observational data such as those present in this work can add useful links for future works, since TYC 8327-1678-1 is not common even among the super Li-rich giants.

6.4 Summary

Based on a high-resolution optical spectrum with a wide spectral coverage, we analysed the chemical composition of the giant star TYC 8327-1678-1, which has a high amount of ^{7}Li in its atmosphere. Below we present the most relevant results:

- The spectroscopic and photometric stellar parameters of TYC 8327-1678-1 indicate that this giant is a low-mass star which is located in an ambiguous region of the H-R diagram. To investigate its status, we used evolutionary tracks by GIRARDI ET AL. (2000) for super solar metallicity (Z = 0.030).

- We used many well-known super Li-rich giants from the literature for comparison purpose and carry out a wide perspective about the most likely scenarios that would provide this lithium enrichment. As a whole, we find that TYC 8327-1678-1 shows

high values for the [C/N] ratio (for its metallicity) and $^{12}C/^{13}C$ ratio, which help us to disregard the RGB bump stage and an intrinsic enrichment.

- We argue that a merging event between a He white dwarf with a red giant star provides the more probable origin for this peculiar giant star. Therefore, TYC 8327-1678-1 is a red giant at clump stage, since models provided by ZHANG ET AL. (2020) do not create final red giants with degenerate helium cores.

In view of all that has been exposed, we expect that models like the one that involves the merging of a low-mass white dwarf and a giant should be enriched with more observational constraints such as rotational velocity, since there has already been a greater incidence of lithium enrichment in rapid rotators and this is often explored in the literature.

Capítulo 7

As gigantes do aglomerado aberto NGC 2345

Neste capítulo apresentamos resultados para as abundâncias elementais de cinco (super)gigantes K pertencentes ao jovem aglomerado aberto NGC 2345. Os parâmetros atmosféricos das gigantes aqui estudadas e suas abundâncias químicas foram determinadas usando espectroscopia de alta resolução na região do optico. Neste estudo, foram determinadas abundâncias para elementos leves (Li, C, N), elementos leves de número atômico ímpar (Na, Al), elementos-α (Mg, Si, Ca, Ti), elementos do grupo do ferro (Cr, Fe, Ni), e elementos produzidos por captura de neutrons (Y, Zr, La, Ce, Nd, Sm, Eu) para cada estrela. As abundâncias dos elementos leves e európio foram obtidas usando a técnica de síntese espectral. Também, as velocidades rotacionais projetadas (v sin i) foram determinadas através da síntese espectral da linha de Fe I em 6151.6 Å. A metalicidade média obtida para o aglomerado aberto é [Fe/H] = -0.33 $\pm$ 0.05 e é considerada baixa se comparada a estudos recentes para aglomerados abertos da Via Láctea, apesar da sua baixa latitude Galáctea (b = -02°.31). Por último, a análise de abundâncias mostra que existe uma boa concordância com o perfil de estrelas do campo que estão na fase de RGB-Clump e que apresentam metalicidade similar.

O conteúdo apresentado a seguir refere-se à publicação: **Holanda, N., Pereira, C.B., & Drake, N. A., 2019, Monthly Notices of the Royal Astronomical Society, 482, 5275 (Artigo 1)**.

7.1 Introduction

In stellar open clusters we can assume that all the stars are formed in the same interstellar cloud at roughly the same time, at the same distance and with similar chemical composition, making them excellent laboratories for the study of stellar and Galactic evolution (see DA SILVEIRA ET AL., 2018; FRIEL, 1995, among others). In particular, young open

clusters are excellent tracers of spiral structure and are helpful tools to study recent star formation in Milky Way, because they are indicators of the variations in the abundance of heavy chemical elements in the Galactic disc (LADA & LADA, 2003). Nevertheless, the precise measurement of elemental abundances required spectroscopic observations at high resolution, which are available only for about 10 per cent of the currently known open clusters (HEITER ET AL., 2014).

In this paper, we focus on the open cluster NGC 2345, a young open cluster, with an age of 0.079 Gyr, using high-resolution spectroscopy with the aim to obtain its abundance pattern of its known member stars. NGC 2345 is located in Canis Majoris (l, b) = (226°.58, -02°.31) at a distance of 2.251 kpc (KHARCHENKO ET AL., 2005), being slightly younger than the Pleiades. The cluster contains five bright K-type giants, one of them is in a binary system. The first report of the NGC 2345 highlights the presence of seven luminous stars at a distance of 10 kpc (STEPHENSON & SANDULEAK , 1971). Later, MOFFAT (1974) made UBV photometry and a spectroscopic observation yield for NGC 2345 a distance of 1.75 kpc and an age of 60 Myr, denoting the existence of five red giants and two blue bright giants. In this study by MOFFAT (1974), the spectrum analysis of #34 reveals that it is formed of two stars, one red giant and other (probably) subgiant star of B type. Fig. 7.1 shows the stellar field of NGC 2345. Following the same strategy as for our previous studies for open clusters (e.g. DA SILVEIRA ET AL., 2018; KATIME SANTRICH ET AL., 2013; PEÑA SUÁREZ ET AL., 2018; SALES SILVA ET AL., 2014), we observed all the known giant stars that belong to the cluster according to MERMILLIOD ET AL. (2008).

Previous spectroscopic analysis done for this cluster showed that it has a surprisingly low metallicity ([Fe/H] = -0.26 ± 0.03) for a thin-disc cluster (REDDY ET AL., 2016). In addition, being very young, NGC 2345 should be composed by massive stars. In fact, as it will be seen, it has a turn-off mass of 5.4 $M_{\odot}$. Low metallicity among massive stars is not usually found as can be seen in fig. 3 of TAKEDA ET AL. (2008) and fig. 17 of ZIELIŃSKI ET AL. (2012). In fact, the two most massive stars from the sample of 322 giants analysed by TAKEDA ET AL. (2008) have masses of, respectively, 4.91 and 4.99 $M_{\odot}$ with metallicities, respectively, of +0.08 and -0.02, while from the sample of 348 giants analysed by ZIELIŃSKI ET AL. (2012) the most massive star has a mass of 3.4 $M_{\odot}$ with a metallicity of -0.18. Therefore, NGC 2345 is a useful target for a high-resolution spectroscopy analysis in order to probe possible effects of mixing and dredge-up events in massive stars and to search for a relationship between abundance ratios and age for a comparison with older clusters. It is interesting that other massive clusters, such as NGC 1545 (ZAČS ET AL., 2011) and NGC 5316 (DRAZDAUSKAS ET AL., 2016) with ages of 0.09 and 0.08 Gyr and Galactocentric distances estimated as 8.59 and 7.4 kpc, respectively, are in a good agreement with the radial Galactic gradient. Unlike NGC 2345 presents a metallicity below the pattern found in clusters at the same distance and/or

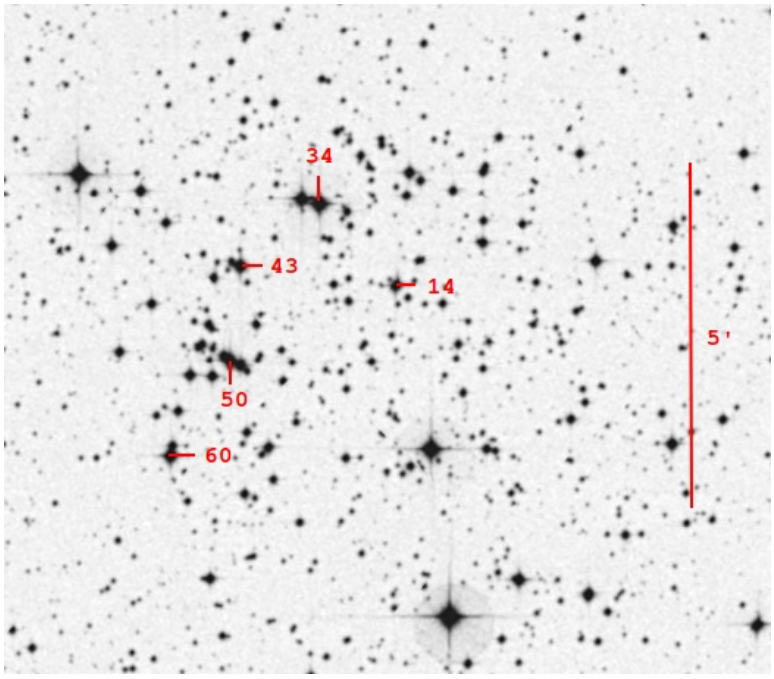

Figura 7.1: Finding chart for stars spectroscopically observed in the field of NGC 2345 (DSS2 blue image from CDS portal). Stars are marked according to ID provided MOFFAT (1974).

with a similar turn-off mass. Another cluster, NGC 3105 (ALONSO-SANTIAGO ET AL., 2018), with stars having masses around 10 $M_{\odot}$, also has a similar low metallicity ([Fe/H] = -0.29), is closer to the radial Galactic gradient pattern than NGC 2345, which is much less massive.

As above mentioned, we used high-resolution spectroscopy to determine the atmospheric parameters and abundances for several chemical elements for the four single red giants and one spectroscopic binary for the K giant in NGC 2345. The abundances of the light elements (lithium, carbon, and nitrogen), europium, and the $^{12}C/^{13}C$ isotopic ratio were determined using spectral synthesis technique, while the abundances of Na, Mg, Al, Ca, Si, Ti, Ni, Cr, Y, Zr, La, Ce, Nd, and Sm were determined using equivalent width measurements. The oxygen abundance was not possible to determine because of the contamination of by telluric lines. In addition, we also determined rotational velocities of the stars in this cluster. There are a few determinations of the rotational velocities of the giants in open clusters, especially in those young clusters. Therefore, determining rotation rates may set important constraints for a binary system and also for the physical mechanism of dredge-up of angular momentum from a fast rotating core in a single star (KATIME SANTRICH ET AL., 2013).

7.2 Observations

The observations were carried out using Échelle spectrograph Fiber-fed Extended Range Optical Spectrograph (FEROS; KAUFER ET AL., 1999) at the 2.2-m Max Planck Gesellschaft/European Southern Observatory (ESO) Telescope in La Silla, Chile. The FEROS provides a full wavelength coverage of 3800-9200 Å with resolving power R = 48000, corresponding to 2.2 pixels of 15 μm. The exposure time of our spectra ranges from 1200 to 2400 s to achieve a typical signal-to-noise ratio (S/N) = 100-150 (individual values are given in Table 7.1. All spectra were reduced with the FEROS Data Reduction System pipeline.

In order to complement the spectroscopic data, we used the UBV photometry of MOFFAT (1974), downloading it from the WEBDA data base. Once we have done this, we employed the isochrone fitting method to determine the age of NGC 2345 as shown in Fig. 7.2. We adopted a colour excess of E(B - V) = 0.616 (DIAS ET AL., 2002). Table 7.1 gives the basic information of the observed stars. The stars were selected from the radial velocity survey of MERMILLIOD ET AL. (2008). The radial velocities obtained for all stars analysed in this study are also shown in Table 7.1. From these data for four stars we obtain a mean radial velocity for the cluster as $\langle RV \rangle = 58.49 \pm 0.41\,km\,s^{-1}$, which is in good agreement with 59.11 ± 1.31 and $57.70 \pm 0.42\,km\,s^{-1}$ reported by MERMILLIOD ET AL. (2008) and REDDY ET AL. (2016), respectively. To calculate the mean, the star #34 was excluded due to its binary nature. In addition, Table 7.1 shows the rotation velocities obtained for the stars analysed in this work.

In Fig. 7.3, we plot the turn-off mass versus age for some clusters including NGC 2345. From the isochrone fit, we derived a turn-off mass of $5.40 \pm 0.15\,M_{\odot}$ and an age of $\log t = 7.9 \pm 0.1$ (or 79.4 Myr). This value is in agreement with the values of $\log t = 7.85$ and $\log t = 7.74$ reported by DIAS ET AL. (2002) and KHARCHENKO ET AL. (2005), respectively.

7.3 Analysis and Results

7.3.1 Atmospheric Parameters

Atmospheric parameters of the stars analysed in this work were determined using the standard spectroscopic method and line list provided by HEKKER & MELÉNDEZ (2007). This list is composed of 20 Fe I and 6 Fe II lines between 5700 and 7800 Å. This line list is appropriate for an analysis of cool giants, avoiding line blending from CN bands (MELÉNDEZ & BARBUY, 1999; SANTOS ET AL., 2009). In Table A1, we show the equivalent widths of the Fe I and Fe II lines used to determine the atmospheric parameters. The equivalent widths were obtained by fitting Gaussian profiles to the observed

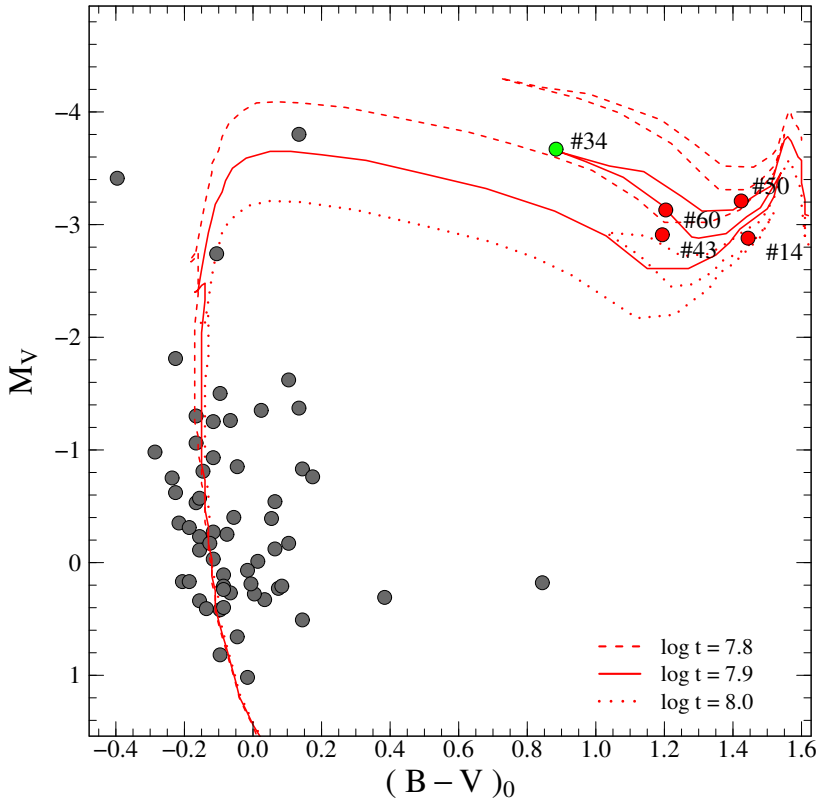

Figura 7.2: Reddening-corrected colourâmagnitude diagram of NGC 2345 with photometric data taken from (MOFFAT, 1974). Our program stars are identified by red filled circles (singles) and green filled circle (binary). We also show isochrones (BERTELLI ET AL., 1994) for elements three different ages: 63.09 Myr ($\log t = 7.8$), 79.43 Myr ($\log t = 7.9$), and 100 Myr ($\log t = 8.0$).

Tabela 7.1: Basic information of the observed stars in NGC 2345. Star number, V, $(B-V)$ and radial velocities (RV) were taken from MOFFAT (1974)[a], MERMILLIOD ET AL. (2008)[b] and REDDY ET AL. (2016)[c] are shown in Columns 1-6. The rotational velocities are shown in the seventh Column. The last two columns provide the date of observation and the exposure times.

Star	V[a]	(B−V)[a]	RV ($\mathrm{km\,s^{-1}}$)	RV[b] ($\mathrm{km\,s^{-1}}$)	RV[c] ($\mathrm{km\,s^{-1}}$)	$v \sin i$ ($\mathrm{km\,s^{-1}}$)	Observation date	Exp (s)
#14	10.73	2.06	58.96 ± 0.41	59.8 ± 0.40	—	4.5 ± 0.4	2016 Mar 11	2 400
#34	9.94	1.50	64.23 ± 0.44	61.18 ± 0.74	63.60 ± 0.40	10.1 ± 0.4	2016 Mar 11	1 200
#43	10.70	1.81	58.43 ± 0.52	58.82 ± 0.27	58.00 ± 0.40	4.7 ± 0.6	2016 Mar 11	2 400
#50	10.40	2.04	58.61 ± 0.60	60.41 ± 0.40	—	5.2 ± 0.4	2016 Mar 11	1 500
#60	10.48	1.82	57.97 ± 0.52	58.41 ± 0.35	57.40 ± 0.30	5.8 ± 0.4	2016 Mar 11	1 500

ones using the task SPLOT in IRAF. The red giants analysed by us have a cool limit of 4000 K and a hot limit of 4850 K. We used local thermodynamical equilibrium (LTE) plane-parallel atmospheric models of KURUCZ (1993) and the spectral analysis code MOOG (SNEDEN, 1973) for the determination of stellar atmospheric parameters. The effective temperature (T_{eff}) was obtained requiring that the abundance of Fe I lines (in the notation $[X/H] = \log(N_X/N_H)_\star - \log(N_X/N_H)_\odot$) did not depend on the lower level excitation potential (χ). The surface gravities ($\log g$) were determined from the iron ionization equilibrium. The microturbulence velocity (ξ) was found requiring that the abundance of Fe I lines did not depend on the reduced equivalent width ($\log(W_\lambda/\lambda)$). Determining these three main parameters through multiple iterations provides us with the value of metallicity as calculated from the used Fe I lines. We compare the derived spectroscopic gravities with the evolutionary gravities $\log g_\star$ using the turn-off mass ($M_{turn-off}$) obtained from the isochrone fittings using the equation

$$\log g_\star = \log\left(\frac{M_\star}{M_\odot}\right) + 0.4\,(V - A_V + BC_V) + 4\log T_{\rm eff} - 2\log r\,({\rm kpc}) - 16.5,$$

In the equation above, V, A_V, and BC_V are, respectively, the visual magnitude, interstellar absorption in V band, and bolometric correction. The surface gravity, mass, and temperature of the star are, respectively, $\log g_\star$, $M_\star$, and T_{eff} and r is the heliocentric distance of the open cluster given in kpc. The solar parameters atmospheric used in this equation are $M_{bol} = 4.75$, $\log g = 4.44$, and $T_{eff} = 5777$ K, as well the bolometric corrections were calculated using the relation given in ALONSO ET AL. (1999). In addition, we adopted the distances of Gaia Data Release 2 (GAIA COLLABORATION ET AL., 2018) and $A_V = 1.909$ (DIAS ET AL., 2002). The result of confronting spectroscopic and photometric gravities gave us a mean difference of -0.03 ± 0.22. The results for all the five giants are given in Table 7.2, as well as the photometric and spectroscopic $\log L/L_\odot$. The errors in the atmospheric parameters, effective temperature, and microturbulent velocity were estimated from the uncertainties in the slopes of relationships A(Fe I) versus ξ and A(Fe I) versus W_λ/λ, respectively. In addition, the standard deviation in the Fe I abundance was used to provide the uncertainty in the $\log g$ parameter. In these procedures, we find uncertainties of $T_{eff} = \pm 70$ - 100, $\log g = \pm 0.1$ - 0.2, and $\xi = \pm 0.15$ - 0.3.

7.3.2 Abundances Analysis

Two techniques were employed to derive the chemical abundances: equivalent width measurements and spectral synthesis. We used equivalent width measurements for the determination of the abundances for Na, Mg, Al, Si, Ca, Ti, Cr, Ni, Y, La, Ce, Nd, and Sm. The adopted line list was the same of our previous papers. All lines were inspected and some of them were excluded due to blending, hence the final line list differs slightly from

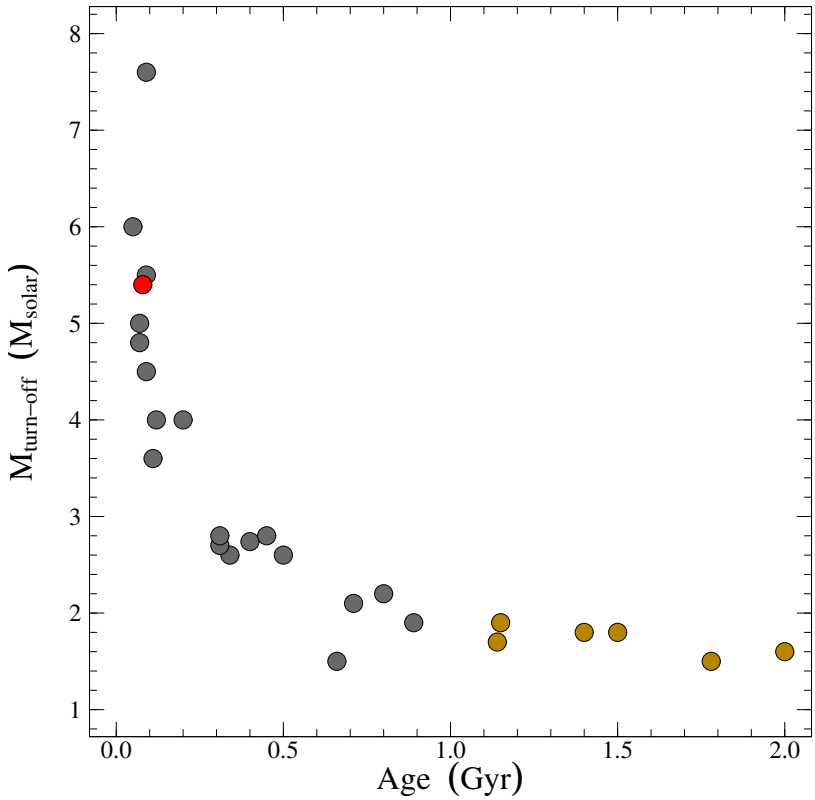

Figura 7.3: Turn-off mass versus age for open clusters and NGC 2345 (the red circle). According to FRIEL (1995), young clusters have age less than 1.0 Gyr (grey circles) and old clusters have age more than 1.0 Gyr (dark yellow circles).

Tabela 7.2: Adopted spectroscopic atmospheric parameters and luminosity for the giant stars of NGC 2345. In addition, we also show the photometric temperature, gravity and luminosity, respectively, in the notation of T_{eff}, $\log g$ and $\log \frac{L}{L_\odot}$.

Star	T_{eff}^{spec} (K)	$\log g^{spec}$	$\xi(\mathrm{km\,s^{-1}})$	[Fe I/H] $\pm\,\sigma$	[Fe II/H] $\pm\,\sigma$	$\log \frac{L}{L_\odot}^{spec}$	T_{eff}^{phot} (K)	$\log g^{phot}$	$\log \frac{L}{L_\odot}^{phot}$
#14	4150	1.10	2.36	-0.33 ± 0.09	-0.34 ± 0.13	3.78	3877	1.03	3.85
#34	4850	1.10	3.00	-0.26 ± 0.12	-0.24 ± 0.06	4.05	4843	1.29	3.86
#43	4350	1.60	2.45	-0.32 ± 0.07	-0.31 ± 0.07	3.36	4250	1.35	3.61
#50	4000	0.70	2.31	-0.37 ± 0.10	-0.37 ± 0.10	4.12	3881	1.01	3.81
#60	4020	1.03	2.54	-0.39 ± 0.08	-0.38 ± 0.10	3.80	4185	0.99	3.84

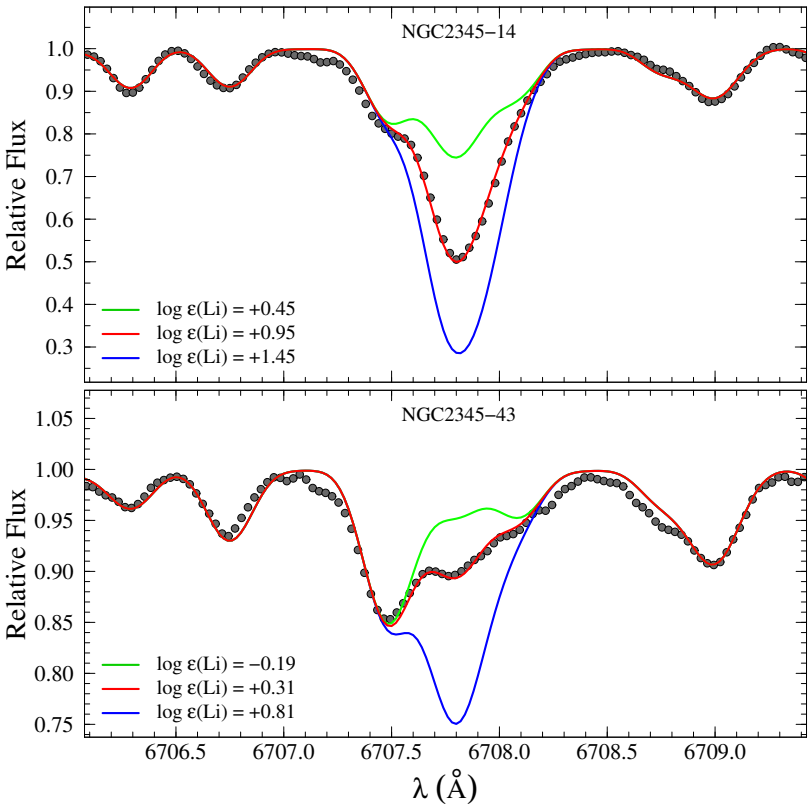

Figura 7.4: Observed (dotted line) and synthetic (solid lines) spectra in the region around the Li I line at $\lambda\,6708$ Å line for the stars #14 and #43.

star to star. As for the determination of the atmospheric parameters, we used LTE model atmospheres of KURUCZ (1993) and the code MOOG for the abundance determinations of the elements above mentioned. In addition, the abundances of the elements were normalized using the solar abundances of ASPLUND ET AL. (2009). Table A2 shows the atomic lines used for the determination of the chemical abundances.

The abundances of the light elements (lithium, carbon, and nitrogen), the $^{12}C/^{13}C$ isotopic ratio, and europium were determined in the same way as in DA SILVEIRA ET AL. (2018) using the same line list for the same spectral regions for the spectral synthesis. The abundance of carbon was determined using the spectral region of the C_2 molecule [C_2 (0,1) band head of the Swan system $A^3\Pi_g$ - $X^3\Pi_u$ at 5635 Å. The electron oscillator strength, $f_{el} = 0.033$, was taken from LAMBERT (1978). The Hönl-London factors for the rotational lines were calculated using formula from KOVŽACS (1969). Franck-Condon factors were calculated according to DWIVEDI ET AL. (1978). C_2 dissociation energy of D_0 (C_2) = 6.15 eV was adopted HUBER & HERZBERG (1979). The wavelengths of the C_2 features of the (0,1) band were taken from PHILLIPS & DAVIS (1968).

The nitrogen abundance was obtained by comparing the observed and theoretical line profiles for the ^{12}CN lines of the (2, 0) band of the CN red system $A^2\Pi - X^2\Sigma$ in the 7994-8020 Åwavelength range. Oscillator strength of the (0,2) band $f_{2,0} = 8.4 \times 10^4$ (SNEDEN & LAMBERT , 1982) was used. Hönl-London factors were calculated using SCHADEE

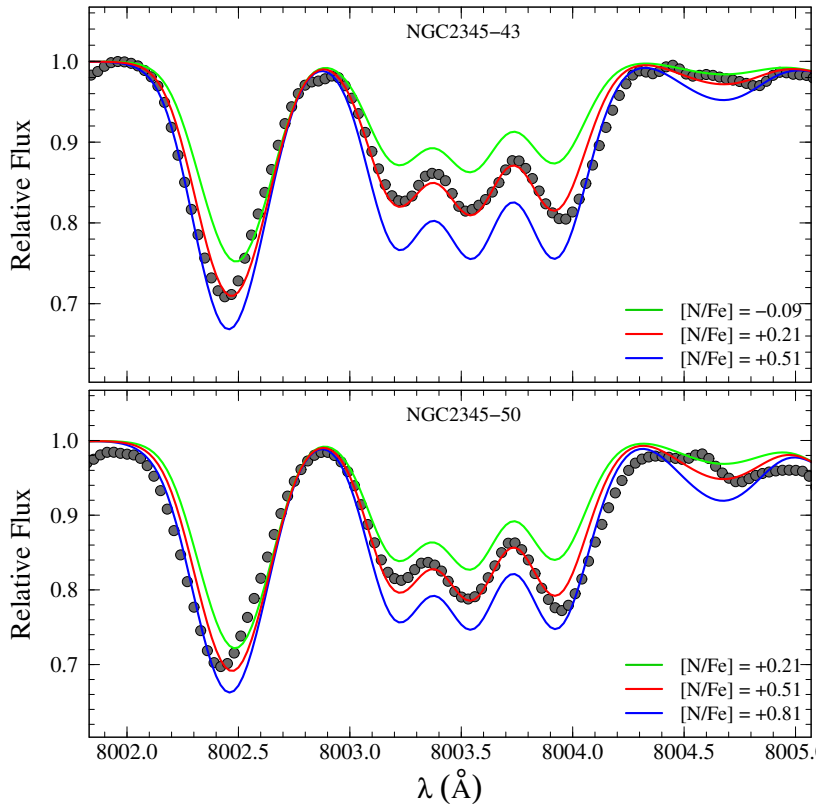

Figura 7.5: Observed (dotted line) and synthetic (solid lines) spectra between 8002 and 8005 Åfor the stars #43 and #50.

(1964) formula. The dissociation energy D_0 (CN) = 7.65 eV was used (BAUSCHLICHER ET AL., 1988; LAMBERT, 1994). The wavelengths of the ^{12}CN lines were taken from DAVIS & PHILLIPS (1963) and those of ^{13}CN lines from WYLLER (1966). The europium abundance was determined using the Eu II line at λ 6645.13 Å and the hyperfine splitting was taken from MUCCIARELLI ET AL. (2008).

Unfortunately, we could not obtain the oxygen abundance based on the forbidden line at 6300 Å because of the contamination with telluric O_2 lines. Therefore, we assumed a [O/Fe] ratio of +0.12 since the oxygen abundance affects the carbon abundance. Figs 7.4, 7.5 and 7.6 show, respectively, the observed and synthetic spectra for the stars NGC 2345 - 14 and 43 around the lithium line at 6708 Å, the observed and synthetic spectra for the stars NGC 2345 - 43 and 50 between 8002 and 8005 Å for CN lines, and the observed and synthetic spectra for the stars NGC 2345 - 14 and 34 around the europium line at 6645 Å. Tables 7.3 and 7.4 show all results of the abundance determinations and the obtained mean cluster abundance. The lithium abundance is given in the notation $\log \epsilon(\mathrm{Li}) = \log [N_{Li}/N_H] + 12$. We also provide the mean abundance, s, of the elements created by the s-process (Y, Zr, La, Ce, and Nd) in the notation [s/Fe].

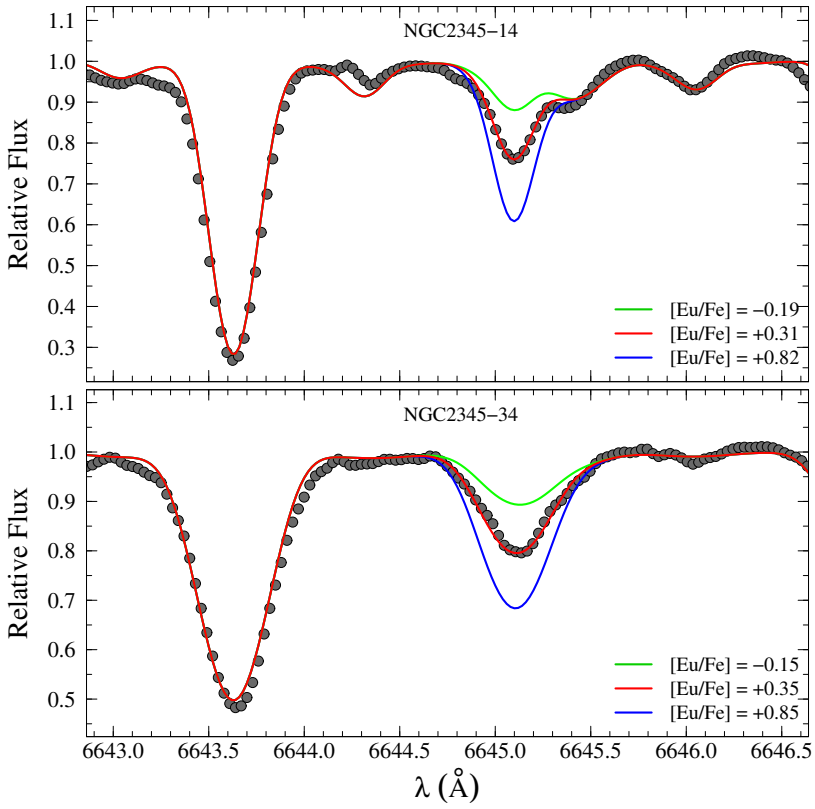

Figura 7.6: Observed (dotted line) and synthetic spectra (solid lines) in the region around the Eu II line at $\lambda\,6645.13$ Å line for the stars #14 and #34.

Tabela 7.3: Light element abundances and $^{12}C/^{13}C$ isotopic ratios.

Star	log ϵ(Li)	[C/Fe]	[N/Fe]	$^{12}C/^{13}C$
#14	+0.95	+0.02	+0.62	> 24
#34	+0.11	−0.05	+0.65	18
#43	+0.31	+0.26	+0.21	> 30
#50	+0.81	+0.11	+0.51	> 26
#60	+0.19	+0.13	+0.63	> 30
Mean	+0.47 ± 0.34	+0.09 ± 0.12	+0.52 ± 0.18	> 25.6

Tabela 7.4: Abundance ratios [X/Fe] and the standard deviations for the targets in NGC 2345.

[X/Fe]	#14	#34	#43	#50	#60	⟨[X/Fe]⟩
[Na I/Fe]	+0.40 (3)	+0.28 (2)	+0.10 (4)	+0.34 (3)	+0.21 (2)	+0.27 ± 0.12
[Mg I/Fe]	+0.09 (5)	+0.10 (2)	+0.21 (3)	+0.26 (3)	+0.22 (4)	+0.18 ± 0.08
[Al I/Fe]	+0.17 (3)	+0.18 (4)	+0.09 (4)	+0.13 (4)	+0.09 (5)	+0.13 ± 0.04
[Si I/Fe]	+0.28 (6)	+0.18 (4)	+0.31 (1)	+0.28 (7)	+0.41 (4)	+0.29 ± 0.08
[Ca I/Fe]	−0.03 (3)	+0.05 (4)	−0.03 (3)	+0.01 (2)	+0.02 (3)	+0.00 ± 0.04
[Ti I/Fe]	0.00 (4)	+0.10 (9)	−0.05 (7)	+0.08 (4)	—	+0.03 ± 0.07
[Cr I/Fe]	+0.06 (11)	−0.04 (8)	+0.03 (15)	+0.03 (7)	−0.04 (7)	+0.01 ± 0.04
[Ni I/Fe]	−0.05 (6)	−0.06 (12)	−0.06 (9)	−0.05 (11)	−0.06 (5)	−0.06 ± 0.01
[Y II/Fe]	+0.29 (3)	+0.16 (2)	+0.26 (3)	+0.30 (3)	+0.19 (2)	+0.24 ± 0.06
[Zr I/Fe]	+0.10 (12)	+0.11 (5)	+0.04 (11)	+0.06 (12)	−0.10 (8)	+0.04 ± 0.08
[La II/Fe]	+0.53 (5)	+0.50 (3)	+0.53 (5)	+0.41 (4)	+0.35 (4)	+0.46 ± 0.08
[Ce II/Fe]	+0.28 (4)	+0.20 (4)	+0.35 (4)	+0.21 (4)	+0.05 (6)	+0.22 ± 0.11
[Nd II/Fe]	+0.35 (5)	+0.41 (10)	+0.41 (7)	+0.22 (8)	+0.20 (11)	+0.32 ± 0.10
[Sm II/Fe]	+0.28 (4)	+0.21 (3)	+0.38 (3)	0.11 (3)	−0.04 (4)	+0.19 ± 0.16
[Eu II/Fe]	+0.31 (1)	+0.35 (1)	+0.41 (1)	+0.26 (1)	+0.28 (1)	+0.32 ± 0.06
[α/Fe]	+0.08	+0.11	+0.11	+0.16	+0.22	+0.14 ± 0.05
[s/Fe]	+0.31	+0.28	+0.32	+0.24	+0.14	+0.26 ± 0.07

Abundance Uncertainties

Tables 7.5 and 7.6 show the influence of the uncertainties of the atmospheric parameters over the chemical abundances for the star #34. In addition, in Table 7.5 we also show the abundance variation due to the uncertainty of 3.0 mÅ in the equivalent width of the observed lines for each chemical specie, considering the FEROS spectral resolution and the S/N (CAYREL, 1988) around 100. The seventh column provides the total abundance uncertainty calculated as the root square of the sum of the various sources of uncertainties. The last column of Table 7.5 provides the abundance dispersion between the lines for each element with more than available lines. Overall, inspecting Table 7.5 reveals that neutral species exhibit higher sensitivity to temperature variation, while ionized species exhibit the greater differences due to the uncertainties in the surface gravities. In addition to carbon and nitrogen abundances, the uncertainties in carbon abundance affect the nitrogen abundance and vice versa once we used CN molecular lines for its determination.

7.4 Discussion

7.4.1 Rotation velocities

The determination of the rotational velocities v sin i was made by using spectral synthesis for the Fe I 6151.6 Åline. We fixed macro-turbulent velocity as 3.0 km s^1 (FEKEL ET AL., 1997) for all stars and also considering the instrumental broadening for the FEROS spec-

Tabela 7.5: Abundance uncertainties for NGC 2345 - 34. From the second to the fourth column we show the variations of abundances caused by the variations of the atmospheric parameters. The fifth column refers to the variation of abundances due to metallicity. The sixth column provides the uncertainty due to a variation of 3.0 mÅ in the equivalent width of each measured line. In seventh column we present the total compounded *rms* uncertainty of the second to the sixth columns. Finally, the last column provides the standard deviation among the abundances given by individual lines for elements with more than three available lines.

Species	$\Delta T_{\rm eff}$ (K) $+90$ K	Δ log g $+0.2$	$\Delta\xi$ $+0.3\,{\rm km\,s^{-1}}$	Δ[Fe/H] $+0.12$ dex	ΔEW $+3$ mÅ	$(\Sigma\sigma^2)^{1/2}$	σ_{obs}
Li I	+0.00	+0.05	−0.10	−0.01	—	+0.11	—
Na I	+0.07	−0.01	−0.04	+0.00	+0.03	+0.09	+0.03
Mg I	+0.03	+0.00	+0.05	−0.01	+0.03	+0.07	+0.11
Al I	+0.05	−0.01	+0.03	−0.01	+0.03	+0.07	+0.14
Si I	+0.02	−0.02	−0.04	+0.01	+0.04	+0.06	+0.09
Ca I	+0.07	−0.02	−0.05	−0.01	+0.04	+0.10	+0.06
Ti I	+0.13	−0.01	+0.04	−0.01	+0.03	+0.14	+0.13
Cr I	+0.08	−0.02	−0.03	−0.01	+0.04	+0.10	+0.19
Fe I	+0.10	+0.00	−0.04	+0.01	+0.04	+0.12	+0.13
Fe II	−0.07	+0.09	−0.10	+0.03	+0.03	+0.16	+0.06
Ni I	+0.10	+0.00	+0.05	+0.00	+0.03	+0.12	—
Y II	−0.01	+0.06	−0.05	+0.04	+0.04	+0.10	—
Zr I	+0.16	−0.02	+0.00	+0.00	+0.07	+0.18	+0.15
La II	+0.00	+0.08	−0.04	+0.03	+0.03	+0.10	+0.02
Ce II	+0.00	+0.08	−0.04	+0.04	+0.04	+0.11	+0.07
Nd II	+0.01	+0.08	−0.07	+0.03	+0.03	+0.11	+0.23
Sm II	+0.02	+0.07	−0.07	+0.03	+0.04	+0.11	+0.10
Eu II	+0.00	+0.10	−0.10	+0.10	—	+0.17	—

Tabela 7.6: Influence of the errors in atmospheric parameters over the abundances of lithium, carbon and nitrogen for NGC 2345 - 34. We also give the dependence of the uncertainty of carbon abundance over the nitrogen abundance and vice-versa.

species	$\Delta T_{\rm eff}$ (K) $+90$ K	Δ log g $+0.2$	$\Delta\xi$ $+0.3\,{\rm km\,s^{-1}}$	Δlog(C) $+0.20$ dex	Δlog(N) $+0.20$ dex	Δlog(O) $+0.20$ dex	$(\Sigma\sigma^2)^{1/2}$
C (C_2)	+0.00	−0.05	−0.05	—	−0.10	+0.05	+0.13
N (CN)	+0.05	+0.00	−0.05	−0.20	—	+0.10	+0.23

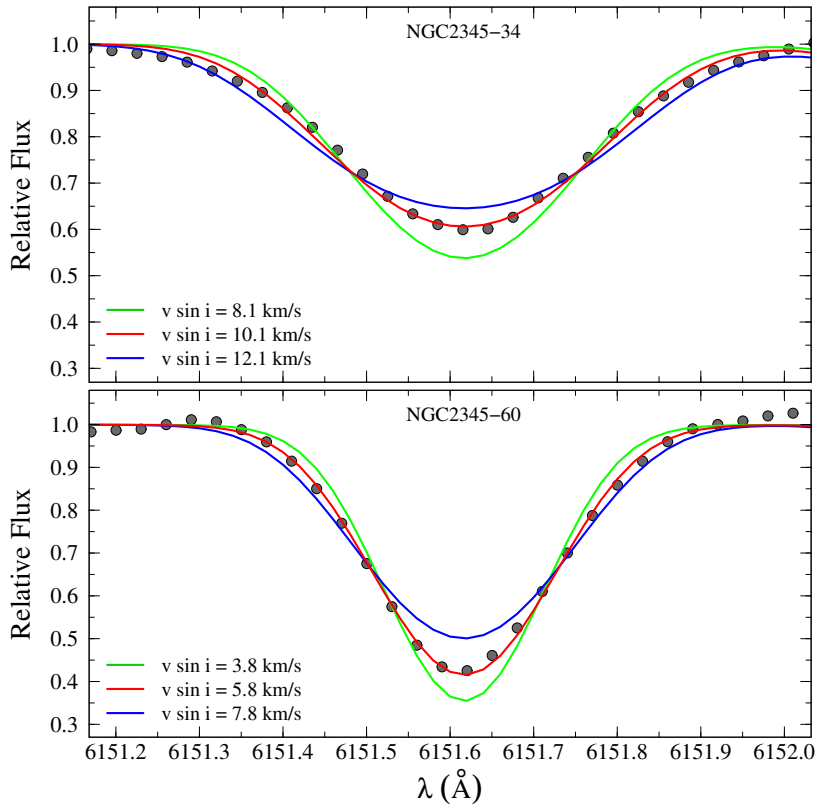

Figura 7.7: Observed (black dots) and synthetic spectra in the region of the Fe I line at 6151.6 Å for giants #34 and #60 of the open cluster NGC 2345. The figure shows the three absorption profiles corresponding to the different rotational velocities.

tral resolution. The instrumental broadening was determined measuring the Gausssian full width at half-maximum of the thorium-argon lines used for the wavelength calibration for FEROS spectrograph. Table 7.1 shows rotational velocities for giants of the open cluster NGC 2345, while Fig. 7.7 shows the synthesis for the Fe I 6151.6 Å line for stars #34 and #60 with different values of v sin i. The best fits for these stars are the rotational velocities of 10.1 and 5.8 km s^{-1} (red solid lines), respectively. The mean projected rotational velocity for NGC 2345 is 5.05 ± 0.58 (excluding the binary star #34). This value is close to the mean value of 4.5 ± 1.2 km s^{-1} for 1288 single giant stars with $v\,sin\,i < 9.0$ km s^{-1} studied by CARLBERG ET AL. (2011). Fig. 7.8 shows the temperature distribution as a function of the projected rotational velocity obtained from CARLBERG ET AL. (2011) (grey circles), consider the star with v sin $i < 20.0$ km s^{-1}. The stars of our sample are shown as red circles and the binary #34 as green circles with photometric (triangles) and spectroscopic (circles) derived temperatures. This comparison reveals the good agreement between the spectroscopic and photometric derived temperatures for stars of NGC 2345.

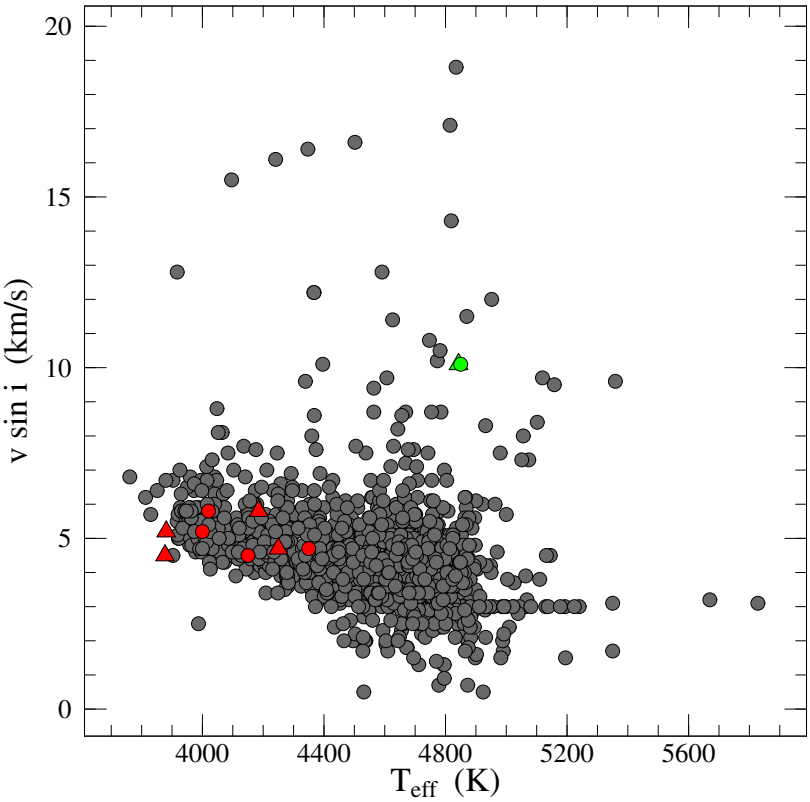

Figura 7.8: Projected rotational velocities and photometric temperature for giants stars. The grey circles represent the stars from the sample studied by CARLBERG ET AL. (2011). Circles and triangles denote, respectively, the spectroscopic and photometric temperatures. Red symbols represent the single stars and green the binary star NGC 2345 - 34.

7.4.2 Abundance Pattern

Metallicity

NGC 2345 presents the mean metallicity of -0.33 ± 0.05 (based on the abundance given by the Fe I lines). This result is slightly different from the result given by REDDY ET AL. (2016), as previously mentioned. REDDY ET AL. (2016) used three giants (#34, #43, and #60) and found a mean metallicity of -0.26 ± 0.03. Using the same three stars we obtained a mean metallicity of -0.32 ± 0.06. Like most of the chemical elements in the thin-disc stars, the abundance of iron also decreases with the Galactocentric distance. The radial Galactic gradient shown in Fig. 7.9 highlights this atypical metallicity of NGC 2345. The linear regression (red dashed line) was done based only on the distribution of the Cepheids and has a slope -0.06 dex kpc^{-1} (GENOVALI ET AL., 2014). In addition, young open clusters were included for a closer comparison are shown as grey circles using data from NETOPIL ET AL. (2016) and distances taken from WEBDA. The grey triangle represents NGC 3105 ALONSO-SANTIAGO ET AL. (2018), which has a metallicity and a Galactocentric distance (10 kpc) similar to that of NGC 2345. The linear fit (blue dashed line) for the clusters distribution presents a slope of -0.08 dex kpc^{-1} ($R_{GC} \leqslant 12.0$ kpc), which are in good agreement with -0.09 dex kpc^{-1} derived by YONG ET AL. (2012). It is important to note the existence of a discontinuity in the Galactic metallicity gradient at 12.0 - 13.0 kpc (YONG ET AL., 2012), which is the so-called transition radius between the inner and outer disc. The inner disc has a more pronounced gradient, while the metallicity gradient of the outer disc is almost flat. Another observation, concerning to the thick-disc clusters in this analysis, shows that the profile of the gradient becomes smoother, as observed in fig. 4 presented by REDDY ET AL. (2016).

The Galactocentric distances projected to the Galactic plane were calculated based on the distances of the cluster to the Sun (d), Galactic longitudes (l), and latitudes (b), with the well-known relation

$$R_{GC}^2 = R_{\odot}^2 + (d \cos b)^2 - 2\, R_{\odot}\, d \cos l \cos b,$$

where $R_{\odot}$ is the Galactocentric distance of the Sun that we assume as 7.95 kpc, rescaling the data compiled by NETOPIL ET AL. (2016) to GENOVALI ET AL. (2014). The distance of 2.251 kpc KHARCHENKO ET AL. (2005) was used to determine the Galactocentric radius for our cluster, $R_{GC} = 9.64$ kpc.

Light elements: Li, C, N, and the $^{12}C/^{13}C$ isotopic ratio

When a star reaches the red giant branch, the increase of the convective envelope dilutes the ^{7}Li (among other species such as ^{12}C, ^{16}O, and ^{18}O) and reduces significantly its surface abundance. Therefore, it is expected to find a typical lithium abundance in

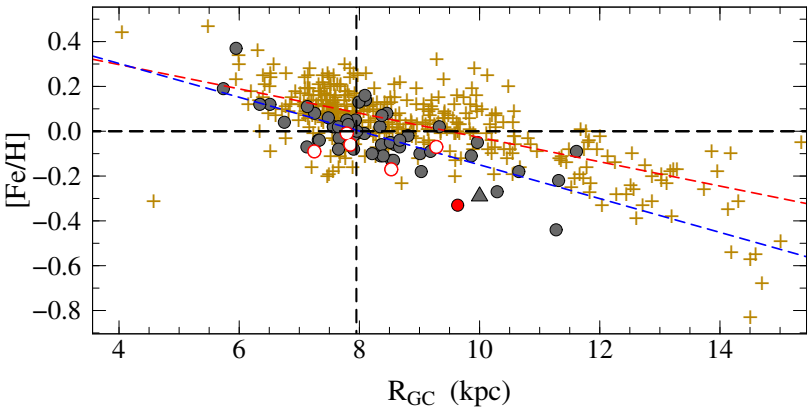

Figura 7.9: The average [Fe/H] versus Galactocentric distance with iron abundance gradients of -0.06 dex kpc^{-1} (red dashed line; GENOVALI ET AL., 2014) and -0.08 dex kpc^{-1} (blue dashed line) for Cepheids and open clusters, respectively. The yellow crosses represent Cepheids studied by GENOVALI ET AL. (2014, 2013) and other sources used by them. The grey filled circles represent young open clusters ($\leqslant$1 Gyr) with metallicities determined through high-resolution spectroscopy and compiled by NETOPIL ET AL. (2016). The grey triangle represents to NGC 3105 studied by ALONSO-SANTIAGO ET AL. (2018) and red open circles are open clusters studied by our group (DA SILVEIRA ET AL., 2018; KATIME SANTRICH ET AL., 2013; PEÑA SUÁREZ ET AL., 2018).

the range -1.0 < log ϵ(Li) < 1.0 (CHARBONNEL & BALACHANDRAN, 2000; GILROY, 1989). In good agreement with this scenario of the first dredge-up, the abundance of lithium is low in the giants studied here. The mean value for the lithium abundance for the stars of our sample is 0.47 ± 0.34, which can be considered overabundant with respect to NGC 2451 (log ϵ(Li) = -0.50) and Cr 140 (log ϵ(Li) = 0.15), which have similar turn-off masses of $\approx$6.0 and $\approx$5.0 $M_\odot$, respectively GILROY (1989). We raise for the need for more new studies in order to obtain lithium abundances in open clusters, in particular in young clusters. Recent study done by DELGADO MENA ET AL. (2016) is essential, but it was concentrated on stars with "higher" gravities (those with log $g > 2.0$). For a faithful comparison with NGC 2345, for example, stars with log $g \leqslant 1.5$ would be required.

In Fig. 7.10, we show our derived [C/Fe] and [N/Fe] ratios in comparison with the same ratios obtained by MISHENINA ET AL. (2006) and LUCK & HEITER (2007) (abundances normalized to ASPLUND ET AL., 2009) for disc red clump giants and local disc field giants. The results for [C/Fe] and [N/Fe] ratios for the five giants analysed in this work, show first dredge-up profile, as can be seen in Table 7.3. As mentioned before, abundance of ^{12}C is reduced as a consequence of the first dredge-up process and, the abundance of ^{14}N increased KARAKAS & LATTANZIO (2014), as is clearly observed in all the stars analysed. The ^{12}C/^{13}C isotope ratio is a useful evolutionary indicator for low- and intermediate-mass stars because it is a tracer of which nuclear processes occur inside these objects. Fig. 7.11 shows the ^{12}C/^{13}C ratio predicted for giants at first dredge-up with standard and thermohaline extra-mixing and thermohaline and rotation-induced

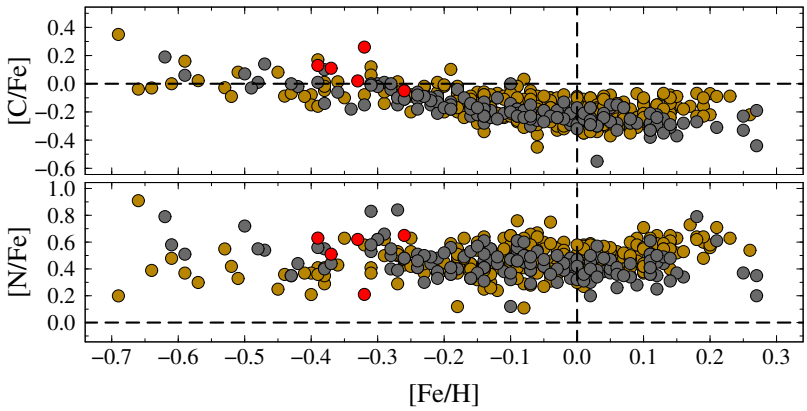

Figura 7.10: Abundance ratios [X/Fe] versus [Fe/H] for carbon and nitrogen. The red circles represent the giants analysed in this work, while the dark yellow circles represent the abundances reported by LUCK & HEITER (2007) and the grey circles represent the abundances reported by MISHENINA ET AL. (2006). The dashed lines indicate the solar value.

mixing for evolutionary models calculated by CHARBONNEL & LAGARDE (2010) and LAGARDE ET AL. (2012). We use data from several sources of the literature in the range $1.58 \leqslant M_{turn-off} \leqslant 5.6$. When we compare the mean of $^{12}C/^{13}C$ ratio obtained for the giants of NGC 2345 with the values predicted by mixing models, it is possible to verify that the best agreement is for the standard model of first dredge-up by LAGARDE ET AL. (2012). However, our $^{12}C/^{13}C$ ratio is not low enough to be in agreement with the thermohaline and rotation-induced mixing model calculated by LAGARDE ET AL. (2012), as was observed in the open clusters analysed by PEÑA SUÁREZ ET AL. (2018) (diamonds) and KATIME SANTRICH ET AL. (2013) (circle). A similar fact was observed by DRAZDAUSKAS ET AL. (2016) in their study of clusters NGC 4609 and NGC 5316, with $M_{turn-off}$ values similar to NGC 2345.

Other elements: Na to Ni

Figs 7.12 and 7.13 show the abundances of the elements from sodium to nickel for the giant stars of the NGC 2345 in comparison with field stars. The mean abundance found for [Na/Fe] by REDDY ET AL. (2016) is close to our result. For example, we determined the mean abundance of $+0.27 \pm 0.12$, while REDDY ET AL. (2016) estimated at $+0.18 \pm 0.02$. Sodium is also an element sensitive to the first dredge-up and other extra-mixing processes, especially in intermediate-mass stars (for the Galactic disc metallicities). Fig. 7.14 shows the theoretical models by LAGARDE ET AL. (2012) for the first dredge-up for a standard stellar evolutionary model (solid line) and thermohaline mixing and rotation-induced mixing model (dashed line). Similar to the $^{12}C/^{13}C$ isotopic ratio, the value found for sodium-over-iron approximates to the standard stellar evolutionary model at first dredge-up and shows less agreement with the prediction given by

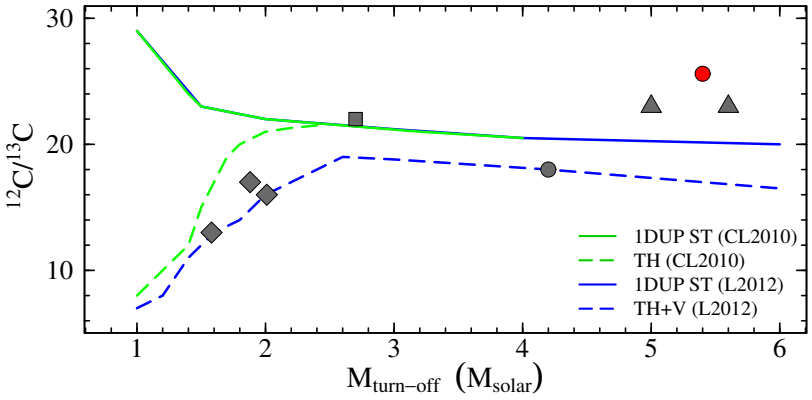

Figura 7.11: $^{12}C/^{13}C$ versus $M_{turn-off}$ in clump stars of open clusters. NGC 2345 is represented by red circle. The grey triangles represent the mean of the $^{12}C/^{13}C$ ratio for NGC 4609 and NGC 5316 DRAZDAUSKAS ET AL. (2016), the grey circle for NGC 3114 KATIME SANTRICH ET AL. (2013), the grey square for NGC 2447 (DA SILVEIRA ET AL., 2018), and the grey diamonds for NGC 2360, NGC 3680, and NGC 5822 (PEÑA SUÁREZ ET AL., 2018). The solid green and blue lines represent the $^{12}C/^{13}C$ isotopic ratio predicted for giants at first dredge-up with standard evolutionary models for solar metallicity calculated, respectively, by CHARBONNEL & LAGARDE (2010) and LAGARDE ET AL. (2012). The green dashed line represents the prediction for thermohaline extra-mixing calculated by CHARBONNEL & LAGARDE (2010). Finally, the blue dashed line represents the prediction for thermohaline and rotation-induced mixing calculated by LAGARDE ET AL. (2012).

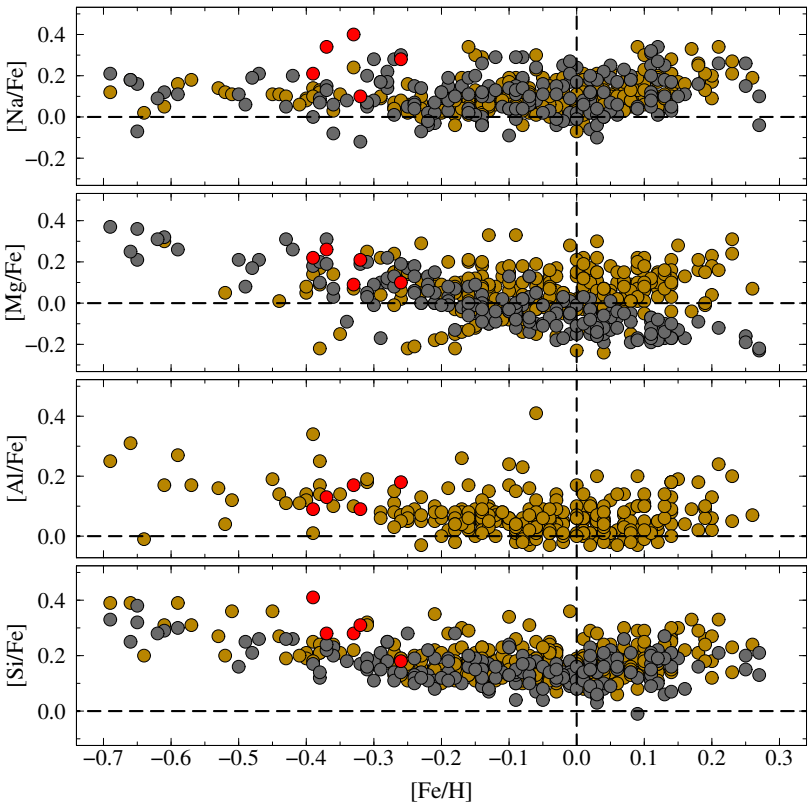

Figura 7.12: Abundance ratios [X/Fe] versus [Fe/H] for the elements from Na to Si. Symbols have the same meaning as in Fig. 7.10.

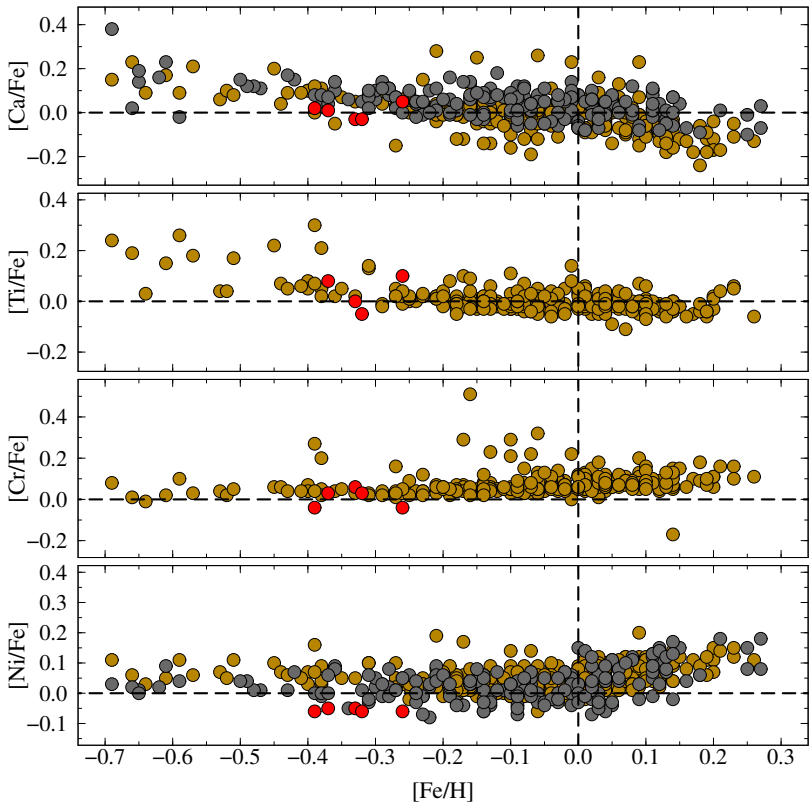

Figura 7.13: Abundance ratios [X/Fe] versus [Fe/H] for the elements from Ca to Ni. Symbols have the same meaning as in Fig. 7.10.

thermohaline and rotation-induced mixing.

The mean of α-elements over iron, defined as $[\alpha/\mathrm{Fe}] = \frac{1}{4}([\mathrm{Mg\,I/Fe}]+[\mathrm{Si\,I/Fe}]+[\mathrm{Ca\,I/Fe}]+[\mathrm{Ti\,/Fe}])$ for the five giants, is $+0.14 \pm 0.05$ (Table 7.4). This result is in agreement with local disc field giants. Comparatively, the mean value for the $[\alpha/\mathrm{Fe}]$ ratio for the stars of thin disc and with metallicities between -0.3 and -0.4 is $+0.12 \pm 0.05$ (LUCK & HEITER , 2007).

We could not obtain the abundance of titanium in NGC 2345-60 due to severe blending of the lines, which made the determination of this abundance very uncertain. Also, due to this exclusion this star presents high abundance in α-elements. For [Al/Fe], we also find the typical value for disc field giants from LUCK & HEITER (2007) in the same metallicity range.

We also observed a low abundance of the iron-peak elements, a fact that was already expected due to low metallicity of the open cluster NGC 2345. The abundance ratios [Cr/Fe] and [Ni/Fe] follow the same trend with iron abundance ([X/Fe] is close to zero). In addition also, a low [Ni/Fe] ratio was found, below the pattern found by LUCK & HEITER (2007) for objects with the same metallicity but still within the observed pattern for red clump giants studied by MISHENINA ET AL. (2006). The average of [Ni/Fe] for our giants is -0.06 $\pm$ 0.01, which is very close to that found by REDDY ET AL. (2016) for a smaller number of stars (-0.07 $\pm$ 0.02).

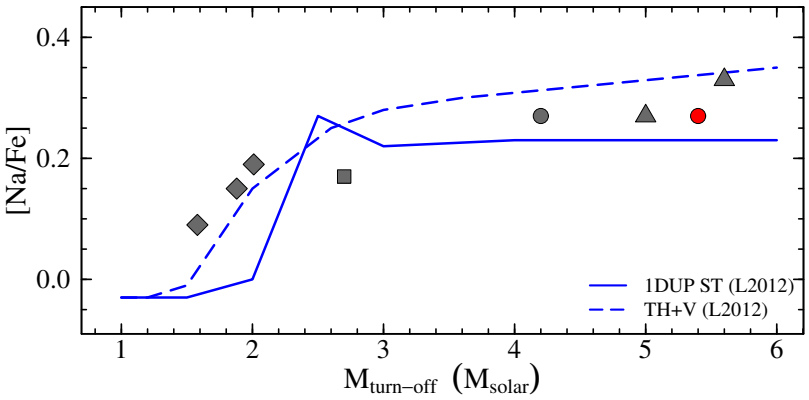

Figura 7.14: Mean [Na/Fe] ratio versus $M_{turn-off}$ for NGC 2345 (red circle) and open cluster of literature. The symbols and models LAGARDE ET AL. (2012) compared have the same meaning as those in Fig. 7.11. However, it is worth nothing that the sodium abundances used for KATIME SANTRICH ET AL. (2013) and DRAZDAUSKAS ET AL. (2016) were determined via NTLE.

Tabela 7.7: Abundance ratios [X/Fe] for the elements from sodium to nickel for NGC 2345 determined in this work in comparison with the same elements analyzed by REDDY ET AL. (2016). The mean presented by REDDY ET AL. (2016) was based on the abundances of the stars #34, #43 and #60.

Species	This work	REDDY ET AL. (2016)
[Na I/Fe]	+0.27 ± 0.12	+0.18 ± 0.02
[Mg I/Fe]	+0.18 ± 0.08	+0.05 ± 0.03
[Al I/Fe]	+0.13 ± 0.04	+0.03 ± 0.02
[Si I/Fe]	+0.29 ± 0.08	+0.25 ± 0.02
[Ca I/Fe]	+0.00 ± 0.04	−0.13 ± 0.03
[Ti I/Fe]	+0.03 ± 0.07	−0.06 ± 0.02
[Cr I/Fe]	+0.01 ± 0.04	−0.01 ± 0.02
[Fe I/H]	−0.33 ± 0.05	−0.26 ± 0.03
[Fe II/H]	−0.33 ± 0.06	−0.26 ± 0.03
[Ni I/Fe]	−0.06 ± 0.01	−0.07 ± 0.02

Finally, we present in Table 7.7 a comparison between the abundances determined by REDDY ET AL. (2016) and our results. In general, the discrepancy is small, since the mean difference between the two works is 0.05 ± 0.07.

Heavy elements: the neutron-capture elements

Fig. 7.15 shows the abundance ratios ([X/Fe]) for the s-process elements for the giants of NGC 2345 in comparison with the same elements studied by LUCK & HEITER (2007) and MISHENINA ET AL. (2006). We also show the mean abundance of the s-process elements as defined in Section 7.3.2 for NGC 2345 and for the two samples of field giant stars above mentioned. Fig. 7.15 shows that NGC 2345 presents a small enrichment of the mean s-process abundances compared to the field giant stars. In this context, we denote

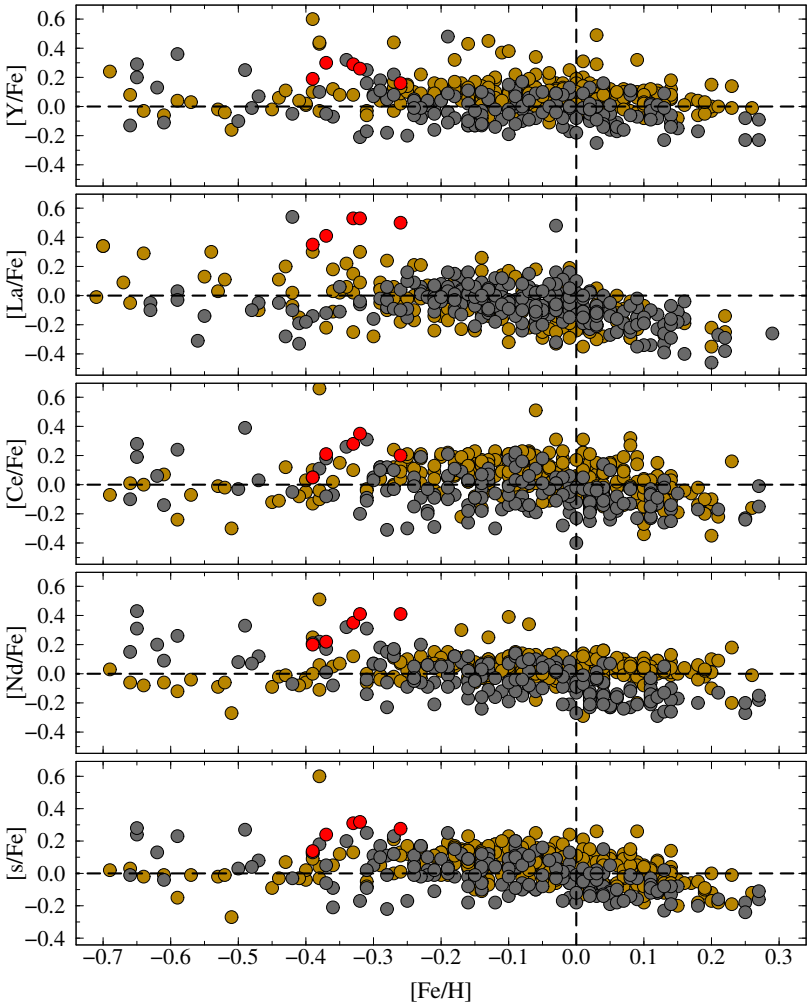

Figura 7.15: Abundance ratios [X/Fe] versus [Fe/H] for the elements from Y to Nd. The bottom frame is the mean value of the s-elements, [s/Fe]. Symbols have the same meaning as in Fig. 10.

that young open clusters are not only more s-process enriched than older open clusters, as first noticed by MAIORCA ET AL. (2012), but are also more enriched the field stars.

The top panels in Fig. 7.16 show samarium and europium abundances of the giants analysed in this work in comparison with the dwarfs and subgiants analysed by Luck (2017) (for samarium) and with the field giants analysed by LUCK & HEITER (2007) and MISHENINA ET AL. (2006) (for europium). The abundances of samarium and europium are in good agreement with the sample of LUCK & HEITER (2007) and MISHENINA ET AL. (2006), respectively. The bottom panel of Fig. 7.16 shows the mean europium abundance of NGC 2345 and the mean europium abundance of other open clusters analysed in other works. The abundance of europium in NGC 2345 is in agreement with the results found in literature, despite the small amount of data for low metallicities (i.e. [Fe/H] $<$ -0.25). For this comparison, we compiled data from ZAČS ET AL. (2011), JACOBSON & FRIEL (2013), REDDY ET AL. (2016, 2012, 2013, 2015), DRAZDAUSKAS ET AL. (2016), and OVERBEEK ET AL. (2016).

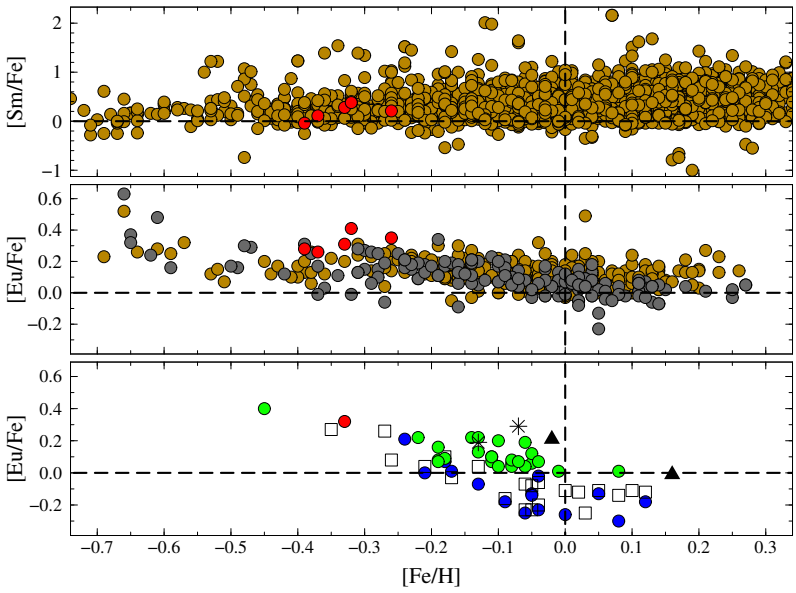

Figura 7.16: Samarium- and europium-over-iron versus iron abundances for field stars (top panels) and open clusters from other studies (bottom panel) for the average [Eu/Fe] abundances. In top panels, we present data from Luck (2017) and Luck & Heiter (2007) (yellow) and Mishenina et al. (2006) (grey). In bottom panel open squares were taken from Jacobson & Friel (2013), green filled circles from REDDY ET AL. (2016, 2012, 2013, 2015), blue filled circles from OVERBEEK ET AL. (2016), black triangles from DRAZDAUSKAS ET AL. (2016), and asterisks from ZAČS ET AL. (2011).

Table 7.8 shows individual abundances for comparison purposes with REDDY ET AL. (2016) results. Larger discrepancies occur in the abundances of heavy elements (mean difference of 0.20 ± 0.14). We assign this discrepancy to the number of lines used, uncertainty in determining the continuum, and different atmospheric parameters. Nevertheless, the giants analysed here have a similar abundance profile to those of the red clump stars analysed by MISHENINA ET AL. (2006).

7.5 Conclusions

The main conclusions of our abundance analysis employing high-resolution optical spectra of the five giants of the open cluster NGC 2345 can be summarized as follows.

- NGC 2345 is a very young open cluster with a turn-off mass of 5.4 ± 0.15 $M_{\odot}$. The metallicity for this open cluster is low ([Fe/H] = -0.33) for its Galactic latitude (-02°.31). Compared to other massive clusters of similar age, such as NGC 1545 (ZAČS ET AL., 2011) and NGC 5316 (DRAZDAUSKAS ET AL., 2016), NGC 2345 still appears peculiar in its metallicity. This was confirmed by analysis of the radial gradient of metallicity, where NGC 2345 stands out together with another very young cluster, NGC 3105 (28 Myr; ALONSO-SANTIAGO ET AL., 2018).

Tabela 7.8: Comparison of the heavy-element abundance ratios [X/Fe] for NGC 2345 derived in this study work and in REDDY ET AL. (2016). The values in REDDY ET AL. (2016) are based on the abundances of stars #34, #43, and #60.

Species	This work	REDDY ET AL. (2016)
[Y II/Fe]	+0.24 ± 0.06	+0.16 ± 0.02
[Zr I/Fe]	+0.04 ± 0.08	−0.05 ± 0.03
[La II/Fe]	+0.46 ± 0.08	+0.01 ± 0.02
[Ce II/Fe]	+0.22 ± 0.11	+0.02 ± 0.02
[Nd II/Fe]	+0.32 ± 0.10	+0.03 ± 0.02
[Sm II/Fe]	+0.19 ± 0.16	+0.12 ± 0.02
[Eu II/Fe]	+0.32 ± 0.06	+0.12 ± 0.05

- We determined rotational velocities for all the known giants of NGC 2345 using spectral synthesis method. NGC 2345 - 34 presents high projected rotational velocity ($v \sin i = 10.1\,\mathrm{km\,s^{-1}}$) that can be attributed to a well-known binarity of this star, evidenced here by its radial velocity compared to the other reports from the literature. In addition, we noticed a scarcity a lithium abundance determination for giants in massive clusters, those with low log g.

- The abundance of sodium and the $^{12}C/^{13}C$ isotopic ratio found for NGC 2345 are similar to the values predicted by the standard models by LAGARDE ET AL. (2012). The values found for these mixing tracers are also very close to that of reported by DRAZDAUSKAS ET AL. (2016) in their study of clusters NGC 4609 and NGC 5316 of similar turn-off masses.

- Finally, the results for C and N for the five giants show a post-first dredge-up profile. Furthermore, there is good agreement between our results and those presented by MISHENINA ET AL. (2006) for abundances of the n-capture elements in red clump giants.

Capítulo 8

As gigantes do aglomerado aberto NGC 6124

Neste trabalho, nós apresentamos resultados de uma análise química de rotadores rápidos e anômalos nascidos no jovem aglomerado aberto NGC 6124. Para tal, nós levantamos abundâncias de espécies sensíveis aos processos de mistura como Li, C, N, Na e a razão isotópica $^{12}C/^{13}C$, bem como outras espécies químicas para uma amostra de quatro gigantes vermelhas entre as sete estrelas que foram observadas desse aglomerado. Este estudo é baseado na análise espectroscópica padrão usando espectros de alta resolução. Nós também realizamos um estudo da velocidade rotacional projetada onde esta amostra exibe valores incomuns – estrelas gigantes comumente apresentam velocidade rotacional de poucos $km\,s^{-1}$. Em paralelo, nós realizamos um estudo de pertencimento, graças ao segundo *data release* da Missão Gaia da Agência Espacial Europeia (ESA – acrônimo do inglês). Baseado nesses dados, nós estimamos a distância de 641 pc, um avermelhamento de 0.82 e uma idade de 141 milhões de anos através do ajuste de isócronas. Após esse procedimento, nós combinamos todas as informações levantadas e investigamos os estágios evolucionários e modelos de mistura, como a termohalina, através da temperatura efetiva espectroscópica e gravidade superficial e elementos traçadores de mistura, como $^{12}C/^{13}C$ e Na, das estrelas estudadas. Nós derivamos uma metalicidade média de -0.20 e um ligeiro enriquecimento de elementos criados no processo-s, tais como Y, Zr, La, Ce e Nd, que está em acordo com o que é conhecido hoje na literatura sobre aglomerados abertos. Finalmente, nós investigamos uma possível correlação entre a rotação estelar e a idade das gigantes pertencentes a aglomerados abertos com dados disponíveis na literatura.

Este capítulo refere-se aoartigo em preparação para submissão no jornal Monthly Notices of the Royal Astronomical Society: **Holanda, N., Drake, N. A., Magrini, L., da Silva, J. R. P., & Pereira, C.B., 2021 (paper 4)**.

8.1 Introduction

Open clusters are numerous and are distributed throughout the Galactic disk. In particular, when we investigate the red giant population of open clusters by combining information from mixing tracers (Li, C, N, O, $^{12}C/^{13}C$, and Na) and heavy elements, we can obtain a privileged perspective on the life story of evolved cluster stars and, as a consequence, useful tests for the chemical evolution of the Galactic disk and stellar evolution models (HEITER ET AL., 2014; BÖCEK TOPCU ET AL., 2016). Though, the rotation effects in the abundances from these red giants with anomalous ($\geqslant 6\,\mathrm{km\,s^{-1}}$) and high ($\geqslant 8$–$10\,\mathrm{km\,s^{-1}}$) projected rotational velocity is still rarely discussed in the literature.

When the stars ascend to the red giant branch (RGB) they experiment a significant expansion, which allows us to expect a low surface rotation as conservation of angular momentum in these objects – the mean rotational velocity for G and K giants is about $2\,\mathrm{km\,s^{-1}}$ (DE MEDEIROS ET AL., 1996). Concerning to exceptions, CARLBERG ET AL. (2011) used a sample of 1297 spectral type K giants for a study of rotation and reported the discovery of 28 rapidly rotating giants, with the projected rotation speeds between 10.0 and $86.4\,\mathrm{km\,s^{-1}}$, which represents 2.2% of all their sample. In this sense, giants stars with high projected rotational velocities are rare and a challenge for astrophysics, yet.

When studying 761 red giant stars neighborhood to the Sun, MASSAROTTI ET AL. (2008) reported evidences to support that the first dredge-up may play a role increase of the rotation of the observable outer layers of giants, hypothesis originally raised by SIMON & DRAKE (1989) for explain rapidly rotating giants. On other hand, some references argue that coalescence of close binary systems and interactions followed by engulfment of a planet or (sub)companion may act as external sources of origin these rapid rotators (CARLBERG ET AL., 2009; PETERSON ET AL., 1983; PRIVITERA ET AL., 2016; SIESS & LIVIO, 1999a).

With regard to open clusters, CARLBERG (2014) found that the red clump stage presents more incidence of rapid rotator stars between a sample of 11 intermediate age open clusters, i.e., it confirms that intermediate mass stars have a higher dispersion in their rotational velocities. Additionally, the authors present results for the open cluster Pismis 18 – with age estimated between 0.7 Gyr (HATZIDIMITRIOU ET AL., 2019) and 1.2 Gyr (PIATTI ET AL., 1998)–, which shows a high mean for rotational velocity of their giants. Thereafter, DELGADO MENA ET AL. (2016) carry out a robust analysis of a sample composed by 67 red giant stars in 12 different open clusters based on high-resolution spectroscopy. Essentially, DELGADO MENA ET AL. determined the stage of their sample, based on stellar parameters, and discuss the possible scenario of formation of Li-rich stars in their sample – the projected rotational velocity has been investigate in the framework of the association between high $v \sin i$ values and engulfment of planets and sub-stellar companions that also may cause overabundance in lithium in its atmosphe-

res. Furthermore, the investigation of projected rotational velocity can reveal important aspects concerning to the internal stellar structure, magnetic activity, tidal interactions, and consequently the stellar evolution (CARLBERG ET AL., 2011; DEHEUVELS ET AL., 2015), topics that are often invoked in the discussion of lithium-rich giant stars.

In this context, NGC 6124 is a young open cluster with a mass of about 352 $M_{\odot}$ (PISKUNOV ET AL., 2008) and, so far, it has not been studied from the chemical perspective. Located in Scorpius region (ℓ, b) = (340°.74, +06°.02), its distance was estimated for diverse sources in the literature with different values: 435 pc KOELBLOED (1959), 470 pc (KHARCHENKO ET AL., 2005), 512 pc (DIAS ET AL., 2002), 631 pc (SOUBIRAN ET AL., 2018). This cluster seems to contains eight red giant stars, of which two are spectroscopic binaries (#29 and #33), with orbits determined by MERMILLIOD ET AL. (2008), and a visual binary star (#36) with a companion of magnitude V = 14.2 reported by WORLEY & DOUGLASS (1996). Among them the binary star #33 is pointed by THE (1965) and VERGNE ET AL. (2010) as suspected as a not member of the cluster. We carried out a study based of seven these eight giant stars (excluded the NGC6124-41 star), which are ordered as follow: in Sect. 8.2 we describe the data and their analysis. After, in Sect. 8.3 we present our results for abundances and compare with field stars and mixing models and models predicted by galactic chemical evolution. In addition, we investigate the possible correlations between v sin i, Age and Li abundance. Finally our conclusions are given in Sect. 8.4.

8.2 Observations and Analysis

8.2.1 Spectroscopic data

The observations were carried out using the Fiber-fed Extended Range Optical Spectrograph (FEROS; KAUFER ET AL., 1999) at the 2.2 m Max Planck Gesellschaft/European Southern Observatory (ESO) Telescope in La Silla, Chile. The FEROS spectra have a resolution $R \equiv \lambda/\delta\lambda \approx 48000$ within the spectral coverage of 3600 – 9200 Å. The exposure time of our high-dispersion ranges from 1200 to 1500 seconds to achieve a typical signal-to-noise ratio of 150 to 200. Furthermore, the FEROS Data Reduction System pipeline was used to reduced all spectra. The program stars, like those previously investigated (DA SILVEIRA ET AL., 2018; HOLANDA ET AL., 2019; MARTINEZ ET AL., 2020; PEÑA SUÁREZ ET AL., 2018; SALES SILVA ET AL., 2014), were selected based on the radial velocity survey done by MERMILLIOD ET AL. (2008).

In these recent works we studied the chemical nature and accentuated aspects related to binarity, peculiarity and stellar and chemical evolution of the Galactic disk through the analysis of the open clusters. Here, we present a similar approach for the seven giants of which the basic information is present in Table 8.1 – such as the spectral type given

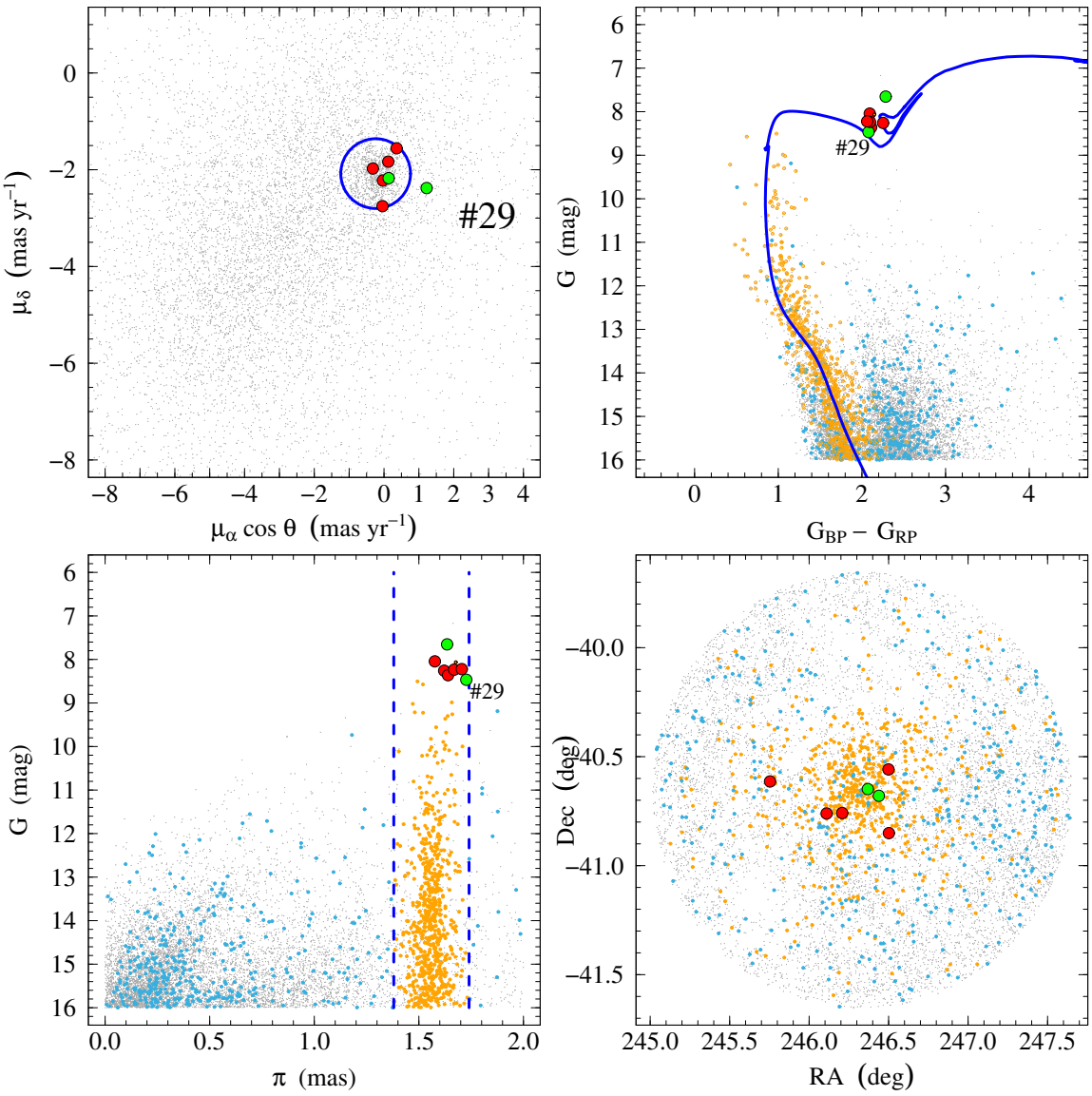

Figura 8.1: Proper motion distribution for stars brighter than $G = 16$ mag with up to 1 deg around of the center of NGC 6124 (Top left), where the blue circle ($R = 1.0$ mas yr^{-1}) delimits the region of belonging to the cluster. (Bottom left) Magnitude versus parallaxes with highlight for star inside the circle denoted at vector-point diagram (blue and yellow points), where blue dashed lines delimit the parallax typical for this open cluster. Color-magnitude diagram (top right) is shown with a isochrone fitting (BRESSAN ET AL., 2012) for stars with proper motions and parallaxes characteristics of the cluster and NGC 6124-29 giant. Bottom right represents the spatial distribution of stars around the NGC 6124 region. The stars analyzed in this work are represented by red and green (spectroscopic binaries) points. Data were taken from GAIA COLLABORATION ET AL. (2018).

by HOUK (1978) and NESTEROV ET AL. (1995), the visual magnitude and the (B−V) color and the radial velocities given in MERMILLIOD ET AL. (2008) (fifth column) and GAIA COLLABORATION ET AL. (2018) (sixth column).

8.2.2 Membership determination

In order to complement the spectroscopic data, we used the astrometric and photometric data from the the ESA *Gaia* Mission – parallaxes, proper motions, and photometry (G, $G_{\rm BP}$ and $G_{\rm RP}$). Data from ESA *Gaia* Mission were used to investigate for a membership analysis and to estimate the distance module, reddening, age, and turn-off mass, with similar method adopted by SUN ET AL. (2019a,b). Figure 8.1 presents a complete overview about the method that we have implemented: the vector point diagram for brightest stars around of the center of NGC 6124 (top left), magnitude versus parallaxes (bottom left), color-magnitude diagram with a isochrone fitting (top right), and the spatial distribution of stars in the cluster region (bottom right). The giant stars analyzed in this work is represented by red circles (single stars or members in wide binaries) while green circles represent spectroscopic binaries.

We considered the limits $G < 16.0$ and $\pi \leqslant 2.0$ and find a overdensity centered at (pmRA, pmDEC) $\approx (-0.24,-2.08)$ mas yr^{-1}, which became our reference to define the region where the cluster NGC 6124 belongs. After that cut, we calculated the membership-radius (i.e., the distance to center cluster's for stars that are member of NGC 6124) that can be defined by $\mathrm{pm_R} \equiv \sqrt{(\mathrm{pmRA} - \langle\mathrm{pmRA}\rangle)^2 + (\mathrm{pmDEC} - \langle\mathrm{pmDEC}\rangle)^2}$. Visually based on the shape and extent of the overdensity, we define a circle with $\mathrm{pm_R} = 1.0$ for stars with similar proper motion (yellow and blue points). In the π versus G diagram we identified a new density centered at $\pi = 1.56$ mas, that define the parallax to cluster. After establishment the upper and lower limits for parallax, we highlighted the true members with yellow color, while blue points consists in false-positive members. Subsequent plots reinforce the quality of this segregation and showed the homogeneous behavior of the yellow points in two different ways. The giant NGC 6124-29 is highlighted which has a proper motion slightly different from the other stars that belong to the cluster (a discussion about this behavior is given in Section 8.3.3).

In the isochrone fitting to determine the age, we found a module of distance of $G - M_G = 10.70$ and a color excess of $E(G_{BP} - G_{RP}) = 1.05$ – this last one correspond to $E(B-V) = 0.82$, which is very good agreement with the average $E(B-V) = 0.80$ found by VERGNE ET AL. (2010). These values were found through vertical and horizontal variations until a simultaneous adjustment of the main-sequence, turn-off, and RGB clump. In this procedure, the tables taken from PAdova and TRieste Stellar Evolution Code (PARSEC: BRESSAN ET AL., 2012) were transformed to *Gaia* photometry through the polynomials of JORDI ET AL. (2010). After all, this procedure confirms

Tabela 8.1: Basic information of the observed stars in NGC 6124. The data were taken from HENDEN ET AL. (2015)[a], HOUK (1978)[b], NESTEROV ET AL. (1995)[c], MERMILLIOD ET AL. (2008)[d], GAIA COLLABORATION ET AL. (2018)[e], and WORLEY & DOUGLASS (1996)[f]. Remarks reefers to single (S), spectroscopic binary one-lined (SB1), and visual double star (VD).

Star	Type	V[a]	(B−V)[a]	RV[d]	RV[e]	RV	$v \sin i$	Observation date	Exp	Remark
		mag	mag	$\mathrm{km\,s^{-1}}$	$\mathrm{km\,s^{-1}}$	$\mathrm{km\,s^{-1}}$	$\mathrm{km\,s^{-1}}$		s	
#1	G6/K0[b]	9.111	1.682	−21.60	−20.71	−19.97 ± 1.32	16.5	2016 Mar 18	1200	S
#14	K0[b]	9.207	1.750	−21.60	−20.40	−20.40 ± 0.27	6.8	2016 Mar 19	1200	S
#29	—	9.319	1.729	−21.17	−22.22	−16.19 ± 0.65	9.7	2016 Mar 20	1500	SB1[d]
#33	M0[c]	8.651	1.923	−20.89	−42.41	−9.33 ± 2.26	26.4	2016 Mar 20	1500	SB1[d]
#35	G5/6[b]	9.040	1.678	−18.97	−18.53	−17.31 ± 2.18	19.5	2016 Mar 20	1500	S
#36	G2/3[b]	9.217	1.840	−21.42	−20.82	−21.23 ± 0.22	6.5	2016 Mar 20	1500	VD[f]
#233	K0[c]	8.893	1.762	−21.69	−22.55	−22.68 ± 0.43	6.2	2016 Mar 20	1200	S

Tabela 8.2: NGC 6124 cluster parameters.

Right ascension (J2000)	16 25 20	WU ET AL. (2009)
Declination (J2000)	-40 39 12	WU ET AL. (2009)
log t (Gyr)	8.15	This work
d (pc)	641	This work
$R_{\rm GC}$ (kpc)	7.35	This work
$E(B-V)$ (mag)	0.82	This work
$E(G_{\rm BP}-G_{\rm RP})$ (mag)	1.05	This work
$V-M_V$ (mag)	11.49	This Work
$G-M_G$ (mag)	10.70	This Work
$\rm M_{turn-off}$ ($M_\odot$)	3.95	This work

Tabela 8.3: Determined spectroscopic atmospheric parameters for the giant stars of NGC 6124.

Star	$T_{\rm eff}$ (K)	log g cm s^{-2}	ϵ (km s^{-1})	[Fe I/H] $\pm\sigma$	[Fe II/H] $\pm\sigma$	$T_{\rm eff}^{(B-V)}$ (K)	log g^{phot} cm s^{-2}
#1	—	—	—	—	—	4930	1.80
#14	4 600	1.65	1.88	-0.22 ± 0.15	-0.22 ± 0.10	4780	1.76
#29	4 700	2.05	1.97	-0.18 ± 0.12	-0.19 ± 0.13	4833	1.83
#33	—	—	—	—	—	4482	1.36
#35	—	—	—	—	—	4939	1.78
#36	4 820	1.75	2.40	-0.19 ± 0.11	-0.18 ± 0.11	4625	1.68
#233	4 860	1.70	2.26	-0.22 ± 0.11	-0.23 ± 0.06	4756	1.62

the best-fit around of log t = 8.15 (or 141 Myr) isochrone. The dispersion of stars in the main-sequence and turn-off stage in our adjustment can be a contribution of high rotation and binarity. These aspects are widely discussed for massive and intermediate clusters in SUN ET AL. (2019a,b) and was not addressed in this work. The basic parameters of NGC 6124 are given in Table 8.2.

8.2.3 Atmospheric parameters

The atmosphere parameters for the giants (#14,#29,#36, and #233) in NGC 6124 were obtained by employing interpolation within KURUCZ (1993) grid, where it was considered local thermodynaminal equilibrium plane-parallel atmospheric models. We adopted neutral and ionised iron lines and its respective log gf and excitation potential (χ) that were taken from LAMBERT ET AL. (1996) (Table A.5). Essentially, this list is formed by lines carefully chosen for the purpose of eliminated blending lines and reduce potential contamination by molecular bands that are formed naturally in cool giant atmospheres. In conjunction with this, we used IRAF[1] to measure the equivalent widths (EW) using the Gaussian fit with the task SPLOT. After that, the spectral analysis code MOOG (2013

[1]The Image Reduction and Analysis Facility is written and supported by the National Optical Astronomy Observatories (NOAO). Available at http://iraf.noao.edu/

version; SNEDEN, 1973) was used for the determination of the stellar atmospheric parameters and abundances of the interest chemical species.

The atmospheric parameters were determined following the three steps: (i) the effective temperature ($T_{\rm eff}$) was obtained by imposing the condition that the abundance of Fe I lines[2] does not depend on the lower-level excitation potential; (ii) the microturbulence velocity (ξ) was found requiring that the abundance of Fe I lines does not depend on the reduced equivalent width (EW/λ); (iii) also, the surface gravity ($\log g$) was found from the iron ionization equilibrium of Fe I and Fe II. Steps (i) and (ii) can be verified through the slopes of linear adjustment of both cases with values close to zero. In this research we adopt an absolute limit of 0.006 for each slope coefficients and applied a $2\,\sigma$ clipping rejection for these iron lines. The fundamental parameters product of this method are given in Table 8.3.

The uncertainties in the atmospheric parameters, effective temperature and microturbulent velocity, it were estimated from the uncertainties in the slopes of relationships described before. The standard deviation in the abundance of Fe I was used to provide the uncertainty in the $\log g$ parameter. In general, we found typical uncertainties in the temperature, microturbulent velocity, surface gravity of $\sigma(\mathrm{T}_{eff}) = \pm 90\,\mathrm{K}$, $\sigma(\xi) = \pm 0.2\,\mathrm{km\,s^{-1}}$, and $\sigma(\log\, g) = \pm 0.1$.

Furthermore, it was not possible to apply the described method to all spectra obtained in our observational mission, since three stars (#1, #33, and #35) have very high $v \sin i$ (Table 8.1). Figure 8.2 shows absorption profile lines around the Hα line for our sample of stars. That said, we have used the atmosphere models based on iron abundance of -0.20 (the mean of four giants with equivalent width measured), microturbulence velocity of $2.0\,\mathrm{km\,s^{-1}}$, and photometric $\log g$ and $T_{\rm eff}$ for these stars. We adopted the polynomials found by GONZÁLEZ HERNÁNDEZ & BONIFACIO (2009) for fitting $(B-V)$ color as function of $T_{\rm eff}$ and for photometric gravity we applied the well-know expression:

$$\log g_\star = \log\left(\frac{M_{\rm turn-off}}{M_\odot}\right) + 0.4\,(V - A_V + BC_V) + 4\,\log T_{\rm eff} - 2\,\log r\,(\mathrm{kpc}) - 16.5,$$

where V, A_V, and $BC_{\rm V}$ are respectively the visual magnitude, interstellar absorption in V band and bolometric correction. The surface gravity, mass, and temperature of the star are, respectively, $\log g_\star$, $M_\star$ and $T_{\rm eff}$ and r is the heliocentric distance of the open cluster given in kpc. The Solar values used in this expression are $M_{\rm bol} = 4.75$, $\log g = 4.44$, and $T_{\rm eff} = 5777\,\mathrm{K}$, as well the bolometric corrections were calculated using the relation given in ALONSO ET AL. (1999). The corresponding mean difference in $T_{\rm eff}^{(B-V)}$ with respect to spectroscopic $T_{\rm eff}$ is $+4 \pm 182\,\mathrm{K}$ and in $log\, g^{phot}$ with respect to

[2] All abundances in the notation: $[\mathrm{X/H}] = \log(\mathrm{N_X/N_H})_\star - \log(\mathrm{N_X/N_H})_\odot$

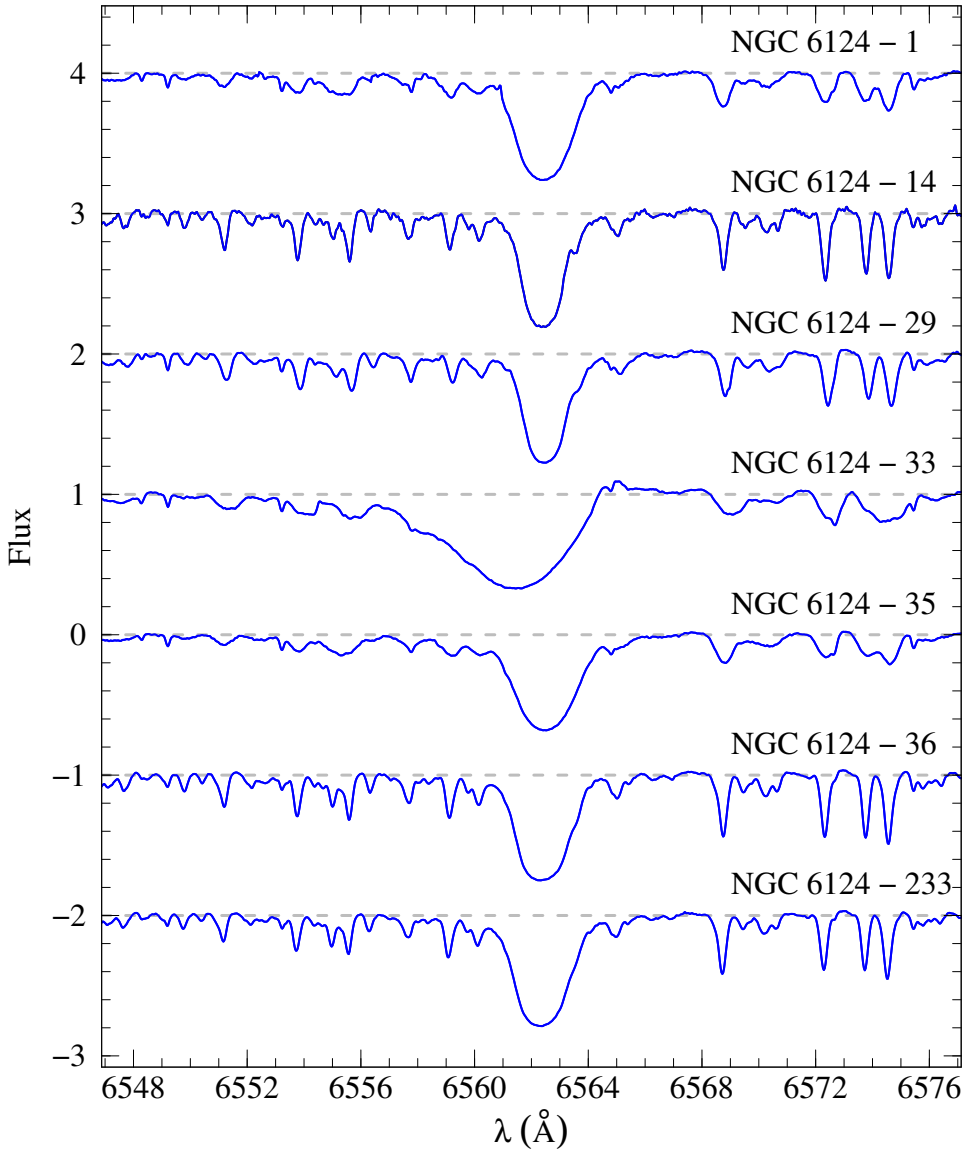

Figura 8.2: Observed spectra in the region Hα of the giants of NGC 6124.

spectroscopic log g is $-0.07 \pm 0.14\,\mathrm{cm/s^2}$.

8.2.4 Abundance determination

As said before, we have used both equivalent widths and spectrum synthesis for the abundance analysis. We measured the equivalent widths of the elements Na, Mg, Al, Si, Ca, Ti, Cr, Ni, Y, Ce, Nd, and Sm in order to obtain their abundances. The line list used is given in Table A.6, with their respective excitation potentials (χ) and log gf (SALES SILVA ET AL., 2014 and references therein). All lines were inspected in order to avoid the blending between lines, hence the final line list differs slightly from star to star.

The abundances of lithium, carbon and nitrogen, the $^{12}C/^{13}C$ isotopic ratio and europium were determined in the same way as in HOLANDA ET AL. (2019), except for lanthanum that was studied by the spectral synthesis here. Unfortunately, we could not

obtain the oxygen abundance based on the forbidden line at λ6300Å because of the contamination with telluric O_2 lines. Also, the line at [O I] 6363 Å is unsuitable because it is weak and contaminated by a CN line. Knowing this, we assumed a [O/Fe] ratio of +0.12 for estimate abundances other light elements, since occurs a interdependence between them.

The carbon abundance was determined using the C_2 (0,1) band head of the Swan system $A^3\Pi_g - X^3\Pi_u$ at 5 635 Å – where the wavelengths were taken from PHILLIPS & DAVIS (1968), the electron oscillator strength from LAMBERT (1978), and the C_2 dissociation energy from HUBER & HERZBERG (1979) –, while the nitrogen abundance and $^{12}C/^{13}C$ were obtained by adjusting the theoretical and observed spectra for the ^{12}CN lines of the (2,0) band of the CN red system $A^2\Pi - X^2\Sigma$ in the 8004 Å region – the wavelengths for ^{12}CN and ^{13}CN were taken from DAVIS & PHILLIPS (1963) and WYLLER (1966), the oscillator strength from SNEDEN & LAMBERT (1982), and the CN dissociation energy from SNEDEN & LAMBERT (1982) and BAUSCHLICHER ET AL. (1988). DRAKE & PEREIRA (2008) provide details about the atomic parameters used in the construction of the input files for the spectral synthesis.

The lithium abundance was determined by spectral synthesis of the resonance λ6708 Å line. We taken the wavelengths and oscillator strengths from SMITH ET AL., 1998 and HOBBS ET AL. (1999) and assumed an isotopic ratio $^6Li/^7Li = 0.0$. After finding ^7Li abundance under LTE conditions, we performed corrections for NLTE effects based on the LIND ET AL. (2009) grids. Both results are shown in Table 8.4, where we can note that there was an increase in abundance for this element if we consider the NLTE effects in λ6708 Å line. In addition to lithium, we also consider corrections for NLTE effects for the sodium lines analyzed in this work – Na 4752λ, 5149λ, 6154λ, and 6161λ lines – according to the grids computed by LIND ET AL. (2011). For corrections related to sodium abundance, there was a decrease in abundance in all the lines measured and our results are shown in Table 8.5.

We determined lanthanum abundance in our sample based on synthesis of 5114 Å, 5303 Å,and 5880 Å lines, whose input files were constructed based on data taken from the Vienna Atomic Line Database (VALD; KUPKA ET AL., 1999). Further, the europium abundances were obtained via synthetic spectra at λ6645.13 Å. In the procedure to determine europium abundance in this line was used the atomic parameters by LAWLER ET AL. (2001) and final result of the calculations for hyperfine splitting was taken from MUCCIARELLI ET AL. (2008), since this line shown a significant hyperfine structure contribution.

As an example of the spectral synthesis method used in the work, we show Figure 8.3, where there is a comparison between the theoretical spectrum (solid lines) and the observed spectrum (gray dots). Our best-fits are represent by red solid line.

All abundances, those obtained by measuring the equivalent widths and those obtained

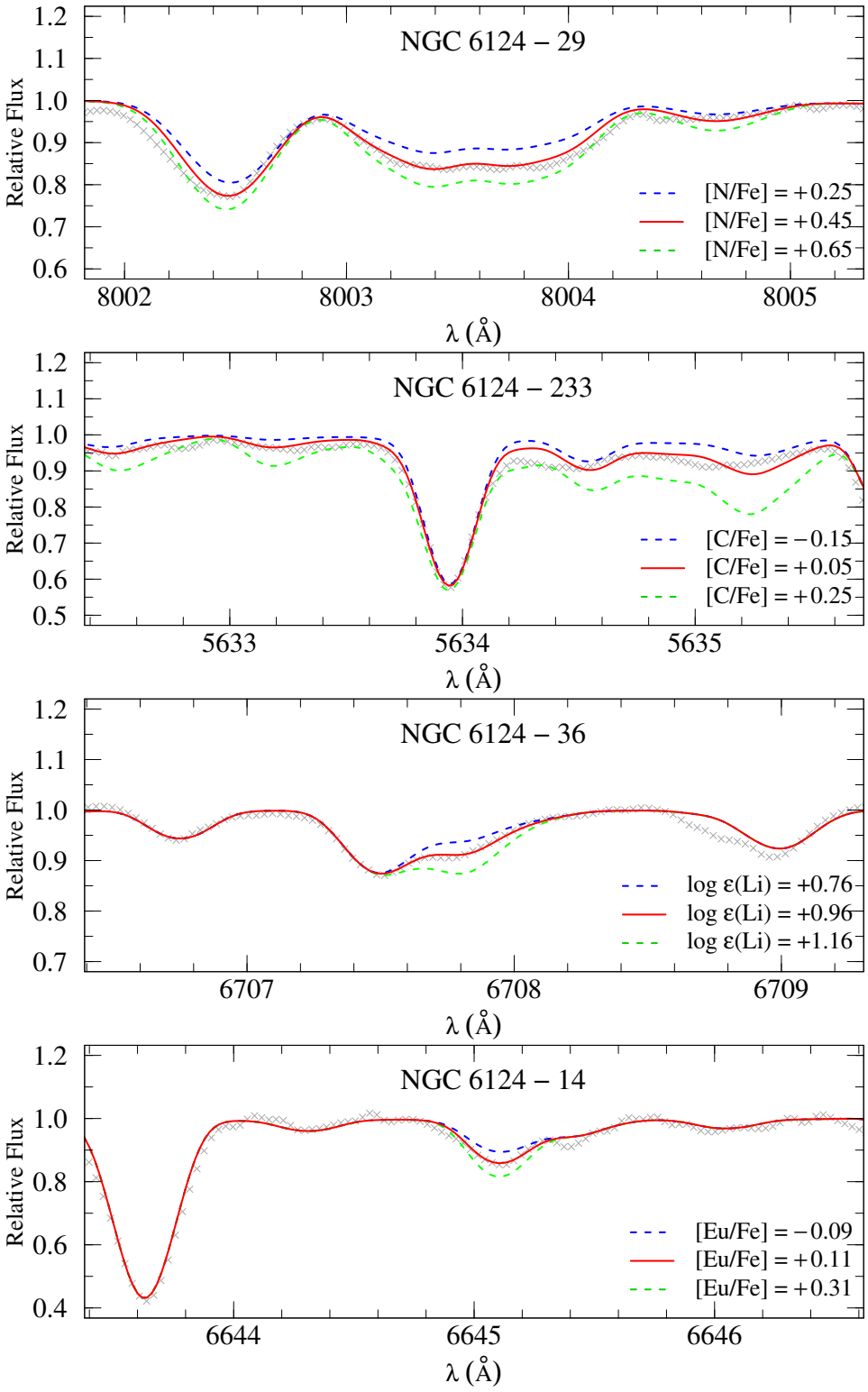

Figura 8.3: Observed (gray crosses and the synthetic best-fit (red line) spectra.

Tabela 8.4: Light element abundances and $^{12}C/^{13}C$ ratio.

Star	log ϵ(Li) LTE	log ϵ(Li) NLTE	[C/Fe]	[N/Fe]	$^{12}C/^{13}C$
#14	+0.21	+0.41	−0.10	+0.59	22
#29	+1.11	+1.43	+0.01	+0.45	14
#36	+0.96	+1.28	−0.03	+0.61	20
#233	+1.14	+1.46	+0.05	+0.44	25
Mean	+0.85 ± 0.44	+1.15 ± 0.50	−0.02 ± 0.06	0.52 ± 0.09	20 ± 5

by spectral synthesis technique, were normalized using the solar abundances of ASPLUND ET AL. (2009) and are given in Tables 8.4 and 8.5. The equivalent widths measured for each specie is show in Table A.6.

8.3 Discussion

8.3.1 Rotation velocities

As has it has been said, the stellar rotation is inferred through the projected rotational velocity, v sin i, and is a powerful characteristic that relates to many aspects for stellar evolution theory and understanding of internal structure. For an approach about the possible contributions of rotational velocity in the chemical profile of the giants analyzed here, we determined the v sin i by using spectral synthesis of the Fe I 6151.6 Å line. We fixed macroturbulent velocity as 3.0 km s^{-1} – as adopted by FEKEL ET AL. (1997) for G and K giants – and consider the instrumental broadening of the FEROS spectral resolution (FWHM ≈ 0.13), while v sin i was obtained using an iterative procedure until we find smallest deviation between the synthetic and observed spectra. Figure 8.4 shows two examples of this procedure, where the best fit of the observed spectra is represented by solid red lines.

Comparing our results with the main studies on this topic in the literature, Figure 8.5 shows the temperature distribution as a function of the projected rotational velocity obtained from CARLBERG ET AL. (2011) for their large sample of giant stars (gray circles) and values found by DELGADO MENA ET AL. (2016) for open cluster giant stars (yellow circles). The stars analyzed in this work are shown as red circles (single or members in wide binaries) and green circles (spectroscopic binaries). This is an important point to consider since binarity can affect the stellar angular momentum. This comparison reveals the atypical nature from the rotational perspective for giants belonging to NGC 6124, where the slower rotating giant presents v sin $i = 6.2$ km s^{-1}. In addition, binaries as #29 and #33 are subject to tidal interactions typical of close binary systems and, therefore, permit us associate these abnormal $v\,sin\,i$ values to their binary nature. Still, the star #33 shows an asymmetric Hα profile (Figure 8.2), which is associated to a high activity

Tabela 8.5: Abundance ratios [X/Fe] and the standard deviations for the targets in NGC 6124. "iron-peak", α and s refers to the average for iron-peak (Cr, Ni), α-elements (Si, Ca, Ti, Mg) and s-elements (Y, Zr, La, Ce, Nd) abundances, respectively.

[X/Fe]	#14	#29	#36	#233	$\langle$ [X/Fe] $\rangle$
Na I	+0.20 (2)	+0.26 (2)	+0.39 (2)	+0.33 (3)	+0.30 ± 0.08
Na I_{NLTE}	+0.14 (2)	+0.20 (2)	+0.31 (2)	+0.28 (3)	+0.23 ± 0.08
Mg I	+0.17 (5)	+0.16 (3)	+0.18 (2)	+0.19 (4)	+0.18 ± 0.01
Al I	+0.12 (5)	+0.09 (4)	+0.11 (3)	+0.13 (4)	+0.11 ± 0.02
Si I	+0.24 (8)	+0.20 (5)	+0.25 (6)	+0.25 (8)	+0.24 ± 0.02
Ca I	+0.01 (10)	+0.02 (6)	+0.07 (6)	+0.11 (10)	+0.05 ± 0.05
Ti I	+0.01 (7)	+0.04 (5)	+0.00 (12)	−0.04 (12)	+0.00 ± 0.03
Cr I	+0.11 (16)	+0.08 (11)	+0.03 (16)	+0.03 (13)	+0.06 ± 0.04
Fe I	−0.22 (74)	−0.18 (62)	−0.19 (68)	−0.22 (75)	−0.20 ± 0.02
Fe II	−0.22 (13)	−0.19 (9)	−0.18 (11)	−0.23 (10)	−0.20 ± 0.02
Ni I	+0.05 (14)	+0.02 (13)	+0.05 (17)	+0.01 (18)	+0.03 ± 0.02
Y II	+0.02 (2)	+0.09 (2)	+0.11 (3)	+0.12 (4)	+0.08 ± 0.05
Zr I	−0.02 (4)	+0.07 (5)	+0.12 (6)	+0.19 (5)	+0.09 ± 0.09
La II	+0.21 (4)	+0.28 (2)	+0.29 (3)	+0.20 (3)	+0.25 ± 0.05
Ce II	+0.11 (7)	+0.13 (5)	+0.19 (5)	+0.25 (7)	+0.17 ± 0.06
Nd II	+0.18 (8)	+0.20 (5)	+0.23 (10)	+0.25 (9)	+0.22 ± 0.03
Sm II	+0.20 (3)	+0.21 (6)	+0.22 (7)	+0.14 (10)	+0.19 ± 0.04
Eu II	+0.11 (1)	+0.14 (1)	+0.19 (1)	+0.11 (1)	+0.14 ± 0.04
iron-peak	+0.08	+0.05	+0.04	+0.02	+0.05 ± 0.03
α	+0.11	+0.11	+0.13	+0.13	+0.12 ± 0.01
s	+0.10	+0.15	+0.19	+0.20	+0.16 ± 0.05

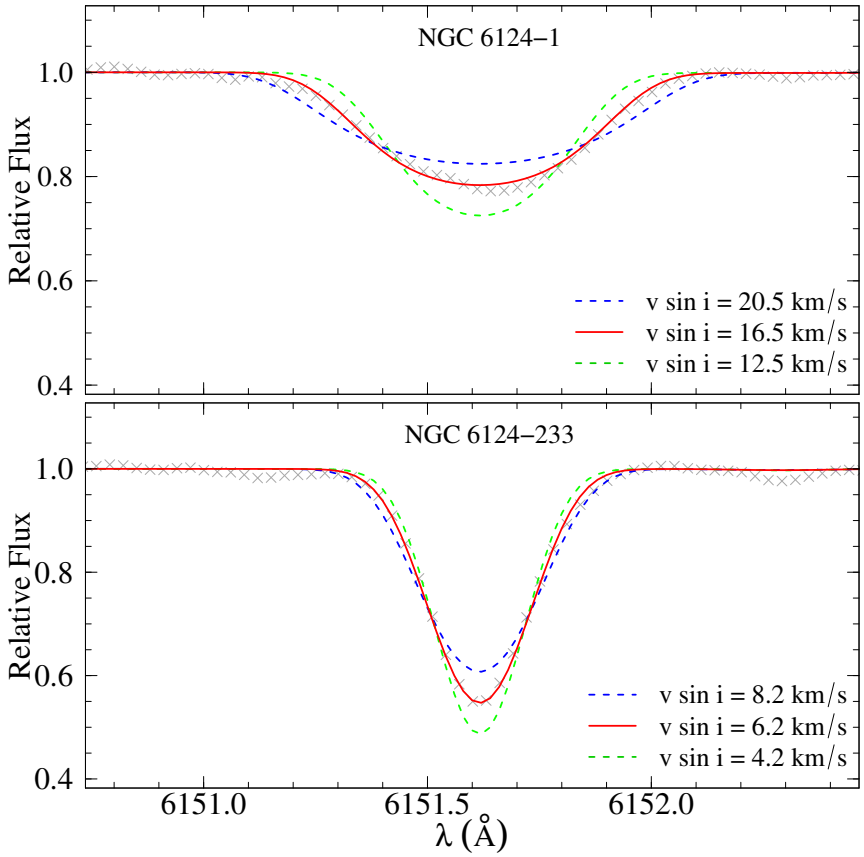

Figura 8.4: Examples of the projected rotational velocity $v \sin i$ determination for the stars NGC 6124-1 and NGC 6124-233, in the region of the Fe I line at 6151.6 Å. Synthetic spectra (colourful lines) for three different values of $v \sin i$ and observed spectra (gray crosses) are shown.

that also is common in close binary systems. The other objects analysed here are single stars or components in wide systems and the mechanism behind their abnormal rotation is supposed to be another. The masses of the giants analyzed in this work are significantly high compared to the masses subject to the Kraft break (KRAFT, 1966, 1970), so, these stars are little affected during the main sequence phase, and retain their angular momentum of birth or sudden acquired during a angular momentum dredge-up, stellar merge or engulfment of a planet or brown dwarf at the ascent to RGB.

Looking at the population of giants taken from intermediate and young open clusters, Figure 8.6, shows the diagram with the mean $v \sin i$ as a function of the age of the clusters with data taken from CARLBERG (2014) and DELGADO MENA ET AL. (2016). We observe that in fact older clusters (with giants of relative lower mass) have smaller $< v \sin i >$ while in younger clusters $< v \sin i >$ increases. As far as NGC 6124 is concern, we obtained two mean values, one for giants of relative low $v \sin i$ (#14, #29, #36, and #233) represented by a red square (7.3 km/s) while another one for the seven giants represented by a red circle (13.1 km/s). To excluding the spectroscopy binaries (#29 and #33) we obtained a mean of 11.1 km/s (red triangle), which still is consider a high value.

In addition, we highlight that the open cluster Pismis 18 has a large frequency of moderate rotators as reported by CARLBERG (2014), and that have two ages determination for a comparison in this context – 0.7 Gyr and 1.2 Gyr adopted by HATZIDIMITRIOU ET AL. (2019) and PIATTI ET AL. (1998), respectively. Although these ages are in agreement within their uncertainties, in the context of rotational velocity and ages for red giants of open clusters, we can confirm that the result of HATZIDIMITRIOU ET AL. (2019) is better matched since an older age for Pismis 18 would be surprisingly atypical since is very rich in moderate rotating stars. Above all, Figure 8.6 confirms CARLBERG's observations that perceived a large dispersion and incidence of fast rotators in stars with relative high mass (more young open clusters).

8.3.2 Abundances

In this section we present the results for abundances for C (C_2), N (CN), Li I, Na I, Mg I, Al I, Si I, Ca I, Ti I, Cr I, Ni I, Y II, Zr I, La II, Ce II, Nd II, Sm II, and Eu II and $^{12}C/^{13}C$ isotopic ratio. For a better discussion and comparison, we use three robust chemical studies from the literature that investigated giant and dwarf stars in the solar neighborhood: LUCK & HEITER (2007) that carried out stellar parameters and abundance data for a sample of 298 nearby giants; MISHENINA ET AL. (2006) that provide the fundamental parameters and abundances for a sample composed by 177 of the local clump giants; and BATTISTINI & BENSBY (2016) that obtained abundances for heavy elements (Z>26.0) for a sample of 593 F and G dwarf stars. Figure 8.7 shows the [X/Fe]

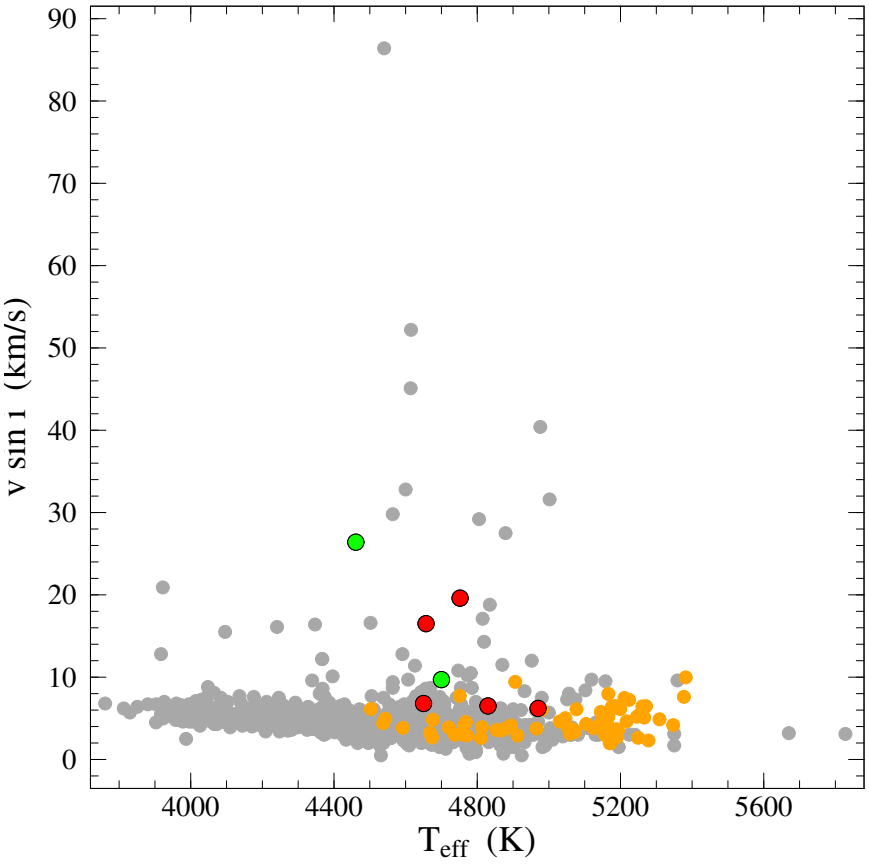

Figura 8.5: Projected rotational velocities, v sin i, for giant stars as a function of temperature. Obtained results for giants in NGC 6124 compared to the samples studied by CARLBERG ET AL. (2011) (gray) and DELGADO MENA ET AL. (2016) (yellow).

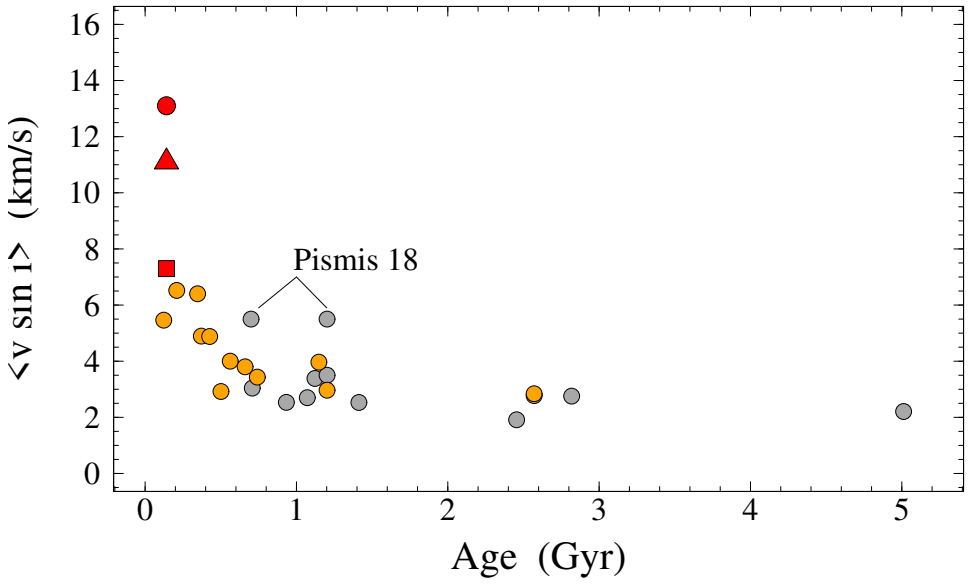

Figura 8.6: Projected rotational velocities (v sin i) as a function of age. We obtained mean for giants in NGC 6124 – square for the four stars chemically studied, circle for the seven observed stars, and triangle without spectroscopic binaries – and compare to the samples studied by CARLBERG (2014) (gray) and DELGADO MENA ET AL. (2016) (yellow).

ratio *versus* [Fe/H] abundances with our results and the abundances reported by LUCK & HEITER (2007) (yellow circles), MISHENINA ET AL. (2006) (gray circles), and BATTISTINI & BENSBY (2016) (blue circles). In the following subsections we will discuss the results for the obtained abundances.

Metallicity

The radial metallicity gradient constitute one of the most important observational constraints in the research of Galactic disk, and its evolution over time can be helpful for studies that aim a understanding of the formation and evolution of the Milky Way (HOU ET AL., 2000; MAGRINI ET AL., 2009). In this sense, we determined the average metallicity of [Fe/H] = −0.20 for the open cluster NGC 6124 taking into account the four giants with measurable equivalent widths. Our result seems in reasonable for a Galactocentric distance of $R_{GC} = 7.35$ kpc, as seen in Figure 8.8. In this calculation, we considered a Galactocentric distance to the Sun of 7.95 kpc and we adopted the well-known relation

$$R_{GC}^2 = R_{\odot}^2 + (d\,\cos\,b)^2 \,-\, 2\,R_{\odot}\,d\,\cos\,l\,\cos\,b,$$

where $R_{\odot}$ is the Galactocentric distance of the Sun, d is the distance of the cluster to the Sun, and l and b are the Galactic longitude and latitude, respectively. NGC 2345 (ALONSO-SANTIAGO ET AL., 2019; HOLANDA ET AL., 2019), for example, present an atypical metallicity for its Galactocentric distance and pose as a challenge for Galactic astrophysics (radial migration?) – which is not the case of NGC 6124, although its mean metallicity is slightly low. Figure 8.8 shows how the metallicity decreases with the Galactocentric distance. We can also see how the radial Galactic gradient modestly differ if we compare the two samples composed by Cepheids (GENOVALI ET AL., 2014, 2013 and references therein) and open clusters analysed by high-resolution spectroscopy (DA SILVEIRA ET AL., 2018; HOLANDA ET AL., 2019; KATIME SANTRICH ET AL., 2013; MARTINEZ ET AL., 2020; PEÑA SUÁREZ ET AL., 2018).

In addition, young open clusters ($\leqslant 0.8$ Gyr) were selected from NETOPIL ET AL. (2016) for a comparison with NGC 6124 with the distances taken from WEBDA[3]. In this plot, we also included two linear fits up to a distance of $R_{GC} = 12.0$ kpc: for the open clusters distribution (Δ[Fe/H]/$\Delta R_{GC} = -0.07$ dex kpc^{-1}) and for the Cepheids (Δ[Fe/H]/$\Delta R_{GC} = -0.06$ dex kpc^{-1} determined by GENOVALI ET AL., 2014). At 12.0 – 13.0 kpc lies the so-called "transition radius", where occurs a substantial change in the gradient of iron abundance that define the end of inner disc and the start of outer disc (YONG ET AL., 2012).

[3]Site dedicated to open star clusters and is the web version of the data base known as BDA. Available on http://webda.physics.muni.cz/

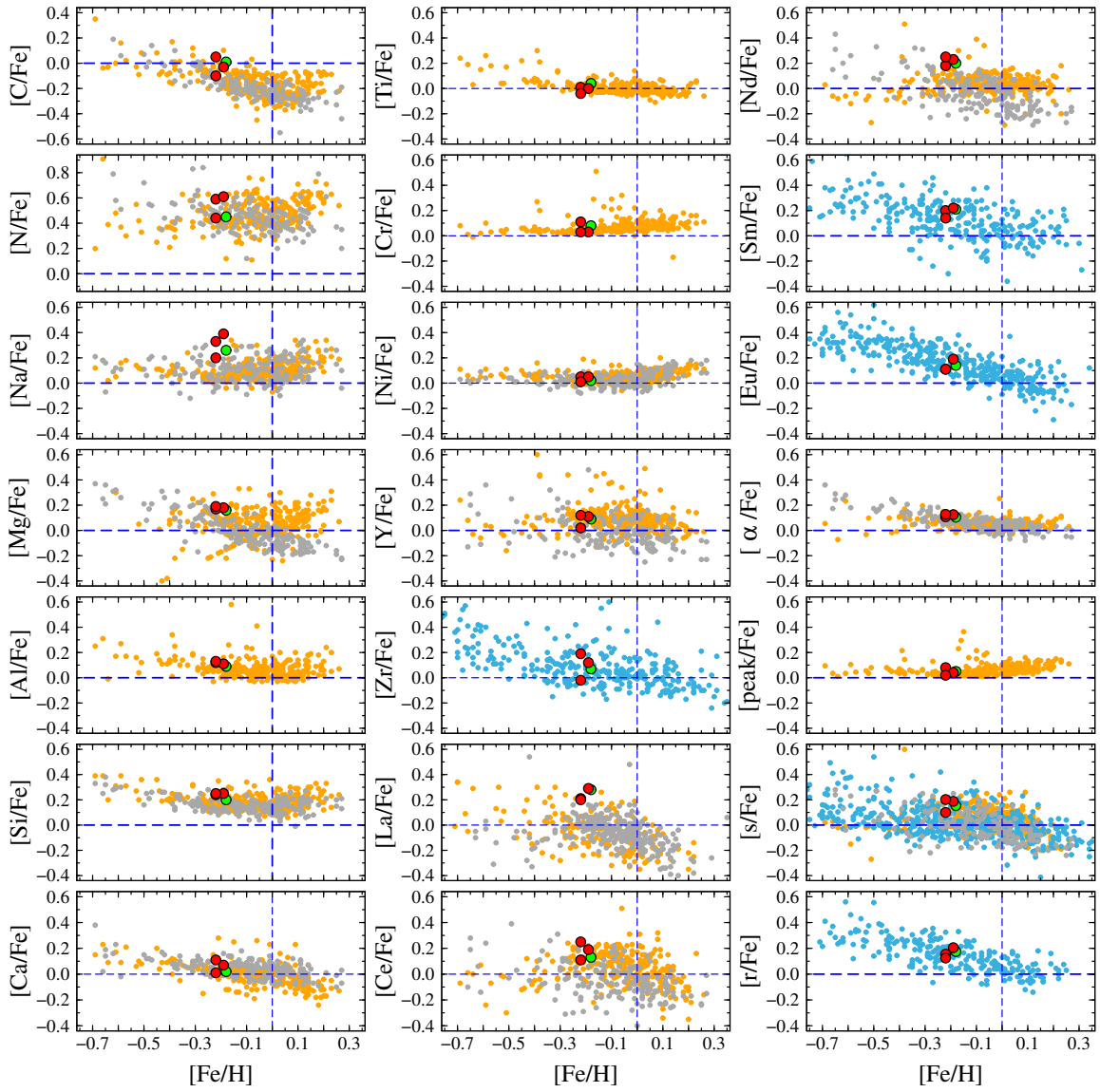

Figura 8.7: Abundance ratios [X/Fe] *versus* [Fe/H] for carbon to europium. [α/Fe], [peak/Fe], [s/Fe], [r/Fe] represent, respectively, the average for the α-elements, iron-peak elements, the elements created by the s-process, and the elements created by the r-process. The red and green circles represent the giants analyzed in this work, while the yellow circles represent the abundances reported by LUCK & HEITER (2007), the gray circles represent the abundances reported MISHENINA ET AL. (2006) and the blue circles represent the abundances reported by BATTISTINI & BENSBY (2016). The blue dashed lines indicate solar values.

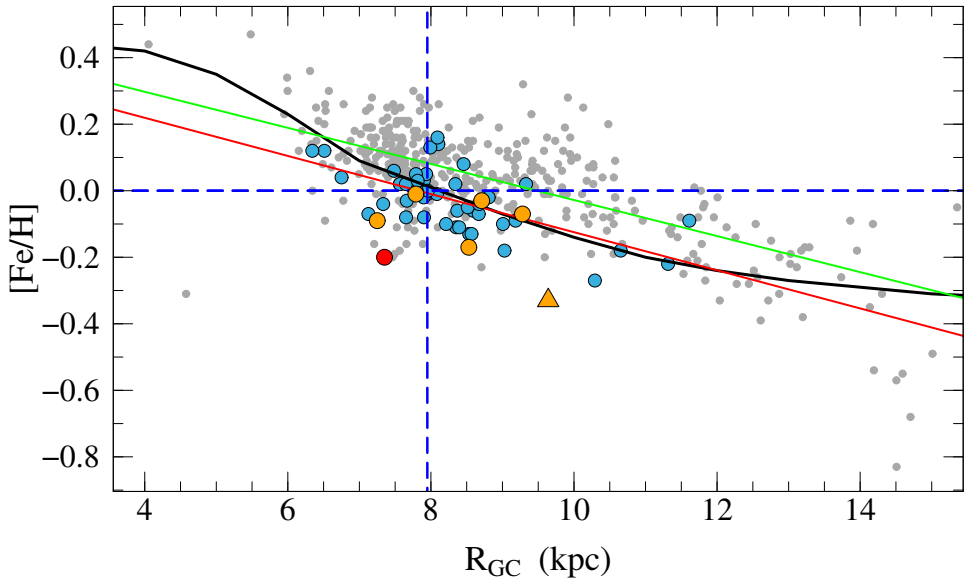

Figura 8.8: The average [Fe/H] versus Galactocentric distance with iron abundance gradients of $-0.06\,\mathrm{dex\,kpc^{-1}}$ (green solid line) and $-0.07\,\mathrm{dex\,kpc^{-1}}$ (red solid line) for Cepheids and open clusters, respectively. The black curve is relative to gradient model by MAGRINI ET AL. (2009). Blue dashed lines represent solar values for Galactocentric distance and [Fe/H]. The gray circles represent Cepheids studied by GENOVALI ET AL. (2014, 2013) and other sources used by them. The blue circles represent young open clusters ($\leqslant 0.8\,\mathrm{Gyr}$) with metallicities determined through high-resolution spectroscopy and compiled by NETOPIL ET AL. (2016). The yellow triangle represents NGC 2345 (HOLANDA ET AL., 2019). In addition, yellow circles are data obtained in our previous works (DA SILVEIRA ET AL., 2018; KATIME SANTRICH ET AL., 2013; MARTINEZ ET AL., 2020; PEÑA SUÁREZ ET AL., 2018).

C, N, and Li elements

We find a homogeneous chemistry for carbon and nitrogen elements in the four analyzed giants. In Figure 8.7, we show the derived [C/Fe] and [N/Fe] ratios in comparison with the same ratios obtained by MISHENINA ET AL. (2006) and LUCK & HEITER (2007) for disc red clump giants and local disc field giants (the results of these references have been normalized to ASPLUND ET AL., 2009). The [C/Fe] and [N/Fe] ratios for the giants analysed in this work show first dredge-up effects, as can be seen in Table 8.4. When ascending to the red giant branch, the abundance of ^{12}C is reduced as a consequence of the first dredge-up process and, the abundance of ^{14}N increases (KARAKAS & LATTANZIO, 2014), as it is clearly observed in all the giant stars analysed here.

Also, the abundance of lithium is expected to drop dramatically when stars evolve into RGB stage. Earlier and recent studies show that only 1% to 2% of giants have $\log \epsilon(\mathrm{Li}) \geqslant 1.50$, which a are the so-called lithium-rich giant stars – for more details about this topic see HOLANDA ET AL. (2020a,b) and the references therein. After NLTE corrections, we found a "moderate" enrichment of lithium in the giants #29 and #233, which motivated us to discuss the abundance of lithium with additional attention. It is well known in the literature that lithium overabundance may be associated with the high rotation in some giant stars and it is estimated that the coincidence of these aspects is around 50% (DRAKE ET AL., 2002). According to DRAKE ET AL., #233 is not considered a rapid rotator (they consider rapid rotator stars only objects with $v \sin i \geqslant 8.0\,\mathrm{km\,s^{-1}}$), however, it is an anomalous rotational velocity and the lithium preservation or production may be related to its atypical rotation. Moreover, #29 is a spectroscopic binary and is in the limit of rapid rotators ($v \sin i = 9.8\,\mathrm{km\,s^{-1}}$) and also presents a anomalous lithium abundance [$\log \epsilon(\mathrm{Li})_{\mathrm{NLTE}} = 1.43$]. In this discussion, we need to mention CASEY ET AL. (2019) who suggest that tidal interactions between binaries are responsible for the lithium enrichment in giant stars. However, JORISSEN ET AL. (2020) reported that the binary frequency among Li-rich K giants is normal when compared to that found for a sample of giants of same spectral type.

For comparative proposes, we show in Figure 8.9 (top panel) lithium abundances as a function of the projected rotational velocity for a sample of 67 red giants in 12 different open clusters studied by DELGADO MENA ET AL. (2016). Despite the completeness of giants analysed by individuals open clusters of DELGADO MENA ET AL.'s sample, we have been constructed an analysis based on the mean lithium abundance and $v \sin i$ for each open cluster (bottom panel). In this respect, we can to infer a increase of incidence of Li-enrichment with the high $v \sin i$ values. In bottom panel, NGC 6124 is the cluster with the highest mean $v \sin i$ value and is the one of the largest value of the lithium abundance. This possible correlation it not new, for example, DE MEDEIROS ET AL. (2000) carry out correlation coefficients for different mass intervals – between

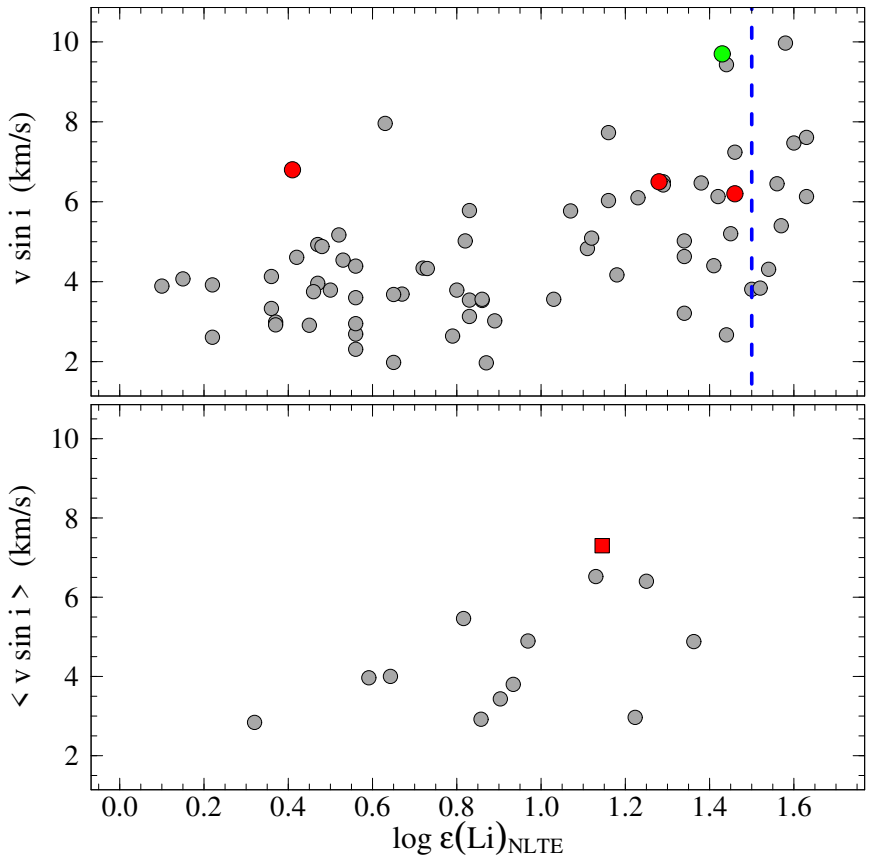

Figura 8.9: Lithium abundance as function of projected rotational velocity $v \sin i$. Our results are compared with a sample of open clusters analysed by DELGADO MENA ET AL. (2016). In the top panel we plotted individual values while in the bottom panel we present the mean rotational velocity for each open cluster. Horizontal blue dashed line represents the limit for normal and Li-rich giant stars ($\log \epsilon(\mathrm{Li}) = 1.5$).

the mass intervals analysed by them, giants with masses of $3.5\,M_{\odot}$ present a correlation coefficient value of 0.297 (poor correlation). Still, this is a questionable correlation since slow rotators are observed with different abundances of lithium, even among super Li-rich giants (HOLANDA ET AL., 2020b).

Na and Al elements and $^{12}C/^{13}C$ ratio

We provide abundances of Na I and Al I based on most clean and not blended lines present in stellar spectra. In particular, the sodium abundance increase thanks due to the first-dredge-up episode for a star that ascends to the red giant branch. However, a significant change is only remarkable from intermediate stellar masses ($M \geqslant 2.0\,M_{\odot}$) according to models for first-dredge-up (KARAKAS & LATTANZIO, 2014). As has shown in Figure 8.7, [Na/Fe] seems slightly enriched in relation to the field stars and clump giants (LUCK & HEITER , 2007; MISHENINA ET AL., 2006), but this comparison takes into account only the conditions based on LTE. After making corrections for NLTE conditions, stars have their sodium abundances reduced (in mean by -0.07 dex). In addition, Figure 8.10 presents the predictions for the abundance of $^{12}C/^{13}C$ isotopic ratio (top) and [Na/Fe] (bottom) and these results provide a new background about sodium and $^{12}C/^{13}C$ isotopic ratio that are traditional mixing tracers. This Figure presents predictions for giants at the first dredge-up, using canonical and non-canonical models: thermohaline mixing from CHARBONNEL & LAGARDE (2010) and LAGARDE ET AL. (2012), thermohaline extra-mixing (CHARBONNEL & LAGARDE, 2010) and thermohaline and rotation-induced mixing (LAGARDE ET AL., 2012); with all these models being relative to solar metallicity ($Z = 0.02$). The mean isotopic ratio $^{12}C/^{13}C$ and [Na/Fe] values, derived under LTE assumption (red circles), for the giants of NGC 6124 indicate a good agreement with both models, the prediction for thermohaline and the rotation-induced mixing from LAGARDE ET AL.. Nevertheless, according to the sodium abundance for a NLTE correction, [Na/Fe] NLTE (red triangle in bottom panel) and the turn-off mass value of our cluster, the abundance of this element is in good agreement with the predictions given by the first dredge-up.

α-elements and iron-peak elements

The α-elements are well-known tracers of the recent chemical evolution which are produced on a time scale of 10 Myr by massive stars, via type II Supernovae. We estimated the produced abundances for a posterior confrontation with the abundance of field stars and open clusters studied using high-resolution spectroscopy and models for chemical evolution of the Galactic disk. As can be seen from Figure 8.7 the abundance ratios [Ca/Fe], [Mg/Fe] and [Ti/Fe] have solar values and have basically the ratios seen in the literature for disc red clump giants and local disc field giants, for the same metallicity (LUCK & HEITER ,

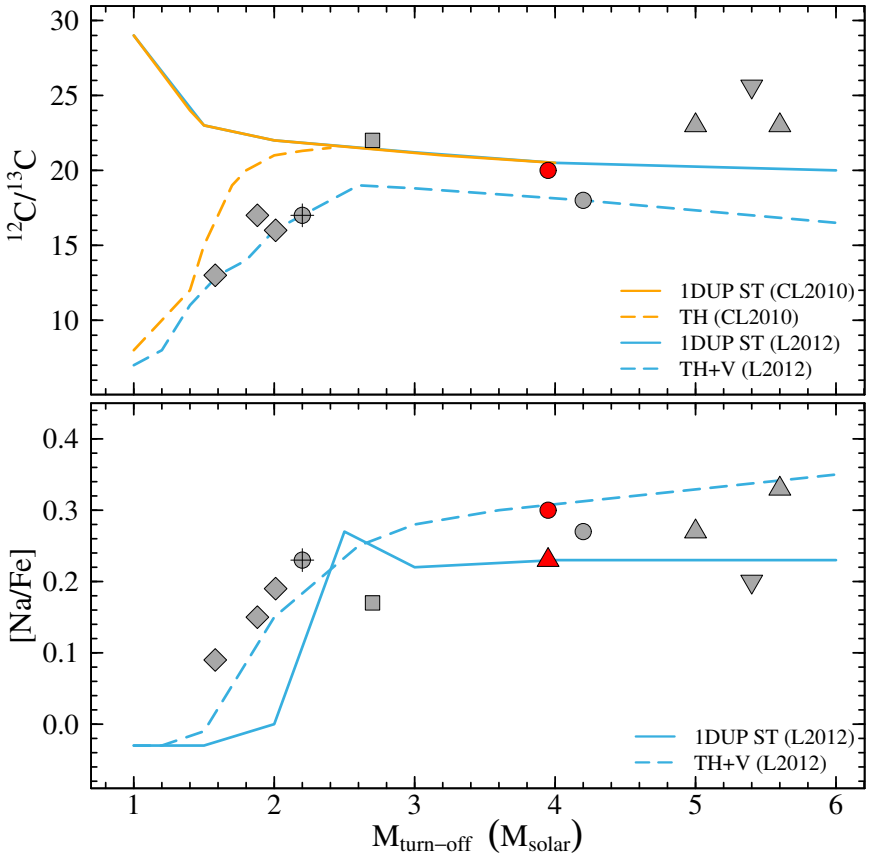

Figura 8.10: $^{12}C/^{13}C$ isotopic ratio (top) and [Na/Fe] (bottom) versus $M_{turn-off}$ in giant stars of open clusters. In both panels, red symbols represent abundances for NGC 6124 when assuming LTE (circle) and NLTE (triangle) conditions; grey symbols correspond to the mean $^{12}C/^{13}C$ isotopic ratio or [Na/Fe] for NGC 4609 and NGC 5316 (triangles; DRAZDAUSKAS ET AL., 2016), NGC 2345 (reverse triangle; HOLANDA ET AL., 2019), NGC 2539 (circle with cross; MARTINEZ ET AL., 2020), NGC 3114 (circle; KATIME SANTRICH ET AL., 2013), NGC 2447 (square; DA SILVEIRA ET AL., 2018), and NGC 2360, NGC 3680, and NGC 5822 (diamonds; PEÑA SUÁREZ ET AL., 2018). Solid lines represent the predicted abundances of these elements for giants at the first dredge-up, using standard solar metallicity evolutionary models, from CHARBONNEL & LAGARDE (CHARBONNEL & LAGARDE, CL2010; yellow) and LAGARDE ET AL. (2012, L2012; blue). Dashed lines indicate the prediction model for thermohaline extra-mixing and thermohaline and rotation-induced mixing from CL2010 (yellow) and L2012 (blue), respectively.

2007; MISHENINA ET AL., 2006). The [Si/Fe] ratio in NGC 6124 with a value of 0.19 dex with low scattering for the analyzed giants here, but it is with good concordance with these two sample of field stars.

The iron-peak elements such as chromium and nickel were also studied in this work. These two elements are tracers of the chemical evolution on a longer time scale (1 Gyr) and are produced mainly by Ia Supernova events. For NGC 6124, we find abundances similar to the solar values for both chemical species which is in a very good agreement with the giants analysed by MISHENINA ET AL. (2006) and LUCK & HEITER (2007).

s- and r-process elements

Low- and intermediate-mass asymptotic giant branch stars are the main source for the formation of the elements created by s-process (slow neutron-capture process; BUSSO ET AL., 1999), while the elements created by r-process (rapid neutron-capture process) have production sources that are widely discussed and is still a challenge for astrophysics – this "slow"and "rapid"are relative to timescale of neutron-capture compared to β-decay. In this context, we measured abundances for some s-process elements produced in the first peak (Y and Zr) and second peak (La, Ce, and Nd) and also were determined the abundances of Sm and Eu elements – this last one a "pure" r-process element, which is formed predominantly due to an intense neutron flux (6%; BISTERZO ET AL., 2016, 2017).

We calculated the mean abundance of the s-process elements[4] and compare the results for NGC 6124 with samples of giant and dwarf stars, as have displayed in Figure 8.7. This Figure make it possible to note that NGC 6124 presents a small enrichment of s-process abundances compared to the sample of stars taken from the literature. In this context, D'ORAZI ET AL. (2009) make the first report of a trend inversely proportional between barium abundances (a second peak element) and ages for a large sample of Galactic open clusters. After, several studies suggest that young open clusters are more s-process elements enriched than the older open clusters (DA SILVEIRA ET AL., 2018; HOLANDA ET AL., 2019; MARTINEZ ET AL., 2020; among others).

In case of the elements predominantly produced in the r-process, Sm and Eu, the abundances found in the giants of NGC 6124 cluster are in good agreement with the dwarf stars studied by BATTISTINI & BENSBY, when we compare stars of same metallicity.

8.3.3 Are NGC 6124-33 and NGC 6124-29 members of the cluster?

Based on the results obtained on polarimetic analysis, VERGNE ET AL. (2010) reinforced the hypothesis raised by THE (1965) that NGC 6124-33 could not be a cluster member.

[4] defined as: $[s/Fe] \equiv ([Y/Fe]+[Zr/Fe]+[La/Fe]+[Ce/Fe]+[Nd/Fe])/5$

Classified as a M0 III-type star by NESTEROV ET AL. (1995), this star until then had been considered as a background star. However, we did not find any evidence based on astrometric data, that is the proper motion and parallax from GAIA data. Figure 8.1 shows that NGC 6124-33 has similar values to those of the stars of the cluster. As far as the radial velocity is concerned, NGC 6124-33 exhibits a radial velocity value that is dissonant from the other giants (Table 8.1), but it is possible that this effect could be due to binarity as earlier raised by MERMILLIOD ET AL. (2008).

NGC 6124-29 was classified by MERMILLIOD ET AL. (2008) as spectroscopic binary and presents variation radial velocity of order $\approx 3\,\mathrm{km\,s^{-1}}$. In our chemical analysis, this spectroscopic binary shows a chemistry similar to the other three giants analyzed here (Figure 8.7). However, unlike the other stars in our sample, NGC 6124-29 has a different proper motion from the NGC 6124 cluster. Figure 8.1 shows proper motion data obtained from *Gaia* DR2 and NGC 6124-29 is outside the circle that delimits the overdensity frontier of the open cluster. Especially, this singular giant star that help us to see open clusters as sources that joining the Galactic disc in the course of time with their stars – hypotheses defended by REDDY & LAMBERT (2019), among others.

8.4 Conclusions

The main findings based on the abundance analysis and projected rotational velocity employing high-resolution optical spectra on giants in open cluster NGC 6124 can be summarized as follows:

1. The open cluster NGC 6124 has three rapid rotators ($v \sin i > 10.0\,\mathrm{km\,s^{-1}}$) and four moderate rotators $v \sin i > 6.0\,\mathrm{km\,s^{-1}}$, which is surprisingly since stellar evolution theory predict low rotation for G-K red giant stars (CARLBERG ET AL., 2011; DE MEDEIROS ET AL., 1996). Among these stars, only two are classified as spectroscopic binary while the others are single or wide binary stars. This high rotation velocity may be due to the merge or swallowing of planets or brown dwarfs, as widely indicated in the literature.

2. We concluded that NGC 6124-33 is a cluster member. Its abundance pattern determined here match the other giant stars that belong to cluster and in addition, our proper motion analysis indicate that this object lies within characteristic density of NGC 6124. Our vector point diagram is complemented with an analysis of individual parallaxes and a color magnitude diagram that define its evolutionary stage. Another star, NGC 6124-29 is lies outside of characteristic overdensity that defines the NGC 6124 in vector point diagram. However, abundances determined via equivalent width and spectral synthesis technique show that this star belong to

the cluster, which is also supported by its parallax and position in color-magnitude diagram.

3. In general, we note that abundances from NGC 6124 present a good concordance with abundances derived from field stars and gradient models for Galactic disk. However, it was observed a possible correlation between the mean lithium abundance and the high mean for $v \sin i$ – this is a open question, since exist considerable incidence of slow rotator with Li-enrichment when we see to data taken from the literature.

Capítulo 9

Conclusões Gerais e Perspectivas

Nós apresentamos quatro estudos baseados em espectros de alta resolução de gigantes vermelhas, sendo elas pertencentes ao campo da galáxia ou a aglomerados estelares abertos. Determinamos os parâmetros atmosféricos e abundâncias químicas para uma longa lista de elementos químicos, o que nos permitiu estudar nossos alvos sob diferentes perspectivas da astrofísica estelar e galáctica.

O problema do lítio segue sem solução. Verificamos que o enriquecimento de lítio pode ocorrer em estágios evolutivos mais avançados, tais como o E-AGB. Ainda, é possível que um *merger* entre uma estrela no RGB e uma companheira anã branca de He explique a formação de parte das gigantes ricas em lítio e, mais que isso, fornecemos vínculos observacionais através do estudo de uma gigante considerada super rica em lítio e com abundâncias de Fe e C atípicas. Ou seja, dentro do universo de estrelas peculiares nós apresentamos soluções para duas estrelas que não são comuns.

Acerca do aglomerado aberto NGC 2345, nós verificamos um ligeiro enriquecimento em elementos produzidos no processo-s – o que já é previsto para aglomerados jovens. Além disso, encontramos uma metalicidade média baixa para sua população de gigantes vermelhas, dada a sua distância galactocêntrica. Também, é um problema em aberto, pois hipóteses como migração e anomalia química local ainda carecem de maturação. Por outro lado, o aglomerado aberto NGC 6124 tem como destaque os valores de $v \sin i$ de suas gigantes. Com apenas duas binárias espectroscópicas bem conhecidas entre os alvos, nós verificamos a hipótese que relaciona idade e $v \sin i$. Também, sob o ponto de vista químico, identificamos um ligeiro enriquecimento de lítio e elementos do processo-s nessa população.

Como perspectivas, esperamos concluir e publicar o trabalho referente ao estudo químico da população de gigantes vermelhas do aglomerado aberto NGC 6124. No momento, o trabalho está na sua fase final. Além disso, temos alguns trabalhos em fase de escrita, são eles: um estudo químico da gigante HD 16424, que é rica em lítio e com baixíssima razão $^{12}C/^{13}C$; reporte e análise de três novas gigantes ricas em lítio descobertas em um *survey* espectroscópico realizado através dos espectrógrafos FEROS e MUSICOS, que foi

acomplado ao telescópio de 1.6 m do Observatório Pico dos Dias; e um estudo químico da população de gigantes vermelhas do aglomerado IC 2714.

Não obstante, nós submetemos dois pedidos de tempo nas chamadas do Observatório Pico dos Dias e Gemini Sul. Pretendemos observar estrelas gigantes de aglomerados abertos pobremente estudados sob o ponto de vista químico e, se tratando do Gemini Sul, reanalizar estrelas de bário conhecidas na literatura e gigantes vermelhas já estudadas por nós no espectro óptico, também pertencentes a aglomerados abertos. Essa nova abordagem se justifica pelo fato do infravermelho nos fornecer uma janela com várias possibilidades novas a serem exploradas, tais como: correlações em fluor e bário e refinamento da metodologia que deve ser aplicada, num futuro próximo, a aglomerados obscurecidos e impossíveis de serem estudados amplamente através da janela ótica.

Ademais, pretendemos revisitar o estudo das binárias próximas nesses aglomerados jovens, visto que sua incidência é significativa e por vezes está diretamente ligada à formação de estrelas peculiares como *stragglers*, gigantes ricas em bário e gigantes ricas em lítio.

Referências Bibliográficas

ALONSO-SANTIAGO, J.; Negueruela, I.; MARCO, A.; Tabernero, H. M.; GONZÁLEZ-FERNÁNDEZ, C.; CASTRO, N. (2019) "A comprehensive study of NGC 2345, a young open cluster with a low metallicity", *A&A*, 631, p. 124, 10.1051/0004-6361/201936109

ALLENDE PRIETO, C.; GARC´A LÓPEZ, R. J.; LAMBERT, D. L.; GUSTAFSSON, B. (1999) "A Consistency Test of Spectroscopic Gravities for Late-Type Stars", *ApJ*, 527, p. 879, 10.1086/308096

AMMONS, S. M.; ROBINSON, S. E.; STRADER, J.; LAUGHLIN, G.; FISCHER, D.; WOLF, A. (2006) "The N2K Consortium. IV. New Temperatures and Metallicities for More than 100,000 FGK Dwarfs", *ApJ*, 638, p. 1004, 10.1086/498490

ABIA, C.; DOM´NGUEZ, I.; GALLINO, R.; BUSSO, M.; STRANIERO, O.; DE LAVERNY, P.; WALLERSTEIN, G. (2003) "Understanding AGB Carbon Star Nucleosynthesis from Observations", *PASA*, 20, p. 314, 10.1071/AS03021

ALEXANDER, J. B. (1967) "A possible source of lithium in the atmospheres of some red giants", *The Observatory*, 87, p. 238

AGUILERA-GÓMEZ, C.; CHANAMÉ, J.; PINSONNEAULT, M. H.; CARLBERG, J. K. (2016) "On Lithium-rich Red Giants. I. Engulfment of Substellar Companions", *ApJ*, 829, p. 127, 10.3847/0004-637X/829/2/127

ALCALÁ, J. M.; BIAZZO, K.; COVINO, E.; FRASCA, A.; BEDIN, L. R. (2011) "IRAS 12556-7731: a "chamaeleonic" lithium-rich M-giant", *A&A*, 531, p. 12, 10.1051/0004-6361/201117174

ALONSO, A.; ARRIBAS, S.; MART´NEZ-ROGER, C. (1999) "The effective temperature scale of giant stars (F0-K5). II. Empirical calibration of T_{eff} versus colours and [Fe/H]", *A&AS*, 140, p. 261, 10.1051/aas:1999521

ALONSO-SANTIAGO, J.; MARCO, A.; NEGUERUELA, I.; TABERNERO, H. M.; CASTRO, N.; et al. (2018) "NGC 3105: a young open cluster with low metallicity", *A&A*, 616, p. 124, 10.1051/0004-6361/201833073

ADAMÓW, M.; NIEDZIELSKI, A.; VILLAVER, E.; WOLSZCZAN, A.; KOWALIK, K.; et al. (2015) "Tracking Advanced Planetary Systems (TAPAS) with HARPS-N. II. Super Li-rich giant HD 107028", *A&A*, 581, 94, 10.1051/0004-6361/201526582

ALLENDE PRIETO, C.; LAMBERT, D. L.; ASPLUND, M. (2001) "The Forbidden Abundance of Oxygen in the Sun", *ApJ*, 556, L63, 10.1086/322874

ASPLUND, M.; GREVESSE, N.; SAUVAL, A. J.; SCOTT, P. (2009) "The Chemical Composition of the Sun", *ARA&A*, 47, p. 481, 10.1146/annurev.astro.46.060407.145222

BAI, Y.; LIU, J. F.; BAI, Z. R.; WANG, S.; FAN, D. W. (2019) "Machine-learning Regression of Stellar Effective Temperatures in the Second Gaia Data Release", *AJ*, 158, p. 93, 10.3847/1538-3881/ab3048

BISTERZO, S.; TRAVAGLIO, C.; WIESCHER, M.; GALLINO, R.; KÖPPELER, F.; STRANIERO, O; et al. "AGB yields and Galactic Chemical Evolution: last updated", *Journal of Physics Conference Series*, 665, p. 012023, 10.1088/1742-6596/665/1/012023

Bisterzo, S.; Travaglio, C.; Wiescher, M.; Käppeler, F.; Gallino, R. (2017) "Galactic Chemical Evolution: The Impact of the ^{13}C-pocket Structure on the s-process Distribution", *ApJ*, 835, p. 97, 10.3847/1538-4357/835/1/97

BATTISTINI, C. & BENSBY (2016) "The origin and evolution of r- and s-process elements in the Milky Way stellar disk", *A&A*, 586, A49, 10.1051/0004-6361/201527385

BAUSCHLICHER, C. W.; LANGHOFF, S. R.; TAYLOR, P. R. (1988), *ApJ*, 332, p. 531, 10.1086/166675

BIAZZO, K.; FRASCA, A.; CATALANO, S.; MARILLI, E. (2007) "Effective temperature vs. line-depth ratio for ELODIE spectra: Gravity and rotational velocity effects", *Astronomische Nachrichten*, 328, p. 938, 10.1002/asna.200710781

BAILER-JONES, C. A. L.; RYBIZKI, J.; FOUESNEAU, M.; MANTELET, G.; ANDRAE, R. (2018) "Estimating Distance from Parallaxes. IV. Distances to 1.33 Billion Stars in Gaia Data Release 2", *AJ*, 156, p. 58, 10.3847/1538-3881/aacb21

BERTELLI, G.; BRESSAN, A.; CHIOSI, C.; FAGOTTO, F.; NASI, E. (1994) "Theoretical isochrones from models with new radiative opacities", *A&A*, 106, p. 275

BINNEY, J.; TREMAINE, S. (2011) "Galactic Dynamics", Princeton University Press

BHARAT KUMAR, Y.; REDDY, B. E.; MUTHUMARIAPPAN, C.; ZHAO, G. (2015) "Far-infrared study of K giants in the solar neighborhood: Connection between Li enrichment and mass-loss", *A&A*, 577, p. 10, 10.1051/0004-6361/201425076

BHARAT KUMAR, Y.; REDDY, B. E. (2009) "HD 77361: A New Case of Super Li-Rich K Giant with Anomalous Low $^{12}C/^{13}C$ Ratio", *ApJL*, 703, p. 46, 10.1088/0004-637X/703/1/L46

BONIFACIO, P.; CAFFAU, E.; LUDWIG, H. -G.; STEFFEN, M. (2012) "LTE Model Atmospheres: MARCS, ATLAS and CO5BOLD", *From Interacting Binaries to Exoplanets: Essential Modeling Tools*, p. 213, Ed. RICHARDS, M. T. and HUBENY, I., 10.1017/S1743921311027402

BÖCEK TOPCU, G.; AFŞAR, M.; SNEDEN, C. (2016) "The chemical compositions and evolutionary status of red giants in the open cluster NGC 6940", *MNRAS*, 463, p. 580, 10.1093/mnras/stw1974

BHARAT KUMAR, Y.; REDDY, B. E.; ZHAO, G. (2018) "", *Journal of Astrophysics and Astronomy*, 39, p. 25, 10.1007/s12036-017-9501-6

BROWN, J. A.; SNEDEN, C.; LAMBERT, D. L.; & DUTCHOVER, E. Jr. (1989) "A Search for Lithium-rich Giant Stars", *ApJS*, 71, p. 293, 10.1086/191375

BUSSO, M.; GALLINO, R.; WASSERBURG, G. J. (1999) "Nucleosynthesis in Asymptotic Giant Branch Stars: Relevance for Galactic Enrichment and Solar System Formation", *ARAA*, 37, p. 239, 10.1146/annurev.astro.37.1.239

BILDSTEN, L.; PAXTON, B.; MOORE, K.; MACIAS, P. J. (2012) "Acoustic Signatures of the Helium Core Flash", *ApJL*, 744, p. 6, 10.1088/2041-8205/744/1/L6

BRESSAN, A.; MARIGO, P.; GIRARDI, L.; SALASNICH, B.; DAL CERO, C.; et al. (2012) "PARSEC: stellar tracks and isochrones with the PAdova and TRieste Stellar Evolution Code", *MNRAS*, 427, p. 127, 10.1111/j.1365-2966.2012.21948.x

BHARAT KUMAR, Y.; REDDY, B. E.; & LAMBERT, D. L. (2011) "Origin of Lithium Enrichment in K Giants", *ApJ*, 730, L12, 10.1088/2041-8205/730/1/L12

BOOTHROYD, A. I.; SACKMANN, I. -J. (1999) "The CNO Isotopes: Deep Circulation in Red Giants and First and Second Dredge-up", *ApJ*, 510, p. 232, 10.1086/306546

BOOTHROYD, A. I.; SACKMANN, I. -J.; WASSERBURG, G. J. (1995) "Hot Bottom Burning in Asymptotic Giant Branch Stars and Its Effect on Oxygen Isotopic Abundances", *ApJL*, 442, L21, 10.1086/187806

CARROLL, B. W.; OSTLIE, D. A. (2017) "An introduction to modern astrophysics", Cambridge University Press

CAYREL, R. (1988) "Data Analysis", *Ed.: CAYREL DE STROBEL, G. and SPITE, M.*, 132, p. 345

CASSISI, S.; SALARIS, M.; BONO, G. (2002) "The Shape of the Red Giant Branch Bump as a Diagnostic of Partial Mixing Processes in Low-Mass Stars", *ApJ*, 565, p. 1231, 10.1086/324695

CAMERON, A. G. W. $ FOWLER, W. A. (1971) "Lithium and the s-PROCESS in Red-Giant Stars", *ApJ*, 164, p. 111, 10.1086/150821

CASTRO, S.; RICH, R. M.; GRENON, M.; BARBUY, B.; MCCARTHY, J. K. (1997) "High-Resolution Abundance Analysis of Very Metal-rich Stars in the Solar Neighborhood", *AJ*, 114, p. 376, 10.1086/118481

CANTIELLO, M.; LANGER, N. (2010) "Thermohaline mixing in evolved low-mass stars", *A&A*, 521, A9, 10.1051/0004-6361/201014305

CARLBERG, J. K. (2014) "Rotational and Radial Velocities of 1.3-2.2 $M_{\odot}$ Red Giants in Open Clusters", *AJ*, 147, p. 138, 10.1088/0004-6256/147/6/138

CHARBONNEL, C. & LAGARDE, N. (2010) "Thermohaline instability and rotation-induced mixing. I. Low- and intermediate-mass solar metallicity stars up to the end of the AGB", *A&A*, 522, A10, 10.1051/0004-6361/201014432

CASTILHO, B. V.; GREGORIO-HETEM, J.; SPITE, F.; BARBUY, B.; SPITE, M. (2000) "Detailed analysis of a sample of Li-rich giants", *A&a*, 364, p. 674

CARLBERG, J. K.; SMITH, V. V.; CUNHA, K.; MAJEWSKI, S. R.; ROOD, R. T. (2010) "The Super Lithium-rich Red Giant Rapid Rotator G0928+73.2600: A Case for Planet Accretion?", *ApJL*, 723, 103, 10.1088/2041-8205/723/1/L103

CARLBERG, J. K.; CUNHA, K.; SMITH, V. V.; MAJEWSKI, S. R. (2012) "Observable Signatures of Planet Accretion in Red Giant Stars. I. Rapid Rotation and Light Element Replenishment", *ApJ*, 757, p. 109, 10.1088/0004-637X/757/2/109

CASEY, A. R.; HO, A. Y. Q.; NESS, M.; HOGG, D. W.; RIX, H.-W. (2019) "Lithium and the s-PROCESS in Red-Giant Stars", *ApJ*, 880, p. 125, 10.3847/1538-4357/ab27bf

CASEY, A. R.; RUCHTI, G.; MASSERON, T.; RANDICH, S.; GILMORE, G.; LIND, K; et al. (2016) "The Gaia-ESO Survey: revisiting the Li-rich giant problem", *MNRAS*, 461, p. 3336, 10.1093/mnras/stw1512

CHARBONNEL, C.; BALACHANDRAN, S. C. (2000) "The Nature of the lithium rich giants. Mixing episodes on the RGB and early-AGB", *A&A*, 359, p. 563

CHRISTENSEN-DALSGAARD, J. (2015) "On the red-giant luminosity bump", *MNRAS*, 453, p. 666, 10.1093/mnras/stv1656

CHEN, B.; FIGUERAS, F.; TORRA, J.; JORDI, C.; LURI, X.; GALADÍ-ENRÍQUEZ, D. (1999) "Constraining galactic structure parameters from a new extinction model and four star", *A&A*, 352, 459

CLAYTON, D. D. (1983) "Principles of stellar evolution and nucleosynthesis", University of Chicago press

CUTRI, R. M.; SKRUTSKIE, M. F.; VAN DYK, S; BEICHMAN, C. A.; CARPENTER, J. M.; et al. (2003) "2MASS All Sky Catalog of point sources"

CARLBERG, J. K.; MAJEWSKI, S. R.; ARRAS, P. "The Role of Planet Accretion in Creating the Next Generation of Red Giant Rapid Rotators", *ApJ*, 700, p. 832, 10.1088/0004-637X/700/1/832

CARLBERG, J. K.; MAJEWSKI, S. R.; PATTERSON, R. J.; BIZYAEV, D.; SMITH, V. V.; CUNHA, K. (2011) "The Frequency of Rapid Rotation Among K Giant Stars", *ApJ*, 732, p. 39, 10.1088/0004-637X/732/1/39

DE MEDEIROS, J. R.; DO NASCIMENTO, J. D., JR.; SANKARANKUTTY, S.; COSTA, J. M.; MAIA, M. R. G. (2000) "Rotation and lithium in single giant stars", *A&A*, 363, p. 239

DELGADO MENA, E.; TSANTAKI, M.; SOUSA, S. G.; KUNITOMO, M.; ADIBEKYAN, V.; ET AL. (2016) "Searching for Li-rich giants in a sample of 12 open clusters. Li enhancement in two stars with substellar companions", *A&A*, 587, p. 66, 10.1051/0004-6361/201527196

DE MEDEIROS, J. R.; DA ROCHA, C.; MAYOR, M. (1996) "The distribution of rotational velocity for evolved stars", *A&A*, 314, P. 499

DEHEUVELS, S.; BALLOT, J.; BECK, P. G.; MOSSER, B.; ØSTENSEN, R.; et al. (2015) "Seismic evidence for a weak radial differential rotation in intermediate-mass core helium burning stars", *A&A*, 580, p. 96, 10.1051/0004-6361/201526449

DE LA REZA, R.; Drake, N. A.; da Silva, L. (1996) "Lithium Enrichment–Mass-Loss Connection in K Giant Stars", *ApJL*,456 , 115, 10.1086/309874

DE LA REZA, R.; DRAKE, N. A.; DA SILVA, L. ; TORRES, C. A. O.; MARTIN, E. L. (1997) "On a Rapid Lithium Enrichment and Depletion of K Giant Stars", *ApJL*, 482, p. 77, 10.1086/310685

DRAZDAUSKAS, A.; TAUTVAIŠIENĖ, G.; SMILJANIC, R.; BAGDONAS, V.; CHORNIY, Y. (2016) "Chemical composition of evolved stars in the young open clusters NGC 4609 and NGC 5316", *MNRAS*, 462, p. 794, 10.1093/mnras/stw1701

DIAS, W. S.; ALESSI, B. S.; MOITINHO, A.; LÉPINE, J. R. D. (2002) "New catalogue of optically visible open clusters and candidates", *A&A*, 389, p. 871, 10.1051/0004-6361:20020668

DWIVEDI, P. H.; BRANCH, D.; HUFFAKER, J. N.; BELL, R. A. (1978) "Rotational Dependence of Franck-Condon Factors for Selected Band Systems of cn, C_2, co, and CH", *ApJS*, 36, p. 573, 10.1086/190511

DELGADO MENA, E.; TSANTAKI, M.; SOUSA, S. G.; KUNITOMO, M.; Adibekyan, V. (2016) "Searching for Li-rich giants in a sample of 12 open clusters. Li enhancement in two stars with substellar companions", *A&A*, 587, p. 66, 10.1051/0004-6361/201527196

DRAKE, N. A.; Pereira, C. B. (2008) "Light Element Abundances in Two Chemically Peculiar Stars: HD 104340 and HD 206983", *AJ*, 135, p. 1070, 10.1088/0004-6256/135/3/1070

DA SILVEIRA, M. D.; PEREIRA, C. B.; DRAKE, N. A. (2018) "Red giants and yellow stragglers in the young open cluster NGC 2447", *MNRAS*, 476, p. 4907, 10.1093/mnras/sty265

DAVIS, S. P.; PHILLIPS, J. G. (1963) "The Red System of the CN Molecule", Univ. California Press, Berkley, CA

D'ORAZI, V.; MAGRINI, L.; RANDICH, S.; GALLI, D.; BUSSO, M.; SESTITO, P. (2009) "Enhanced Production of Barium in Low-Mass Stars: Evidence from Open Clusters", *ApJL*, 693, p. 31, 10.1088/0004-637X/693/1/L31

DEEPAK; REDDY, B. E. (2019) "Study of Lithium-rich giants with the GALAH spectroscopic survey", *MNRAS*, 484, p. 2000, 10.1093/mnras/stz128

DA SILVA, L.; GIRARDI, L.; PASQUINI, L.; SETIAWAN, J.; VON DER Lühe, O.; et al. (2006) "Basic physical parameters of a selected sample of evolved stars", *A&A*, 458, p. 609, 10.1051/0004-6361:20065105

DRAKE, N. A.; DE LA REZA, R.; DA SILVA, L.; LAMBERT, D. L. (2020) "Rapidly Rotating Lithium-rich K Giants: The New Case of the Giant PDS 365", *AJ*, 123, 2703, 10.1086/339968

DA SILVA, L.; DE LA REZA, R.; BARBUY, B. (1995) "Carbon Isotope Ratios in Very Lithium-Rich K Giants", *ApJ*, 448, L41, 10.1086/309593

DRAKE, N. A.; DE LA REZA, R.; SMITH, V. V.; CUNHA, K. "On producers of cosmic organic compounds: exploring the boron abundance in lithium-rich K giant stars", *IAU Symposium*, 332, p. 237, 10.1017/S1743921317006871

EATON, J. A. (1995) "Hα Measurements for Cool Giants", *AJ*, 109, p. 1797, 10.1086/117409

FEKEL, F. C. (1997) "Rotational Velocities of Late-Type Stars", *PASP*, 109, p. 514, 10.1086/133908

FRIEL, E. D. (1995) "The Old Open Clusters Of The Milky Way", *ARAA*, 33, p. 381, 10.1146/annurev.aa.33.090195.002121

FERREIRA, F. A.; SANTOS, J. F. C.; CORRADI, W. J. B.; MAIA, F. F. S.; ANGELO, M. S. (2019) "Three new Galactic star clusters discovered in the field of the open cluster NGC 5999 with Gaia DR2", *MNRAS*, 483, p. 5508, 10.1093/mnras/sty3511

FERREIRA, F. A.; CORRADI, W. J. B.; MAIA, F. F. S.; ANGELO, M. S.; SANTOS, J. F. C., JR. (2020) "Discovery and astrophysical properties of Galactic open clusters in dense stellar fields using Gaia DR2", *MNRAS*, 496, p. 2021, 10.1093/mnras/staa1684

FEKEL, F. C.; BALACHANDRAN, S. (1993) "Lithium and Rapid Rotation in Chromospherically Active Single Giants", *ApJ*, 403, p. 708, 10.1086/172242

GELLER, A. M.; LEINER, E. M.; BELLINI, A.; GLEISINGER, R.; HAGGARD, D.; et al. (2017a) "On the Origin of Sub-subgiant Stars. I. Demographics", *ApJ*, 840, p. 66, 10.3847/1538-4357/aa6af3

GELLER, A. M.; LEINER, E. M.; CHATTERJEE, S; LEIGH, N. W. C.; MATHIEU, R. D.; et al. (2017b) "On the Origin of Sub-subgiant Stars. III. Formation Frequencies", *ApJ*, 842, p. 1, 10.3847/1538-4357/aa72ef

GAO, Q.; SHI, J.-R; YAN, H.-L.; YAN, T.-S.; XIANG, M.-S.; et al. (2019) "", *ApJS*, 245, p. 33, 10.3847/1538-4365/ab505c

GAIA COLLABORATION; BROWN, A. G. A.; VALLENARI, A.; PRUSTI, T.; DE BRUIJNE, J. H. J.; et al. (2018) "Gaia Data Release 2. Summary of the contents and survey properties", *A&A*, 616, p. 1, 10.1051/0004-6361/201833051

GIRARDI, L.; BRESSAN, A.; BERTELLI, G.; CHIOSI, C. (2000) "Evolutionary tracks and isochrones for low- and intermediate-mass stars: From 0.15 to 7 M_{sun}, and from Z=0.0004 to 0.03", *A&AS*, 141, p. 371, 10.1051/aas:2000126

GRAY, D. F. (2005) "The observation and analysis of stellar photospheres", Cambridge University Press

GENOVALI, K.; LEMASLE, B.; BONO, G.; ROMANIELLO, M.; FABRIZIO, M.; et al. (2014) "On the fine structure of the Cepheid metallicity gradient in the Galactic thin disk", *A&A*, 566, p. 37, 10.1051/0004-6361/201323198

GIRARDI, L. (2016) "Red Clump Stars", *ARAA*, 54, p. 95, 10.1146/annurev-astro-081915-023354

GENOVALI, K.; LEMASLE, B.; BONO, G.; ROMANIELLO, M.; PRISMAS, F.; et al. (2013) "", *A&A*, 554, p. 132, 10.1051/0004-6361/201321650

GRATTON, R. G. & D'ANTONA, F. (1989) "HD 39853 : a high velocity K5 III star with an exceptionally large Li content", *A&A*, 215, p. 66

GILROY, K. K. (1989) "Carbon Isotope Ratios and Lithium Abundances in Open Cluster Giants", *ApJ*, 347, p. 835, 10.1086/168173

GONZÁLEZ HERNÁNDEZ, J. I.; BONIFACIO, P. (2009) "A new implementation of the infrared flux method using the 2MASS catalogue", *A&A*, 497, p. 497

HOBBS, L. M.; THORBURN, J. A.; REBULL, L. M. (1999) "Lithium Isotope Ratios in Halo Stars. III", *ApJ*, 523, p. 797, 10.1086/307757

HUBER, K. P., HERZBERG, G. (1979), "Molecular Spectra and Molecular Structure, IV: Constants of Diatomic Molecules", Van Nostrand Reinhold, New York

HERWIG, F. (2005) "Evolution of Asymptotic Giant Branch Stars", *ARA&A*, 43, p. 435, 10.1146/annurev.astro.43.072103.150600

HOLANDA, N.; PEREIRA, C. B.; DRAKE, N. A. (2019) "Chemical analysis of K giants in the young open cluster NGC 2345", *MNRAS*, 482, p. 5275, 10.1093/mnras/sty2991

HOLANDA, N.; DRAKE, N. A.; PEREIRA, C. B. (2020a) "HD 150382: A Lithium-rich Star at the Early-AGB Stage?", *AJ*, 159, p. 9, 10.3847/1538-3881/ab5528

HILLS, J. G.; DAY, C. A. (1976) "Stellar Collisions in Globular Clusters", *ApL*, 17, p. 87

HOU, J. L.; PRANTZOS, N.; BOISSIER, S. (2000) "Abundance gradients and their evolution in the Milky Way disk", *A&A*, 362, p. 924

HOLANDA, N.; DRAKE, N. A.; PEREIRA, C. B. (2020b) "TYC 8327-1678-1: a new super lithium-rich K giant", *MNRAS*, 498, p. 77, 10.1093/mnras/staa2271

HOLANDA, N.; DRAKE, N. A.; DA SILVA, J. R. P.; PEREIRA, C. B. (2020c) "NGC 6124: a young open cluster with anomalous- and fast-rotating giant stars", em preparação

HENDEN, A. A.; LEVINE, S.; TERRELL, D.; WELCH, D. L. (2015) "APASS - The Latest Data Release", *American Astronomical Society Meeting Abstracts*, 255, p. 336

HEKKER, S.; MELÉNDEZ, J. (2007) "Precise radial velocities of giant stars. III. Spectroscopic stellar parameters", *A&A*, 475, p. 1003, 10.1051/0004-6361:20078233

Houk, N. (1978) "Michigan catalogue of two-dimensional spectral types for the HD stars"

HOUK, N.; SWIFT, C. (1999) "Michigan catalogue of two-dimensional spectral types for the HD Stars ; vol. 5"

HAWKINS, K.; MASSERON, T.; JOFRÉ, P.; GILMORE, G.; ELSWORTH, Y.; HEKKER, S. (2016) "An accurate and self-consistent chemical abundance catalogue for the APOGEE/Kepler sample", *A&A*, 594, p. 43, 10.1051/0004-6361/201628812

Hatzidimitriou, D.; Held, E. V.; Tognelli, E.; Bragaglia, A.; Magrini, L.; Bravi, L.; et al. (2019) "The Gaia-ESO Survey: The inner disc, intermediate-age open cluster Pismis 18", *A&A*, 626, p. 90, 10.1051/0004-6361/201834636

HEITER, U.; SOUBIRAN, C.; NETOPIL, M.; PAUZEN, E. (2014) "On the metallicity of open clusters. II. Spectroscopy", *A&A*, 561, p. 93, 10.1051/0004-6361/201322559

IVANOVA, N.; JUSTHAM, S.; CHEN, X. et al. (2013) "Common envelope evolution: where we stand and how we can move forward", *Astron Astrophys Rev*, 21, p. 59, https://doi.org/10.1007/s00159-013-0059-2

IBEN, I. JR.; RENZINI, A. (1983) "Asymptotic giant branch evolution and beyond", *ARAA*, 21, p. 271, 10.1146/annurev.aa.21.090183.001415

IBEN, I. JR. (1967) "Stellar Evolution. VI. Evolution from the Main Sequence to the Red-Giant Branch for Stars of Mass 1 M_{sun}, 1.25 M_{sun}, and 1.5 M_{sun}", *ApJ*, 147, p. 624

IBEN, I. (1968) "Age and Initial Helium Abundance of Stars in the Globular Cluster M15", *Nature*, 230, p. 143, 10.1038/220143a0

JORDI, C.; GEBRAN, M.; CARRASCO, J. M.; DE BRUIJNE, J.; VOSS, H.; et al. (2010) "Gaia broad band photometry", *A&A*, 523, p. 48, 10.1051/0004-6361/201015441

JORISSEN, A.; VAN WINCKEL, H.; SIESS, L.; ESCORZA, A.; POURBAIX, D.; VAN ECK, S. (2020) "Li-rich K giants, dust excess, and binarity", *A&A*, 639, p. 7, 10.1051/0004-6361/202037585

JACOBSON, H. R.; FRIEL, E. D. (2013) c"Zirconium, Barium, Lanthanum, and Europium Abundances in Open Clusters", *AJ*, 145, p. 107, 10.1088/0004-6256/145/4/107

KATIME SANTRICH, O. J.; PEREIRA, C. B.; DRAKE, N. A. (2013) "Chemical analysis of giant stars in the young open cluster NGC 3114", *A&A*, 554, p. 2, 10.1051/0004-6361/201220252

KRAFT, R. P. (1966) "Stellar Rotation and Stellar Evolution among Cepheids and Other Luminous Stars in the Hertzsprung Gap", *ApJ*, 144, p. 1008, 10.1086/148699

KRAFT, R. P. (1970) "Stellar Rotation", *Spectroscopic Astrophysics. An Assessment of the Contributions of Otto Struve*, p. 385, Ed. HERBIG, G. H.; STRUVE, O.

KHARCHENKO, N. V.; PISKUNOV, A. E.; RÖSER, S.; SCHILBACH, E.; SCHOLZ, R. -D. (2005) "109 new Galactic open clusters", *A&A*, 440, p. 403, 10.1051/0004-6361:20052740

KIRBY, E. N.;GUHATHAKURTA, P.; ZHANG, A. J.; HONG, J.; GUO, M.; et al. (2016) "Lithium-rich Giants in Globular Clusters", *ApJ*, 819, p. 135, 10.3847/0004-637X/819/2/135

KARAKAS, A. I.; LATTANZIO, J. C. (2014) "The Dawes Review 2: Nucleosynthesis and Stellar Yields of Low- and Intermediate-Mass Single Stars", *PASA*, 31, p. 30, 10.1017/pasa.2014.21

KAUFER, A.; STAHL, O.; TUBBESING, S.; NØRREGAARD, P.; AVILA, G.; et al. (1999) "Commissioning FEROS, the new high-resolution spectrograph at La-Silla", *The Messenger*, 95, p. 8

KRUMHOLZ, M. R.; MCKEE, C. F.; BLAND-HAWTHORN, J. (2019) "Star Clusters Across Cosmic Time", *ARAA*, 57, p. 227, 10.1146/annurev-astro-091918-104430

KUPKA, F.; PISKUNOV, N.; RYABCHIKOVA, T. A.; STEMPELS, H. C.; Weiss, W. W. (1999) "VALD-2: Progress of the Vienna Atomic Line Data Base", *A&AS*, 138, p. 119, 10.1051/aas:1999267

KOELBLOED, D. (1959) "Three-colour photometry of the three southern open clusters NGC 3532, 6475 (M7) and 6124", 14, p. 265

KOVŽaCS I. (1969) "Rotational Structure in the Spectra of Diatomic Molecules, Akademiai Kiado", Budapest

KURUCZ, R. "ATLAS9 Stellar Atmosphere Programs and 2 km/s grid"

LAGARDE, N.; REYLÉ, C.; ROBIN, A. C.; TAUTVAIŠIENĖ, G.; DRAZDAUSKAS, A.; et al. (2019), *A&A*, 621, A24, 10.1051/0004-6361/201732433

LANDSMAN, W.; APARICIO, J.; BERGERON, P.; Di STEFANO, R.; STECHER, T. P. (1997) "S1040 in M67: A Post–Mass Transfer Binary with a Helium Core White Dwarf", *ApJL*, 481, p. 93, 10.1086/310654

LAMBERT, D. L.; HEATH, J. E.; LEMKE, M.; DRAKE, J. (1996) "The Chemical Composition of Field RR Lyrae Stars. I. Iron and Calcium", *ApJS*, 103, p. 183, 10.1086/192274

LAPASSET, E., CLARIÁ, J. J.; MERMILLIOD, J.-C. (2000) "UBV photometric study and basic parameters of the southern open cluster NGC 2539" , *A&A*, 361, p. 945

LEINER, E.; MATHIEU, R. D.; GELLER, A. M. (2017) "On the Origin of Sub-subgiant Stars. II. Binary Mass Transfer, Envelope Stripping, and Magnetic Activity", *ApJ*, 840, p. 67, 10.3847/1538-4357/aa6aff

LUGARO, M.; KARAKAS, A. I.; BRUNO, C. G.; ALIOTTA, M.; NITTLER, L. R.; et al. (2017) "Origin of meteoritic stardust unveiled by a revised proton-capture rate of ^{17}O", *Nature Astronomy*, 1, p. 27, 10.1038/s41550-016-0027

LIND, K.; ASPLUND, M.; BARKLEM, P. S. (2009) "Departures from LTE for neutral Li in late-type stars", *A&A*, 503, p. 541, 10.1051/0004-6361/200912221

LIND, K.; ASPLUND, M.; BARKLEM, P. S; BELYAEV, A. K. (2011) "Non-LTE calculations for neutral Na in late-type stars using improved atomic data", *A&A* 528, A103, 10.1051/0004-6361/201016095

LUCK, R. E. & HEITER, U. (2007) "Giants in the Local Region", *AJ*, 133, p. 2464, 10.1086/513194

LAGARDE, N.; DECRESSIN, T.; CHARBONNEL, C.; EGGENBERGER, P.; EKSTRÖM, S.; PALACIOS, A. (2012) "Thermohaline instability and rotation-induced mixing. III. Grid of stellar models and asymptotic asteroseismic quantities from the pre-main sequence up to the AGB for low- and intermediate-mass stars of various metallicities", *A&A*, 543, p. 108, 10.1051/0004-6361/201118331

LATTANZIO, J.; FORESTINI, M. (1999) "Nucleosynthesis in AGB Stars", *Asymptotic Giant Branch Stars*, Le Bertre, T. and Lebre, A. and Waelkens, C., 191, p. 31

LAWLER, J. E.; WICKLIFFE, M. E.; DEN HARTOG, E. A.; SNEDEN, C. (2001) "Improved Laboratory Transition Parameters forEu II and Application to the Solar Europium Elemental and Isotopic Composition", *ApJ*, 563, p. 1075, 10.1086/323407

LAMBERT, D. L. (1978) "The abundances of the elements in the solar photosphere - VIII. Revised abundances of carbon, nitrogen and oxygen", *MNRAS*, 182, p. 249, 10.1093/mnras/182.2.249

LUO, A.-L.; ZHAO, Y.-H.; ZHAO, G.; DENG, L.-C.; LIU, X.-W.; et al. (2015) "The first data release (DR1) of the LAMOST regular survey", *Research in Astronomy and Astrophysics*, 15, p. 1095, 10.1088/1674-4527/15/8/002

LIU, W. M.; CHABOYER, B. (2000) "The Relative Age of the Thin and Thick Galactic Disks", *ApJ*, 544, p. 818, 10.1086/317231

LADA, C. J.; LADA, E. A. (2003) "Embedded Clusters in Molecular Clouds", *ARAA*, 41, p. 57, 10.1146/annurev.astro.41.011802.094844

LAMBERT, D. L. (1994), in Jorgensen U. G., ed., Lecture Notes in Physics, Vol. 428, IAU Colloq. 146, Molecules in the Stellar Environment. Springer- Verlag, Berlin, p. 1

MAGRINI, L.; SESTITO, P.; RANDICH, S.; GALLI, D. (2009) "The evolution of the Galactic metallicity gradient from high-resolution spectroscopy of open clusters", *A&A*, 494, p. 95, 10.1051/0004-6361:200810634

MACIEL, W. J. (1999) "Introdução à Estrutura e Evolução Estelar", Vol. 24. *EDUSP*

MIHALAS, D. (1978) "Stellar Atmospheres", *stat*

MARTINEZ, C. F.; HOLANDA, N; PEREIRA, C. B.; DRAKE, N. A. (2020) "High-resolution spectroscopy of red giants and 'yellow stragglers' in the southern open cluster NGC 2539", *MNRAS*, 494, p. 1470, 10.1093/mnras/staa647

McCrea, W. H. (1964) "Extended main-sequence of some stellar clusters", *MNRAS*, 128, p. 147, 10.1093/mnras/128.2.147

MUCCIARELLI, A.; CAFFAU, E.; FREYTAG, B.; LUDWIG, H. -G.; BONIFACIO, P. (2008) "The solar photospheric abundance of europium. Results from CO5BOLD 3D hydrodynamical model atmospheres", *A&A*, 484, p. 841, 10.1051/0004-6361:20079327

MISHENINA, T. V.; BIENAYMÉ, O.; GORBANEVA, T. I.; CHARBONNEL, C.; SOUBIRAN, C.; et al. (2006) "Elemental abundances in the atmosphere of clump giants", *A&A*, 456, p. 1109, 10.1051/0004-6361:20065141

MASSAROTTI, A.; LATHAM, D. W.; STEFANIK, R. P.; FOGEL, J. (2008) "Rotational and Radial Velocities for a Sample of 761 HIPPARCOS Giants and the Role of Binarity", , 209, p. 135, 10.1088/0004-6256/135/1/209

MONACO, L.; BPFFIN; H. M. J.; BONIFACIO, P.; VILLANOVA, S.; CARRARRO, G.; et al. (2014) "A super lithium-rich red-clump star in the open cluster Trumpler 5", *A&A*, 564, p. 6, 10.1051/0004-6361/201323348

MAIORCA, E.; MAGRINI, L.; BUSSO, M.; RANDICH, S.; PALMERINI, S.; TRIPPELLA, O. (2012) "News on the s Process from Young Open Clusters", *ApJ*, 747, p. 53, 10.1088/0004-637X/747/1/53

MELÉNDEZ, J.; BARBUY, B. (1999) "Oscillator Strengths and Damping Constants for Atomic Lines in the J and H Bands", *ApJS*, 124, p. 527, 10.1086/313261

MOFFAT, A. F. J. (1974) "NGC 2345, a moderately young open cluster in CMa", *A&A*, 16, 33

MCDONALD, I.; ZIJLSTRA, A. A.; WATSON, R. A. (2017) "Fundamental parameters and infrared excesses of Tycho-Gaia stars", *MNRAS*, 471, p. 770, 10.1093/mnras/stx1433

MERMILLIOD, J. C.; MAYOR, M.; UDRY, S. (2008) "Red giants in open clusters. XIV. Mean radial velocities for 1309 stars and 166 open clusters", *A&A*, 485, p. 303, 10.1051/0004-6361:200809664

NESVACIL, N.; STÜTZ, CH.; WEISS, W. W. "ATLAS model atmospheres", *GAIA Spectroscopy: Science and Technology*, p. 173, Ed. MUNARI, U.

NETOPIL, M.; PAUNZEN, E.; HEITER, U.; SOUBIRAN, C (2016) "On the metallicity of open clusters. III. Homogenised sample", *A&A*, 585, p. 150, 10.1051/0004-6361/201526370

NESTEROV, V. V.; KUZMIN, A. V.; ASHIMBAEVA, N. T.; VOLCHKOV, A. A.; RÖSER, S.; BASTIAN, U. (1995) "The Henry Draper Extension Charts: A catalogue of accurate positions, proper motions, magnitudes and spectral types of 86933 stars", *A&AS*, 110, p. 367

NEUGEBAUER, G.; HABING, H. J.; VAN DUINEN, R.; AUMANN, H. H.; BAUD, B.; et al. (1984) "The Infrared Astronomical Satellite (IRAS) mission", *ApJL*, 278, p. 1, 10.1086/184209

PETERSON, R. C.; TARBELL, T. D.; CARNEY, B. W. (1983) "The rotation of horizontal-branch stars. I. Members of the field", *ApJ*, 265, p. 972, 10.1086/160739

PISKUNOV, A. E.; SCHILBACH, E.; KHARCHENKO, N. V.; RÖSER, S.; SCHOLZ, R. D. (2008) "Tidal radii and masses of open clusters", 477, p. 165, 10.1051/0004-6361:20078525

PRIVITERA, G.; MEYNET, G.; EGGENBERGER, P.; GEORGY, C.; EKSTRÖM, S.; et al. (2016) "High surface magnetic field in red giants as a new signature of planet engulfment?", *A&AL*, 593, p.15, 10.1051/0004-6361/201629142

PIATTI, A. E.; CLARIÁ, J. J.; BICA, E.; GEISLER, D.; MINNITI, D. (1998) "A Photometric and Spectroscopic Study of the Southern Open Clusters PISMIS 18, PISMIS 19, NGC 6005, and NGC 6253", *AJ*, 116, p. 801, 10.1086/300443

PAGEL, B. E. (2009). "Nucleosynthesis and chemical evolution of galaxies", Cambridge University Press.

PEÑA SUÁREZ, V. J.; SALES SILVA, J. V.; KATIME SANTRICH, O. J.; DRAKE, N. A.; PEREIRA, C. B. (2018) "High-resolution Spectroscopic Observations of Single Red Giants in Three Open Clusters: NGC 2360, NGC 3680, and NGC 5822", *ApJ*, 854, p. 184, 10.3847/1538-4357/aaa017

PHILLIPS, J. G.; DAVIS, S. P. (1968) "The Swan system of the C2 molecule. The spectrum of the HgH molecule", Vol. 2, Univ. of California Press, California

PORTEGIES ZWART, S. F.; MCMILLAN, S. L. W.; GIELES, M. (2010) "Young Massive Star Clusters", *ARAA*, 48, p. 431, 10.1146/annurev-astro-081309-130834

PICKLES, A.; Depagne, É. (2010) "All-Sky Spectrally Matched UBVRI - ZY and u^2 g^2 r^2 i^2 z^2 Magnitudes for Stars in the Tycho2 Catalog", *PASP*, 898, p. 1437, 10.1086/657947

OVERBEEK, J. C.; FRIEL, E. D.; JACOBSON, H. R. (2016) "New Neutron-capture Measurements in 23 Open Clusters. I. The r-Process", *ApJ*, 824, p. 75, 10.3847/0004-637X/824/2/75

REBULL, L. M.;CARLBERG, J. K.; GIBBS, J. C.; DEEB, J. E.; LARSEN, E.; et al. (2015) "On Infrared Excesses Associated with Li-rich K Giants", *AJ*, 150, p. 123, 10.1088/0004-6256/150/4/123

REDDY, A. B. S.; LAMBERT, D. L.; GIRIDHAR, S. (2016) "The evolution of the Milky Way: new insights from open clusters", *MNRAS*, 463, p. 4366, 10.1093/mnras/stw2287

REDDY, B. E.; TOMKIN, J.; LAMBERT, D. L.; ALLENDE PRIETO, C. (2003) "The chemical compositions of Galactic disc F and G dwarfs", *MNRAS*, 340, p. 304, 10.1046/j.1365-8711.2003.06305.x

REDDY, A. B. S.; LAMBERT, D. L. (2019) "Comprehensive abundance analysis of red giants in the open clusters Stock 2, NGC 2168, 6475, 6991, and 7762", *MNRAS*, 485, p. 3623, 10.1093/mnras/stz468

REDDY, A. B. S.; GIRIDHAR, S.; LAMBERT, D. L. (2012) "Comprehensive abundance analysis of red giants in the open clusters NGC 752, 1817, 2360 and 2506", *MNRAS*, 419, p. 1350, 10.1111/j.1365-2966.2011.19791.x

REDDY, A. B. S.; GIRIDHAR, S.; LAMBERT, D. L. (2013) "Comprehensive abundance analysis of red giants in the open clusters NGC 2527, 2682, 2482, 2539, 2335, 2251 and 2266", *MNRAS*, 431, p. 3338, 10.1093/mnras/stt412

REDDY, A. B. S.; GIRIDHAR, S.; LAMBERT, D. L. (2015) "Comprehensive abundance analysis of red giants in the open clusters NGC 1342, 1662, 1912, 2354 and 2447", *MNRAS*, 450, p. 4301, 10.1093/mnras/stv908

REDDY, B. E.; LAMBERT, D. L. (2005) "Three Li-rich K Giants: IRAS 12327-6523, 13539-4153, and 17596-3952", *AJ*, 129, p. 2831, 10.1086/430190

SALES SILVA, J. V.; PEÑA SUÁREZ, V. J.; KATIME SANTRICH, O. J.; PEREIRA, C. B.; DRAKE, N. A.; ROIG, F. (2014) "High-resolution Spectroscopic Observations of Binary Stars and Yellow Stragglers in Three Open Clusters : NGC 2360, NGC 3680, and NGC 5822", *ApJ*, 148, p. 83, 10.1088/0004-6256/148/5/83

SANTOS, N. C.; LOVIS, C.; PACE, G.; MELENDEZ, J.; NAEF, D. (2009) "Metallicities for 13 nearby open clusters from high-resolution spectroscopy of dwarf and giant stars. Stellar metallicity, stellar mass, and giant planets", *A&A*, 493, p. 309, 10.1051/0004-6361:200811093

SCHADEE, A. (1964) "The formation of molecular lines in the solar spectrum", *Bull. Astron. Inst. Netherlands*, 17, p. 311

SMILJANIC, R.; FRANCIOSINI, E.; BRAGAGLIA, A.; TAUTVAIŠIENĖ, G.; FU, X.; et al. (2018) "The Gaia-ESO Survey: properties of newly discovered Li-rich giants",*A&A*, 617, A4, 10.1051/0004-6361/201833027

SMITH, V. V.; LAMBERT, D. L. (1989) "Synthesis of Lithium and s-Process Elements in Small Magellanic Cloud Asymptotic Giant Branch Stars", *ApJ*, 345, 75, 10.1086/185556

SMITH, V. V.; LAMBERT, D. L.; NISSEN, P. E. (1998) "Isotopic Lithium Abundances in Nine Halo Stars", *ApJ*, 506, p. 405, 10.1086/306238

SUN, W.; LI, C.; DENG, L.; DE GRIJS, R. (2019a) "Tidal-locking-induced Stellar Rotation Dichotomy in the Open Cluster NGC 2287?", *ApJ*, 883, p. 182, 10.3847/1538-4357/ab3cd0

SUN, W.; DE GRIJS, R.; DENG, L.; ALBROW, M. D. (2019b) "Stellar Rotation and the Extended Main-sequence Turnoff in the Open Cluster NGC 5822", *ApJ*, 876, p. 113, 10.3847/1538-4357/ab16e4

SNEDEN, C. (1973) "Carbon and Nitrogen Abundances in Metal-Poor Stars.", Thesis (PH.D.), THE UNIVERSITY OF TEXAS AT AUSTIN

SNEDEN, C.; LAMBERT, D. L. (1982) "The CN red system in the solar spectrum", *ApJ*, 259, p. 381, 10.1086/160175

SACKMANN, I. -J.; BOOTHROYD, A. I. (1999) "Creation of ^{7}Li and Destruction of ^{3}He, ^{9}Be, ^{10}B, and ^{11}B in Low-Mass Red Giants, Due to Deep Circulation", *ApJ*, 510, p. 217, 10.1086/306545

SACKMANN, I. -J.; SMITH, R. L.; DESPAIN, K. H. (1974) "Carbon and eruptive stars: surface enrichment of lithium, carbon, nitrogen, and ^{13}C by deep mixing", *ApJ*, 187, p. 555, 10.1086/152666

SKRUTSKIE, M. F.; CUTRI, R. M.; STIENING, R.; WEINBERG, M. D.; SCHNEIDER, S.; et al. (2006) "", *AJ*, 131, p. 1163, 10.1086/498708

SCALO, J. M.; DESPAI, K. H.; ULRICH, R. K. (1975) "Studies of evolved stars. V. Nucleosynthesis in hot-bottom convective envelopes", *ApJ*, 196, p. 805, 10.1086/153471

SMITH, V. V.; LAMBERT, D. L. (1990) "On the Occurrence of Enhanced Lithium in Magellanic Cloud Red Giants", *ApJ*, 361, p. 69, 10.1086/185829

STEPHENSON, C. B.; SANDULEAK, N. (1971) "Luminous stars in the Southern Milky Way", *Publications of the Warner & Swasey Observatory*, 1, 1

SIESS, L.; LIVIO, M. (1999a) "The accretion of brown dwarfs and planets by giant stars - I. Asymptotic giant branch stars", *MNRAS*, 304, p. 925, 10.1046/j.1365-8711.1999.02376.x

SIESS, L.; LIVIO, M. (1999b) "The accretion of brown dwarfs and planets by giant stars - II. Solar-mass stars on the red giant branch", *MNRAS*, 308, 1133, 10.1046/j.1365-8711.1999.02784.x

STRASSMEIER, K. G.; WEINGRILL, J.; GRANZER, T.; BIHAIN, G.; WEBER, M.; et al. (2015) "Stellar rotation, binarity, and lithium in the open cluster IC 4756", *A&A*, 580, p. 66, 10.1051/0004-6361/201525756

SOUBIRAN, C.; CANTAT-GAUDIN, T.; ROMERO-GÓMEZ, M.; CASAMIQUELA, L.; JORDI, C.; et al. (2018) "Open cluster kinematics with Gaia DR2", *A&A*, 619, p. 155, 10.1051/0004-6361/201834020

STRASSMEIER, K.; WASHUETTL, A.; GRANZER, T.; SCHECK, M.; WEBER, M. (2000) "", *A&AS*, 142, p. 275, 10.1051/aas:2000328

SODERBLOM, D. R. (2010) "The Ages of Stars", *ARAA*, 48, p. 581, 10.1146/annurev-astro-081309-130806

SIMON, T.; DRAKE, S. A. (1989) "The Evolution of Chromospheric Activity of Cool Giant and Subgiant Stars", *ApJ*, 346, p. 303, 10.1086/168012

SINGH, R.; REDDY, B. E.; BHARAT KUMAR, Y.; ANTIA, H. M. (2019) "Survey of Li-rich Giants among Kepler and LAMOST Fields: Determination of Li-rich Giants' Evolutionary Phase", *ApJ*, 878, p. 21, 10.3847/2041-8213/ab2599

THE, P. -S. (1965) "A photometric study of the galactic cluster NGC 6124", *Contributions from the Bosscha Observervatory*, 33, p. 1,

THIELEMANN, F. -K.; ARGAST, D.; BRACHWITZ, F.; MARTINEZ-PINEDO, G.; RAUSCHER, T.; et al. (2002) "Nucleosynthesis and Stellar Evolution", *Ap&SS*, 281, p. 25, 10.1023/A:1019543110473

THIELEMANN, F. -K.; EICHLER, M.; PANOV, I. V.; WEHMEYER, B. (2017) "Neutron Star Mergers and Nucleosynthesis of Heavy Elements", *Annual Review of Nuclear and Particle Science*, 67, p. 253, 10.1146/annurev-nucl-101916-123246

TAKEDA, Y.; SATO, B.; MURATA, D. (2008) "Stellar Parameters and Elemental Abundances of Late-G Giants", *PASJ*, 60, p. 781, 10.1093/pasj/60.4.781

TAKEDA, Y.; TAJITSU, A. (2017) "On the observational characteristics of lithium-enhanced giant stars in comparison with normal red giants^{y}", *PASJ*, 69, p. 74, 10.1093/pasj/psx057

TING, Y.-S.; HAWKINS, K.; RIX, H.-W. (2018) "A Large and Pristine Sample of Standard Candles across the Milky Way: ∼100,000 Red Clump Stars with 3% Contamination", *ApJL*, 858, 7, 10.3847/2041-8213/aabf8e

Vergne, M. M.; FEINSTEIN, C.; MART´NEZ, R.; ORSATTI, A. M.; ALVAREZ, M. P. (2010) "Optical polarization observations in the Scorpius region: NGC 6124", *MNRAS*, 403, p. 2041, 10.1111/j.1365-2966.2010.16242.x

WALLERSTEIN, G.; KNAPP, G. R. (1998) "CARBON STARS", *ARAA*, 36, p. 369, 10.1146/annurev.astro.36.1.369

WALLERSTEIN, G. & SNEDEN, C. (1982) "A K giant with an unusually high abundance of lithium : HD 112127", *ApJ*, 255, p. 577, 10.1086/159859

WU, Z.-Y.; ZHOU, X.; MA, J.; DU, C.-H. (2009) "The orbits of open clusters in the Galaxy", *MNRAS*, 399, p. 2146, 10.1111/j.1365-2966.2009.15416.x

WORLEY, C. E.; DOUGLASS, G. G. (1996) "VizieR Online Data Catalog: The Washington Visual Double Star Catalog, 1996.0 (Worley+, 1996", I/237

WYLLER, A. A. (1966) "New C^{13} Indicators in Stellar Spectra", *ApJ*, 143, p. 828, 10.1086/148560

WRIGHT, E. L.; EISENHARDT, P. R. M.; MAINZER, A. K.; RESSLER, M. E.; CUTRI, R. M (2010) "The Wide-field Infrared Survey Explorer (WISE):

Mission Description and Initial On-orbit Performance", *AJ*, 140, p. 1868, 10.1088/0004-6256/140/6/1868

VERAS, D. (2016) "Post-main-sequence planetary system evolution", *R. Soc. open sci*, 3, p. 150571, http://dx.doi.org/10.1098/rsos.150571

ZHANG, X.; JEFFERY, C. S.; LI, Y.; BI, S. (2020) "Population Synthesis of Helium White Dwarf-Red Giant Star Mergers and the Formation of Lithium-rich Giants and Carbon Stars", *ApJ*, 889, p. 33, 10.3847/1538-4357/ab5e89

ZHOU, Y. T.; SHI, J. R.; YAN, H. L.; GAO, Q.; ZHANG, J. B.; et al. (2018) "Super lithium-rich K giant with low ^{12}C to ^{13}C ratio", *A&A*, 615, p. 74, 10.1051/0004-6361/201730389

ZAČS, L.; ALKSNIS, O.; BARZDIS, A.; LAURA, A.; MUSAEV, F. A.; BONDAR, A.; SPERAUSKAS, J. (2011) "Spectroscopy of red giants in the open clusters NGC 1545 and Tr2", *MNRAS*, 417, p. 649, 10.1111/j.1365-2966.2011.19309.x

ZHAO, G.; ZHAO, Y.-H.; CHU, Y.-Q.; JING, Y.-P.; DENG, L.-C.; et al. (2012) "LAMOST spectral survey — An overview", *Research in Astronomy and Astrophysics*, 12, p. 723, 10.1088/1674-4527/12/7/002

ZIELIŃSKI, P.; NIEDZIELSKI, A.; WOLSZCZAN, A.; ADAMÓW, M.; NOWAK, G. (2012) "The Penn State-Toruń Centre for Astronomy Planet Search stars. I. Spectroscopic analysis of 348 red giants", *A&A*, 547, p. 91, 10.1051/0004-6361/201117775

YONG, D.; CARNEY, B. W.; FRIEL, E. D. (2012) "Elemental Abundance Ratios in Stars of the Outer Galactic Disk. IV. A New Sample of Open Clusters", *AJ*, 144, p. 95, 10.1088/0004-6256/144/4/95

YAN, H.-L.; SHI, J.-R.; Zhou, Y.-T.; CHEN, Y.-S.; LI, E.-T.; et al. (2018) "The nature of the lithium enrichment in the most Li-rich giant star", *Nature*, 2, 790, 10.1038/s41550-018-0544-7

Apêndice A

Tabelas Extras

Tabela A.1: Properties of the Li-rich giants adopted for comparison with HD 150382. The references code are as follow: TT17: TAKEDA & TAJITSU (2017); ST00: STRASSMEIER ET AL. (2000); GD89:GRATTON & D'ANTONA (1989); DS95; DA SILVA ET AL. (1995); RL05: REDDY & LAMBERT (2005); RL16: REDDY ET AL. (2016); KR: BHARAT KUMAR & REDDY (2009); KR11: BHARAT KUMAR ET AL. (2011); CA00: CASTILHO ET AL. (2000); DR02: DRAKE ET AL. (2002); AL11: ALCALÁ ET AL. (2011); CA16: CASEY ET AL. (2016); SM18: SMILJANIC ET AL. (2018).

Name	$T_{\rm eff}$	log g	[Fe/H]	log ϵ(Li)	v sin i	$^{12}C/^{13}C$	Ref.
HD 150382*	4 070	1.35	−0.09	2.10	3.7	18.0	This Work
HD 203136	5 084	2.80	+0.14	2.40	5.1	5.4	TT17, ST00
HD 232862	4 938	3.79	−0.20	2.57	20.2	–	TT17
HD 212430	4 923	2.48	−0.19	1.94	2.0	–	TT17
KIC 9821622	4 923	2.91	−0.25	1.85	1.9	–	TT17
HD 170527	4 896	2.57	−0.35	3.24	22.9	–	TT17
HD 12203	4 842	2.49	−0.32	2.14	2.0	7.5	TT17, KR11
HD 194937	4 786	2.56	−0.03	3.15	1.8	–	TT17
HD 8676	4 774	2.53	−0.11	3.81	1.8	–	TT17
HD 183492	4 765	2.58	+0.06	2.28	2.0	–	TT17
HD 167304	4 761	2.43	+0.04	2.79	2.8	–	TT17, KR11
HD 10437	4 756	2.55	+0.00	3.62	1.9	–	TT17, KR11
HD 214995	4 626	2.43	+0.04	3.06	4.9	–	TT17
PDS 100	4 524	1.98	−0.05	2.59	8.3	9.0	TT17, DR02

Continued on next page

Name	$T_{\rm eff}$	log g	[Fe/H]	log ϵ(Li)	v sin i	^{12}C/^{13}C	Ref.
HD 6665	4 524	2.61	+0.28	2.8	5.2	–	TT17
HD 9746	4 520	2.14	−0.10	3.73	7.2	28.0	TT17
HD 30834	4 283	1.79	−0.24	2.63	2.3	–	TT17
HD 205349	4 138	0.89	−0.18	1.88	6.5	–	TT17
HD 787*	3 980	1.70	+0.00	2.20	2.8	15.0	DS95, TT17
HD 37719	4 650	2.40	+0.09	2.70	–	–	KR11
HD 40168	4 800	2.50	+0.10	1.50	–	–	KR11
HD 51367	4 650	2.55	+0.20	2.58	–	8.5	KR11
HD 88476	5 100	3.10	−0.10	2.12	–	9.0	KR11
HD 107484	4 640	2.50	+0.18	2.04	–	12.5	KR11
HD 118319	4 700	2.20	−0.25	1.88	–	–	KR11
HD 133086	4 940	2.98	+0.02	2.03	–	7.0	KR11
HD 145457	4 850	2.75	−0.08	2.49	–	10.0	KR11
HD 150902	4 690	2.55	+0.09	2.64	–	5.0	KR11
IRAS 12327−6523*	4 200	1.25	−0.40	1.60	7.5	6.0	RL05
IRAS 13539−4153	4 300	2.25	−0.13	4.10	5.0	20.0	RL05
IRAS 17596−3952	4 600	2.50	+0.10	2.20	35.0	–	RL05
HD 19745	4 700	2.25	−0.05	3.70	3.0	16.0	RL05
HD 31993	4 500	2.50	+0.00	1.70	–	–	CA00
HD 95799	4 900	2.50	+0.00	3.30	–	–	CA00
IRAS 19012-0747*	3 800	1.50	+0.00	2.50	–	–	CA00
HD 77361	4 580	2.50	−0.02	3.82	2.8	4.3	KR09
HD 233517	4 475	2.25	−0.37	4.22	–	–	KR09
HD 219025	4 500	2.30	−0.10	3.00	23.0	–	JA99
HD 157457	4 950	2.30	−0.30	1.50	1.0	–	JA99
HD 16771	5 050	2.70	−0.12	2.67	3.7	12.0	RL16
HD 33789	5 000	3.00	−0.30	1.50	29.0	–	FC93
HD 39853*	3 900	1.16	−0.50	2.80	3.1	7.0	GD89
PDS 365	4 540	2.20	−0.09	3.3	20.0	12.0	DR02
IRAS 12556−7731*	3 460	0.60	−0.05	2.40	8.0	–	AL11
J 08095783−4701385	4 964	2.43	−0.15	3.21	–	–	CA16
J 08102116−4740125	4 591	2.27	−0.12	3.33	–	–	CA16
J 08110403−4852137	4 762	2.59	−0.12	3.25	–	–	CA16
J 08395152−5315159	4 726	2.55	+0.01	2.28	–	–	CA16
J 10300194−6321203	4 612	2.37	−0.06	2.88	–	–	CA16
J 10323205−6324012	4 607	2.53	+0.13	2.98	–	–	CA16
J 10495719−6341212	4 789	2.55	+0.03	2.94	–	–	CA16

Continued on next page

Name	$T_{\rm eff}$	log g	[Fe/H]	log ϵ(Li)	v sin i	^{12}C/^{13}C	Ref.
J 10503631−6512237	4 708	2.49	−0.05	2.61	–	–	CA16
J 11000515−7623259	4 505	2.22	+0.06	2.64	–	–	CA16
J 18033785−3009201	4 467	2.34	+0.07	3.11	–	–	CA16
J 19230935+0123293	4 845	2.37	−0.12	2.75	–	–	CA16
J 19242472+0044106	4 740	2.70	+0.08	2.72	–	–	CA16
J 19252571+0031444	4 825	2.87	−0.10	2.22	–	–	CA16
J 19252758+0153065	4 617	2.80	+0.21	2.92	–	–	CA16
J 19252837+0027037	4 731	2.91	+0.18	2.82	–	–	CA16
J 19253819+0031094	4 655	2.51	−0.25	2.85	–	–	CA16
J 19261007−0010200	4 752	2.84	+0.12	2.88	–	–	CA16
J 19264038−0019575	4 782	2.91	+0.02	3.13	–	–	CA16
J 19301883−0004175*	4 070	1.63	−0.52	2.43	–	–	CA16
J 19304281+2016107	4 766	2.63	−0.10	2.60	–	–	CA16
J 08405643−5308309	4 486	2.54	−0.12	2.60	$\leqslant 7.0$	–	SM18
J 17522490−2927512	4 644	2.80	+0.18	2.42	$\leqslant 7.0$	–	SM18
J 17531013−2932063	4 557	2.72	+0.27	2.30	$\leqslant 7.0$	–	SM18
J 18181062−3246291	4 558	2.27	−0.03	2.30	2.5	–	SM18
J 18182698−3242584	4 425	2.33	+0.10	4.04	6.0	–	SM18
J 18265248+0627259	4 982	2.88	−0.08	2.69	37.1	–	SM18
J 19251759+0053140	4 621	2.78	+0.36	2.24	$\leqslant 7.0$	–	SM18
J 19223053+0138518	4 579	2.49	+0.26	2.27	$\leqslant 7.0$	–	SM18
J 19261134+0051569	4 745	2.47	−0.53	3.25	7.5	–	SM18
J 19263808+0054441	4 655	2.82	+0.38	2.29	12.0	–	SM18
J 19264134+0137595	4 645	2.56	+0.28	3.45	$\leqslant 7.0$	–	SM18
J 19264917−0027469	4 458	2.19	−0.39	3.33	7.1	–	SM18
J 19265013+0149070	4 770	2.68	−0.50	3.32	13.2	–	SM18
J 19265193+0044004	4 880	2.54	−0.33	2.80	2.1	–	SM18
J 19270600+0134446	4 584	2.38	+0.19	3.53	$\leqslant 7.0$	–	SM18
J 19270815+0017461	4 514	2.28	−0.29	2.37	7.8	–	SM18
J 19273856+0024149	4 446	2.39	−0.16	2.37	12.0	–	SM18
J 19274706+0023447	4 608	3.21	+0.13	2.70	18.0	–	SM18
J 19280508+0100139	4 623	2.49	+0.11	3.49	8.2	–	SM18
J 19283226+0033072	4 600	2.64	+0.29	3.46	$\leqslant 7.0$	–	SM18

* objects in early-AGB stage.

Tabela A.2: List of spectral lines with atomic parameters and equivalent width (EW) for HD 150382.

Element	λ (Å)	χ (eV)	$\log gf$	EW (mÅ)
Mg I	5 711.10	4.34	−1.750	154
	6 319.24	5.11	−2.160	76
	6 319.49	5.11	−2.670	36
	8 712.69	5.93	−1.260	69
	8 736.04	5.94	−0.340	144
Al I	6 696.03	3.14	−1.481	119
	6 698.67	3.14	−1.630	95
	7 835.32	4.04	−0.580	93
	7 836.13	4.02	−0.400	111
	8 772.88	4.02	−0.250	138
Ca I	5 867.57	2.93	−1.610	90
	6 798.47	2.71	−2.520	66
Ti I	4 758.12	2.25	+0.420	138
	5 295.78	1.05	−1.631	139
	6 091.18	2.27	−0.370	125
Cr I	4 936.34	3.11	−0.250	123
	4 953.71	3.12	−1.480	60
	5 241.45	2.71	−1.921	66
	5 272.01	3.45	−0.420	90
	5 287.20	3.44	−0.870	75
	5 628.62	3.42	−0.740	76
	5 719.81	3.01	−1.580	66
	5 787.04	3.01	−1.551	74
	5 844.59	3.01	−1.772	67
	5 884.43	3.01	−1.860	56
Fe I	4 988.95	4.15	−0.790	113
	5 002.79	3.40	−1.440	140
	5 031.91	4.37	−1.520	71
	5 253.03	2.28	−3.790	99
	5 315.05	4.37	−1.400	77
	5 373.71	4.47	−0.710	112
	5 417.03	4.42	−1.530	71
	5 441.34	4.31	−1.580	82
	5 560.21	4.43	−1.040	85

Continued on next page

Element	λ (Å)	χ (eV)	$\log gf$	EW (mÅ)
	5 584.77	3.57	−2.170	93
	5 635.82	4.26	−1.740	73
	5 638.26	4.22	−0.720	131
	5 691.50	4.30	−1.370	81
	5 705.47	4.30	−1.360	85
	5 717.83	4.28	−0.979	107
	5 731.76	4.26	−1.150	108
	5 814.81	4.28	−1.820	69
	5 934.65	3.93	−1.020	132
	6 027.05	4.08	−1.090	111
	6 093.64	4.61	−1.350	60
	6 096.66	3.98	−1.780	85
	6 120.25	0.91	−5.950	109
	6 165.36	4.14	−1.470	89
	6 187.99	3.94	−1.570	100
	6 311.50	2.83	−3.230	98
	6 392.54	2.28	−4.030	104
	6 436.41	4.19	−2.460	44
	6 551.68	0.99	−5.790	117
	6 608.03	2.28	−4.030	100
	6 653.85	4.14	−2.520	37
	6 703.57	2.76	−3.160	120
	6 704.48	4.22	−2.660	30
	6 739.52	1.56	−4.950	109
	6 793.26	4.07	−2.470	56
	7 132.99	4.08	−1.610	100
Fe II	5 284.10	2.89	−3.010	74
	5 325.56	3.22	−3.170	48
	5 425.25	3.20	−3.210	50
	6 247.55	3.89	−2.340	38
	6 432.68	2.89	−3.580	47
Ni I	5 003.75	1.68	−3.070	113
	5 010.94	3.63	−0.979	78
	5 035.36	3.64	+0.290	148
	5 157.98	3.61	−1.510	60
	6 007.31	1.68	−3.400	108
	6 176.82	4.09	−0.260	97

Continued on next page

Element	λ (Å)	χ (eV)	$\log gf$	EW (mÅ)
	6 177.25	1.83	−3.460	90
	6 204.61	4.09	−1.080	60
	6 223.99	4.11	−0.910	63
	6 378.26	4.15	−0.821	68
Y II	5 087.43	1.08	−0.170	119
	5 289.81	1.03	−1.850	47
Zr I	4 772.30	0.62	−0.060	114
	4 784.94	0.69	−0.600	93
	4 805.87	0.69	−0.580	85
	4 828.05	0.62	−0.750	82
	5 046.55	1.53	−0.180	52
	5 385.13	0.52	−0.640	99
	5 437.77	0.15	−2.120	67
	5 620.13	0.52	−1.090	86
	6 032.60	1.48	−0.350	39
	6 127.46	0.15	−1.060	130
	6 134.57	0.00	−1.280	125
	6 140.46	0.52	−1.410	58
	6 143.18	0.07	−1.100	134
Ce II	4 562.37	0.48	+0.330	108
	5 274.24	1.04	+0.130	68
	6 043.37	1.21	−0.480	33
Nd II	4 947.02	0.56	-1.130	37
	5 089.83	0.20	-1.160	76
	5 092.79	0.38	-0.610	74
	5 276.87	0.86	-0.440	51
	5 356.97	1.26	-0.280	34

Tabela A.3: Observed Fe I and Fe II lines for NGC 2345.

				Equivalent Widths (mÅ)				
				NGC 2345 - #				
Element	λ (Å)	χ (eV)	$\log gf$	14	34	43	50	60
Fe I	5 775.080	4.220	−1.300	119	116	112	113	120
	5 848.129	4.607	−0.900	102	80	97	108	106
	5 902.473	4.593	−1.750	43	—	42	40	37
	6 027.050	4.076	−1.300	131	141	124	126	130

Continued on next page

				Equivalent Widths (mÅ)				
				NGC 2345 - #				
Element	λ (Å)	χ (eV)	$\log gf$	14	34	43	50	60
	6 093.644	4.607	−1.410	65	64	69	71	—
	6 096.665	3.984	−1.810	92	76	85	91	93
	6 098.244	4.558	−1.800	59	45	—	—	—
	6 120.249	0.915	−5.950	119	46	99	131	133
	6 151.618	2.176	−3.300	—	146	—	—	—
	6 187.990	3.943	−1.650	112	91	109	110	113
	6 574.228	0.990	−5.000	—	143	—	—	—
	6 703.567	2.759	−3.150	132	114	127	144	140
	6 725.357	4.103	−2.300	65	40	59	61	63
	6 726.666	4.607	−1.170	88	85	90	82	86
	7 421.558	4.638	−1.800	43	31	39	56	46
	7 547.896	5.099	−1.100	45	—	40	44	44
	7 723.208	2.279	−3.620	—	133	144	—	—
Fe II	5 264.812	3.230	−3.130	—	140	63	—	53
	5 425.257	3.200	−3.220	–	128	68	57	54
	6 247.557	3.892	−2.300	58	—	—	—	—
	6 369.462	2.891	−4.110	41	92	38	39	35
	6 432.680	2.891	−3.570	71	143	70	—	59
	6 456.383	3.904	−2.050	68	—	80	64	64

Tabela A.4: Observed lines of other elements for NGC 2345.

				Equivalent Widths (mÅ)				
				NGC 2345 - #				
Element	λ (Å)	χ (eV)	$\log gf$	14	34	43	50	60
Na I	4 751.820	2.100	−2.095	83	47	—	90	77
	5 148.840	2.100	−2.095	75	—	—	—	—
	6 154.220	2.100	−2.095	130	82	102	130	—
	6 160.750	2.100	−1.261	—	108	112	144	141
Mg I	4 730.040	4.340	−2.390	—	—	114	118	107
	6 319.240	5.110	−2.160	61	—	—	—	—
	6 319.490	5.110	−2.670	30	—	—	—	—
	7 387.700	5.750	−0.870	95	—	—	—	—
	8 712.690	5.930	−1.260	—	—	85	—	75

Continued on next page

				Equivalent Widths (mÅ) NGC 2345 - #				
Element	λ (Å)	χ (eV)	$\log gf$	14	34	43	50	60
	8 717.830	5.910	−0.970	103	97	89	100	106
	8 736.040	5.940	−0.340	132	143	—	148	145
Al I	6 698.670	3.140	−1.630	104	52	77	103	96
	7 835.320	4.040	−0.580	—	83	—	89	92
	7 836.130	4.020	−0.400	111	82	92	105	107
	8 772.880	4.020	−0.250	121	123	116	124	121
	8 773.910	4.020	−0.070	—	—	135	—	145
Si I	5 793.080	4.930	−2.060	74	90	78	73	69
	6 125.030	5.610	−1.540	—	57	—	—	—
	6 131.577	5.620	−1.685	32	—	37	28	—
	6 145.020	5.610	−1.430	46	—	49	40	43
	6 155.140	5.620	−0.770	95	116	100	88	93
	7 760.640	6.200	−1.280	—	—	—	18	—
	7 800.000	6.180	−0.720	—	78	—	—	—
	8 728.010	6.180	−0.360	59	—	70	44	72
	8 742.450	5.870	−0.510	95	—	—	92	—
Ca I	5 867.572	2.930	−1.610	84	41	71	84	79
	6 166.440	2.520	−1.140	147	135	—	—	—
	6 455.600	2.510	−1.290	—	126	139	—	—
	6 464.680	2.520	−2.420	—	—	—	—	108
	6 798.467	2.710	−2.520	58	15	32	60	46
Ti I	4 778.260	2.240	−0.330	103	44	92	117	—
	4 820.410	1.500	−0.440	—	141	—	—	—
	5 009.660	0.020	−2.260	—	126	—	—	—
	5 062.100	2.160	−0.460	—	44	90	—	—
	5 223.630	2.090	−0.561	114	—	95	—	—
	5 295.780	1.050	−1.631	—	62	—	—	—
	5 503.900	2.580	−0.190	—	—	—	124	—
	5 689.480	2.300	−0.470	107	—	85	118	—
	5 922.120	1.050	−1.470	—	113	—	—	—
	6 091.180	2.270	−0.420	127	56	93	138	—
	6 126.220	1.070	−1.420	—	108	—	—	—
	6 554.240	1.440	−1.220	—	72	126	—	—
Cr I	4 790.340	2.544	−1.480	92	—	—	105	—
	4 870.800	3.078	−0.010	—	115	—	—	—

Continued on next page

				Equivalent Widths (mÅ)				
				NGC 2345 - #				
Element	λ (Å)	χ (eV)	$\log gf$	14	34	43	50	60
	4 887.680	2.543	−2.071	58	—	42	65	—
	4 936.340	3.112	−0.250	118	73	101	129	—
	4 953.710	3.120	−1.480	—	—	—	70	37
	5 067.720	2.708	−1.070	—	60	—	—	—
	5 144.660	2.709	−1.371	106	49	—	—	94
	5 200.210	3.384	−0.580	—	—	—	—	103
	5 238.960	2.708	−1.270	85	34	—	93	—
	5 241.450	2.709	−1.921	—	—	36	61	—
	5 265.160	3.427	−0.350	—	—	93	—	113
	5 272.010	3.448	−0.420	—	—	74	86	—
	5 287.200	3.437	−0.870	73	—	46	75	61
	5 304.180	3.462	−0.670	—	34	—	—	—
	5 312.870	3.448	−0.550	—	37	—	70	—
	5 344.790	3.448	−0.990	—	—	38	—	—
	5 628.620	3.420	−0.740	64	—	55	71	—
	5 664.040	3.434	−0.710	92	58	79	92	—
	5 712.750	3.010	−1.030	—	—	—	107	—
	5 719.810	3.012	−1.580	58	—	38	64	46
	5 787.040	3.012	−1.551	—	—	45	67	—
	5 838.650	3.010	−1.821	—	—	—	68	45
	5 844.590	3.012	−1.772	59	—	42	67	—
	5 884.430	3.012	−1.860	59	—	37	55	—
Ni I	4 913.980	3.740	−0.600	—	—	—	97	—
	4 953.210	3.740	−0.580	—	110	—	—	—
	4 967.520	3.800	−1.600	—	—	—	52	—
	5 003.750	1.677	−3.070	—	—	110	—	—
	5 010.940	3.635	−0.979	95	96	94	—	—
	5 084.110	3.677	−0.180	—	—	—	118	—
	5 157.980	3.606	−1.510	59	—	—	—	53
	5 388.344	1.935	−3.510	—	61	—	—	—
	5 435.856	1.986	−2.580	—	128	—	—	—
	5 748.360	1.677	−3.240	—	—	109	—	—
	6 007.310	1.677	−3.400	—	88	105	—	—
	6 086.290	4.270	−0.470	—	—	—	76	—
	6 111.080	4.090	−0.830	—	—	—	69	—

Continued on next page

				Equivalent Widths (mÅ) NGC 2345 - #				
Element	λ (Å)	χ (eV)	$\log gf$	14	34	43	50	60
	6 128.980	1.677	−3.429	—	105	—	—	—
	6 176.820	4.089	−0.260	106	110	99	107	99
	6 177.250	1.826	−3.460	—	66	86	99	97
	6 186.720	4.110	−0.900	—	—	—	73	—
	6 204.610	4.089	−1.080	70	52	57	72	73
	6 223.990	4.106	−0.910	59	—	60	60	70
	6 327.600	1.677	−3.170	—	136	—	—	—
	6 378.260	4.154	−0.821	—	—	78	—	—
	6 532.873	1.945	−3.350	—	97	—	—	—
	6 586.320	1.951	−2.780	148	116	—	—	—
	6 772.320	3.660	−1.013	—	—	—	116	—
Y II	5 200.415	0.990	−0.570	156	—	143	163	—
	5 289.815	1.030	1.850	56	72	54	63	50
	5 402.783	1.840	−0.440	95	104	72	100	91
Zr I	4 772.300	0.620	−0.060	116	22	82	131	—
	4 784.940	0.690	−0.600	69	—	44	97	66
	4 805.870	0.690	−0.580	72	—	41	83	—
	4 828.050	0.620	−0.750	74	—	40	91	79
	5 046.550	1.530	−0.180	—	—	17	—	—
	5 385.130	0.520	−0.640	91	13	53	107	—
	5 437.770	0.150	−2.120	—	—	—	63	35
	5 620.130	0.520	−1.090	79	—	47	88	67
	5 885.620	0.070	−1.730	69	—	27	80	—
	6 032.600	1.480	−0.350	35	—	—	45	24
	6 127.460	0.150	−1.060	130	23	84	150	—
	6 134.570	0.000	−1.280	122	16	74	146	—
	6 140.460	0.520	−1.410	55	—	24	67	41
	6 143.180	0.070	−1.100	140	31	—	—	—
La II	4 934.830	1.250	−0.920	—	36	—	—	—
	5 303.530	0.320	−1.350	82	—	71	86	77
	5 880.630	0.235	−1.830	65	—	48	75	—
	6 320.429	0.170	−1.520	107	—	85	115	100
	6 390.480	0.320	−1.410	103	96	75	—	89
	6 774.330	0.120	−1.709	109	98	82	108	103
Ce II	4 486.909	0.295	−0.180	—	—	—	—	123

Continued on next page

				Equivalent Widths (mÅ)				
				NGC 2345 - #				
Element	λ (Å)	χ (eV)	$\log gf$	14	34	43	50	60
	4 562.370	0.480	0.210	—	—	—	—	122
	4 628.160	0.520	0.140	130	—	—	—	125
	5 187.457	1.211	0.170	90	79	68	—	71
	5 274.236	1.044	0.130	77	94	71	—	75
	5 330.580	0.869	−0.400	72	68	—	—	64
	5 975.818	1.326	−0.450	—	—	26	—	—
	6 043.373	1.205	−0.480	—	43	31	—	—
Nd II	4 706.540	0.000	−0.710	119	124	104	—	—
	4 709.720	0.182	−0.970	—	119	—	—	—
	4 763.620	0.380	−1.270	—	—	—	56	50
	4 777.720	0.380	−1.220	—	94	—	—	—
	4 797.150	0.559	−0.690	—	—	—	77	75
	4 859.030	0.320	−0.440	—	—	—	—	111
	4 914.380	0.380	−0.699	—	—	99	—	97
	4 959.119	0.320	−0.800	—	135	—	—	—
	4 987.160	0.742	−0.790	—	—	54	72	—
	5 063.722	0.976	−0.620	—	42	—	—	57
	5 092.800	0.380	−0.610	—	100	85	93	91
	5 212.361	0.200	−0.960	—	108	—	—	—
	5 306.460	0.859	−0.970	—	—	—	—	44
	5 311.460	0.980	−0.420	—	96	—	—	—
	5 356.970	1.263	−0.280	45	—	—	52	45
	5 485.700	1.263	−0.120	71	76	69	75	65
	5 740.875	1.160	−0.530	53	45	41	54	52
	5 811.570	0.859	−0.860	57	—	42	60	49
Sm II	4 478.654	0.659	−0.360	—	85	—	—	—
	4 499.475	0.248	−0.870	80	—	—	—	65
	4 536.510	0.104	−1.280	—	49	—	—	—
	4 566.202	0.333	−0.590	90	—	75	90	—
	4 642.230	0.380	−0.460	—	—	—	—	75
	4 676.900	0.040	−0.870	102	91	—	106	89
	4 704.400	0.000	−0.860	108	—	89	112	97
	4 791.600	0.100	−1.440	—	—	62	—	—

Tabela A.5: Observed Fe I and Fe II lines for NGC 6124.

				Equivalent Widths (mÅ)			
				NGC 6124 - #			
Element	λ (Å)	χ (eV)	log gf	14	29	36	233
Fe I	5002.79	3.40	-1.440	124	141	—	134
	5014.94	3.94	-0.270	—	—	—	166
	5022.24	3.98	-0.490	148	—	—	165
	5031.91	4.37	-1.520	74	73	—	71
	5044.21	2.85	-2.040	130	141	147	—
	5074.75	4.22	-0.160	152	160	—	—
	5159.06	4.28	-0.650	—	—	126	115
	5242.49	3.63	-0.970	141	—	160	—
	5253.03	2.28	-3.790	104	78	81	71
	5288.52	3.69	-1.510	110	120	121	112
	5315.05	4.37	-1.400	78	85	88	78
	5321.11	4.43	-1.190	82	77	83	78
	5322.04	2.28	-2.840	142	133	155	136
	5364.87	4.45	+0.230	—	159	—	—
	5373.71	4.47	-0.710	96	99	111	104
	5389.48	4.42	-0.250	—	—	143	135
	5417.03	4.42	-1.530	72	69	74	68
	5441.34	4.31	-1.580	79	69	73	67
	5445.04	4.39	+0.041	167	153	—	166
	5522.45	4.21	-1.400	83	93	90	82
	5531.98	4.91	-1.460	48	43	45	—
	5560.21	4.43	-1.040	87	83	92	86
	5567.39	2.61	-2.560	—	149	168	152
	5576.09	3.43	-0.850	166	166	—	—
	5584.77	3.57	-2.170	92	—	87	82
	5624.02	4.39	-1.330	85	87	98	89
	5633.95	4.99	-0.120	102	105	110	101
	5635.82	4.26	-1.740	69	61	69	63
	5638.26	4.22	-0.720	116	121	128	119
	5691.50	4.30	-1.370	98	92	96	86
	5705.47	4.30	-1.360	78	82	77	70
	5717.83	4.28	-0.979	—	118	116	—
	5731.76	4.26	-1.150	101	99	111	104

Continued on next page

				Equivalent Widths (mÅ) NGC 6124 - #			
Element	λ (Å)	χ (eV)	log gf	14	29	36	233
	5806.73	4.61	-0.900	92	91	103	90
	5814.81	4.28	-1.820	50	49	51	50
	5852.22	4.55	-1.180	89	93	91	81
	5883.82	3.96	-1.210	127	—	130	120
	5916.25	2.45	-2.990	146	—	—	144
	5934.65	3.93	-1.020	130	136	145	129
	6024.06	4.55	-0.060	144	145	159	162
	6027.05	4.08	-1.090	109	112	126	120
	6056.01	4.73	-0.400	—	107	118	116
	6079.01	4.65	-0.970	79	80	88	80
	6082.71	2.22	-3.580	112	—	115	106
	6093.64	4.61	-1.350	—	68	61	60
	6096.66	3.98	-1.780	76	80	82	76
	6120.25	0.91	-5.950	64	64	58	44
	6151.62	2.18	-3.290	131	—	140	124
	6157.73	4.08	-1.110	124	130	146	132
	6165.36	4.14	-1.470	90	88	95	88
	6173.34	2.22	-2.880	160	159	—	157
	6187.99	3.94	-1.570	94	91	100	93
	6200.31	2.60	-2.440	141	143	164	150
	6311.50	2.83	-3.230	106	—	—	—
	6322.69	2.59	-2.430	154	149	170	156
	6380.74	4.19	-1.320	113	115	110	103
	6392.54	2.28	-4.030	78	—	82	66
	6419.95	4.73	-0.090	118	—	140	135
	6436.41	4.19	-2.460	44	—	—	33
	6469.19	4.83	-0.620	—	—	119	110
	6551.68	0.99	-5.790	82	80	62	49
	6574.23	0.99	-5.020	133	121	135	111
	6597.56	4.79	-0.920	78	74	83	72
	6608.03	2.28	-4.030	84	84	80	72
	6609.11	2.56	-2.690	161	153	167	154
	6646.93	2.61	-3.990	71	—	—	55
	6653.85	4.14	-2.520	28	33	26	25
	6699.14	4.59	-2.190	21	18	23	20

Continued on next page

				Equivalent Widths (mÅ) NGC 6124 - #			
Element	λ (Å)	χ (eV)	log gf	14	29	36	233
	6703.57	2.76	-3.160	112	105	116	103
	6704.48	4.22	-2.660	18	21	16	12
	6713.74	4.79	-1.600	48	40	39	37
	6739.52	1.56	-4.950	77	68	68	56
	6745.96	4.07	-2.770	24	—	20	18
	6750.15	2.42	-2.620	152	155	—	159
	6752.71	4.64	-1.200	—	—	95	81
	6783.70	2.59	-3.980	79	—	—	—
	6793.26	4.07	-2.470	36	—	32	34
	6806.85	2.73	-3.210	109	103	113	105
	6810.26	4.61	-0.990	96	86	93	87
	6820.37	4.64	-1.170	86	90	93	85
	6851.64	1.61	-5.320	71	—	—	46
	6858.15	4.61	-0.930	86	92	89	89
	7130.92	4.22	-0.700	153	—	161	160
	7132.99	4.08	-1.610	81	104	98	97
Fe II	4620.52	2.84	-3.230	94	95	123	116
	4993.35	2.81	-3.670	73	—	84	91
	5132.66	2.81	-4.000	58	—	73	72
	5197.56	3.23	-2.250	128	—	—	—
	5234.62	3.22	-2.240	124	131	—	—
	5325.56	3.22	-3.170	69	67	95	95
	5414.05	3.22	-3.620	49	50	78	74
	5425.25	3.20	-3.210	71	72	99	97
	5991.37	3.15	-3.560	66	—	92	—
	6084.10	3.20	-3.800	—	—	—	68
	6149.25	3.89	-2.720	67	59	81	79
	6247.55	3.89	-2.340	86	90	110	—
	6416.92	3.89	-2.680	60	61	82	82
	6432.68	2.89	-3.580	77	65	96	96

Tabela A.6: Observed lines of other elements for NGC 6124.

				Equivalent Widths (mÅ)			
				NGC 6124 - #			
Element	λ (Å)	χ (eV)	log gf	14	29	36	233
Na I	4751.82	2.10	-2.095	—	—	—	35
	5148.84	2.10	-2.058	—	49	—	—
	6154.22	2.10	-1.560	85	—	95	85
	6160.75	2.10	-1.261	103	105	117	105
Mg I	4730.04	4.34	-2.390	108	—	—	100
	5711.10	4.34	-1.750	147	148	—	152
	8712.69	5.93	-1.260	53	—	—	—
	8717.83	5.91	-0.970	105	95	105	96
	8736.04	5.94	-0.340	133	146	142	140
Al I	6696.03	3.14	-1.481	76	—	—	—
	6698.67	3.14	-1.630	52	59	56	46
	7835.32	4.04	-0.580	73	79	—	72
	7836.13	4.02	-0.400	86	85	84	81
	8772.88	4.02	-0.250	119	100	116	107
Si I	5793.08	4.93	-2.060	81	70	84	85
	6125.03	5.61	-1.540	46	48	61	55
	6131.58	5.62	-1.685	42	—	—	—
	6145.02	5.61	-1.430	52	57	63	60
	6155.14	5.62	-0.770	99	96	112	109
	7760.64	6.20	-1.280	22	26	32	31
	7800.00	6.18	-0.720	57	—	—	81
	8728.01	6.18	-0.360	—	—	—	93
	8742.45	5.87	-0.510	114	—	134	128
Ca I	5581.80	2.52	-0.670	—	—	153	—
	5857.46	2.93	+0.110	161	—	—	—
	5867.57	2.93	-1.610	52	54	50	55
	6161.30	2.52	-1.270	122	129	128	118
	6166.44	2.52	-1.140	122	118	129	123
	6169.04	2.52	-0.800	145	146	—	149
	6169.56	2.53	-0.480	161	—	—	169
	6449.82	2.52	-0.500	—	—	—	157
	6455.60	2.51	-1.290	116	114	119	112

Continued on next page

				Equivalent Widths (mÅ) NGC 6124 - #			
Element	λ (Å)	χ (eV)	log gf	14	29	36	233
	6471.66	2.51	-0.690	150	147	—	146
	6499.65	2.52	-0.810	145	—	—	152
	6798.47	2.71	-2.520	24	—	20	19
Ti I	4512.74	0.84	-0.480	152	—	148	—
	4562.64	0.02	-2.660	93	—	—	65
	4617.28	1.75	+0.389	—	—	136	126
	4758.12	2.25	+0.420	106	113	94	87
	4759.28	2.25	+0.511	—	—	100	94
	4820.41	1.50	-0.440	—	—	134	—
	5087.06	1.43	-0.840	110	—	101	91
	5113.45	1.44	-0.880	—	—	90	74
	5147.48	0.00	-2.010	—	148	157	137
	5295.78	1.05	-1.631	—	76	63	55
	5866.46	1.07	-0.839	150	—	155	135
	6091.18	2.27	-0.370	71	68	—	54
	6126.22	1.05	-1.370	110	108	105	89
	6258.11	1.44	-0.360	—	—	134	120
Cr I	4790.34	2.54	-1.480	60	59	51	44
	4836.87	3.10	-1.090	56	—	54	49
	4936.34	3.11	-0.250	—	—	86	77
	4953.71	3.12	-1.480	—	—	20	—
	5013.31	2.71	-0.770	100	—	—	—
	5067.72	2.71	-1.070	90	94	88	77
	5144.66	2.71	-1.371	68	62	67	55
	5192.00	3.39	-0.400	—	—	68	—
	5200.21	3.38	-0.580	72	—	—	—
	5238.96	2.71	-1.270	—	55	44	40
	5241.45	2.71	-1.921	—	—	18	13
	5272.01	3.45	-0.420	—	—	50	—
	5287.20	3.44	-0.870	37	43	39	35
	5304.18	3.46	-0.670	51	50	—	31
	5318.81	3.44	-0.670	43	50	43	—
	5344.79	3.45	-0.990	28	—	17	—
	5628.62	3.42	-0.740	41	—	38	—
	5712.75	3.01	-1.030	72	68	—	45

Continued on next page

				Equivalent Widths (mÅ) NGC 6124 - #			
Element	λ (Å)	χ (eV)	log gf	14	29	36	233
	5719.81	3.01	-1.580	—	24	26	24
	5787.04	3.01	-1.551	40	34	—	30
	5788.39	3.01	-1.491	31	37	33	20
	5844.59	3.01	-1.772	31	—	—	—
	5884.43	3.01	-1.860	16	—	—	—
Ni I	4519.98	1.68	-3.080	—	—	—	108
	4866.27	3.54	-0.220	—	120	—	131
	4953.21	3.74	-0.580	105	96	119	108
	5003.75	1.68	-3.070	—	—	—	91
	5010.94	3.63	-0.979	89	81	99	91
	5157.98	3.61	-1.510	—	—	50	42
	5388.34	1.94	-3.510	77	74	74	68
	5435.86	1.99	-2.580	116	112	135	—
	5578.73	1.68	-2.830	127	127	—	—
	5587.87	1.94	-2.390	—	—	143	—
	5748.36	1.68	-3.240	—	—	107	98
	5847.01	1.68	-3.460	94	—	98	—
	6007.31	1.68	-3.400	—	—	88	82
	6108.12	1.68	-2.600	151	—	—	154
	6128.98	1.68	-3.429	102	103	110	104
	6176.82	4.09	-0.260	—	93	104	101
	6177.25	1.83	-3.460	68	65	68	60
	6204.61	4.09	-1.080	—	63	60	55
	6223.99	4.11	-0.910	60	62	60	59
	6327.60	1.68	-3.170	122	121	130	—
	6378.26	4.15	-0.821	75	—	81	71
	6532.87	1.94	-3.350	76	—	—	68
	6586.32	1.95	-2.780	118	110	126	115
Y II	5087.43	1.08	-0.170	—	—	143	133
	5200.41	0.99	-0.570	—	—	—	127
	5289.81	1.03	-1.850	35	33	47	47
	5402.78	1.84	-0.440	60	57	74	76
Zr I	4772.30	0.62	-0.060	49	49	35	37
	4815.63	0.60	-0.270	—	—	22	—
	5385.13	0.52	-0.640	—	25	20	—

Continued on next page

				Equivalent Widths (mÅ) NGC 6124 - #			
Element	λ (Å)	χ (eV)	log gf	14	29	36	233
	5680.91	0.54	-0.860	—	—	—	13
	6127.46	0.15	-1.060	42	38	30	22
	6134.57	0.00	-1.280	35	30	27	21
	6143.18	0.07	-1.100	46	43	37	30
Ce II	4418.79	0.86	+0.270	—	—	90	92
	4486.91	0.29	-0.180	93	—	—	—
	4562.37	0.48	+0.210	91	90	—	115
	4628.16	0.52	+0.140	86	82	—	—
	5187.46	1.21	+0.170	47	47	59	59
	5274.24	1.04	+0.130	64	56	63	59
	5330.58	0.87	-0.400	29	28	43	42
	5975.82	1.33	-0.450	—	—	19	18
	6043.37	1.21	-0.480	21	—	—	29
Nd II	4706.54	0.00	-0.710	83	76	103	93
	4914.38	0.38	-0.699	73	—	74	76
	4987.16	0.74	-0.790	—	—	40	32
	5063.72	0.98	-0.620	—	—	31	28
	5092.80	0.38	-0.610	57	59	66	—
	5130.59	1.30	+0.450	—	—	66	—
	5234.19	0.55	-0.510	—	61	—	81
	5293.16	0.82	+0.100	92	—	—	—
	5306.46	0.86	-0.970	—	—	22	17
	5311.46	0.98	-0.420	40	—	—	—
	5485.70	1.26	-0.120	40	39	47	45
	5740.88	1.16	-0.530	19	—	28	26
	5811.57	0.86	-0.860	25	20	25	26
Sm II	4206.12	0.38	-0.720	—	37	—	—
	4220.66	0.54	-0.440	—	—	—	65
	4318.94	0.28	-0.250	—	—	—	88
	4421.13	0.38	-0.489	—	—	—	52
	4467.34	0.66	+0.150	—	—	—	66
	4478.65	0.66	-0.360	—	47	60	—
	4499.48	0.25	-0.870	—	—	44	41
	4523.91	0.43	-0.390	—	—	72	—
	4566.20	0.33	-0.590	55	—	—	54

Continued on next page

				Equivalent Widths (mÅ)			
				NGC 6124 - #			
Element	λ (Å)	χ (eV)	log gf	14	29	36	233
	4642.23	0.38	-0.460	67	59	67	59
	4676.90	0.04	-0.870	68	56	64	55
	4704.40	0.00	-0.860	—	59	82	74
	4791.60	0.10	-1.440	—	26	30	28